Title
Cardiac Memory in the Genesis of Arrhythmias

Author
Landaw, Julian William

Publication Date
2019

Peer reviewed|Thesis/dissertation

UNIVERSITY OF CALIFORNIA

Los Angeles

Cardiac Memory in the Genesis of Arrhythmias

A dissertation submitted in partial satisfaction

of the requirements for the degree

Doctor of Philosophy in Biomathematics

by

Julian William Landaw

2019

ABSTRACT OF THE DISSERTATION

Cardiac Memory in the Genesis of Arrhythmias

by

Julian William Landaw
Doctor of Philosophy in Biomathematics
University of California, Los Angeles, 2019
Professor Zhilin Qu, Chair

Dynamical instabilities in the heart promote arrhythmias and sudden cardiac death (SCD), one of the most common causes of death in individuals with cardiovascular disease. Beat-to-beat changes in electrophysiological properties at the cellular level can promote arrhythmogenesis at the whole-heart level, yet the precise mechanisms are not well understood.

Cardiac cells possess memory, whereby certain physiological properties depend on the prior history. Here, we analyze the effects of short-term cardiac memory from two sources: the slow recovery of ion channels and the slow accumulation of ion concentrations over time. We demonstrate that under diseased conditions, namely early repolarization syndrome and long QT syndrome, action potentials become unstable during fixed pacing due to enhanced effects of memory on action potential duration. We develop new iterated map models that explicitly incorporates the effects of memory on action potential duration, and show that the dynamics of the iterated map models match very closely to the dynamics of detailed action potential models. Using the iterated map models, we propose new techniques of controlling action potential instability under the influence of memory and confirm their efficacy in the detailed action potential models.

Finally, we show that action potential instability at the cellular level can generate arrhythmias at tissue-scale levels. In a model of early repolarization syndrome driven by activation of small-conductance Ca^{2+}-activated K^+ (SK) channels, action potential instability promotes phase 2 reentry. Spiral wave dynamics become unstable due to early repolarization driven by the transient outward K^+ current (I_{to}), suggesting that action potential instability induced by memory is a mechanism of arrhythmias like ventricular fibrillation.

The dissertation of Julian William Landaw is approved.

James N. Weiss

Riccardo Olcese

Tom Chou

Zhilin Qu, Committee Chair

University of California, Los Angeles

2019

I dedicate this work to my mom,

who has always supported me through the good and the bad.

Thank you for everything that you've done for me.

Table of Contents

List of Figures

Acknowledgments

It's been quite the journey. None of my work in graduate school could have been achieved without the mentorship and support from countless people in my life, from all of my wonderful friends and family to my professors and research mentors at UC Berkeley and UCLA.

I would first like to thank my PhD mentor Dr. Zhilin Qu. I first got to know him during a summer research rotation in 2014 after having just finished my first year in medical school. It was soon very clear to me that I wanted to join his lab. Not only was the research very exciting and inspiring for me at an intellectual level, but he also provided a very fun working environment where I could explore new ideas and run with them. During our one-on-one meetings, we would bounce new thoughts and ideas off each other while at the same having a fun time enjoying each other's company. The past few years working with Dr. Qu have been so wonderful, and I could not have asked for a better mentor. Thank you Zhilin for all that you've done for me.

While working with Dr. Qu, I also had the privilege of getting to know several fantastic collaborators and fellow mentees. The extent of my work could not have been accomplished without the direction and advice from members of the UCLA arrhythmia group. I would like to acknowledge in particular Dr. James N. Weiss, Dr. Riccardo Olcese, Dr. Alan Garfinkel, Dr. Hrayr Karagueuzian, and Dr. Thao P. Nguyen. Each of them provided unique advice to me over the years that have molded me to what I am today and to how I hope to be as a future researcher and physician scientist. I have learned so much from our weekly Wednesday meetings, where I had the opportunity not only to hear about future directions in our research but also to present my research and receive feedback on my work and how to improve on delivering presentations.

I would also like to acknowledge my fellow MSTP student Michael Liu as well as Dr. Zhen Song, both of whom were with me at every point in my journey as a graduate student working with Dr. Qu. I will never forget all the help and advice I received from them, especially when it came to writing good code and improving computer programming techniques necessary for running CPU and GPU simulations in our lab. I am also very happy for getting to know Dr. Christopher Ko during our weekly meetings when he was a graduate student of Dr. Weiss.

None of my work could have been accomplished without the professors in the Biomathematics department at UCLA who were excellent teachers and advisors and gave me the tools necessary to be a mathematical modeler in biology. In particular, I would like to acknowledge Dr. Tom Chou, Dr. Kenneth Lange, Dr. Marc Suchard, Dr. Van Savage, and Dr. Janet Sinsheimer.

I would also like to thank my undergraduate research mentor Dr. Rainer Sachs, who gave me the opportunity to work for him as an undergraduate student researcher at UC Berkeley. It was with him that I saw first-hand the power of mathematical modeling in biology and medicine, and his encouragement helped inspire me to pursue a career as a physician scientist.

Finally, I would like to thank all my friends and family who have consistently supported me throughout my journey. To my mom Elizabeth, my dad Elliot, and my older brother Max, thank you for giving me a supportive environment growing up that allowed me to be who I am today. I am very thankful to have been brought up in a very intellectual household that also has a very fun and goofy sense of humor. To my sister-in-law Liz, who has really become a caring sister to me the past few years, and who has made me a proud uncle to my adorable niece Noa. To my friends, especially my best friend and wonderful companion Jennifer, who have been with me through all these years. An extra special thanks goes to my mom, who has done almost everything imaginable she could do to make sure I was cared for and safe. I always strive to make her proud, and I hope I have.

Vita

2013–present	Medical Scientist Training Program (T32 GM008082), UCLA David Geffen School of Medicine
2018–present	NRSA Fellowship (F30 HL140864)
2017	Graduate Division Award, UCLA Graduate Divison
2016	M.S. (Biomathematics)
2016–present	Graduate Student Researcher, Cardiology Department, UCLA
2016–2018	Systems and Integrative Biology Training Program (T32 GM008185); renewed 2017
2016–2018	Instructor for Problem-Based Learning (PBL), UCLA David Geffen School of Medicine
2014–2016	Instructor for Statistics in Medicine, UCLA David Geffen School of Medicine
2012	B.A. (Applied Mathematics & Statistics), UC Berkeley; Graduated with highest honors
2012	Dorothea Klumpke Roberts Prize for truly exceptional scholarship in mathematics, Department of Mathematics, UC Berkeley
2012	Phi Beta Kappa member, UC Berkeley

Publications

Landaw, J. and Qu, Z. Control of voltage-driven instabilities in cardiac myocytes with memory. *Chaos: An Interdisciplinary Journal of Nonlinear Science*, 28(11):113122, 2018.

Landaw, J. and Qu, Z. Memory-induced nonlinear dynamics of excitation in cardiac diseases. *Physical Review E*, 97(4):042414, 2018

Landaw, J., Garfinkel, G., Weiss, J. N., and Qu, Z. Memory-induced chaos in cardiac excitation. *Physical Review Letters*, 118(13):138101, 2017

Radivoyevitch, T., Hlatky, L., Landaw, J., and Sachs, R. K. Quantitative modeling of chronic myeloid leukemia: Insights from radiobiology. *Blood*, 119(19):4363-4371, 2012.

CHAPTER 1

Introduction to Cardiac Electrophysiology, Modeling, and Memory

The human heart beats about once every second, and so in the course of a normal life span totals about 2-3 million heartbeats. Normally, each heartbeat causes muscular contraction of the heart, pumping oxygenated blood from the left atrium and ventricle to the rest of the body and deoxygenated blood from the right atrium and ventricle to the lungs. Fundamentally, contractions of the heart are initiated by a complex electrical network of heart cells, or myocytes.

Sudden cardiac death (SCD) is one of the most common causes of death in individuals with cardiovascular disease. Roughly 1 in 4 people in the United States die each year due to heart disease [NC13], and of those, about 50% are due to SCD [AKSA+18, MJ12, GBC+11]. In SCD, the heart abruptly loses its ability to pump blood efficiently, either due to sino-atrial node (SAN) malfunction or due to electrical turbulence in the ventricles [QHGW14]. While much has been done in the past half-century to understand, prevent, and treat SCD, much is still unknown. Problems in understanding the mechanisms of SCD stem from the fact that it is a multi-disciplinary problem in biology and medicine, physics, and mathematics [Win83, QHGW14]. In addition, there are many different conditions and diseases that cause lethal arrhythmias and SCD.

Cardiac electrophysiology studies the electrical system of the heart, and advances in the field have led to a clearer understanding of disease mechanisms and treatments of arrhythmias. Foundations of cardiac electrophysiology began as

early as 5th century BC in China, but most progress in the field occurred in the last 100 years [Lüd09]. Here, before diving into the definition of cardiac memory and the main findings in the thesis, we will briefly go over basics of cardiac electrophysiology, define precisely what we mean by "cardiac memory," and current methods used to study the cardiac electrical system using tools in computer simulation and mathematical modeling.

1.1 Cardiac Electrophysiology

Contractions of the heart are caused by electrical stimuli originating in the sino-atrial node (SAN). The electrical impulses propagate first to the left and right atria and then to the left and right ventricles via the atrial-ventricular node (AVN) (Fig. 1.1(a)). Normally, this process of electrical excitation leading to a synchronous contraction of the heart occurs every beat and is adaptive to changes in heart rate, stress, sympathetic surges, etc.

Cardiac tissue is made of rod-like cells known as myocytes. With some exceptions (e.g. fibroblasts), myocytes are electrically active. During a heart beat, each myocyte undergoes a change in voltage or membrane potential known as an *action potential*. An action potential is caused by active changes in ionic currents flowing into the cell (inward currents) or out of the cell (outward currents). In the next section, we will go over what sorts of changes occur during an action potential, which will ultimately pave the way for an understanding of cardiac memory.

1.1.1 Action Potentials

Preceding a heart beat, each electrically active cell in the network maintains a negative potential or voltage, known as the resting membrane potential, between the inside and outside of the cell. During a heartbeat, each cell undergoes an action potential (AP), a change in electrical potential over time, in which the

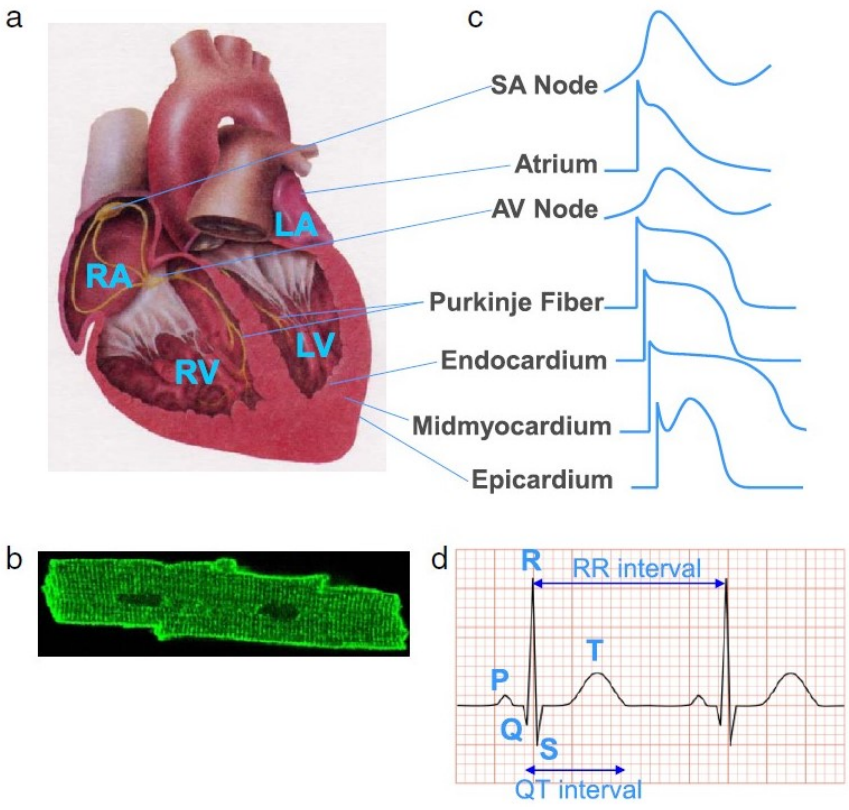

Figure 1.1: From Qu *et al.* [QHGW14]. Anatomy and action potentials of the heart. **(a).** Structure of the heart. RA = right atrium, LA = left atrium, RV = right ventricle, LV = left ventricle. **(b).** Image of a ventricular myocyte. **(c).** Representative action potentials from different areas of the heart. SA nodal action potentials are generated automatically and repetitively via cellular oscillations, while all other action potentials are elicited from external stimuli from neighboring cells. **(d).** A representative electrocardiogram (ECG). The ECG records the net electrical activity of the human heart, and can be used to diagnose diseased states.

voltage transiently increases and then decreases back to resting state. Some cells, for example those in the SAN, generate action potentials by undergoing intrinsic voltage oscillations. These cells are known as pace-maker cells, as they are able to generate action potentials without any external driving. Other cells in the heart, like those in the ventricles (Fig. 1.1(b)) are externally driven and depend on electrical excitation from neighboring cells.

Cells from different regions of the heart may elicit action potentials with different morphologies from one another (Fig. 1.1(c)). Myocytes in the SAN and AVN are oscillatory or pace-maker cells, and so the morphologies of the action potentials are different compared to non-oscillatory cells. In pace-maker cells, voltages vary between -60 and $40\,\mathrm{mV}$, while resting membrane potentials of atrial and ventricular myocytes are around $-80\,\mathrm{mV}$ [QHGW14].

1.1.2 The Hodgkin-Huxley Model

It was not until the 20th century that properties of APs in neurons began to be well understood. In the early 20th century, it was only just postulated that APs were due to changes in the permeability of neural axon membranes to ions such as Na^+ and K^+ [Ber02]. Arguably the biggest breakthrough in electrophysiology occurred with the findings by Hodgkin and Huxley, which were published in 1952 [HH52] and led to them winning the Nobel prize in Physiology and Medicine in 1963. In their model, the Hodgkin-Huxley (HH) model, the cell membrane of a squid giant axon is modeled as a capacitor in an electric circuit, where embedded proteins in the cell membrane called ion channels modulate the conductance of ionic current through the membrane. Labeling I_{ion} as the net sum of currents flowing through the cell membrane, then the change of voltage of the cell follows the following differential equation:

$$C_m \frac{dV}{dt} = -I_{\mathrm{ion}}, \tag{1.1}$$

where C_m is the capacitance of the cell membrane. The negative (-) sign in front of I_{ion} in Eq. (1.1) is by convention: a current of positive ions is considered positive if it is flowing out of the cell, which would cause a negative change in voltage. Hodgkin and Huxley first identified three currents: a sodium (Na^+) current I_{Na}, a potassium (K^+) current I_{K}, and a leak current (I_{l}) of, at the time, unknown ions (later determined to be of chloride, Cl^-). Each current flows through ion channels with a certain conductance, and via Ohm's Law:

$$I_{\text{Na}} = g_{\text{Na}}(V - E_{\text{Na}}), \quad I_{\text{K}} = g_{\text{K}}(V - E_{\text{K}}), \quad I_{\text{l}} = g_{\text{l}}(V - E_{\text{l}}), \tag{1.2}$$

where g_{Na}, g_{K}, and g_{l} are values of the conductances of the respective ion channels, and E_{Na}, E_{K}, and E_{l} are the Nernst potentials of the respective ions, which satisfy

$$E_X = -\frac{RT}{zF} \ln \frac{[X]_i}{[X]_o}, \tag{1.3}$$

where R is the gas constant ($\approx 8.314\,\text{J} \cdot \text{mol}^{-1} \cdot \text{K}^{-1}$), T is the temperature, and for ion X, z is the valence or charge, and $[X]_i$ and $[X]_o$ are the concentrations of X inside and outside the cell. Under normal physiological conditions, $E_{\text{Na}} \approx 70\,\text{mV}$ and $E_{\text{K}} \approx -95\,\text{mV}$. Therefore, when activated, I_{Na} is an inward current that will tend to depolarize the cell to higher voltages, and I_{K} is an outward current that repolarizes the cell to negative voltages.

Setting $I_{\text{ion}} = I_{\text{Na}} + I_{\text{K}} + I_{\text{l}}$ as the sum of the currents, Eqs. (1.1) and (1.2) model a resistorr-capacitor (RC) circuit (Fig. 1.2(a)). What comes next is how to determine the conductances g_{Na}, g_{K}, and g_{l}. Hodgkin and Huxley [HH52] determined that the conductances are variable, and not only do they change in time but are also are voltage-dependent. Fig. 1.2(b) shows experimental results from Hodgkin and Huxley, demonstrating how the conductance g_{K} changes when the voltage is depolarized to 25 mV and then repolarized back to resting membrane potential. The higher voltage causes the conductance to increase and saturate to a certain level, and when repolarized back to resting state the conductance drops

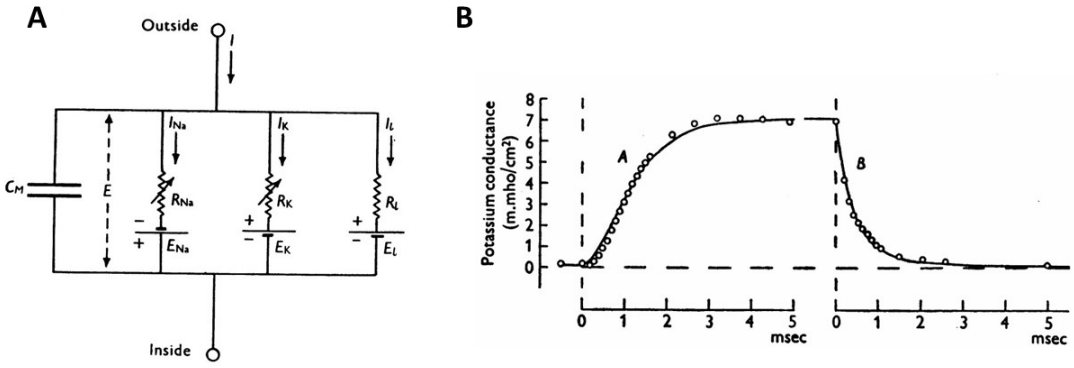

Figure 1.2: From Hodgkin and Huxley 1952 [HH52]. The Hodgkin Huxley model. **(a)**. Model of an action potential as a circuit with the cell membrane acting as a capacitor with capacitance C_m and ionic currents I_{Na}, I_{K}, and I_{l} flowing through resistors with Nernst potentials E_{Na}, E_{K}, and E_{l}, respectively. **(b)**. Conductance of the K^+ current, I_{K}, with the voltage depolarized to 25 mV and then brought back to resting membrane potential.

and exponentially decays towards 0. They determined that g_{K} can be modeled as

$$g_{\mathrm{K}} = \bar{g}_{\mathrm{K}} n^4, \tag{1.4}$$

where $\bar{g}_{\mathrm{K}}$ is a constant that is the maximum conductance of the I_{K}, and n is variable satisfies a differential equation

$$\frac{dn}{dt} = \frac{n_\infty - n}{\tau_n}, \tag{1.5}$$

where $n_\infty = n_\infty(V)$ is a voltage-dependent steady state value of n at a given voltage V. n is known as a gating variable and modulates the conductance through ion channels. The power of 4 in Eq. (1.4) was determined in a purely statistical manner by fitting curves to the data as in Fig. 1.2(b), but turns out to have predicted the existence of four voltage-sensitive domains or "gates" in K^+ channels [SGS05], in which all 4 gates must be open in order for a particular K^+ channel to be permeable to K^+.

The conductance of I_{Na} turns out to be a bit more difficult:

$$g_{\mathrm{Na}} = \bar{g}_{\mathrm{Na}} m^3 h, \tag{1.6}$$

where m and h are two independent gating variables that satisfy the differential equations

$$\frac{dm}{dt} = \frac{m_\infty - m}{\tau_m}, \qquad \frac{dh}{dt} = \frac{h_\infty - h}{\tau_h}. \tag{1.7}$$

The gating variable m, like n, is an activation gating variable which increases at higher voltages. However, unlike seen in the conductance for I_{K}, there is also a gating variable h which is an inactivation gating variable that decreases at higher voltages.

1.1.3 Beyond Hodgkin-Huxley and Cardiac Action Potential Modeling

Hodgkin and Huxley provided a framework for explaining and modeling action potentials. Via Eq. (1.1), the changes in voltage during an action potential are governed by changes in the ionic currents, I_{ion}. Hodgkin and Huxley examined three particular currents in a squid giant axon, I_{Na}, I_{K}, and I_{l}, and determined that while voltage is governed by the flow of ionic currents, the ionic currents themselves depend on voltage via the voltage-dependent gating variables n, m, and h.

Since then, a wide variety of ion channels were discovered and investigated not only in neurons but also in cardiac myocytes. Many differences exist between the electrophysiological properties of neurons and cardiac myocytes, but arguably the biggest difference is the existence of complex calcium (Ca^{2+}) cycling required for excitation-contraction (EC) coupling. EC coupling via Ca^{2+} is fundamentally the link between the electrical activity of the heart and contraction of the heart [Ber08] in order to pump blood to the rest of the body. The L-type Ca^{2+} channel, $I_{\mathrm{Ca,L}}$, is essential for EC coupling [BTN89, FAP97, Reu85, SC73, LHX04]. $I_{\mathrm{Ca,L}}$ is a voltage-gated Ca^{2+} channel which has the effect of not only allowing Ca^{2+} to enter the cell from the outside (and utimately trigger a cascade of events allowing

contraction of the cell), but it also provides an inward current that, in cardiac tissue, prolongs the duration of action potential.

The *action potential duration*, or *APD*, is a measurement of how long a cell is depolarized during an action potential before the cell repolarizes back to resting membrane potential. While in neurons the APD tends to be on the order of 1 ms, in cardiac tissue the APD is much longer and on order of 100 ms. The APD is a fundamental concept in cardiac electrophysiology. For example, APD in cardiac ventricular tissue determines the QT interval on electrocardiogram (ECG), and abnormalities in the QT interval (either due to genetic abnormalities or drug interactions) can be a marker for arrhythmias [JM92, QXO+13, GZM08, Rod06, WSS+95, CR01, TM99]. We will return to APD in the next section.

After Hodgkin and Huxley, action potentials in cardiac myocytes have been modeled following a very similar strategy. I_{ion} in Eq. (1.1) has been modified and extended to include many different ionic currents, i.e., [QHGW14]

$$I_{\text{ion}} = I_{\text{Na}} + I_{\text{Ca,L}} + I_{\text{Ks}} + I_{\text{Kr}} + I_{\text{K1}} + I_{\text{NCX}} + I_{\text{NaK}} + \dots, \tag{1.8}$$

where each current in general follows similar Hodgkin-Huxley formulations as in Eqs. (1.2)-(1.7). Since the first cardiac action potential model in Purkinje fibers formulated by Denis Noble in 1962 [Nob62], many different action potential models have been developed specific to different areas of cardiac tissue (e.g. SAN cells versus ventricular cells) as well as to different animal species [LR91, LR94, tTNNP04, tTP06, MSS+08, OVVR11]. In what are termed "first generation models" [QHGW14], the action potential models have a fairly limited number of ionic currents, with intracellular ionic concentrations $[K^+]_i$ and $[Na^+]_i$ held constant and $[Ca^{2+}]_i$ changing only due to Ca^{2+} currents (ignoring complex intracellular Ca^{2+} cycling). However, while perhaps not the same physiologically accurate, these models such as the Luo-Rudy I (LR1) model [LR91] are still commonly used since they are fairly simple and action potential properties in these

models can be more easily scrutinized. A later model, the Luo-Rudy 1994 (LRd) model [LR94], is perhaps the prototypical "second-generation models" [QHGW14] which includes many more currents as well as intracellular Ca^{2+} compartments responsible for complex intracellular Ca^{2+} cycling.

Finally, it is important to point out that although the models thus far are for single cells, it is possible to add a spatial component and combine many cells together in a 1D, 2D, or 3D tissue. By extending onto Eq. (1.1), tissues of coupled myocytes can be modeled by the following partial differential equation:

$$\frac{\partial V}{\partial t} = -\frac{I_{\text{ion}}}{C_m} + D\Delta V. \tag{1.9}$$

ΔV is the Laplacian operator which sums over all second partial derivatives with respect to each spatial dimension. D is the diffusion coefficient, which models the conductance of currents between neighboring cells via gap junctions. Through Eq. (1.9), one can study cardiac tissue-scale phenomenon while also having control over single-cell properties.

1.2 Nonlinear Dynamics of Action Potential Duration and Calcium Cycling

In the previous section, we went over the basics of cardiac electrophysiology at the single cell level, giving an overview of what an action potential is and how cardiac action potentials are modeled via Hodgkin-Huxley formulations. Ultimately, the goal of mathematical and computational modeling is to accurately represent the real, physical and biological world and make predictions. Can mathematical and computational models of cardiac action potentials provide mechanisms of disease and arrhythmias in cardiac tissue?

Under diseased conditions, beat-to-beat changes in action potentials are the underlying cause of arrhythmias. We describe here two forms of cellular insta-

bilities that can occur and that have been widely - voltage instabilities or action potential duration (APD) instabilities, and Ca^{2+} instabilities.

1.2.1 APD Restitution and Instability

The APD of a cardiac myocyte can vary dependent on the heart rate, or how rapidly the cell is stimulated to trigger an action potential. This phenomenon of APD varying due to the rate of stimulation, or pacing cycle length (PCL), is known as APD restitution [QHGW14]. For the most part, APD shrinks under fasting pacing. This is because under fast pacing, voltage-dependent gates have less time to recover during the diastolic interval (DI), which is the interval of time between the end of one action potential and the initiation of the next one.

The APD restitution can be measured experimentally in isolated ventricular myocytes via an S1S2 pacing protocol. A cell is paced periodically under a fixed pacing rate (S1) for several beats so that the action potentials and APD will equilibrate and reach steady state. Then, a premature stimulus (S2) is applied some interval of time after the end of the preceding AP (Fig. 1.3(a)). By doing this, the DI is controlled, and one can measure the APD of the action potential triggered by the premature stimulus. This procedure determines a one variable function of APD on DI:

$$\text{APD} = f(\text{DI}). \tag{1.10}$$

Eq. (1.10) is known as an APD restitution curve (Fig. 1.3(b)).

Given the APD restitution curve in Eq. (1.10), one can examine APD stability. Under constant periodic pacing (i.e. the heart is pacing at a fixed heart rate) with T the fixed pacing cycle length (PCL), then $\text{APD} + \text{DI} = T$ after any given stimulus. We can then write

$$a_{n+1} = f(d_n) = f(T - a_n), \tag{1.11}$$

where a_n and a_{n+1} are the APDs of action potentials triggered by the n^{th} and

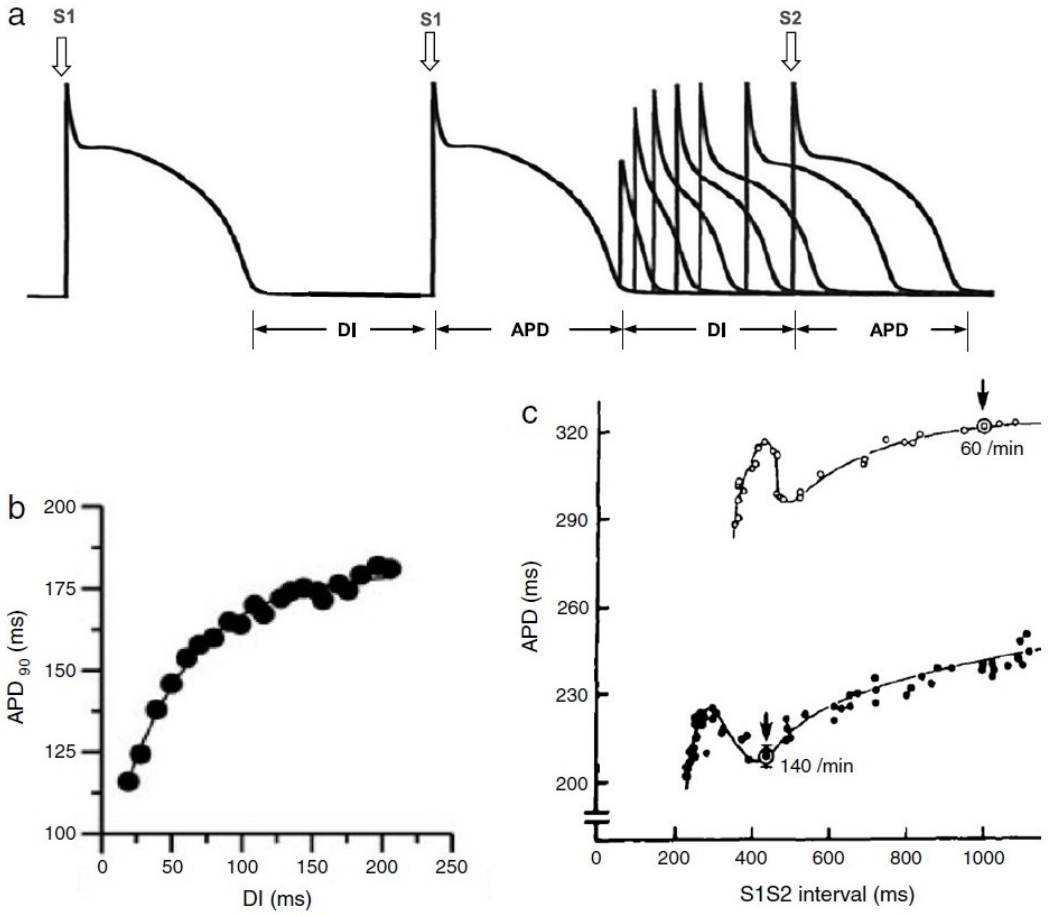

Figure 1.3: From Qu *et al.* [QHGW14]. The APD restitution. **(a)**. The S1S2 restitution protocol. A cell is paced periodically for several beats (S1), followed by a premature stimulus (S2). The APD of the action potential from the S2 stimulus recorded. **(b)**. APD restitution curve. By varying the timing of the S2 stimulus in the S1S2 restitution protocol, APD versus DI can be measured. Experimental results from a rabbit ventricular myocyte [GXD+05]. **(c)**. APD restitution curves under two different S1 pacing periods. Results from Franz *et al.* [FSS+83].

$(n+1)^{\text{st}}$ stimulus, respectively, d_n is the DI of the n^{th} beat (after the n^{th} stimulus but before the $(n+1)^{\text{st}}$ stimulus), and $T = a_n + d_n$. The equation $a_{n+1} = f(T - a_n)$ provides a discretized, 1-dimensional *iterated map* of APD. Given a_0, then $a_1 = f(T - a_0)$, $a_2 = f(T - a_1)$, $a_3 = f(T - a_2)$, and so on.

The APD fixed point a^*, with the corresponding DI fixed point d^*, satisfy $a^* = f(d^*) = f(T - a^*)$. As first noticed by Nolasco and Dahlen in 1968 [ND68], denoting $\alpha = \frac{df}{da_n}\big|_{a^*,d^*}$ to be the derivative of the APD restitution curve at the fixed point, then the fixed point is unstable provided

$$|\alpha| > 1. \tag{1.12}$$

In other words, if the magnitude of the slope or derivative of the APD restitution curve at the APD/DI fixed point is greater than one, then the fixed point is unstable.

With a magnitude of the derivative greater than 1, small perturbations of APD about the fixed point will exponentially diverge away from the fixed point over several iterations under f. For a brief proof: suppose again that a^* is the APD fixed point that satisfies $a^* = f(T - a^*)$, and suppose that $a_0 = a^* + \epsilon$, where $|\epsilon| \ll 1$ is a small perturbation away. Then,

$$a_1 = f(T - a_0) = f(T - a^* - \epsilon) = f(T - a^*) - \epsilon f'(T - a^*) + o(\epsilon) = a^* - \alpha\epsilon + o(\epsilon), \tag{1.13}$$

where the third equality comes from Taylor expanding $f(T - a^* - \epsilon)$ about $T - a^*$. $o(\epsilon)$ involves higher powers of ϵ, which is negligible compared to ϵ when ϵ is close to zero. Neglecting $o(\epsilon)$, then $a_1 - a^* = -\alpha\epsilon$. Originally, a_0 deviated from the fixed point ϵ away, and after one iteration is $-\alpha\epsilon$ away. Over n iterations, the deviation becomes $(-1)^n\alpha^n\epsilon$. If $|\alpha| > 1$, APD will exponentially diverge away from the fixed point, and therefore the fixed point is unstable. Conversely, if $|\alpha| < 1$, then the deviation will decay to 0 and APD will get closer and closer to the fixed point with every additional iteration. Therefore, APD is stable.

The APD fixed point can be either stable or unstable. If the S1S2 restitution curve is monotonically increasing (i.e. APD increases as DI increases) and the APD fixed point is unstable, then APD will oscillate about between two values above and below the APD fixed point. This phenomenon is known as *APD alternans*, and it can manifest in the human heart as T-wave alternans (TWA), which is a finding on electrocardiogram (ECG) that often preceeds arrhythmias under different diseased conditions [QXGW10]. If the S1S2 restitution curve is non-monotonic, then much more complex dynamics can occur, including chaos. These complex dynamics of APD have been seen in experiments [WOGJ95] and in action potential models [QWG97, XHS+07].

1.2.2 Intracellular Ca^{2+} Instability

APD instability is one form of instability that can occur in cardiac action potentials. Since voltage is coupled to many different processes in the system, APD instability can cause other instabilities to occur as well.

However, it is also possible that other intracellular processes to be unstable even with the voltage system stable. One such system is the Ca^{2+} cycling system. Ca^{2+} is regulated not only by ionic Ca^{2+} currents such as the L-type Ca^{2+} current, $I_{Ca,L}$, but also by complex intracellular Ca^{2+} cycling involving the sarcoplasmic reticulum (SR). The SR contains stores of Ca^{2+} at very high concentrations. During an action potential, Ca^{2+} enters the cell via $I_{Ca,L}$ and triggers calcium-induced-calcium-release (CICR), which causes the SR to release large amounts of Ca^{2+} from the SR into the cytoplasm of the cell. This positive feedback, whereby a small amount of Ca^{2+} triggers even more Ca^{2+} to enter the intracellular space, can cause instabilities in Ca^{2+} cycling including Ca^{2+} alternans [QHGW14]. Ca^{2+} alternans has been observed experimentally even when APD is fixed [CGG+99, DEO02, DOE04]. Spatially discordant instabilities in Ca^{2+} cycling including Ca^{2+} waves have also been seen in experimental studies

[DEO02, KB02, XW09, ASK+09, GBAC09, TKL12].

Much has been done to demonstrate and analyze Ca^{2+} instabilities in cardiac myocytes. To give one example of a mathematical model used to study Ca^{2+} cycling instability, Qu *et al.* [QSW07] developed an iterated map model providing a mechanism for Ca^{2+} alternans due to steep fractional release of SR Ca^{2+}. As postulated by Eisner *et al.* [ECD+00], Ca^{2+} is caused by a very steep or sensitive relationship between SR Ca^{2+} release (due to CICR) and SR Ca^{2+} at the time of stimulus of the next action potential. In the iterated map model, Qu *et al.* developed the relationship

$$l_{n+1} = l_n - g(l_n) + h(c^p_{n+1}), \tag{1.14}$$

where l_n is the SR Ca^{2+} load right at the next stimulus, g describes the relationship between the SR Ca^{2+} load and how much Ca^{2+} is released from the SR, c^p_{n+1} is the peak Ca^{2+} concentration in the intracellular space during the next action potential, and h represents how much Ca^{2+} reenters the SR after the action potential (via the SERCA pump). They assume that c^p_{n+1} is simply the amount Ca^{2+} in the intracellular space (b) plus how much Ca^{2+} is released from the SR into the space ($g(l_n)$) and minus how much Ca^{2+} is taken up back into the SR (l_n), i.e.,

$$c^p_{n+1} = b + g(l_n) - l_n. \tag{1.15}$$

Together, Eqs. (1.14) and (1.15) give the following one-dimensional iterated map:

$$l_{n+1} = l_n - g(l_n) + h\left[b + g(l_n) - l_n\right]. \tag{1.16}$$

As in the stability analysis of the APD restitution curve (Eq. (1.11)), stability of the map can be determined by calculating the derivative of the map at the fixed point. In so doing, the map is unstable provided

$$|(1 - g')(1 - h')| > 1, \tag{1.17}$$

where $g' = \frac{dg}{dl_n}\big|_{l^*}$ and $h' = \frac{dh}{dc^p_{n+1}}\big|_{l^*}$ are the derivatives of g and h evalulated when $l_n = l^*$, the SR Ca^{2+} fixed point.

1.3 The Role of Cardiac Memory

In the APD restitution model of APD dynamics, it is assumed that APD is solely a function of the previous beat's DI. In many cases, this assumption is perfectly valid, and performing stability analyses of APD restitution curves (i.e. evaluating derivatives of the curves at the APD fixed points) provide mechanisms for APD instability and arrhythmogenesis in cardiac tissue.

However, during an action potential, many other dynamical variables besides APD and DI occur. In fact, APD restitution curves can change dependent on the S1 pacing period of the S1S2 pacing protocol (Fig. 1.3(c)). There may be many cellular processes going on that depend on the cell's prior pacing history. Though many ion channels have gating variables with very rapid kinetics that reach a steady state equilibrium by the end of an action potential, some ion channels have very slow activation or recovery. One example is the slow delayed rectifier K^+ current I_{Ks}. Experimental studies have demonstrated that I_{Ks} activates with a time constant of about 1000 ms and deactivates with a time constant between 100 and 400 ms [JPV07, VIO+01]. Denoting x to be a gating variable of I_{Ks}, then

$$\frac{dx}{dt} = \frac{x_\infty - x}{\tau_x}, \tag{1.18}$$

where τ_x is 100 to 400 ms at low voltages near resting membrane potential, and about 1000 ms when the cell is depolarized. Compared to other gating kinetics, e.g. that for I_{Na}, I_{Ks} is very slow and can have a different behavior depending on whether the cell is paced rapidly or slowly.

In addition to slow recovery of ion channels, there is also slow accumulation of ion concentration. From one beat to the next, $[K^+]_i$, $[Na^+]_i$, and $[Ca^{2+}]_i$ may change due the flow of currents, but in any given action potential the amount of ions flowing into or out of the cell will not substantially affect the intracellular concentrations. However, over a course of, say, dozens or hundreds or thousands of action potentials, the intracellular ion concentrations may increase or decrease

substantially, thereby changing conductances of the ion channels.

The phenomenon by which the prior pacing history affects action potential properties is called *short-term cardiac memory* [FSLS88]. To model memory, one may consider the dependence of APD not just on the previous DI (as in the case of the APD restitution curve), but also add dependencies to APDs and DIs even further back [CLS04, KTS+05]:

$$a_{n+1} = f(d_n, a_n, d_{n-1}, a_{n-1}, \dots). \tag{1.19}$$

One may also introduce a phenomenological memory variable, such as by Chialvo *et al.* [CMJ90] and Fox *et al.* [FBGJ02]:

$$\begin{aligned} M_{n+1} &= e^{-\frac{d_n}{\tau}} \left[1 - (1 - M_n)e^{-\frac{a_n}{\tau}}\right] \\ a_{n+1} &= (1 - \alpha M_{n+1}) f(d_n) \end{aligned} \tag{1.20}$$

M describes the effect of memory from the slow recovery of K^+ channels. In various studies using the iterated map model in Eq. (1.20) or similar ones incorporating memory, it has been shown that memory suppresses instabilities [CMJ90, FBGJ02, KTS+05, OGJ97, TSGK03, FRD+03, TRGG04, CF04, BQK+07, GCGJ+13, MJT08, WMT15]. However, we demonstrate that under diseased conditions, the memory effect can be enhanced and actually promote instabilties and complex action potential dynamics.

1.4 Thesis Outline

Chapters 2-4 focus on action potential dynamics at the single-cell level. Chapter 2, titled *Memory-Induced Nonlinear Dynamics of Excitation in Cardiac Diseases*, investigates the effects of memory from two sources: slow recovery of K^+ channels and slow accumulation of Ca^{2+}. Under two diseased conditions - early repolarization syndrome and long QT syndrome - we show that the effects of

memory are enhanced and induce complex action potential dynamics under fixed pacing.

Chapter 3, titled *Control of Voltage-Driven Instabilities in Cardiac Myocytes with Memory*, demonstrates that action potential dynamics induced by memory are very difficult to control. We propose three pacing controlling methods to suppress action potential instabilities and analyze their efficacies.

Chapter 4, titled *Induction of Action Potential Dynamics by the Accumulation of Calcium and Sodium in Cardiac Myocytes*, analyzes the effects of both Ca^{2+} and Na^{+} in promoting a phenomenon known as intermittent EAD behavior. As shown in prior experiments and simulations, action potential duration (APD)-to-Ca^{2+} positive feedback produces a bistable system, and Na^{+} accumulation functions as a bistable switch that periodically switches the system between having action potentials with EADs (long APDs) and having action potentials without EADs (normal APDs) for a certain number of beats. We recapitulate the findings in experiment and simulation, and develop an iterated map model incorporating the effects of Ca^{2+} and Na^{+}. Analysis of the iterated map model demonstrates that intermittent EAD behavior arises due to a supercritical Hopf bifurcation. Our findings using the iterated map model are confirmed using a detailed action potential model.

Chapters 5 and 6 focus on tissue-scale arrhythmogenesis promoted by memory-induced action potential instability. Chapter 5, titled *Small-Conductance Ca^{2+}-Activated K^{+} Channels Promote J-wave Syndrome and Phase 2 Reentry*, demonstrates that the small-conductance Ca^{2+}-activated K^{+} channel (SK) current, I_{SK}, promotes J-wave syndrome and phase 2 reentry under certain conditions. Namely, when I_{SK} is spiky enough to induce spike-and-dome action potential morphology similar to the effects of the transient outward K^{+} current (I_{to}), then the effects of memory are enhanced, action potential dynamics become unstable, and the instability promotes phase 2 reentry in a 1D-cable of ventricular myocytes.

Chapter 6, titled *The Transient Outward Potassium Current ($_{to}$) Plays a Critical Role in Spiral Wave Breakup*, reveals that I_{to} promotes APD instability and spiral wave breakup in 2D tissue models of cardiac ventricular tissue. We show that when the conductance of I_{to} is either too small or too large, then spiral waves are stable. However, when I_{to} conductance is in a certain range, then spiral waves breakup. Other currents, such as $I_{\mathrm{Ca,L}}$, I_{Kr}, I_{Ks}, and I_{K1}, comparatively have little effect on spiral wave behavior. Our findings are consistent in five different detailed action potential models.

CHAPTER 2

Memory-Induced Nonlinear Dynamics of Excitation in Cardiac Diseases

2.1 Introduction

Dynamical instabilities in the heart can promote arrhythmias such as ventricular tachycardia and fibrillation (VT/VF) [Gla96, QW15], which are the leading causes of sudden cardiac death [ZW98]. Different mechanisms of dynamical instabilities have been demonstrated at both single-cell and tissue scales [KMC12, Kar13, QHGW14]. In single cells, nonlinear dynamics including period-doubling bifurcations leading to period-2 (called alternans in cardiac electrophysiology) and other states of higher periodicity, as well as quasiperiodicity and chaos have been widely demonstrated [ND68, GGS81, GWSG84, CGJJ90, KKH+93, WOGJ95, SXS+09]. These dynamics originate from the nonlinearity in membrane voltage, intracellular calcium (Ca^{2+}) cycling, or coupling of the two [QHGW14, SSK05].

Low-dimensional iterated maps have been widely used to understand the dynamical mechanisms of complex cardiac excitations. The earliest and most widely used iterated map model was based on action potential (AP) duration (APD) restitution properties of cardiac myocytes [ND68]. APD restitution is a property well-known in cardiology and widely measured in experiments [ES83, FSS+83, RBHH87, DL88, MCR92]. One type of APD restitution is called the S1S2 APD restitution (see Fig. 2.1(a)), in which the cell is periodically paced (S1) to a steady

state and then a premature or delayed stimulus (S2) is applied to obtain the dependence of APD on the preceding diastolic interval (DI). The S1S2 APD restitution can be mathematically defined as

$$a_{n+1} = f(d_n), \tag{2.1}$$

where a_{n+1} is the APD of the $(n+1)^{\text{st}}$ beat and d_n is the DI of the n^{th} beat (immediately preceding a_{n+1}). Under periodic pacing, the APD and DI of the same beat satisfy the relation $a_n + d_n = mT$, and so Eq. (2.1) can be rewritten as

$$a_{n+1} = f(mT - a_n), \tag{2.2}$$

where T is the pacing period and mT is the actual excitation period. For example, $m = 1$ indicates that every stimulus gives rise to an AP (1:1 capture), $m = 2$ means every two stimuli result in an AP (2:1 capture), and so on. Eq. (2.2) or similar ones have been widely used to investigate APD dynamics under periodic stimulation [ND68, GWSG84, CGJJ90, KKH+93, WOGJ95, VCMJ90, Kar94, QSW07]. A period-doubling bifurcation occurs when the slope of the APD-restitution curve at the fixed point exceeds 1. Chaos may occur when f is either a nonmonotonic function of DI or a monotonic function with stimulation failure [QSW07]. In this study, we refer to Eq. (2.2) as the "APD-restitution map model."

Note that in Eq. (2.1), the APD depends only on its immediately preceding DI, indicating no memory. However, cardiac systems exhibit memory [ES83, FSLS88, KDT+04], in which the APD depends not only on its immediately preceding DI, but also on earlier APDs and DIs. Therefore, Eq. (2.2) is no longer accurate or valid to describe the APD dynamics when memory is present. A higher-dimensional iterated map is needed to incorporate the memory effect. In general, one can write

$$a_{n+1} = f(d_n, a_n, d_{n-1}, a_{n-1}, \dots), \tag{2.3}$$

and use this map to investigate the nonlinear dynamics caused by memory [KTS+05]. Another way of incorporating memory into the iterated map model is to induce

phenomenologically a memory variable. One such model was developed by Chialvo *et al.* [CMJ90] and Fox *et al.* [FBGJ02], which is described by the following equations:

$$M_{n+1} = e^{-\frac{d_n}{\tau}} \left[1 - (1 - M_n)e^{-\frac{a_n}{\tau}}\right] \tag{2.4}$$

$$a_{n+1} = (1 - \alpha M_{n+1}) f(d_n) \tag{2.5}$$

where M is the memory variable and τ is the time constant of memory. M in Eq. (2.4) describes the memory effect mainly from the slow recovery of K^+ channels. In a study by Schaeffer *et al.* [SCG+07], an iterated map model was developed to describe the memory effect from slow intracellular ion accumulation. Since M is always positive, the steepness of the restitution function in Eq. (2.5) is reduced, and thus memory in Eqs. (2.4) and (2.5) always suppresses instability [CMJ90, FBGJ02]. The effects of memory on cardiac excitation dynamics have been investigated in many other previous studies [KTS+05, OGJ97, TSGK03, FRD+03, TRGG04, CF04, BQK+07, GCGJ+13, MJT08, WMT15], which have also shown that memory suppresses dynamical instabilities.

In a recent study [LGWQ17], we showed that under certain diseased conditions, memory can induce dynamical instabilities and complex APD dynamics. One such diseased condition is the presence of a strong transient outward potassium (K^+) current (I_{to}), which can cause a sudden shortening of APD, the so-called spike-and-dome AP morphology [GWP+00, SW05, DSPW06] (also see Fig. 2.2(a)). I_{to} can induce complex APD dynamics, including alternans and high periodicity as well as chaos, which have been shown in experiments [LA93] and computer simulations [Hop06, MKMC09, CPM+09, QXGW10]. This condition may occur under cardiac diseases such as Brugada syndrome and ischemia [LA93, AY15]. Another condition we studied is the condition of reduced repolarization reserve in which either the outward currents are reduced or the inward currents are increased from normal conditions. This causes the lengthening of APD and the genesis of early af-

terdepolarizations (EADs) [JM92, QXO+13]. This condition may occur in cardiac diseases such as long QT syndrome [GZM08, Rod06, WSS+95, CR01] and heart failure [TM99]. In our previous study [LGWQ17], we carried out computer simulations using a simplified AP model, the 1991 Luo and Rudy (LR1) model [LR91], to simulate the complex APD dynamics under the two conditions. We developed a novel iterated map model which accurately captures the dynamics from the AP model and revealed the mechanistic role of memory in promoting these dynamics. This is contrary to the understanding of the memory effects on cardiac excitation dynamics from previous studies [KTS+05, CMJ90, FBGJ02, OGJ97, TSGK03, FRD+03, TRGG04, CF04, BQK+07, GCGJ+13, MJT08, WMT15] which have shown that memory suppresses dynamical instabilities.

In this study, we extend our previous work to investigate the effects of memory on APD dynamics. We investigate two sources of memory. In the first one, memory is from the slow recovery of a K^+ channel. In the second one, memory is from the slow accumulation of intracellular ion concentrations. Since the LR1 model does not have intracellular ion concentration dynamics (they are fixed), we use the model developed by ten Tusscher *et al.* [tTNNP04], the TP04 model, to study the effects of memory due to ion concentration accumulation, namely intracellular Ca^{2+} concentration ($[Ca^{2+}]_i$) accumulation. We first carry out computer simulations of the AP models to demonstrate bifurcations and complex APD dynamics under the two diseased conditions. We then develop iterated map models that incorporate memory to accurately capture the complex dynamics and bifurcations. Finally, we perform theoretical analyses of the iterated map models to reveal the underlying mechanisms and the roles of memory in promoting the complex dynamics.

The article is organized as follows. In Section 2.2, we describe the AP models, namely the LR1 model and the TP04 model, and our modifications to model the diseased conditions that exhibit the corresponding APD dynamics. The Results

section, Section 2.3, is divided into two major sections based on the two sources of memory. Section 2.3.1 investigates the effects of memory originating from the slow recovery of K^+ channels. We choose to use the LR1 model since it does not exhibit ion accumulation, so memory originates only from slow ion channel recovery. In Section 2.3.1.1, we add I_{to} to the LR1 model to model Brugada syndrome and show that I_{to} can unmask or greatly exacerbate the memory effect caused by slow recovery of the time-dependent K^+ current (I_K). In Section 2.3.1.2, we show that adding I_{to} to the LR1 model can give rise to complex APD dynamics, including alternans and chaos, which cannot be described by the traditional iterated map model using the S1S2 APD restitution curve. In Section 2.3.1.3, we develop a new iterated map model that incorporates the memory effect from the slow recovery of I_K. Since the memory is mainly determined by the slow kinetics of the X-gating variable, we call the new iterated map model the "X-memory map model." In Section 2.3.1.4, we show that the X-memory map model can accurately capture the complex APD dynamics from the AP model and the presence of memory results in a nonmonotonic first return map to generate chaos. In Section 2.3.1.5, we perform a stability analysis of the X-memory map model, investigating the dependence of the APD dynamics on different parameters, and validate some of the predictions using the AP model. In Section 2.3.1.6, we investigate the second diseased condition, long QT syndrome, in which inward currents are increased and/or outward currents are reduced. We show that memory is also unmasked or exacerbated and the resulting complex APD dynamics cannot be accurately captured by the traditional APD-restitution map model. On the other hand, the X-memory map model can accurately capture bifurcations and the complex APD dynamics from the AP model.

Section 2.3.2 investigates the effects of memory originating from slow $[Ca^{2+}]_i$ accumulation. We choose to use the TP04 model since it exhibits slow ion accumulation but its ion channel recovery is fast. Following the same approach as in

Section 2.3.1, we simulated the two diseased conditions: adding I_{to} to simulate Brugada syndrome, and increasing inward currents and reducing outward currents to simulate long QT syndrome. We develop a new iterated map model that incorporates the memory effects from slow $[Ca^{2+}]_i$ accumulation, and call this model the "Ca^{2+}-memory map model." We show that the traditional APD-restitution map model cannot while the Ca^{2+}-memory map model can accurately capture the bifurcations and the complex APD dynamics from the AP model. In the final section, *Section IV*, we discuss briefly the implications of our findings from the AP models and the new iterated map models to cardiac arrhythmogenesis and potential applications to other excitable systems.

2.2 Action Potential Models and Simulation Methods

We carry out computer simulations using two AP models with the voltage (V) governed by the following differential equation:

$$C_m \frac{dV}{dt} = -I_{\text{ion}} + I_{\text{sti}}, \tag{2.6}$$

where $C_m = 1\,\mu\text{F/cm}^2$ is the membrane capacitance, I_{ion} is the total ionic current density, and I_{sti} is the stimulus current density, a square pulse for a set duration of time. I_{ion} is the sum of the ionic currents, each driven by the flow of Na^+, K^+, and/or Ca^{2+} flowing in and out of the cell. The number of individual currents and their mathematical formulations depend on specific AP models. The first model we use is the LR1 model [LR91], which is one of the simplest cardiac AP models with physiological ionic current formulations. In this model, we use $I_{\text{sti}} = 80\,\mu\text{A/cm}^2$ with a 0.5 ms duration. The second model we use is a much more complex one, a human ventricular AP model developed by ten Tusscher *et al.*[tTNNP04]. In this model, we use $I_{\text{sti}} = 52\,\mu\text{A/cm}^2$ with a 1 ms duration.

Since there is no I_{to} in the LR1 model, we include an I_{to} current taken from

the model by Mahajan *et al.* [MSS+08],

$$I_{\text{to}} = g_{\text{to}} x_{\text{to}} y_{\text{to}} (V - E_{\text{K}}), \tag{2.7}$$

where g_{to} is the maximum conductance, x_{to} is the activation gating variable, y_{to} is the inactivation gating variable, and E_{K} is the reversal potential of the K^+ channel. We take the formulation of the fast I_{to} (i.e., $I_{\text{to,f}}$) from the Mahajan *et al.* model. I_{to} formulations (both slow and fast I_{to}) are present in the TP04 model. For simplicity and consistency, we remove the two original I_{to} formulations and added the above I_{to} formulation (Eq. (2.7)) to the TP04 model.

A time-adaptive forward-Euler method is used in computer simulations. The time step is $\Delta t = 0.05\,\text{ms}$ if the change in voltage $\Delta V < 0.1\,\text{mV}$, otherwise the time step is $\Delta t = 0.005\,\text{ms}$. The cell is paced periodically with period T.

2.3 Results

2.3.1 Complex APD Dynamics Caused by Memory Originating from Slow Recovery of Ion Channels

We first investigate the effects of memory originating from slow recovery of membrane ion channels. During an AP, ion channels activate and then inactivate/deactivate, and after the AP it takes a certain amount of time for the ion channels to fully recover. Different ion channels have different recovery times, ranging from a few milliseconds to seconds or even longer. Memory manifests from slowly recovering ion channels. One potential source of memory is the slow component of the delayed rectifier K^+ current (I_{Ks}) [SJ90, ZLRR95, SR05], which activates and recovers slowly, on the order of several hundred milliseconds to a couple seconds. In this section, we use the LR1 model to investigate the effects of memory induced by slow K^+ channel recovery. Since the ion concentrations are fixed in the LR1 model, one avoids the confluent effects of memory caused by

slow ion accumulation. In the LR1 model, the time-dependent K^+ current (I_K) is a slowly activating and recovering current.

2.3.1.1 Memory Unmasked/Exacerbated by I_{to}

To demonstrate the effects of I_{to} on memory, we plot S1S2 APD restitution curves of the AP model with and without I_{to} for different S1 pacing periods, T_{S1S1} (see Fig. 2.1(a) for the S1S2 pacing protocol). The difference in APD restitution as a result of applying different pre-pacing S1S1 intervals is a measure of the memory effect.

Fig. 2.1(b) shows S1S2 APD restitution curves of the original LR1 model for two different S1 pacing periods $T_{S1S1} = 400\,\text{ms}$ and $1000\,\text{ms}$. The shorter S1 pacing period results in an APD restitution curve that shifts slightly to the right. Thus, in the LR1 model without I_{to}, the effect of memory on APD restitution is small.

The presence of I_{to} causes significant changes in AP morphology and the resulting APD restitution curves. I_{to} is an outward K^+ current that spikes during phase-1 and is almost completely inactivated during phase 2 (Figs. 2.2(a) and (b)). Fig. 2.2(c) demonstrates the effects on AP morphology by I_{to}. In the original model (black trace in 2.2(c)), the phase-1 notch of the AP terminates at roughly $10\,\text{mV}$. I_{to} causes a more pronounced phase-1 notch. If the I_{to} conductance is larger than a critical value, the voltage repolarizes immediately after the notch, resulting in early repolarization without a phase 2 plateau, known as a spike (red trace in 2.2(c)). If the I_{to} conductance is smaller than the critical value, there is a rebound depolarization during phase 2, known as a spike-and-dome (blue trace in 2.2(c)).

I_{to} creates an "all-or-none" behavior leading to so-called spike-and-dome AP morphology, in which small changes in I_{to} conductance result in either a spike-

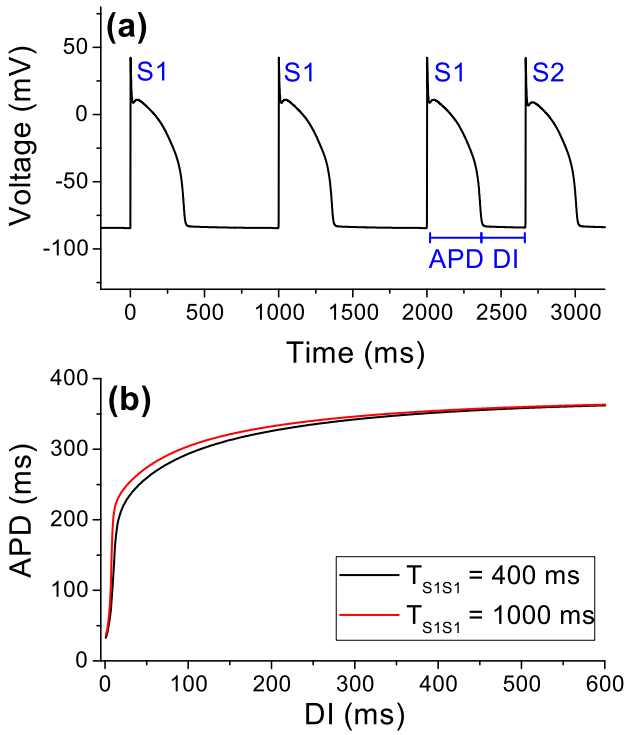

Figure 2.1: The S1S2 restitution protocol and S1S2 APD restitution curves from the original LR1 model. **(a)**. APs demonstrating the S1S2 restitution protocol. Here, $T_{\mathrm{S1S1}} = 1000\,\mathrm{ms}$, and the S2 stimulus is applied after the third S1 beat with a diastolic interval $\mathrm{DI} = 300\,\mathrm{ms}$. **(b)**. Restitution curves showing the dependence of APD on DI for different S1 pacing periods $T_{\mathrm{S1S1}} = 400\,\mathrm{ms}$ and $T_{\mathrm{S1S1}} = 1000\,\mathrm{ms}$. Note that the two curves differ only slightly, indicating a small memory effect.

and-dome with a long APD or a spike with a short APD, as seen in the blue and red APs in Fig. 2.2(c). Fig. 2.2(d) shows this sensitive dependence of APD on g_{to}, the maximum conductance of I_{to}. Increasing g_{to} initially decreases APD slightly, then increases APD up to about 500 ms, at which point APD decreases sharply from 500 ms down to 100 ms. Fig. 2.2(e) reveals the effects of I_{to} on the restitution curves in the presence of varying levels of g_{to}. The presence of I_{to} causes the restitution curve to have a more sensitive dependence on DI. In particular, there is a critical value of DI where the dependence of APD is very steep. As g_{to} increases, the APD restitution curves shift to the right.

Fig. 2.2(f) reveals the effect of changing the S1 pacing period, from $T_{\text{S1S1}} =$ 400 ms to 2000 ms. The longer S1 pacing period causes the APD restitution curve to shift significantly to the right by about 300 ms. Compare this to the case without I_{to} (Fig. 2.1(b)), where instead the shorter pacing period causes a very slight shift to the right and by only a few milliseconds. This indicates that in the presence of I_{to}, there is a significant effect of memory. Since the I_{to} formulation we added to the LR1 model is the fast I_{to}, the time constants are small, typically less than 100 ms, and thus memory is not directly from I_{to} itself. The memory still originates from the slow recovery of I_{K}, but I_{to} unmasks and exacerbates the memory effect, causing a large effect on S1S2 APD restitution behaviors.

2.3.1.2 I_{to}-Induced Complex APD Dynamics

We next demonstrate how APD dynamics are effected by I_{to}. In the prior section, we showed that in the absence of I_{to}, the S1S2 restitution curves remain nearly identical when the S1 pacing period is either $T_{\text{S1S1}} = 400$ ms or 1000 ms. Using the APD-restitution map model (Eq. (2.2)), where the function f is numerically obtained by using the S1S2 APD restitution curves from the simulation of the LR1 model (e.g. from Fig. 2.1(b)), we can obtain the bifurcation diagrams showing the global APD dynamics captured by the restitution map.

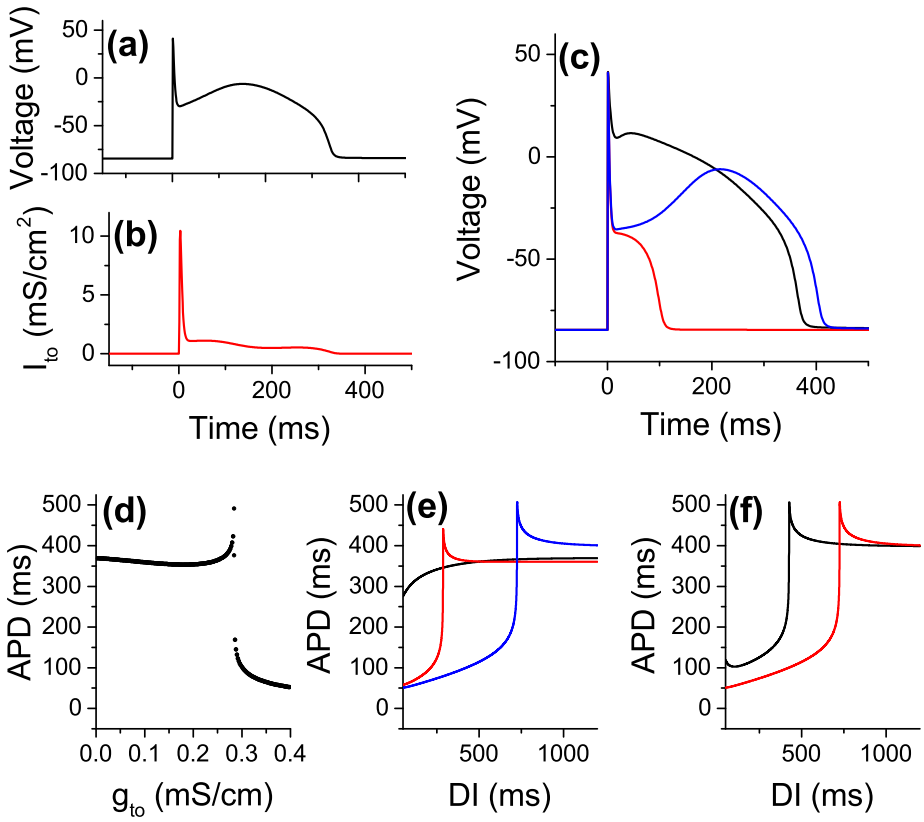

Figure 2.2: The effects of I_{to} on AP morphology and APD. **(a)**. AP with a pronounced phase-1 notch. **(b)**. I_{to} activity during the AP in (a). **(c)**. APs in the absence of I_{to} (black) and in the presence of I_{to} inducing a spike (red, $g_{\text{to}} = 0.3\,\text{mS/cm}^2$) and spike-and-dome (blue, $g_{\text{to}} = 0.28\,\text{mS/cm}^2$). **(d)**. Dependence of APD on g_{to}. The pacing period is $T = 2000\,\text{ms}$. Initially, increasing g_{to} decreases APD, then increases APD up to a critical value when APD $= 500\,\text{ms}$, at which point an increase in g_{to} causes a sudden drop in APD to 100 ms. **(e)**. Dependence of APD restitution curves on g_{to}. The S1 pacing period is $T_{\text{S1S1}} = 2000\,\text{ms}$. Without I_{to} (black), the restitution curve is flat except for DI $< 200\,\text{ms}$. With I_{to} (red and blue), there is a sensitive dependence of APD around a critical value of DI. The higher value of g_{to} (blue, $g_{\text{to}} = 0.278\,\text{mS/cm}^2$) causes a restitution curve that is right-shifted from that of the lower value (red, $g_{\text{to}} = 0.24\,\text{mS/cm}^2$). **(f)**. Dependence of APD restitution curves on the S1 pacing period T_{S1S1}, in the presence of I_{to} with $g_{\text{to}} = 0.278\,\text{mS/cm}^2$. $T_{\text{S1S1}} = 400\,\text{ms}$ for black trace, 2000 ms for red trace. We use $T_{\text{S1S1}} = 2000\,\text{ms}$ instead of 1000 ms (as in Fig. 2.1) in order to avoid alternans during S1 pacing.

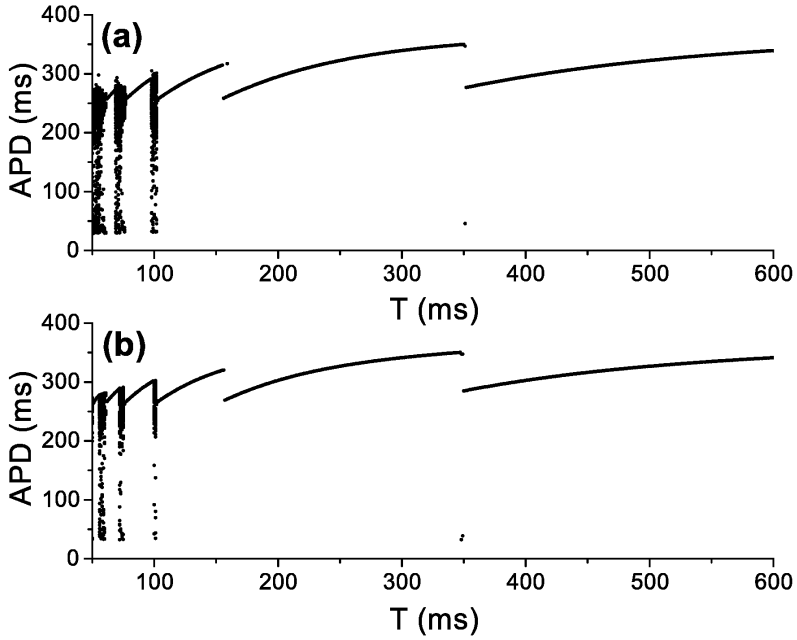

Figure 2.3: APD dynamics of the LR1 model in the absence of I_{to}. **(a)**. Bifurcation diagram of the AP model under constant-T pacing. **(b)**. Bifurcation diagram generated from the APD-restitution map model (Eq. (2.2)) using the S1S2 APD restitution curve with $T_{\text{S1S1}} = 1000\,\text{ms}$ (red curve in Fig. 2.1(b)). The two diagrams are nearly identical.

The bifurcation diagrams generated from the AP model (Fig. 2.3(a)) and generated from Eq. (2.2) using the APD restitution curve for $T_{\mathrm{S1S1}} = 1000\,\mathrm{ms}$ in 2.1(b) (Fig. 2.3(b)) are nearly identical, both showing $2:1$ and $3:1$ stimulation failure followed by chaos as T decreases. These results show that the APD-restitution map model (Eq. (2.2)) is sufficient in capturing the global APD dynamics of the AP model.

In the presence of I_{to}, we have shown that the S1S2 APD restitution curves change under different S1 pacing periods. As in the case without I_{to}, we compare the bifurcation diagrams generated by the APD-restitution map model (Eq. (2.2)) to the one obtained from the AP model. Fig. 2.4 demonstrates the APD dynamics in the case where $g_{\mathrm{to}} = 0.278\,\mathrm{mS/cm^2}$ and the steady-state curve of $y_{\mathrm{to,f}}$ is shifted by $8\,\mathrm{mV}$ to more negative voltages. The choice of g_{to} and the modification of $y_{\mathrm{to,f}}$ provide an example where stimulation failure does not occur.

In the presence of I_{to}, complex APD dynamics, including alternans and chaos, occur at slower pacing periods (Fig. 2.4). The bifurcation diagram of the AP model, seen in Fig. 2.4(b), shows instability occurring in the range $536\,\mathrm{ms} \leq T \leq 1183\,\mathrm{ms}$, and in addition there is a window of chaos for pacing periods between 536 ms and 639 ms. The bifurcation diagrams generated from the APD-restitution map model (Eq. (2.2)) using restitution curves with $T_{\mathrm{S1S1}} = 400\,\mathrm{ms}$ (Fig. 2.4(c)) and $T_{\mathrm{S1S1}} = 2000\,\mathrm{ms}$ (Fig. 2.4(d)) each reveals a window of instability that is significantly smaller than the window of instability of the AP model. In the $T_{\mathrm{S1S1}} = 400\,\mathrm{ms}$ case, instability occurs in the range $534\,\mathrm{ms} \leq T \leq 897\,\mathrm{ms}$, and in the $T_{\mathrm{S1S1}} = 2000\,\mathrm{ms}$ case, the instability range is $820\,\mathrm{ms} \leq T \leq 1196\,\mathrm{ms}$. Besides the narrow range of instability, the APD-restitution map model (Eq. (2.2)) does not have a chaotic region near the left-most bifurcation point as revealed in the AP model. This demonstrates that the APD-restitution map model (Eq. (2.2)), without incorporating memory, cannot correctly capture the dynamics of the AP model.

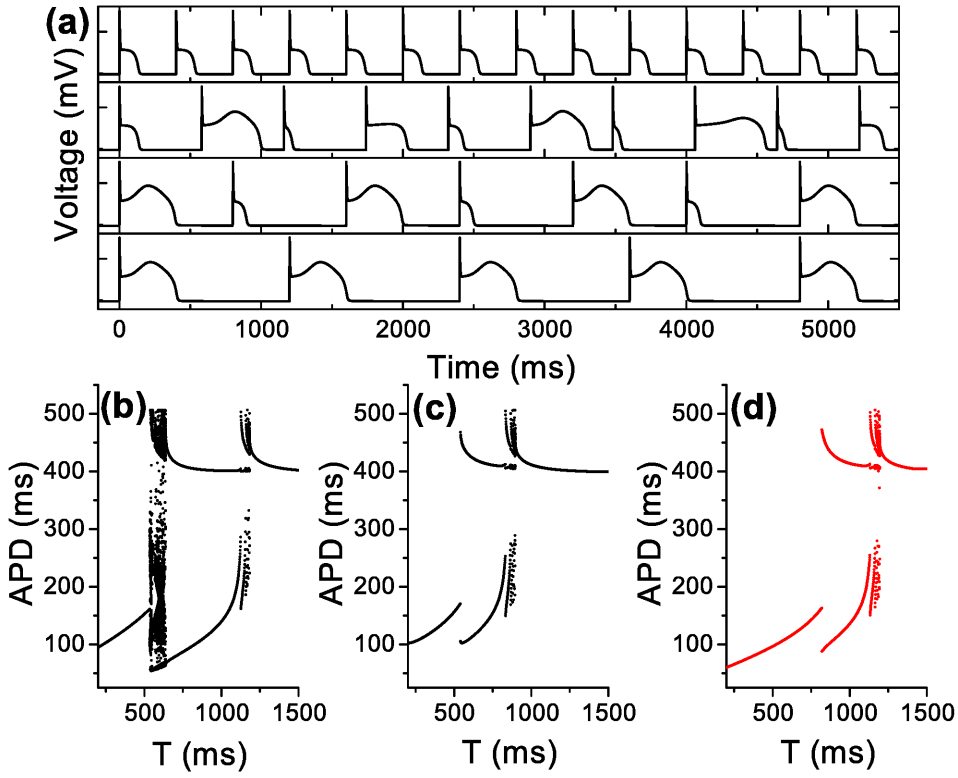

Figure 2.4: APD dynamics of the LR1 model in the presence of I_{to}, with $g_{\text{to}} = 0.278\,\text{mS/cm}^2$ and the y-gate shifted by 8 mV to more negative voltages. **(a)**. Sample APs from the model when the pacing period is (from top to bottom) $T = 400$ ms (stable APs with spikes), 580 ms (chaos), 800 ms (alternans), and 1200 ms (stable APs with spike-and-domes). **(b)**. Bifurcation diagram of the AP model. **(c)**. Bifurcation diagram generated from Eq. (2.2) using the S1S2 restitution curve with $T_{\text{S1S1}} = 400$ ms, shown in Fig. 2.2(d). **(d)**. Bifurcation diagram generated from the APD-restitution map model (Eq. (2.2)) using the S1S2 restitution curve with $T_{\text{S1S1}} = 2000$ ms, also shown in Fig. 2.2(d).

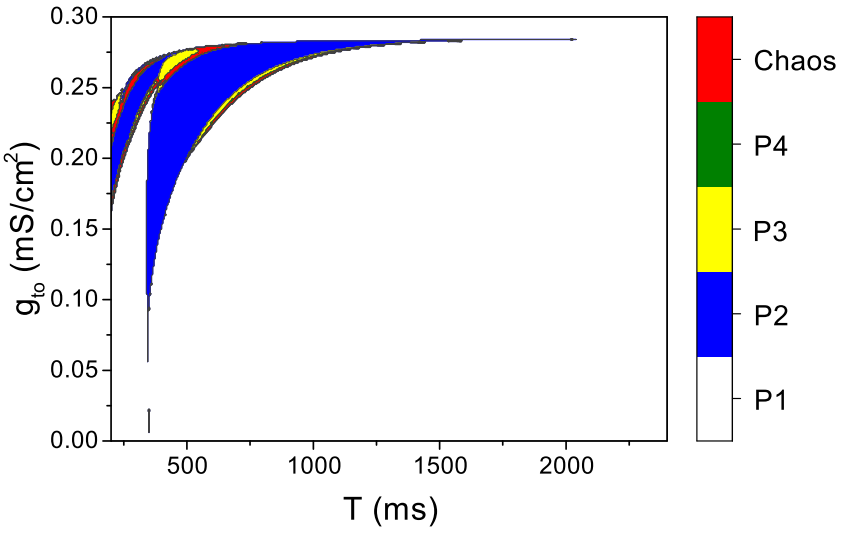

Figure 2.5: Contour plot of the excitation dynamics of the AP model as a function of g_{to}, the maximal conductance of I_{to}, and the pacing period T. P1 = period-1, P2 = period-2 (alternans), P3 = period-3, P4 = period-4.

To show how I_{to} affects the APD dynamics, we change the intensity of I_{to} by changing its maximum conductance g_{to} and plot a contour map that reveals the APD dynamics of the model for different pacing periods. Fig. 2.5 shows the results, demonstrating how increasing the intensity of I_{to} increases and shifts the region of instability towards longer pacing periods. Increased levels of g_{to} cause instability to occur for longer pacing periods until g_{to} reaches a threshold. In this particular example, when $g_{\text{to}} = 0.284\,\text{mS/cm}^2$ alternans occurs for pacing periods up to $T = 2000\,\text{ms}$, equivalent to 30 beats/min. When g_{to} is larger, the AP becomes a spike without the spike-and-dome morphology, and no instability occurs.

2.3.1.3 An Iterated Map model Incorporating the Memory Effects

In the absence of I_{to} the APD-restitution map model (Eq. (2.2)) can well capture the overall APD dynamics, as demonstrated in Fig. 2.3. However, in the presence of I_{to}, the iterated map model fails to appropriately capture the APD dynamics due to a significant effect of memory. To reveal the effects of memory on APD dynamics, we develop a new iterated map model that explicitly incorporates memory. As discussed previously, the source of memory in the LR1 model is the slow activation and deactivation kinetics of the X-gating variable, described by the following differential equation [LR91]:

$$\frac{dX}{dt} = \frac{X_\infty - X}{\tau_X}, \tag{2.8}$$

where $X_\infty \equiv X_\infty(V)$ is the voltage-dependent steady-state of X, and $\tau_X \equiv \tau_X(V)$ is the voltage-dependent time constant of X. The dependence of X_∞ and τ_X on voltage is given in the LR1 model, and is shown in Fig. 2.6(a)-(b). Importantly, the τ_X curve shows that the time constant is about 200 ms at resting membrane potentials of around -85 mV and peaks at around 600 ms, when the cell is depolarized. All other gating variables in the model have very fast time constants less than 100 ms for all voltages, and thus cannot contribute to the source of memory.

Fig. 2.6(c) provides an example showing the relation between X and voltage of a cell undergoing alternans. X increases during the AP, and then decreases during the DI. In the example given, a_n and a_{n+1} are corresponding APDs of short and long APDs, respectively. The value of X preceding the short AP (x_n) is larger compared to X preceding the long AP (x_{n+1}). In other words, a larger initial X value gives rise to a shorter AP and vice versa. Physiologically, this corresponds to a larger repolarization force [SR05] due to a higher open probability of the K^+ channels, giving rise to early repolarization. Note that the maximum X value is much smaller during the short AP than during the long AP.

Since the X-gating variable is responsible for the memory in the LR1 model,

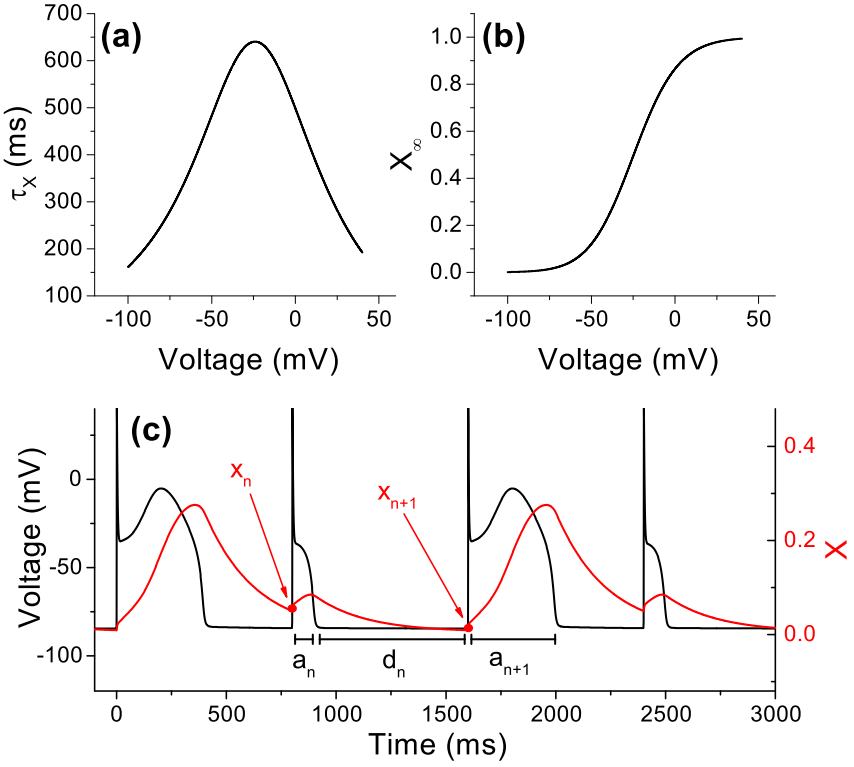

Figure 2.6: Behavior of the X-gating variable. **(a)**. Voltage dependence of the time constant τ_X. **(b)**. Voltage dependence of the steady state X_∞. **(c)**. Sample plot of X alongside APs undergoing alternans. X increases during the APs and decreases during the DIs, and a larger value of X precedes a spike (short APD, a_n) while the smaller value of X precedes a spike-and-dome (long APD, a_{n+1}).

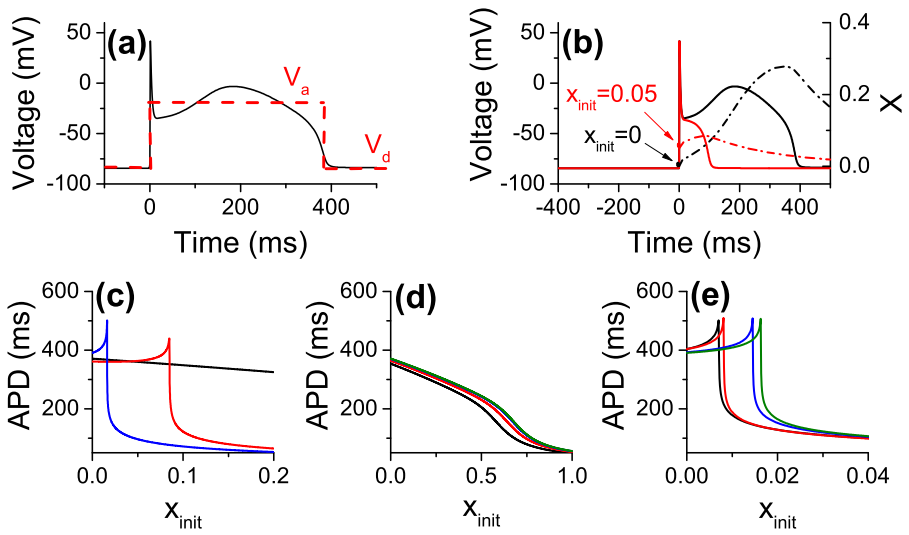

Figure 2.7: Effects of the X-gating variable on APD. **(a)**. Square wave approximation of an AP used for the derivation of the map in Eq. (2.9). The resting membrane potential is V_d and the depolarized membrane potential is V_a. **(b)**. The dependence of APD on the initial value of X, x_{init}. When $x_{\text{init}} = 0$ the resulting AP exhibits a spike-and-dome, whereas when $x_{\text{init}} = 0.05$ the resulting AP is a spike. The AP with a longer APD (spike-and-dome) causes X to increase for a longer period of time. **(c)**. APD dependence curves on x_{init} for different maximal conductance levels $g_{\text{to}} = 0\,\text{mS/cm}^2$ (black), $0.24\,\text{mS/cm}^2$ (blue), $0.278\,\text{mS/cm}^2$(red). **(d)**. Without I_{to} ($g_{\text{to}} = 0\,\text{mS/cm}^2$) APD dependence curves on X for different diastolic intervals preceding the AP, DI = 50 ms (black), 100 ms (red), 200 ms (blue), 1000 ms (green). **(e)**. Same as (d), but with I_{to} ($g_{\text{to}} = 0.278\,\text{mS/cm}^2$).

we develop an iterated map equation describing the relation between x_n and x_{n+1}, and the relation between a_n and x_n. To develop the iterated map equation for x_n, we approximate the AP to be a square wave in which the cell has a constant voltage V_a during the AP and a constant voltage V_d during its diastolic phase. See Fig. 2.7(a) for a visualization of the square wave approximation of an AP. Under this approximation, $\tau_a \equiv \tau_X(V_a)$ is the time constant of X during the AP, and $\tau_d \equiv \tau_X(V_d)$ is the time constant during the DI. Similarly, $x_a \equiv X_\infty(V_a)$ is the steady state open probability during the AP, and $x_d \equiv X_\infty(V_d)$ is the steady state open probability during the DI.

Let x_n be the value of X at the beginning of an AP with APD a_n and DI d_n (as shown in Fig. 2.6(c)). Assuming the square wave approximation with the time constants and steady state values given, Eq. (2.8) can be integrated exactly. Assuming that at equilibrium X is completely deactivated during the resting potential, so that $x_d \equiv 0$, this gives rise to the following map:

$$x_{n+1} = \left(x_a - (x_a - x_n)e^{-\frac{a_n}{\tau_a}}\right) e^{-\frac{d_n}{\tau_d}} \equiv w(x_n, a_n, d_n). \tag{2.9}$$

Eq. (2.9) provides an iterated map for X from beat to beat, assuming the APD and DI values a_n and d_n are provided as well. We assume that a_n is completely determined by x_n, i.e.,

$$a_n = g(x_n), \tag{2.10}$$

where g provides the APD-dependence on the memory variable x_n. And since the pacing period T satisfies the equation $mT = a_n + d_n$, then

$$d_n = mT - a_n, \tag{2.11}$$

where m is the number of stimuli before giving a new beat.

Together, Eqs. (2.9)-(2.11) form a complete 1-dimensional iterated map. We next determine the function g in Eq. (2.10), which captures the dependence of APD on the value of X at the beginning of the AP, x_{init}. In a similar fashion to the S1S2 restitution protocol which serves to find the dependence of APD on DI, here we use another simulation protocol to determine the dependence of APD on x_{init}. At a fixed pacing period, e.g. $T = 1000\,\text{ms}$, after a certain number of N pre-paced beats we change the value of x_{init} at the time of the $(N+1)^{\text{st}}$ stimulus and record the resulting APD. Fig. 2.7(b) provides examples of APs when $x_{\text{init}} = 0$ and $x_{\text{init}} = 0.05$, in which 100 pre-paced beats were used. $x_{\text{init}} = 0$ results in an AP with a spike-and-dome and an APD of about 400 ms, whereas when $x_{\text{init}} = 0.05$ the resulting AP is a spike with a shortened APD of about 100 ms.

I_{to} causes shifts in the APD-dependence curves on x_{init}, as demonstrated in Fig. 2.7. Without I_{to} ($g_{\text{to}} = 0\,\text{mS/cm}^2$) the APD has a maximum at 375 ms when

$x_{\text{init}} = 0$ and smoothly decreases as x_{init} increases. When I_{to} is included, there appears a critical x_{init} value in which APD sharply declines from over 300 ms to less than 100 ms, indicating a sensitive dependence of APD on x_{init}. For values less than the critical x_{init} value, the APD is temporarily increasing as a function of x_{init}, but is then decreasing beyond the critical value. In Fig.2.7(c), the red and blue curves show the APD dependence on x_{init} for $g_{\text{to}} = 0.24\,\text{mS/cm}^2$ and $g_{\text{to}} = 0.278\,\text{mS/cm}^2$. When the conductance of I_{to} is weaker (red curve), the critical value occurs around $x_{\text{init}} = 0.08$, while when the conductance is stronger (blue curve), the critical value occurs around $x_{\text{init}} = 0.02$. In general, the critical x_{init} value shifts to the left as g_{to} increases, due to a change in the balance of I_{to}-induced early repolarization.

We next test how accurately x_{init} alone affects APD. To do so, we check the APD dependence on x_{init} when the DI itself varies as well. Fig. 2.7(d)-(e) each shows four different curves for different values of DI, 50 ms, 100 ms, 200 ms, and 1000 ms, without and with I_{to}. In both cases, the curves shift to the left for decreasing values of DI, but is more pronounced when DI = 50 ms and 100 ms. The curves corresponding to DI = 200 ms and DI = 1000 ms vary by only about 0.002. Therefore, this indicates that the recovery of other ionic currents visibly affects the APD only when DI $<$ 100 ms. As shown in Fig. 2.4, dynamical instabilities occur for DI $\gg$ 100 ms, indicating that recovery of I_{K} plays the major role in causing instability in the presence of I_{to}. This also justifies not incorporating DI as an explicit variable in the iterated map model in Eq. (2.12). For the same reason, in this study, we ignore the APD dynamics at very fast pacing and plot our bifurcation diagrams for $T > 200$ ms (except for Figs. 2.3 and 2.16). In general, one can rewrite Eq. (2.12) as $a_n = g(x_n, d_n)$ to include contributions from the recovery of other ionic currents, which could be important for APD dynamics at fast heart rates.

2.3.1.4 Memory-Induced Instabilities and Complex APD Dynamics in the X-memory Map Model

The X-memory map model (Eqs. (2.9)-(2.11)) explicitly incorporates memory and its coupling with APD, in contrast to the APD-restitution map model using the S1S2 restitution curve as in Eq. (2.2). As shown in Fig. 2.4, when I_{to} is included, the APD-restitution map model (Eq. (2.2)) does not adequately capture the APD dynamics in the AP model. We here show that the X-memory map model (Eqs. (2.9)-(2.11)) does in fact accurately capture the APD dynamics and bifurcations of the AP model.

We first use the same model parameters and modifications that were used to generate Fig. 2.4, in which $g_{\text{to}} = 0.278\,\text{mS/cm}^2$ and the y_{to}-gate steady state in the formulation for I_{to} was shifted by 8 mV to more negative voltages. Under the square-wave assumption used to generate Eq. (2.9), we set the map parameters $x_a = 0.6$, $\tau_a = 600\,\text{ms}$, and $\tau_d = 200\,\text{ms}$. Computationally, we determine the APD dependence on X, the function g in Eq. (2.10). By varying the cycle length T in Eq. (2.11) we generate a bifurcation diagram by iterating together Eqs. (2.9)-(2.11).

The resulting bifurcation diagram is shown in Fig. 2.8. The diagram is very similar in topology to the bifurcation diagram obtained directly from the AP model, as seen in Fig. 2.4(b). In particular, both diagrams have windows of chaos near the initial period-doubling bifurcation point near $T = 500\,\text{ms}$, which was completely absent in the bifurcation diagrams generated from the APD-restitution map model, as in Fig. 2.4(c)-(d).

The APD dependence on x_{init} shown in Fig. 2.7(c) is nonmonotonic, in which as x_{init} increases, the value of APD increases until around $x_{\text{init}} = 0.02$ when the curve suddenly drops to APD values less than 150 ms. Similarly, the S1S2 restitution curves are nonmonotonic. As shown previously, a nonmonotonic APD

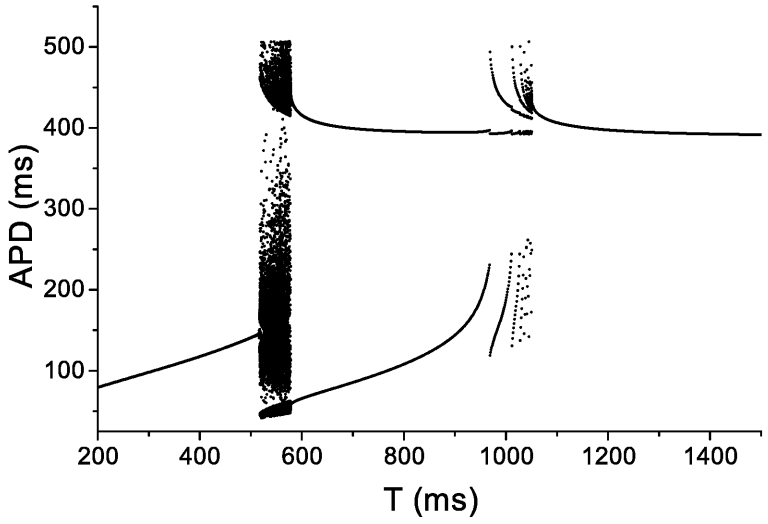

Figure 2.8: Bifurcation diagram of the APD dynamics captured by the X-memory map model, Eqs. (2.9)-(2.11), with $x_a = 0.6$, $\tau_a = 600\,\text{ms}$, $\tau_d = 200\,\text{ms}$, and g provided by interpolating the blue curve in Fig. 2.7(c).

restitution curve can give rise to chaos [QSW07], as is shown in Fig. 2.4(c)-(d). To avoid the confluent effect of nonmonotonicity on the genesis of chaos, we changed the parameters of the LR1 model to result in monotonic APD restitution curves, which is shown in the next example below.

The parameter changes are the following: $g_{\text{to}} = 0.21\,\text{mS/cm}^2$, $G_{\text{si}} = 0.1035\,\text{mS/cm}^2$, $G_{\text{K1}} = 1.330\,34\,\text{mS/cm}^2$, and $\tau_x \to 5\tau_x$. In addition, the y_{to} steady state curve was shifted by 8 mV to more positive voltages (in the prior case, the curve was shifted to more negative voltages). Note that setting $\tau_X \to 5\tau_X$, so that the voltage-dependent time constant of the X-gating variable was increased 5-fold, effectively amplifies the effect of memory by requiring 5 times the amount of time for X to reach equilibrium.

The results under these different parameter changes and modifications are shown in Fig. 2.9. Figs. 2.9(a)-(b) show that indeed the restitution curves and the APD dependence on x_{init} are now monotonic. Because each restitution curve is

monotonic, the APD-restitution map in Eq. (2.2) would only give rise to alternans (Fig. 2.9(c)-(d)). However, as seen in Fig. 2.9(e), the bifurcation diagram of the AP model shows very complex behavior, including very clear period-doubling bifurcation routes to enter and exit chaos.

Since we made the modification $\tau_X \to 5\tau_X$, we also appropriately change the iterated map values τ_a and τ_d in the X-memory map model. Since $\tau_a = 600\,\text{ms}$ and $\tau_d = 200\,\text{ms}$ in the original case, here we multiply these values 5-fold so that $\tau_a = 3000\,\text{ms}$ and $\tau_d = 1000\,\text{ms}$. $x_a = 0.6$ as before. The dynamics of the X-memory map model is shown in the bifurcation diagram in Fig. 2.9(f). The behavior of the X-memory map model matches very closely with the behavior of the AP model, as the bifurcation diagram also reveals period-doubling bifurcation routes to enter and exit chaos, and share other characteristics including large period-2 (alternans) and period-3 windows.

The X-memory map model accurately matches the dynamics of the AP model, even under crudely approximating an AP as a square wave. In contrast, the APD-restitution map in Eq. (2.2) does not capture the complex behavior and underestimates the regions of instability. This demonstrates that the effects of memory produce more complex behaviors.

2.3.1.5 Theoretical analysis and predictions of the X-memory map model

The X-memory map model (Eqs. (2.9)-(2.11)) has model parameters x_a, τ_a, τ_d, and g, the APD dependence on curve. We assume here that g takes on the form of a Hill function, so that

$$a_n = g(x_n) = a_{\min} + \frac{a_{\max} - a_{\min}}{1 + \left(\frac{x_n}{k_x}\right)^h}, \tag{2.12}$$

where $a_{\min}$ and $a_{\max}$ are the minimum and maximum APDs, h is the Hill coefficient, and k_x is the half-max value. A Hill function was chosen to match

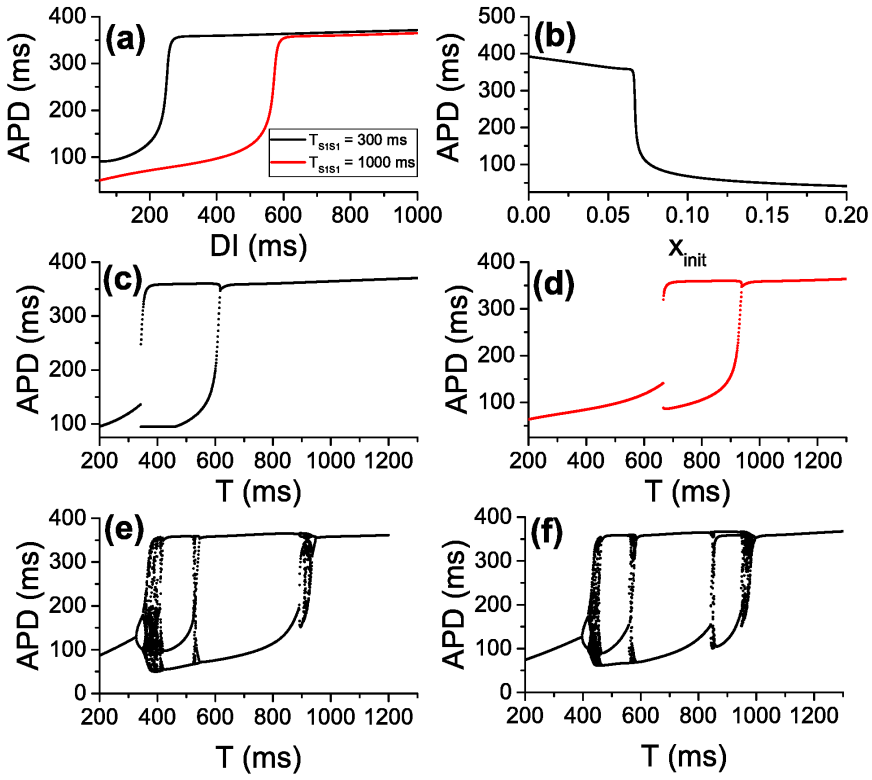

Figure 2.9: Complex APD dynamics captured by the X-memory map model (Eqs. (2.13)-(2.15)), with the following parameter modifications of the AP model: $g_{\rm to} = 0.21\,{\rm mS/cm^2}$, $G_{\rm si} = 0.1035\,{\rm mS/cm^2}$, $G_{\rm K1} = 1.330\,34\,{\rm mS/cm^2}$, $\tau_x \to 5\tau_x$, and the $y_{\rm to}$ steady state curve shifted by 8 mV to more positive voltages. **(a)**. S1S2 restitution curves of the AP model with S1 pacing periods $T_{\rm S1S1} = 300\,{\rm ms}$ and 1000 ms. **(b)**. APD dependence on X. **(c)**. Bifurcation diagram of the APD-restitution map model (Eq. (2.2)) using the black curve in (a). **(d)**. Bifurcation diagram of the APD-restitution map model (Eq. (2.2)) using the red curve in (a). **(e)**. Bifurcation diagram of the AP model. **(f)**. Bifurcation diagram of the X-memory map model (Eqs. (2.9)-(2.11)), with $x_a = 0.6$, $\tau_a = 3000\,{\rm ms}$, $\tau_d = 1000\,{\rm ms}$, and g provided by interpolating the curve in (b).

the sigmoid-like shapes of the APD dependence curves on X, for example in Fig. 2.9(b). So now, Eqs. (2.9), (2.11), and (2.12) form an iterated map model, written together below:

$$x_{n+1} = w(x_n, a_n, d_n) = \left(x_a - (x_a - x_n)e^{-\frac{a_n}{\tau_a}}\right) e^{-\frac{d_n}{\tau_d}}, \tag{2.13}$$

$$a_n = g(x_n) = a_{\min} + \frac{a_{\max} - a_{\min}}{1 + \left(\frac{x_n}{k_x}\right)^h}, \tag{2.14}$$

$$d_n = mT - a_n. \tag{2.15}$$

This produces a 1-dimensional iterated map for X since

$$x_{n+1} = w(x_n, a_n, d_n) = w(x_n, g(x_n), mT - g(x_n)) \equiv W(x_n). \tag{2.16}$$

And in addition, via the function g, there is a one-to-one correspondence between x_n and a_n. In particular, the inverse of g is obtained via the following formula:

$$x_n = g^{-1}(a_n) = k_x \left[\frac{a_{\max} - a_n}{a_n - a_{\min}}\right]^{\frac{1}{h}}, \tag{2.17}$$

so that

$$a_{n+1} = g(x_{n+1}) = g(W(x_n)) = g(W(g^{-1}(a_n))) \equiv H(a_n) \tag{2.18}$$

Eq. (2.18) is the APD return map for the X-memory map model. Sample return maps are provided in Fig. 2.10 when varying the Hill parameter h, the pacing period T, and the time constant τ_d. When varying h (Fig. 2.10(a)), the slope of the return map near the fixed point gets steeper as h increases. An iterated map is unstable when the slope (or derivative) at the fixed point has absolute value exceeding unity, and thus h is a key factor in determining stability. In addition, as seen in Fig. 2.10(b)-(c), increasing T or decreasing τ_d tends to shift the return map to the right, and therefore shifting the fixed point. Fig. 2.10(d) shows a return map from a chaotic region in the actual AP model. Note that the Hill function is monotonic and so is the S1S2 APD restitution curve. For a nonmonotonic APD restitution function, the first return map from Eq. (2.2) is still

nonmonotonic. However, the addition of the memory equation into the iterated map model results in a nonmonotonic map, agreeing with the one from simulation of the AP model. This indicates that memory plays a key role in promoting chaos by converting a monotonic APD return map to a nonmonotonic one.

Fig. 2.10(e) provides a sample bifurcation diagram from the X-memory map model, using the default map parameter values $x_a = 0.6$, $\tau_a = 3000\,\text{ms}$, $\tau_d = 1000\,\text{ms}$, $h = 25$, $k_x = 0.07$. Just as for the full AP model, the diagram shows period-doubling bifurcation routes to enter and exit chaos, with rather large period-2 and period-3 windows. See Fig. 2.9(c) to compare with the bifurcation diagram from the AP model.

We now perform a stability analysis of the fixed point of the X-memory map model. The APD fixed point, denoted a^*, satisfies $a^* = H(a^*)$ so that

$$a^* = H(a^*) = g\left[\left(x_a - (x_a - x^*)e^{-\frac{a^*}{\tau_a}}\right)e^{-\frac{T-a^*}{\tau_d}}\right], \tag{2.19}$$

where $x^* = g^{-1}(a^*)$ is the corresponding X fixed point. To analyze the stability of the fixed point, we find $H'(a^*)$, the derivative of H in Eq. (2.18) evaluated at the fixed point a^*.

$$H'(a^*) = g'(x^*)\left[\left(\frac{1}{\tau_d} - \frac{1}{\tau_a}\right)x^* + e^{-\frac{T-a^*}{\tau_d}}\left(\frac{e^{-\frac{a^*}{\tau_a}}}{g'(x^*)} + \frac{x_a}{\tau_a}\right)\right], \tag{2.20}$$

where

$$g'(x^*) = -\frac{h}{x^*}\frac{(a_{\max} - a^*)(a^* - a_{\min})}{a_{\max} - a_{\min}}. \tag{2.21}$$

The map is unstable whenever $|H'(a^*)| > 1$.

Based on Eq. (2.11), for $|H'(a^*)| > 1$, a large $g'(x^*)$ is needed, indicating that a sensitive response of APD on X is necessary. The presence of I_{to} results in such a steep response to promote the instability. However, the stability also depends on other parameters, such as τ_a and τ_d. Since it is not obvious from Eq. (2.20) to assess their roles, we simulate the X-memory map model directly to show their effects. Fig. 2.11 provides some relationships between the model parameters T, τ_d,

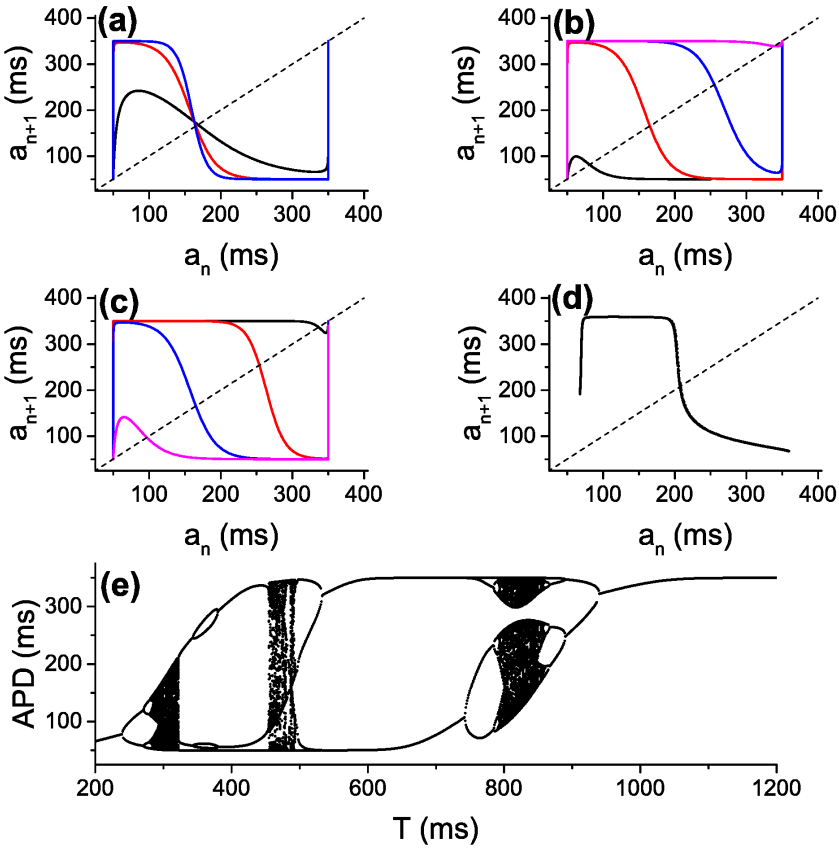

Figure 2.10: Return maps of the X-memory map model (Eqs. (2.13)-(2.15)) and of the AP model. Default parameter values are $x_a = 0.6$, $\tau_a = 3000\,\text{ms}$, $\tau_d = 1000\,\text{ms}$, $h = 25$, $k_x = 0.07$, $T = 500\,\text{ms}$. **(a)**. Return maps for $h = 10$ (black) 20 (red), 40 (blue). **(b)**. Return maps for varying $T = 250\,\text{ms}$ (black), $500\,\text{ms}$ (red), $750\,\text{ms}$ (blue), $1000\,\text{ms}$ (magenta). **(c)**. Return maps for $\tau_d = 250\,\text{ms}$ (black), $500\,\text{ms}$ (red), $1000\,\text{ms}$ (blue), $2000\,\text{ms}$ (magenta). **(d)**. Return map from the AP model as in Fig. 2.9(c) in a chaotic region with $T = 530\,\text{ms}$. **(e)**. Bifurcation diagram of the X-memory map model (Eqs. (2.13)-(2.15)), with parameter values $x_a = 0.6$, $\tau_a = 3000\,\text{ms}$, $\tau_d = 1000\,\text{ms}$, $h = 25$, $k_x = 0.07$.

τ_a, and h, and the overall stability of the X-memory map model. The periodicity of the iterated map is provided for different parameter values of T, τ_d, τ_a, and h, with white regions indicating stability (P1), blue regions indicating period-2 (P2), and yellow, green, and red regions indicating higher orders of periodicity (P3, P4, and chaos).

Fig. 2.11(a) shows the APD dynamics in the parameter space of the time constant τ_d and the pacing period T, with constants $\tau_a = 3000\,\text{ms}$ and $h = 25$ fixed. There is a linear relationship between τ_d and T on stability, in which an increase in τ_d causes both an expansion and a shift to the right of the instability region for varying values of T. Fig. 2.11(b) shows the APD dynamics in the parameter space of h and T, with constants $\tau_a = 3000\,\text{ms}$ and $\tau_d = 1000\,\text{ms}$ fixed. As one would expect, an increase in h causes the window of instability to increase and expands the chaotic regimes until h is very large. Fig. 2.11(c) shows the APD dynamics in the parameter space of h and τ_d while keeping constants $\tau_a = 3000\,\text{ms}$ and $T = 500\,\text{ms}$ fixed. Again as expected, increasing h increases the regime of instability and chaos, while at the same time increasing τ_d reduces the instability region. Finally, Fig. 2.11(d) shows the APD dynamics in the parameter space of the time constants τ_a and τ_d while keeping constants $h = 25$ and $T = 500\,\text{ms}$ fixed. Similar to that seen in Fig. 2.11(a), there is at first a linear relationship between τ_a and τ_d, in which an increase in τ_a causes an increase in the instability region for various values of τ_d. However, when both τ_a and τ_d get too large, the instability region wraps around and closes.

The previous analysis using the X-memory map model examines the effects of different parameters on stability, in particular on the parameters τ_d and τ_a that affect the activation and inactivation kinetics of I_{K}. We now test our results on the AP model. Since τ_d affects only the inactivation of I_{K} during the DI, changing τ_d will ideally have little effect on AP morphology (in contrast to changing τ_a). We change the model formulation of τ_X to equal a set value τ_d during the DI, as

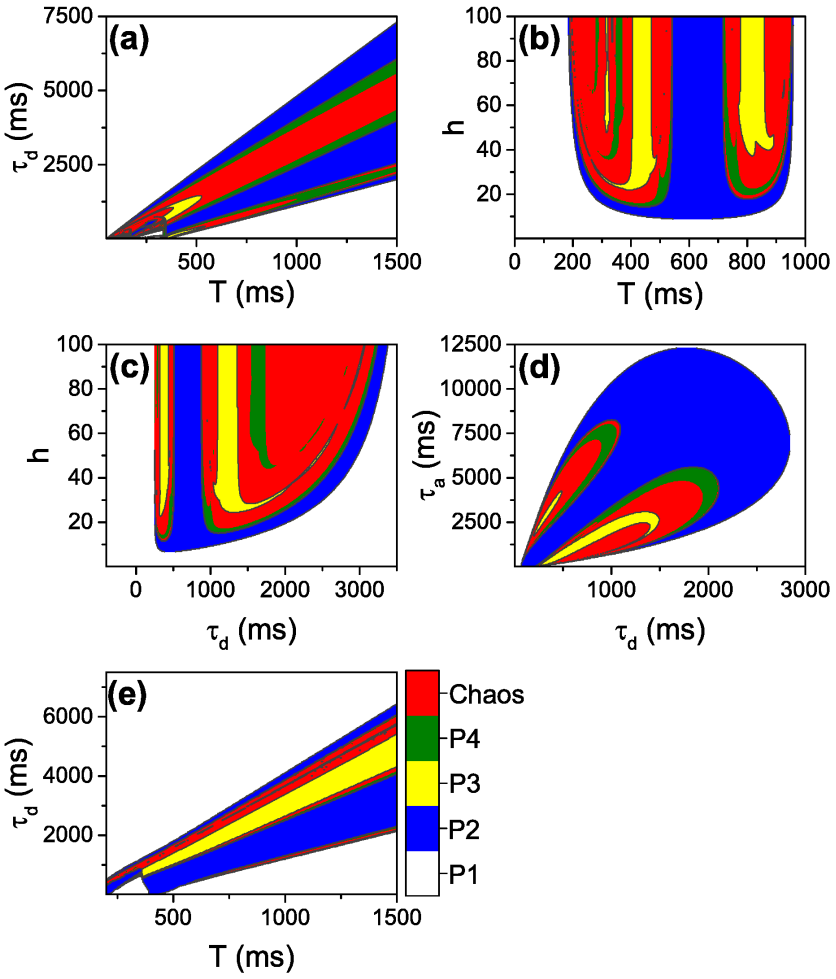

Figure 2.11: Stability maps when varying parameters of the X-memory map model (Eqs. (2.13)-(2.15)). Default parameter values are as follows: $x_a = 0.6$, $\tau_a = 3000\,\text{ms}$, $\tau_d = 1000\,\text{ms}$, $h = 25$, $k_x = 0.07$. **(a)**. Contour map showing stable and unstable regions when varying the time constant τ_d and pacing period T. **(b)**. Stable and unstable regions when varying the Hill coefficient h and T. **(c)**. Stable and unstable regions when varying h and τ_d. **(d)**. Stable and unstable regions when varying the APD and DI time constants τ_a and τ_d. **(e)**. Stable and unstable regions of the modified AP model using the τ_X modification in Eq. (2.22), with the following parameter modifications: $g_{\text{to}} = 0.21\,\text{mS/cm}^2, G_{\text{si}} = 0.1035\,\text{mS/cm}^2, G_{\text{K1}} = 1.330\,34\,\text{mS/cm}^2, \tau_x \to 5\tau_x$, and the y_{to} steady state curved shifted by 8 mV to more positive voltages.

follows:

$$\tau_X = \begin{cases} \tau_d & V < -75\,\mathrm{mV} \\ \overline{\tau_X} & \text{otherwise} \end{cases}. \tag{2.22}$$

$\overline{\tau_X}$ is the original formulation of τ_X in the AP model, for example that shown in Fig. 2.6(a). τ_d is now a new parameter in the AP model, and as before we vary τ_d as well as the pacing period T for stability analysis. Fig. 2.11(e) shows the results using the AP model with the same parameter and formulation modifications to generate Fig. 2.9, including $\overline{\tau_X} \to 5\overline{\tau_X}$. The figure shows a clear resemblance to Fig. 2.11(a), showing that increasing τ_d results in a shift and expansion of the region of instability. The theoretical prediction matches closely with the simulation results.

2.3.1.6 The Memory Effects on EAD-Induced Complex APD Dynamics

Short-term memory is also nontrivial for the excitation dynamics in the setting of long QT syndrome. Long QT syndrome is a cardiac disease with a high risk of syncope and sudden death, caused by genetic mutations or drugs that either decrease outward currents or increase inward currents, prolonging the APD [Sch06, Rod06]. One of the consequences of APD prolongation is the occurrence of EADs (Fig. 2.12(a)), which are abnormal depolarizations during the AP. In previous studies [TSY+09, SXS+09, SXN+10], we have shown that the presence of EADs can lead to chaotic excitation dynamics. Fig. 2.12(b) is a bifurcation diagram against the pacing period T from a simulation of the LR1 model, showing a period-doubling bifurcation leading to complex excitation patterns and chaos. Fig. 2.12(c) is a higher resolution bifurcation diagram around the first bifurcation point, demonstrating with more detail the period doubling leading to chaos. The underlying mechanism of chaos was attributed to steep and nonmonotonic APD restitution functions [SXS+09]. However, a detailed comparison between the bi-

furcation from the AP model and that from the iterated map model has not been carried out until our recent study which showed that memory plays a key role [LGWQ17].

Following the same pacing protocol as we have done for the case of I_{to} (there is no I_{to} presence in this case), we calculate the S1S2 APD restitution curves for two different S1 pacing periods (Fig. 2.13(a)). The S1S2 APD restitution curves exhibit a staircase type increase against DI, with each higher step corresponding to an extra EAD in the AP. Faster S1 pacing causes the APD restitution curve to shift to the right (note that this is in contrast to the case in the presence of I_{to}, in which the APD restitution curve shifts to the left under faster S1 pacing, as shown in Fig. 2.2(f) and Fig. 2.9(a). Fig. 2.13(b) and (d) show the bifurcation diagrams obtained using the APD-restitution map model (Eq. (2.2)) and the S1S2 APD restitution curves. However, higher resolution bifurcation diagrams around the onset of instability (Figs. 2.13(c) and (e)) show sudden transitions for stable APD to APD alternans, completely missing the supercritical period doubling bifurcation sequences of the AP model.

We then use the same method as in the case with I_{to} and measure the X-dependence curve of APD. Fig. 2.14(a) shows a staircase dependence of APD on x_{init}. Using the X-memory map model (Eqs. (2.9)-(2.11)) with the X-dependence curve of APD in Fig. 2.14(a), we generate a new bifurcation diagram (Fig. 2.14(b)), which shows almost exactly the same bifurcation sequence as in the AP model. Fig. 2.14(c) shows the bifurcation sequence around the first instability point, which clearly demonstrates period doubling leading to chaos in a very similar manner as in the AP model (compare to Fig. 2.12(c)). These results indicate that memory plays an important role in generating the complex EAD-related excitation dynamics.

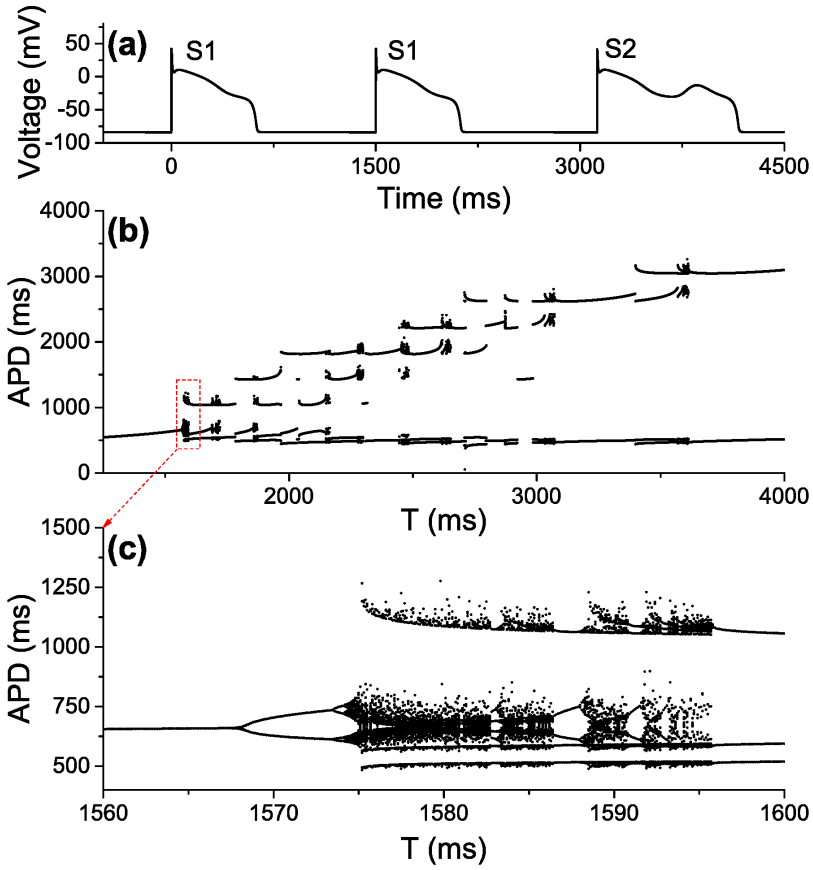

Figure 2.12: EAD and APD dynamics in the LR1 model with $\tau_X \to 10\tau_X$ and without I_{to} included. All other parameter values are taken from the original model formulation. **(a)**. An S1S2 protocol resulting in an EAD on the S2 beat, with $T_{\text{S1S1}} = 1500\,\text{ms}$, and DI $= 1000\,\text{ms}$ before the S2 beat. **(b)**. Bifurcation diagram of the AP model. **(c)**. Close up of the bifurcation diagram around the first bifurcation point.

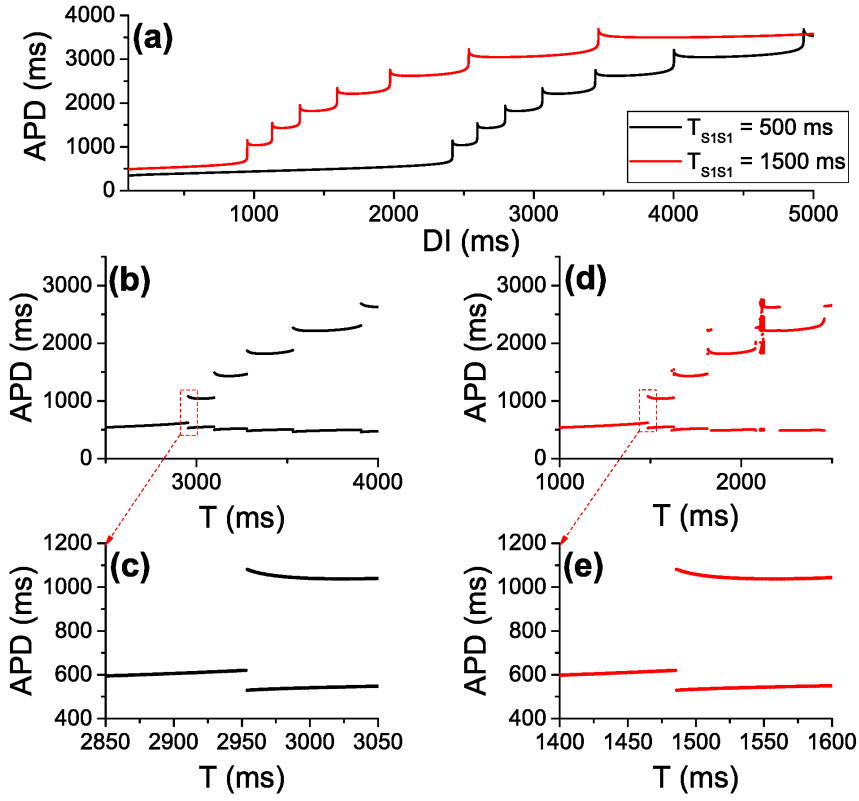

Figure 2.13: EAD dynamics predicted by S1S2 APD restitution curves. **(a)**. S1S2 restitution curves for two S1 pacing periods $T_{\mathrm{S1S1}} = 500\,\mathrm{ms}$ and $1500\,\mathrm{ms}$. **(b)**. Bifurcation diagram using the APD-restitution map model (Eq. (2.2)) and the restitution curve with S1 pacing period $T_{\mathrm{S1S1}} = 500\,\mathrm{ms}$ (black curve in (a)). **(c)**. Close up of the bifurcation diagram around the first bifurcation point. **(d)**. Bifurcation diagram using the APD-restitution map model (Eq. (2.2)) and the restitution curve with S1 pacing period $T_{\mathrm{S1S1}} = 1500\,\mathrm{ms}$ (red curve in (a)). **(e)**. Close up of the bifurcation diagram around the first bifurcation point.

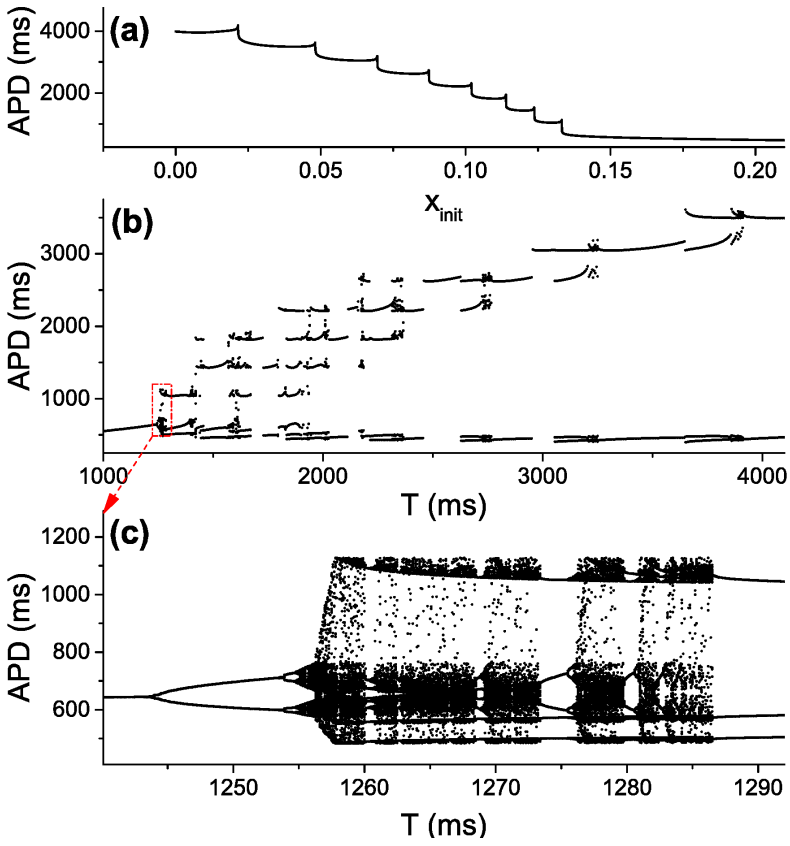

Figure 2.14: Bifurcation diagrams from the X-memory map model (Eqs. (2.9)-(2.11)) in the presence of EADs. **(a)**. The dependence of APD on x_{init}. **(b)**. Bifurcation of the X-memory map model (Eqs. (2.9)-(2.11)), using the curve in panel (a) for g and model parameters $x_a = 0.6$, $\tau_a = 6000\,\text{ms}$, and $\tau_d = 2500\,\text{ms}$. **(c)**. Close-up of the bifurcation diagram in (b) around the first bifurcation point.

2.3.2 Complex APD Dynamics Caused by Memory Originating from Intracellular Ion Concentration Accumulation

Besides slow recovery of ion channels, it also takes a certain amount of time for intracellular ion (Na^+, K^+, and Ca^{2+}) concentrations to reach new steady states after a change, such as after a sudden change in the heart rate [FR00], causing memory in the system. Here, we demonstrate the effects of memory caused by slow $[Ca^{2+}]_i$ accumulation. We use a human ventricular cell model developed by ten Tusscher *et al.* [tTNNP04], the TP04 model, to investigate the effects of memory originating from intracellular ion concentration accumulation. For consistency, we remove the original I_{to} (both fast and slow I_{to}) and replace them with the same I_{to} formulation as before from Mahajan *et al.* [MSS+08].

We use the TP04 model because all ionic gating variables have relatively fast time constants during the diastolic phase. In particular, the two slowly activating potassium currents, I_{Kr} and I_{Ks}, rapidly deactivate during the diastolic phase. The two gating variables of I_{Kr}, X_{r1} and X_{r2}, and the gating variable of I_{Ks}, X_s, have time constants $\tau_{x_{r1}} < 130\,\text{ms}$, $\tau_{x_{r2}} < 2\,\text{ms}$, and $\tau_{x_s} < 5\,\text{ms}$ at voltages lower than $-75\,\text{ms}$. And so, while the gating variables of these currents do have long time constants as high as 1200 ms in the model for voltages higher than $-40\,\text{mV}$, the gating variables deactivate rapidly during the diastolic interval. In contrast, $[Ca^{2+}]_i$ as well as intracellular Na^+ and K^+ concentrations ($[Na^+]_i$ and $[K^+]_i$) accumulate very slowly.

Since $[Na^+]_i$ and $[K^+]_i$ accumulation is much slower than $[Ca^{2+}]_i$ accumulation, to avoid any confluent effects we fixed the concentrations $[Na^+]_i = 12\,\text{mM}$ and $[K^+]_i = 138\,\text{mM}$ in the TP04 model so that the memory effect is primarily driven by the accumulation of $[Ca^{2+}]_i$.

2.3.2.1 Memory and complex APD dynamics caused by ion concentration accumulation

We begin our analysis as before, by examining the APD restitution curves of the TP04 model with and without I_{to} and comparing the bifurcation diagrams of the APD-restitution map model (Eq. (2.2)) using the restitution curves with those of the AP model.

Fig. 2.15 shows the APD restitution curves of the AP model with and without I_{to}, in each case using two different pacing periods. Without I_{to} (Fig. 2.15(a)), the restitution curves using S1 pacing periods $T_{\text{S1S1}} = 750\,\text{ms}$ and $T_{\text{S1S1}} = 3000\,\text{ms}$ are both monotonically increasing, similar to the restitution curves generated from the LR1 model without I_{to} (Fig. 2.1(b)). There is an upward shift in the curves by about 5 ms for the larger S1 pacing period ($T_{\text{S1S1}} = 3000\,\text{ms}$), indicative of some underlying source of memory in the TP04 model but that has minimal effect on restitution.

In the presence of I_{to}, with maximum conductance $g_{\text{to}} = 0.18\,\text{mS/cm}^2$, the APD restitution curves show some similarity to the restitution curves generated from the LR1 model in the presence of I_{to} (Fig. 2.2(d)), namely that they are nonmonotonic, have steep regions with a sensitive dependence of APD on DI, and the larger S1 pacing period shifts the restitution curve to the right. Here however, the shift in the two curves is substantial, in which an S1 pacing period of $T_{\text{S1S1}} = 9000\,\text{ms}$ leads to a restitution curve that is about 6000 ms right-shifted from the restitution curve using an S1 pacing period of $T_{\text{S1S1}} = 250\,\text{ms}$. Note that using an S1 pacing period as large as $T_{\text{S1S1}} = 9000\,\text{ms}$ is necessary in order to avoid instability in the APs of the pre-paced beats.

Fig. 2.16(a) shows the bifurcation diagram of the AP model in the absence of I_{to}. For almost all pacing periods the AP model shows stability, except for a brief region around $T = 275\,\text{ms}$ showing chaotic APD dynamics where there is a

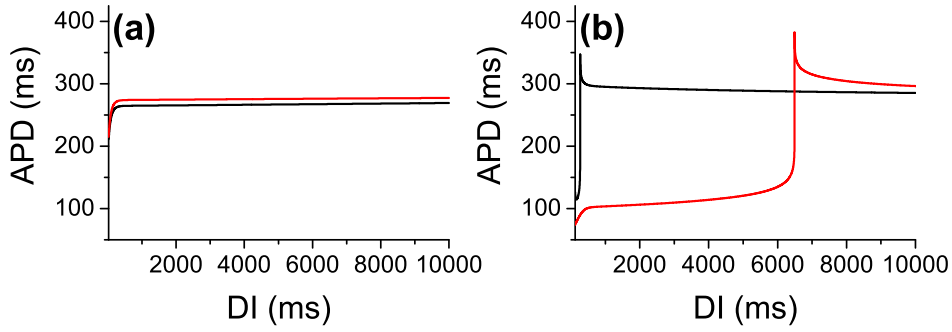

Figure 2.15: APD restitution curves of the modified TP04 model without and with I_{to}. **(a)**. APD restitution curves in the absence of I_{to}, for S1 pacing periods $T_{S1S1} = 750\,\text{ms}$ (black) and $T_{S1S1} = 3000\,\text{ms}$ (red). **(b)**. APD restitution curves in the presence of I_{to} with $g_{to} = 0.18\,\text{mS/cm}^2$, for S1 pacing periods $T_{S1S1} = 250\,\text{ms}$ (black) and $T_{S1S1} = 9000\,\text{ms}$ (red).

transition between 1:1 and 2:1 block. There is also a transition between 2:1 block and 3:1 block around $T = 125\,\text{ms}$.

Now, we examine the stability of the APD-restitution map model (Eq. (2.2)) using the APD restitutions in Fig. 2.15. Using the APD restitutions generated from the AP model without I_{to}, the resulting bifurcation diagrams are shown in Fig. 2.16(b). Two bifurcation curves are generated using the two APD restitution protocols for the S1 pacing periods $T_{S1S1} = 750\,\text{ms}$ (black trace) and $T_{S1S1} = 3000\,\text{ms}$ (red trace). The red curve is shifted upward from the black curve due to the slight upward shift seen in the APD restitution curves as in Fig. 2.15(a). For the most part the two diagrams show stability with very small instability occurring at the transitions between 1:1 and 2:1 block and between 2:1 block and 3:1 block. Overall, the two diagrams show very similar characteristics with the bifurcation diagram of the AP model.

We now examine what happens in the presence of I_{to}. The bifurcation diagram of the AP model is shown in Fig. 2.17(a). Vastly different from the bifurcation diagram of the model without I_{to}, there is a large instability window with several chaotic windows, interspersed with periodic windows. The first period-doubling

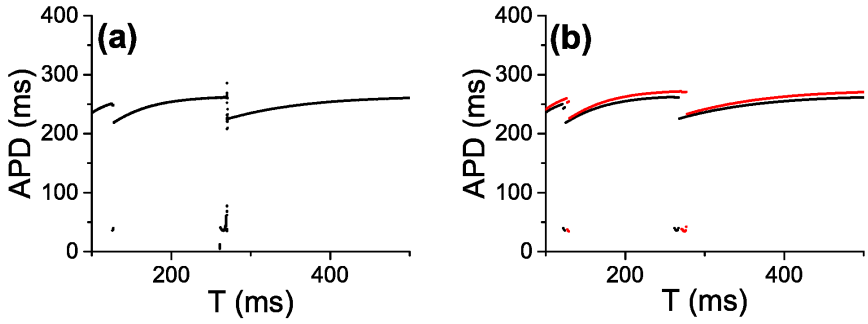

Figure 2.16: Bifurcation diagrams of the AP model and of the APD-restitution map model (Eq. (2.2)), without I_{to}. **(a)**. Bifurcation diagram of the AP model without I_{to}. **(b)**. Bifurcation diagrams of the APD-restitution map model (Eq. (2.2)) using the APD restitution curves in Fig. 2.15(a). Black trace corresponds to $T_{S1S1} = 750\,\text{ms}$, red trace corresponds to $T_{S1S1} = 3000\,\text{ms}$.

bifurcation point occurs around $T = 330\,\text{ms}$, and for even very slow pacing periods up to $T = 9000\,\text{ms}$ there is still APD alternans and higher periodicity including chaos.

Using the APD-restitution map model (Eq. (2.2)), we develop bifurcation diagrams generated from the APD restitution curves in Fig. 2.15(b) with different S1 pacing periods. The rightward shift in restitution by about 6000 ms produces two bifurcation curves with very different regions of APD instability, as seen in Figs. 2.17(b)-(c). With the restitution curve generated from an S1 pacing period $T_{S1S1} = 250\,\text{ms}$, the range of instability occurs between pacing periods $T = 400\,\text{ms}$ and 600 ms, while with the restitution curve generated from an S1 pacing period $T_{S1S1} = 9000\,\text{ms}$, the range of instability is between $T = 6650\,\text{ms}$ and 6850 ms. The regions of chaos and instability with periods greater than 2 are due to the nonmonotonicity of the APD restitution curves, just as in the case with the LR1 model in the presence of I_{to} (see Fig. 2.4(c)-(d)).

The bifurcation diagrams generated from the APD-restitution map model (Eq. (2.2)) in the presence of I_{to} reveal windows of instability about 200 ms in

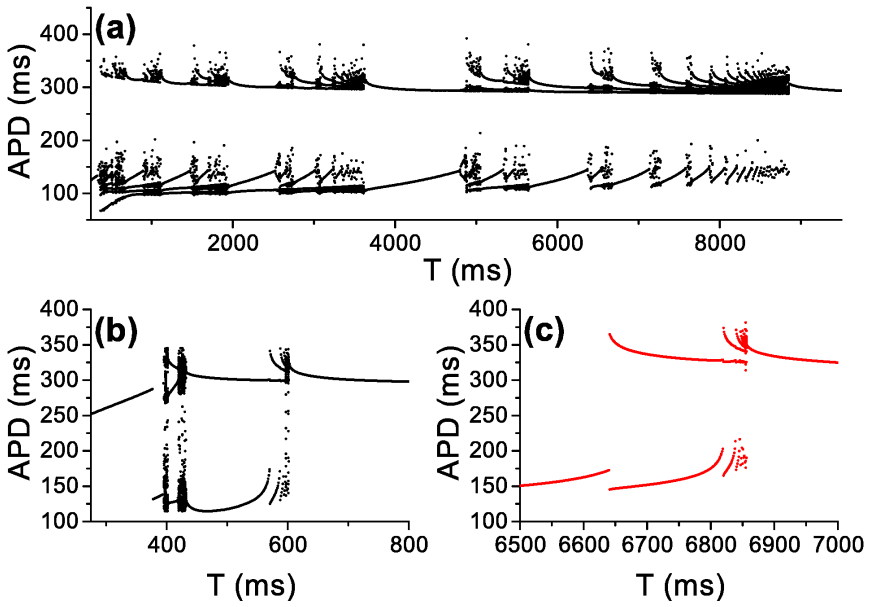

Figure 2.17: Bifurcation diagrams of the AP model and of the APD-restitution map model (Eq. (2.2)), in the presence of I_{to} with maximum conductance $g_{\text{to}} = 0.18\,\text{mS/cm}^2$. **(a)**. Bifurcation diagram of the AP model. **(b)**. Bifurcation diagram of the APD-restitution map model using the black trace ($T_{\text{S1S1}} = 250\,\text{ms}$) in the APD restitution curves in Fig. 2.15(b). **(c)**. Bifurcation diagram of the APD-restitution map model using the red trace ($T_{\text{S1S1}} = 9000\,\text{ms}$) in Fig. 2.15(b).

length. However, the bifurcation diagram of the AP model reveals an instability window that is much greater, with several chaotic windows. It is clear in this case that the APD-restitution model in Eq. (2.2) does not at all predict the APD dynamics of the AP model. The memory in the TP04 model driven by the slow accumulation of $[Ca^{2+}]_i$ produces massive effects on the AP model dynamics, leading to a much greater window of instability and chaos.

2.3.2.2 An Iterated Map Model Incorporating the Memory Effects

In the previous section, we discussed the role of the X-gating variable of I_{K} with a model formulation that was fairly simple and purely voltage-dependent, and using a square wave approximation of the AP led to the derivation of the iterated

map in Eq. (2.9). However, the formulations of $[Ca^{2+}]_i$ in the TP04 model are rather complicated and depend on various other model variables including the sarcoplasmic reticulum (SR) Ca^{2+} concentration. A phenomenological model of the effects of ion accumulation on APD was used in Schaeffer *et al.* [SCG+07], but due to the complex effects of $[Ca^{2+}]_i$ on APD dynamics in the TP04 model, we must rely on further computer simulation results, which are described in detail below.

We examine the interrelationship between APD and c_{init}, the $[Ca^{2+}]_i$ at the beginning of the AP. There are two things to consider, one is the change in $[Ca^{2+}]_i$ during an AP with a known APD, and the other is the dependence of APD on c_{init}. For the former, we fix square wave APs with a given APD a_1 with a pacing period T until equilibrium has been reached, and then switch to square wave APs with a given APD a_2. A snapshot of this protocol is shown in Fig. 2.18(a), where $T = 1000\,\text{ms}$, $a_1 = 350\,\text{ms}$, and $a_2 = 50\,\text{ms}$. Before time 0, the system is at equilibrium and the dynamics of $[Ca^{2+}]_i$ (the dotted-red tracing) is exactly the same during each AP, with $c_{\text{init}} = 0.125\,\mu\text{M}$.

After time 0, the APDs switch to the lower duration of $a_2 = 50\,\text{ms}$, and immediately there is a drop in c_{init} of the successive APs (solid red dots of Fig. 2.18(a)). Fig. 2.18(b) shows a time series of c_{init} as a function of beat number, where c_{init} at time 0, in Fig. 2.18(a), corresponds to the 0^{th} beat. After the APD switch, there is an exponential trend of c_{init} towards a new equilibrium of approximately $0.04\,\mu\text{M}$. Notice that it takes about 45 beats, or 45 s, for the system to reach this new equilibrium, indicative of very slow $[Ca^{2+}]_i$ dynamics. This is in sharp contrast to the slow X-gating variable dynamics in the LR1 model, with a time constant on the order of about 1 s.

Assuming that the time series takes on an exponential trend towards an equilibrium initial $[Ca^{2+}]_i$, c^*, then we have

$$c_{n+1} - c^* = (c_n - c^*) \exp\left[f(a_n)\right], \tag{2.23}$$

where c_n is the initial $[Ca^{2+}]_i$ of the n^{th} AP, a_n is the APD of the n^{th} AP, and $f(a_n)$ is an APD-dependent function dictating the rate at which the system reaches equilibrium. c^* is also APD-dependent, as shown in Figs. 2.18(a) and (b). Rearranging Eq. (2.23) gives

$$c_{n+1} = c_n \exp\left[f(a_n)\right] + c^* \left(1 - \exp\left[f(a_n)\right]\right), \tag{2.24}$$

and for simplicity we neglect the $c^* \left(1 - \exp\left[f(a_n)\right]\right)$ term to remove the dependence of c^*. Our justification is that this term is negligible so long as $f(\text{APD}) \ll 1$, which with very long time constants is the case as shown in Fig. 2.18(b). This yields the following simplified iterated map:

$$c_{n+1} = c_n \exp\left[f(a_n)\right]. \tag{2.25}$$

We next analyze the function $f(a_n)$ using computer simulation results. We use the bifurcation diagram in Fig. 2.17(c) to pick out pacing periods in chaotic regions that result in multiple (ideally, infinite) APDs. For each AP, we record the APD and initial $[Ca^{2+}]_i$ of the current AP (c_{init}) as well as of the succeeding AP (c_{init+1}). Eq. (2.25) gives the relationship $f(a_n) = \log\left(\frac{c_{n+1}}{c_n}\right)$, so we perform a log-transform of the ratios of initial $[Ca^{2+}]_i$, $\log\left(\frac{c_{init+1}}{c_{\text{init}}}\right)$. This expression is a measurement of the net cytosolic Ca^{2+} gain from and loss into the extracellular space and the SR during an AP. A value greater than zero is indicative of net $[Ca^{2+}]_i$ gain, and a value less than zero is indicative of net $[Ca^{2+}]_i$ loss. If the value equals zero, then there is no net gain or loss of $[Ca^{2+}]_i$ during an AP, and equilibrium is reached.

The results are shown in Fig. 2.18(c). The pacing periods $T = 1704, 2649, 3600, 4875, 5602,$ and 7600 ms give rise to chaotic APD dynamics, resulting in hundreds of unique APD values that give rise to different values of $\log\left(\frac{c_{init+1}}{c_n}\right)$. The figure shows that, generally speaking, $\log\left(\frac{c_{init+1}}{c_{\text{init}}}\right)$ increases as APD increases. In addition, increasing the pacing period T reduces $\log\left(\frac{c_{init+1}}{c_{\text{init}}}\right)$. These two results are not

surprising. A longer APD results in longer Ca^{2+} influx due to $I_{Ca,L}$, and a longer pacing period, for a fixed APD, results in a longer DI that allows for longer Ca^{2+} efflux due to I_{NCX}. From observation, the dependence of $\log\left(\frac{c_{init+1}}{c_{init}}\right)$ is roughly linear with respect to both APD and T, hence giving the relationship

$$\log\left(\frac{c_{init+1}}{c_{\text{init}}}\right) = f(\text{APD}) \approx \gamma_a \text{APD} - \gamma_T T + \delta, \tag{2.26}$$

where γ_a and γ_T are the coupling coefficients for APD and T respectively, and δ is a constant. Substituting this expression for f in Eq. (2.25) gives

$$c_{n+1} = c_n \exp\left[f(a_n)\right] = c_n \exp\left[\gamma_a a_n - \gamma_T T + \delta\right] \tag{2.27}$$

We now switch our focus to the dependence of APD on c_{init}. Again, we use the data used to generate the bifurcation diagram in Fig. 2.17(c), where for each AP we record the APD as well as c_{init}. For all data points with $T > 2000\,\text{ms}$, we do a scatter plot of APD against c_{init}, and the results are shown in Fig. 2.18(d). The restriction $T > 2000\,\text{ms}$ avoids any other memory effects and assures that the APD is dependent only on c_{init}. Strikingly, there is a clear one-to-one dependence of APD on c_{init} in which any particular c_{init} gives rise to a unique APD value, without ambiguity. Thus, we may write a functional relationship between APD and c_{init}:

$$\text{APD} = g(c_{\text{init}}), \tag{2.28}$$

so that in the n^{th} AP, the APD a_n depends on the initial $[Ca^{2+}]_i$ c_n via

$$a_n = g(c_n). \tag{2.29}$$

And together, Eqs. (2.27) and (2.29) give rise to a complete iterated map model:

$$a_n = g(c_n) \tag{2.30}$$

$$c_{n+1} = c_n \exp\left[\gamma_a a_n - \gamma_T T + \delta\right]. \tag{2.31}$$

We refer to this iterated map model as the "Ca^{2+}-memory map model." The function g is obtained by linearly interpolating the data in Fig. 2.18(d). The

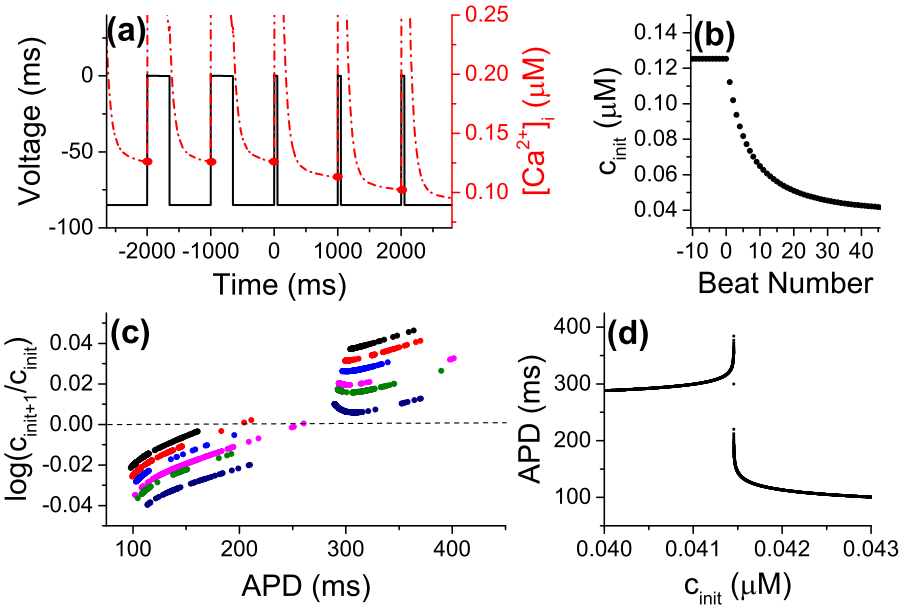

Figure 2.18: APD and $[Ca^{2+}]_i$ dynamics of the AP model. **(a)**. Ca^{2+} transients responding to square-wave APs with $T = 1000\,\text{ms}$, with durations switching from APD $= 350\,\text{ms}$ (for all times $t < 0\,\text{ms}$) to APD $= 50\,\text{ms}$ (starting at time $t = 0\,\text{ms}$). **(b)**. Response of c_{init} after the APD switch. **(c)**. Dependence of $\log\left[\frac{c_{init+1}}{c_{\text{init}}}\right]$ on APD. The data points were chosen from pacing periods $T = 1704\,\text{ms}$ (black), $2649\,\text{ms}$ (red), $3600\,\text{ms}$ (blue), $4875\,\text{ms}$ (magenta), $5602\,\text{ms}$ (green), $7600\,\text{ms}$ (dark blue), that result in chaotic behavior resulting in APs with hundreds of unique APDs. **(d)**. Dependence of APD on c_{init}. Data chosen from all APs generating the bifurcation diagram in Fig. 2.17(c) for $T > 2000\,\text{ms}$.

constants γ_a, γ_T, and δ are obtained from observing the data in Fig. 2.18(c). We obtain the values $\gamma_a = 2 \times 10^{-4}\,\text{ms}^{-1}$, $\gamma_T = 3.625 \times 10^{-6}\,\text{ms}^{-1}$, and $\delta = -0.0275$.

As usual, by varying T we create a bifurcation diagram of the Ca^{2+}-memory map model, and the result is shown in Fig. 2.19. The diagram shows stunning similarity to the bifurcation diagram of the AP model shown in Fig. 2.17(c), revealing numerous period-doubling bifurcation routes to chaos interspersed with periodic windows. In addition, the complete region of instability ranges from about 200 ms to 8500 ms, which is nearly the same as in the AP model.

Fig. 2.20 compares return maps between the AP model and the Ca^{2+}-memory

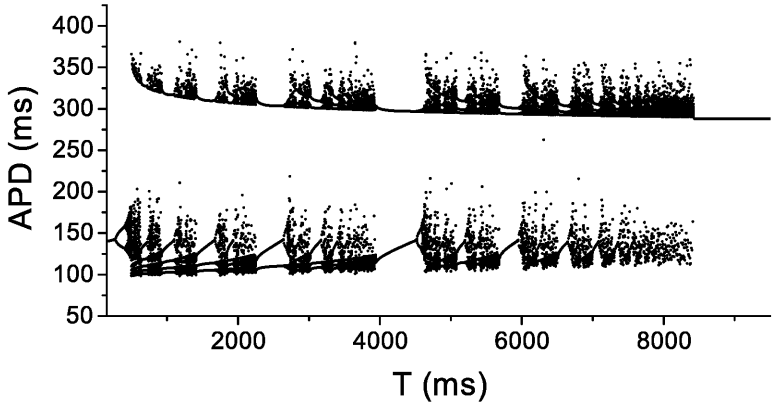

Figure 2.19: Bifurcation of the Ca^{2+}-memory map model (Eqs. (2.30) and (2.31)), with function g, the APD dependence on c_{init}, the linear interpolant of the data in Fig. 2.18(d), and parameter values $\gamma_a = 2 \times 10^{-4}\,\text{ms}^{-1}$, $\gamma_T = 3.625 \times 10^{-6}\,\text{ms}^{-1}$, and $\delta = -0.0275$.

map model (Eqs. (2.30) and (2.31)) used to generate the bifurcation in Fig. 2.19. Fig. 2.20(a) provides two return maps of the AP model undergoing chaotic APD dynamics with $T = 3250\,\text{ms}$ and $6600\,\text{ms}$, and Fig. 2.20(b) are two return maps of the Ca^{2+}-memory map model using the same pacing periods $T = 3250\,\text{ms}$ and $6600\,\text{ms}$. Matching the pacing periods between the two graphs, the return maps in the Ca^{2+}-memory map model are very similar to the return maps in the AP model. Panel (b) contains more information due to the iterated map being continuous and the chaotic dynamics in the AP model not attaining all possible APDs. For example, for $T = 6600\,\text{ms}$ (the red curves in Fig. 2.20), in the AP model, APDs below about $a_n = 110\,\text{ms}$ and between $a_n = 230\,\text{ms}$ and $280\,\text{ms}$ do not occur. The return map shows only one discontinuity, or jump between large and small APDs, occurring around $a_n = 300\,\text{ms}$. However, the corresponding return map from the Ca^{2+}-memory map model shows two additional discontinuities occurring at $a_n = 100\,\text{ms}$ and $250\,\text{ms}$.

Properties of the Ca^{2+}-memory map model incorporating memory effects from $[Ca^{2+}]_i$ accumulation closely match those of the AP model. This provides clear ev-

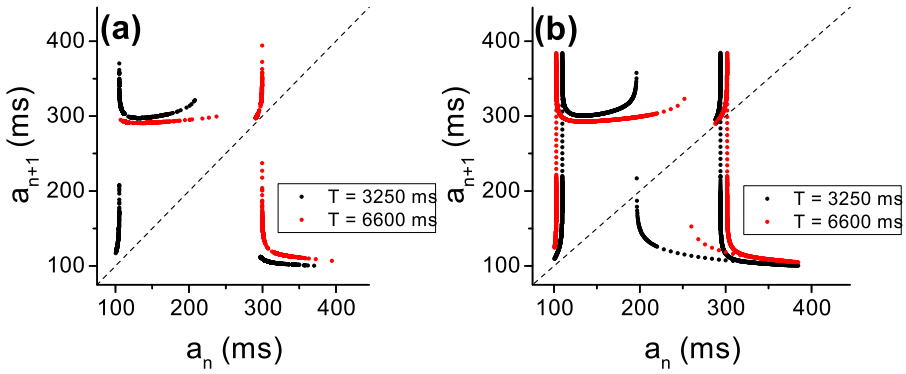

Figure 2.20: Comparing return maps between the AP model and Ca^{2+}-memory map model (Eqs. (2.30) and (2.31)). **(a)**. AP model return maps in chaotic regimes for $T = 3250\,\text{ms}$ and $6600\,\text{ms}$. **(b)**. Return maps of the Ca^{2+}-memory map model for the same pacing periods $T = 3250\,\text{ms}$ and $6600\,\text{ms}$, where the function g is the linear interpolant of the data in Fig. 2.18(d), and parameter values $\gamma_a = 2 \times 10^{-4}\,\text{ms}^{-1}$, $\gamma_T = 3.625 \times 10^{-6}\,\text{ms}^{-1}$, and $\delta = -0.0275$.

idence that the Ca^{2+}-memory map model sufficiently matches the APD dynamics of the AP model.

2.3.2.3 Theoretical Analysis and Predictions of the Ca^{2+}-Memory Map Model

In the previous section we used the Ca^{2+}-memory map model (Eqs. (2.30) and (2.31)), in which Eq. (2.31) is an explicit equation with parameters γ_a, γ_T, T, and δ, but the function g in Eq. (2.30) was a linear interpolation of data provided by simulations of the AP model. In this section, we do as before in the case of the X-memory map model and set the function g in Eq. (2.28) as a Hill function of the form $\text{APD} = g(c_{\text{init}}) = a_{\min} + \frac{a_{\max} - a_{\min}}{1 + \left(\frac{c_{\text{init}}}{k_c}\right)^h}$, where $a_{\min}$ and $a_{\max}$ are the minimum and maximum APDs attainable, k_c is the half-max c_{init}, and h is the Hill coefficient. This gives the following complete iterated map model:

$$a_n = g(c_n) = a_{\min} + \frac{a_{\max} - a_{\min}}{1 + \left(\frac{c_n}{k_c}\right)^h} \tag{2.32}$$

$$c_{n+1} = f(c_n, a_n) = c_n \exp\left(\gamma_a a_n - \gamma_T T + \delta\right) = H(c_n). \tag{2.33}$$

Eqs. (2.32) and (2.33) together give a complete 1-dimensional map whose steady state stability is determined by the derivative of the function H at steady state:

$$H'(c^*) = \left[1 + c^* \gamma_a g'(c^*)\right] e^{\gamma_a g(c^*) - \gamma_T T + \delta}, \tag{2.34}$$

where c^* is the steady state of H (i.e. $H(c^*) = c^*$). For the period-doubling bifurcation to occur ($H'(c^*) < -1$), it requires a steeply decreasing function g with respect to c_n, i.e., a large negative $g'(c^*)$ is needed so that

$$c^* \gamma_a g'(c^*) < -2 \tag{2.35}$$

can be satisfied. Increasing γ_a can also potentiate the inequality in Eq. (2.35) and thus instability. Once Eq. (2.35) is satisfied, increasing δ or decreasing γ_T will potentiate the instability.

We now examine the model directly by iterating the map in Eqs. (2.32) and (2.33) for specific parameter values. Based on simulation results from the AP model shown in Fig. 2.18, we estimate the parameter values $\gamma_a = 2 \times 10^{-4}\,\mathrm{ms}^{-1}$, $\gamma_T = 3.625 \times 10^{-6}\,\mathrm{ms}^{-1}$, and $\delta = -0.0275$. To model the function g in Eq. (2.33), we estimate a Hill function that closely matches the dependence of APD on c_{init} from the AP model, as shown in Fig. 2.18(d). No Hill function will perfectly fit it since the graph is nonmonotonic with a jump discontinuity. Our chosen parameter values are $a_{\min} = 125\,\mathrm{ms}$, $a_{\max} = 350\,\mathrm{ms}$, $k_c = 4.1456 \times 10^{-2}\,\mu\mathrm{M}$, and $h = 500$. The bifurcation diagram of this model is shown in Fig. 2.21(a), and shows period-doubling bifurcation routes to enter and exit chaos, similar to the bifurcation diagram of the AP model (Fig. 2.17(c)) as well as the bifurcation diagram of the X-memory map model in the previous section (Fig. 2.9(f)). The

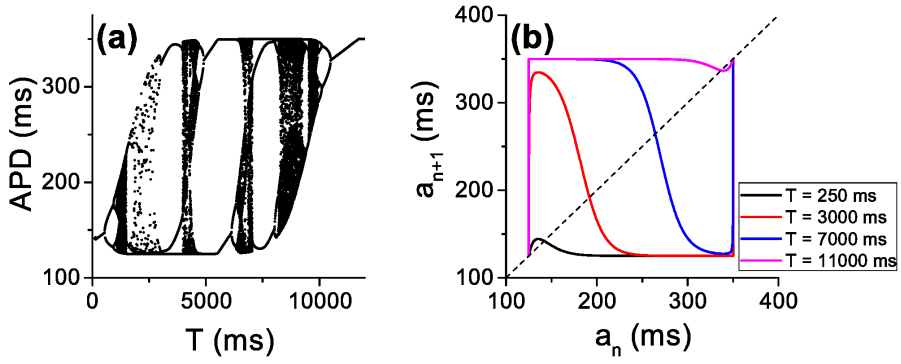

Figure 2.21: Dynamics of the Ca^{2+}-memory map model (Eqs. (2.32) and (2.33)), with parameters $a_{\min} = 125\,\text{ms}$, $a_{\max} = 350\,\text{ms}$, $k_c = 4.1456 \times 10^{-2}\,\mu\text{M}$, $h = 500$, $\gamma_a = 2 \times 10^{-4}\,\text{ms}^{-1}$, $\gamma_T = 3.625 \times 10^{-6}\,\text{ms}^{-1}$, and $\delta = -0.0275$. **(a)**. Bifurcation diagram. **(b)**. Return maps for pacing periods $T = 250\,\text{ms}, 3000\,\text{ms}, 7000\,\text{ms}$, and $11\,000\,\text{ms}$. The dotted black line is the fixed point line $a_{n+1} = a_n$.

region of instability is between pacing periods $T = 550\,\text{ms}$ and $10\,500\,\text{ms}$, which is roughly similar to that seen in the AP model. In Fig. 2.21(b) we provide four return maps with different pacing periods. The return maps are very similar to the ones from the X-memory map model, shown in Fig. 2.10(b). An increase in T tends to shift the return map to the right, shifting the fixed point of APD to more positive values.

To confirm our predictions of the effects of γ_T and δ on the stability of the model, we modify these parameters in the Ca^{2+}-memory map model using the linear interpolant of the data in Fig. 2.18(d) to model the function g in Eq. (2.32). We make the changes $\gamma_T \to 1.25\gamma_T$ and $\delta \to \delta + 0.005$. The results are shown in Fig. 2.22. Indeed, comparing Fig. 2.22(a) and (b), there is a shift in the region of instability by about 1380 ms. The left bifurcation points shifts from about 270 ms to 1650 ms, and the right bifurcation point from about 8430 ms to 9810 ms. And by increasing γ_T by 25% we expect the left and right bifurcation points to decrease by 20%. Indeed, the left bifurcation point shifts from about 270 ms to 215 ms and

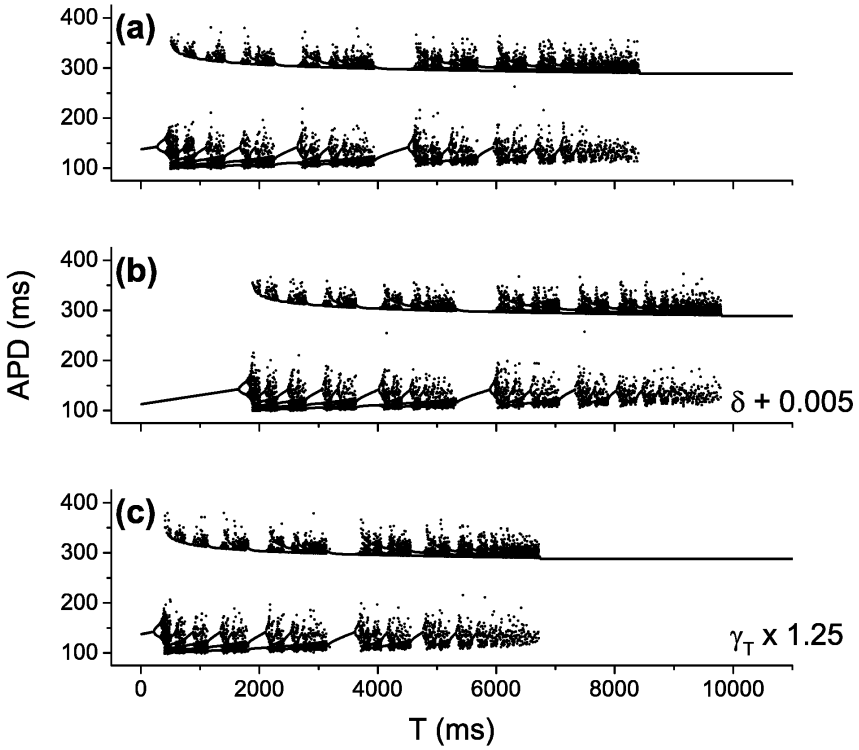

Figure 2.22: The effects of δ and γ_T on APD dynamics in the Ca^{2+}-memory map model (Eqs. (2.30) and (2.31)). **(a)**. Bifurcation under control conditions, using the linear interpolant of the curve in Fig. 2.18(d) for g and other parameters $\gamma_a = 2.4 \times 10^{-4}\,\mathrm{ms}^{-1}$, $\gamma_T = 3.625 \times 10^{-6}\,\mathrm{ms}^{-1}$, and $\delta = -0.0275$. **(b)**. Bifurcation diagram with $\delta \to \delta + 0.005 = -0.0225$. **(c)**. Bifurcation diagram with $\gamma_T \to 2\gamma_T = 7.25 \times 10^{-6}\,\mathrm{ms}^{-1}$.

the right bifurcation point shifts from about 8430 ms to 6745 ms.

Finally, we return back to the AP model and examine the effects of changing parameters in the model on APD dynamics. Two key regulators of $[Ca^{2+}]_i$ are the L-type Ca^{2+} current, $I_{\mathrm{Ca,L}}$, and the Na-Ca exchanger, I_{NCX}. Each have maximum conductance parameters $g_{\mathrm{Ca,L}}$ and g_{NCX}, which we change in the model. Fig. 2.23 shows bifurcation diagrams of (a) control conditions, (b) $g_{\mathrm{Ca,L}}$ reduced by 2%, and (c) g_{NCX} reduced by 10%. The diagrams show that the reduction of $I_{\mathrm{Ca,L}}$ and I_{NCX} conductance shifts the bifurcation points significantly to the right by about 3500 ms. We currently ignore the left bifurcation point because, in the AP model,

many sources could contribute to APD dynamics besides $[Ca^{2+}]_i$ accumulation at such fast pacing periods.

To examine how reducing $I_{Ca,L}$ and I_{NCX} can cause a 3500 ms shift in the right bifurcation point, we do as before and compare the dependences of $\log\left(\frac{c_{init+1}}{c_{init}}\right)$ to APD, which corresponds to the function f in Eq. (2.25). To get as many data points as possible, we choose a pacing period $T = 3600$ ms that results in chaotic APD dynamics in control and $I_{Ca,L} \times 0.98$ conditions, and period-3 APD dynamics in the $I_{NCX} \times 0.9$ condition. Fig. 2.23(d) shows the results. Indeed, the data corresponding to $I_{Ca,L}$ and I_{NCX} reduction lie above the data points under control conditions by about a value of 0.05, which corresponds to an increase in $-\gamma_T T + \delta$ in Eq. (2.25), so that either δ increases, γ_T decreases, or a combination of both. In either case, the theoretical analysis suggests that decreasing $I_{Ca,L}$ or I_{NCX} causes an increase in δ and/or a decrease in γ_T, which shifts the right bifurcation point to the right, just as we see in the simulation results.

2.3.2.4 EAD-Induced Complex APD Dynamics in the Presence of $[Ca^{2+}]_i$ Accumulation

Similar to the case of the LR1 model, we also generate EADs in the TP04 model in the absence of I_{to} (Fig. 2.24(a)). To do so, we set the maximum conductances of $I_{Ca,L}, I_{Kr}$, and I_{Ks} to be $g_{Ca,L} = 6 \times 10^{-4}$ mS/cm^2, $g_{Kr} = 0.01$ mS/cm^2, and $g_{Ks} = 0.036$ mS/cm^2, and introduce a late Na^+ current by performing the following changes to the formulations of the steady-state h- and j-gates in I_{Na}:

$$\begin{aligned} h_\infty &= \gamma + (1-\gamma)\overline{h_\infty} \\ j_\infty &= \gamma + (1-\gamma)\overline{j_\infty}, \end{aligned} \tag{2.36}$$

where $\overline{h_\infty}$ and $\overline{j_\infty}$ are the steady state formulations of the two gates in the TP04 model, and γ is a "pedestal" parameter that determines to what extent the h- and $j-$ gates deactivate. Here, we set $\gamma = 0.01$.

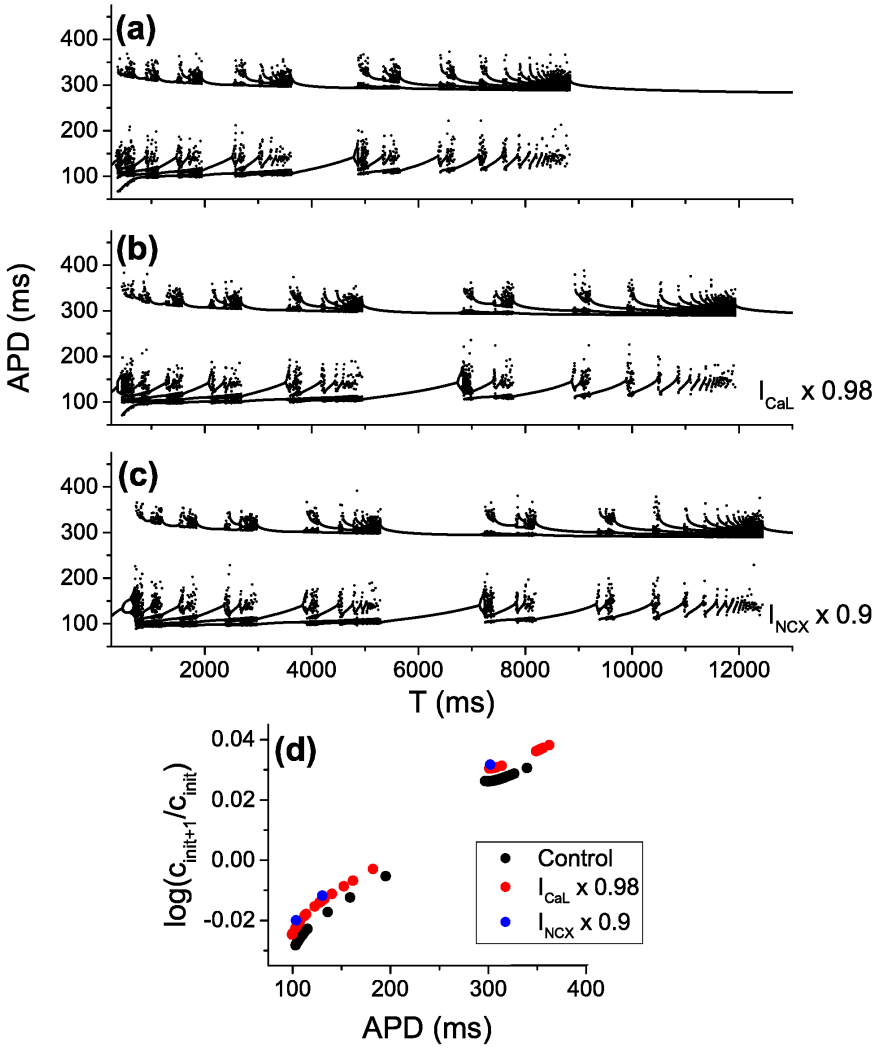

Figure 2.23: The effects of changing $I_{\mathrm{Ca,L}}$ and I_{NCX} on the APD dynamics of the AP model. **(a)**. Bifurcation diagram under control conditions. **(b)**. Bifurcation diagram when $g_{\mathrm{Ca,L}}$ is reduced by 2%. **(c)**. Bifurcation diagram when g_{NCX} is reduced by 10%. **(d)**. The effects of reducing $I_{\mathrm{Ca,L}}$ by 2% and I_{NCX} by 10% on the dependence of $\log\left(\frac{c_{init+1}}{c_{\mathrm{init}}}\right)$ on APD. In each case, simulations use a pacing period $T = 3600\,\mathrm{ms}$, where Control and $I_{\mathrm{Ca,L}} \times 0.98$ conditions result in chaotic APD dynamics and the $I_{\mathrm{NCX}} \times 0.9$ condition results in period-3 APD dynamics.

Fig. 2.24(b) is a bifurcation diagram against the pacing period T from the simulation of the TP04 model. Between each transition leading to an extra EAD (i.e. 0 EADs to 1 EAD, 1 EAD to 2 EADs, etc.), there is a period doubling bifurcation route to enter chaos as T increases. Fig. 2.24(c) shows a close-up of the bifurcation diagram around the first transition between 0 EADs and 1 EAD, more clearly illustrating period doubling leading to chaos.

We calculate the S1S2 APD restitution curves for two different S1 pacing periods, $T_{\mathrm{S1S1}} = 2000\,\mathrm{ms}$ and $6000\,\mathrm{ms}$ (Fig. 2.25(a)). Just as in the LR1 model with EADs, the S1S2 restitution curves show staircase dependences of APD against DI. The bifurcation diagrams obtained using the S1S2 APD restitution curves and Eq. (2.2) are given in Figs. 2.25(b) and (d), with corresponding close-ups around the first bifurcation points in Figs. 2.25(c) and (e), respectively. The bifurcation diagrams differ largely from those from the AP model, indicating that APD restitution alone cannot capture the complex excitation dynamics.

We then plot APD versus c_{init} and $\log\left(\frac{c_{init+1}}{c_{\mathrm{init}}}\right)$ versus APD from the AP model the same way as we did in the I_{to} case (Figs. 2.26(a) and (b)). Using these functions and the Ca^{2+}-memory map model (Eqs. (2.30) and (2.31)), we obtain a bifurcation diagram (Fig. 2.26(c)) which is nearly identical to the one obtained from the AP model (Fig. 2.24(c)). This shows that the memory from $[Ca^{2+}]_i$ accumulation plays an important role in generating the complex APD dynamics induced by the occurrence of EADs in the AP model.

2.4 Discussion and Conclusions

In this study, we investigated the effects of short-term cardiac memory on excitation dynamics under two diseased conditions, early repolarization syndrome [AY15] and long QT syndrome [Rod06]. The memory originates from two sources, slow ion channel recovery and slow $[Ca^{2+}]_i$ accumulation. We show that contrary

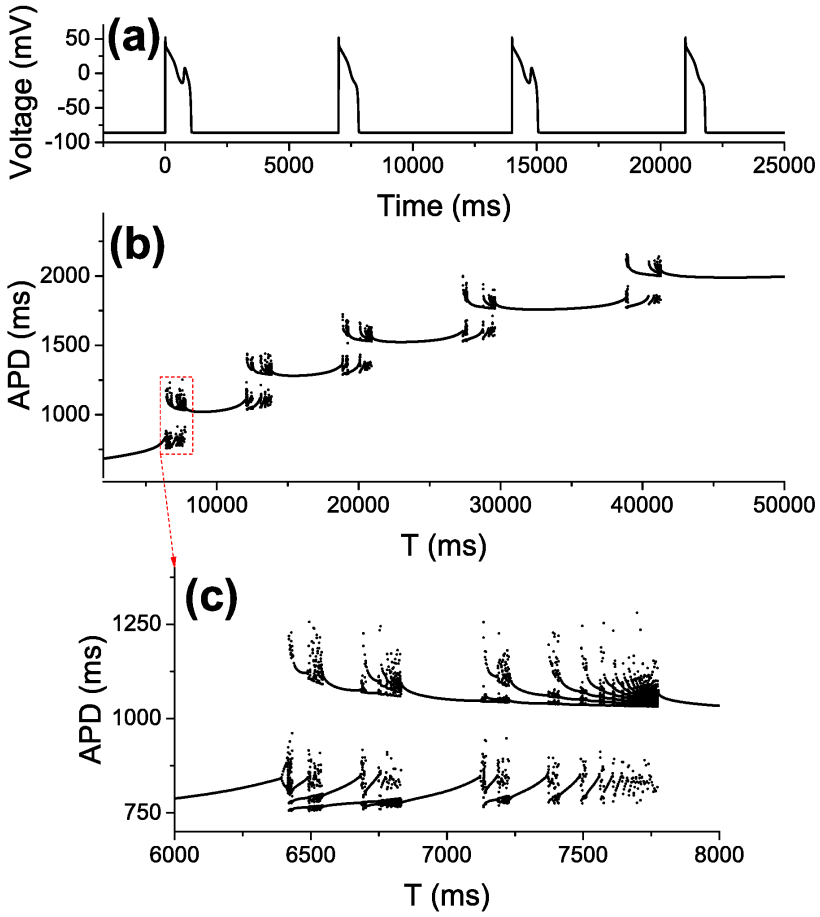

Figure 2.24: Complex APD dynamics induced by EADs in the TP04 model, with $g_{\mathrm{Ca,L}} = 6 \times 10^{-4}\,\mathrm{mS/cm^2}$, $g_{\mathrm{Kr}} = 0.01\,\mathrm{mS/cm^2}$, $g_{\mathrm{Ks}} = 0.0036\,\mathrm{mS/cm^2}$, and $\gamma = 0.01$ in Eq. (2.36). **(a).** APs showing EAD alternans, $T = 7000\,\mathrm{ms}$. **(b).** Bifurcation diagram of the AP model. **(c).** Close-up of the bifurcation diagram around the first bifurcation point, transitioning from no EADs to one EAD in the AP.

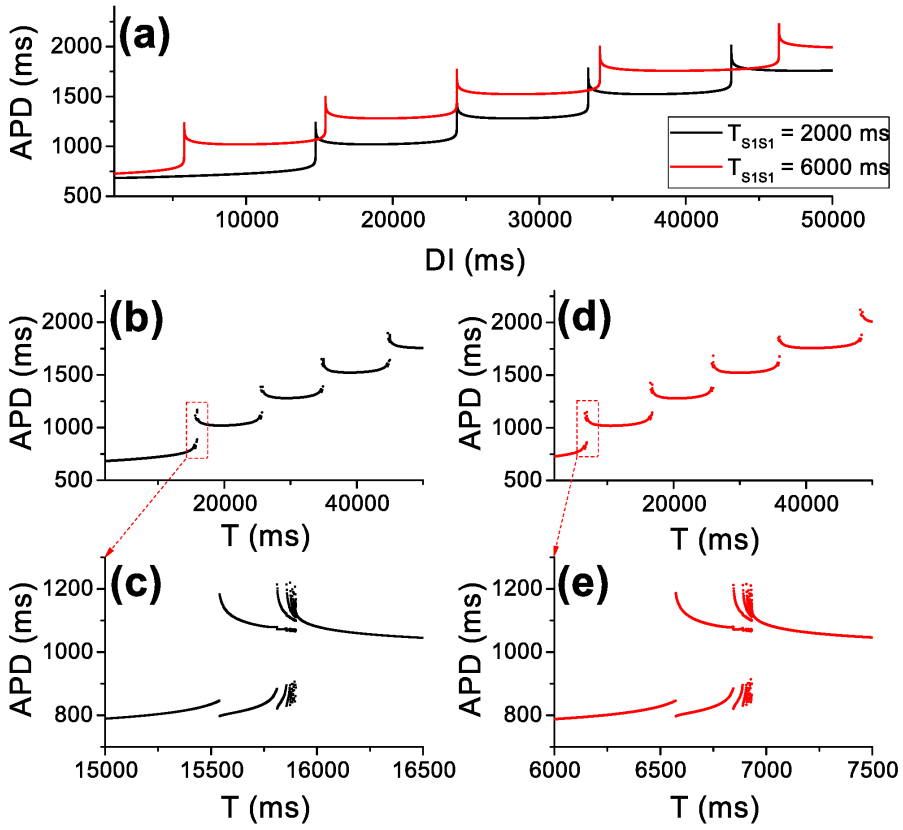

Figure 2.25: Bifurcation diagrams from the APD-restitution map model (Eq. (2.2)) and S1S2 APD restitution curves from the TP04 model in the context of long QT syndrome. **(a)**. S1S2 restitution curves for S1 pacing periods $T_{\mathrm{S1S1}} = 2000\,\mathrm{ms}$ (black) and 6000 ms (red). **(b)**. Bifurcation diagram of the APD-restitution map model (Eq. (2.2)) using the black trace in (a). **(c)**. Close-up of the bifurcation diagram in (b) around the first bifurcation point. **(d)**. Bifurcation of the APD-restitution map model (Eq. (2.2)) using the red trace in (a). **(e)**. Close-up of the bifurcation diagram in (d) around the first bifurcation point.

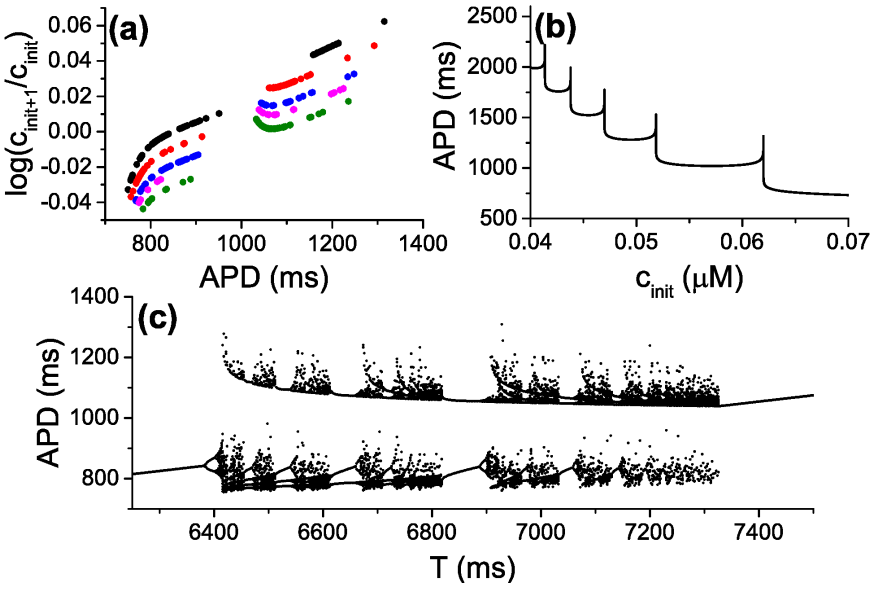

Figure 2.26: APD dynamics predicted by the Ca^{2+}-memory map model (Eqs. (2.30) and (2.31)) in the presence of EADs. **(a)**. Plots of $\log\left(\frac{c_{init+1}}{c_{\text{init}}}\right)$ vs. APD from the AP model for 5 different pacing periods leading to chaotic EAD dynamics. $T = 6430\,\text{ms}$ for black points, 6805 ms for red points, 7190 ms for blue points, 7395 ms for magenta points, 7710 ms for green points. **(b)**. Plot of APD vs. c_{init} in the AP model. **(c)**. Bifurcation diagram of the Ca^{2+}-memory map model (Eqs. (2.30) and (2.31)). The paramters in Eq. (2.31) were chosen to be $\gamma_a = 1.2 \times 10^{-4}\,\text{ms}^{-1}$, $\gamma_T = 2.5 \times 10^{-5}\,\text{ms}^{-1}$, and $\delta = 0.05845$, based on approximating the data in panel (a). The function g in Eq. (2.31) is the linear interpolant of the data in panel (b).

to many previous studies which have shown that memory suppresses dynamical instabilities [CMJ90, FBGJ02, KTS+05, OGJ97, TSGK03, FRD+03, TRGG04, CF04, BQK+07, GCGJ+13, MJT08, WMT15], under these diseased conditions, memory can induce or potentiate complex excitation dynamics, including chaos. In addition to memory, the all-or-none behaviors (dome vs. no dome or EAD vs. no EADs) in the diseased conditions, which result in steeply changing APD restitution curves, are also key to the genesis of the complex APD dynamics. We developed new iterated map models that properly incorporate memory from the two different sources, which can well describe the complex dynamics and recapitulate the bifurcation sequences from the AP models. Using the iterated map models, we unraveled the mechanisms underlying memory-induced chaos and complex APD dynamics induced by I_{to} or EADs.

The role of chaos in the genesis and maintenance of cardiac arrhythmias has been investigated previously [SXS+09, XHS+07, Qu11]. Different mechanisms of chaos and complex excitation dynamics have been demonstrated in cardiac myocytes. In this study, we reveal a novel mechanism of chaos of cardiac excitation, which may provide further understanding of the role of chaos in arrhythmogenesis in the presence of short-term cardiac memory.

In this study, we investigated the effects of memory originating from slow recovery of ion channels and slow accumulation of $[Ca^{2+}]_i$. We fixed $[Na^+]_i$ and $[K^+]_i$ in our simulations in order to avoid memory effects from slow accumulation of these ions. However, it is well known that, in particular, $[Na^+]_i$ accumulates very slowly, and thus it can impact the APD dynamics in an even longer time scale, i.e., longer-term memory effect. These effects have been already investigated in recent simulation studies [XLG+15, KMC17]. It will be of importance to develop an improved iterated map model that incorporates the memory caused by slow $[Na^+]_i$ accumulation, which is our next task of revealing the mechanisms of short-term cardiac memory on excitation dynamics.

Finally, we would like to point out that the mechanistic insights gained from the present study may not only be limited to complex ecitation dynamics in cardiac myocytes, but also to those in other electrically excitable cells. For example, the bursting dynamics in neurons [RE98, RA98, SR03, AC09] and pancreatic β-cells [KS98] are irregular, which can result from either random ion channel openings or dynamical chaos. Since the bursting dynamics are also governed by fast-slow dynamics [TSY+09, KS98, NHCG98, Izh00, SCC05] similar to the EAD dynamics in cardiac myocytes, the same mechanism of memory-induced chaos may be applicable to irregular bursting dynamics in these cases.

CHAPTER 3

Control of Voltage-Driven Instabilities in Cardiac Myocytes with Memory

3.1 Introduction

Cardiac arrhythmias and sudden cardiac death are known to be associated with dynamical instabilities in the heart [Gla96, QHGW14, KMC12, Kar13]. Control of dynamical instabilities in cardiac systems has been widely studied [GSDW92, CC96, DSI+00, CRC+06, HG02, HCT+97, RFK99, TRGG04, KMKR+10, CSM+01, EK02, AWS+13] and is considered a potential therapeutic strategy. Different controlling methods have been proposed and shown to be effective in controlling the instabilities in computer simulations and experiments.

Among the different controlling methods, the method proposed by Hall *et al.* [HG02, HCT+97] has been widely used [TRGG04, KMKR+10, CSM+01, EK02], in which a perturbation was applied to the pacing period T, i.e.

$$T' = T + \frac{\alpha}{2}\left(a_n - a_{n-1}\right), \tag{3.1}$$

where α is the parameter describing the strength of control, and a_n is the APD of the n^{th} beat. This method is a form of delayed feedback control, which we call *Delayed Negative Feedback Control* (DNFC). Another widely studied method was proposed by Jordan and Christini [JC04] and by Wu and Patwardhan [WP04, WP06], called constant diastolic interval (DI) control, in which the cardiac myocyte or tissue is paced with the DI set as a constant. Recent studies [MKMT14,

Che17, Ota17, ZJT17] also investigated this method.

In cardiac myocytes, there is a well-known property called APD restitution. In the absence of memory, APD restitution is mathematically described as [GWSG84, ND68, QSW07]

$$a_{n+1} = f(d_n) = f(T - a_n), \tag{3.2}$$

where a_{n+1} is the APD of the $(n+1)^{\text{st}}$ beat and d_n is its immediate proceeding DI. It is well known that instabilities can occur when the slope of the APD restitution function is greater than 1. Substituting T by T' in Eq. (3.2), and performing a linear stability analysis, one obtains the following stability criterion:

$$\frac{f'(d^*) - 1}{f'(d^*)} < \alpha < \frac{2}{f'(d^*)}, \tag{3.3}$$

where d^* is the steady state DI. In other words, under DNFC, the system is conditionally controllable so long as α is bound by Eq. (3.3). On the other hand, with constant-DI control, the system is unconditionally controllable since once DI is fixed, then APD is fixed in Eq. (3.2).

However, it is well known that complex APD dynamics can originate from Ca^{2+}-driven instabilities or the coupling of Ca^{2+} and voltage [QSW07, SSK05], and it is understood [JC04, Qu04] that constant-DI pacing might fail to control this instability. This is obvious from experiments in which Ca^{2+} alternans occur under voltage or AP clamp conditions in which both DI and APD are fixed [CGG+99, DEO02, DOE04]. In an experimental study [WP06], Wu and Patwardhan showed that alternans occurred under both constant-cycle-length pacing and constant-DI pacing, indicating that constant-DI pacing failed to suppress alternans in the real heart. Based on the fact that constant-DI pacing may stabilize voltage-driven instabilities but may fail in stabilizing Ca^{2+}-driven instabilities, it was proposed to use this method to distinguish voltage-driven instabilities from Ca^{2+}-driven instabilities [Che17].

Besides Ca^{2+}-driven instabilities, Eq. (3.2) does not include memory effects

since Eq. (3.2) assumes APD depends only on its immediately preceding DI. In the presence of memory, the APD also depends on previous APDs and DIs, i.e.,

$$a_{n+1} = f(d_n, a_n, d_{n-1}, a_{n-1}, \dots). \tag{3.4}$$

If one fixes DI by setting $d_n = d_{n-1} = \dots = d_0$, then Eq. (3.4) becomes

$$a_{n+1} = f(d_0, a_n, a_{n-1}, \dots). \tag{3.5}$$

In theory, alternans and complex dynamics can still occur in Eq. (3.2) if the function f exhibits a steep dependence on APD, and thus constant-DI control may fail to stabilize voltage-driven instabilities in the presence of memory. It is also not clear how effective are the other control methods, such as the DNFC method, in controlling the APD dynamics in the presence of memory.

Most of the previous studies on cardiac memory effect [TRGG04, CGJJ90, OGJ97, FBGJ02, TSGK03, KTS+05, FRD+03, CF04, BQK+07, SCG+07, GCGJ+13, MJT08, WMT15] showed that memory itself suppresses voltage-driven instabilities, but studies have also shown that memory may promote APD instabilities [OGJ97, SAGB95]. If memory suppresses APD instabilities, then it is not difficult to imagine that control may become easier in the presence of memory. However, a recent study by Otani [Ota17] discussed the possibility of constant-DI pacing failure in controlling the voltage-driven instabilities if a steep APD dependence on the memory variable exists. As shown in a study by Sun *et al.* [SAGB95], the presence of memory drives alternans and more complex behaviors in AV nodal conduction. Our recent studies [LGWQ17, LQ18b] showed that the steep dependence can indeed exist under certain diseased conditions, i.e., the all-or-none behaviors caused by the diseases reult in steep APD dependence on the memory variables, which causes complex APD dynamics.

In this study, we investigate the efficacy of the DNFC method and the constant-DI pacing control in controlling the voltage-driven instabilities under two diseased

conditions in which the memory effect is exacerbated. We also propose a simple feedback pacing control method to control instability which we call *Negative Feedback Control* (NFC). The first diseased condition is called early repolarization which occurs in Brugada syndrome, J-wave syndrome, and short QT syndrome [AY15]. In this case, enhanced outward currents and/or reduced inward currents cause an abrupt shortening in APD. The second diseased condition is reduced repolarization reserve which occurs in long QT syndrome [Rod08, Rod06] and heart failure [LLD+02, LLLN04, TZ04]. In this case, enhanced inward currents and/or reduced outward currents promote early afterdepolarizations (EADs), causing an abrupt lengthening in APD. In both cases, the steep APD response combined with the memory effect results in complex APD dynamics, which are purely voltage-driven instabilities [LGWQ17, LQ18b]. We show that under normal conditions in which the memory effect is minimal, all three controlling methods can effectively stabilize instabilities caused by steep APD restitution. However, under diseased conditions, constant-DI pacing control is the least effective controlling algorithm, almost completely failing to stabilize the APD. The DNFC method can stabilize the instabilities for certain pacing period T with properly control strength α, but fails to eliminate instabilities. In other words, even for an optimal α, complex APD dynamics still occur for certain pacing periods. The NFC method is most effective, which can eliminate instabilities for a certain range of control strength α. Under a very strong memory effect, all three methods fail. We demonstrate these results using computer simulations of AP models and theoretical analyses of iterated map models. Our results imply that under these diseased conditions, pacing control may only be marginally effective in stabilizing the voltage-driven instabilities due to memory and the steep APD response arising from all-or-none behaviors.

3.2 Methods

We carry out computer simulations using two AP models with the voltage (V) governed by the following differential equation:

$$C_m \frac{dV}{dt} = -I_{\text{ion}} + I_{\text{sti}}, \tag{3.6}$$

where $C_m = 1\,\mu\text{F/cm}^2$ is the membrane capacitance, I_{ion} is the total ionic current density, and I_{sti} is the stimulus current density applied for a given duration.

The first action potential model we use is the phase I Luo and Rudy (LR1) 1991 model [LR91], which is one of the simplest cardiac AP models with physiological ionic current formulations. Since there is no I_{to} in the LR1 model, to model the condition of early repolarization or Brugada syndrome, we add an I_{to} to it, which is the formulation of the fast I_{to} (i.e., $I_{\text{to,f}}$) from the model by Mahajan *et al.* [MSS+08]:

$$I_{\text{to}} = g_{\text{to}} x_{\text{to}} y_{\text{to}} (V - E_{\text{K}}), \tag{3.7}$$

where g_{to} is the maximum I_{to} conductance, x_{to} is the activation gating variable, y_{to} is the inactivation gating variable, and E_{K} is the reversal potential of K^+. In this model, the pacing stimulus we use is $I_{\text{sti}} = 80\,\mu\text{A/cm}^2$ for a 0.5 ms duration. With the addition of I_{to}, we refer to this model as the *LR1+I_{to} model*. We set $g_{\text{to}} = 0.21\,\text{mS/cm}^2$ and make the following parameter and model changes [LGWQ17]: $G_{\text{si}} = 0.1035\,\text{mS/cm}^2$, $G_{\text{K1}} = 0.133\,034\,\text{mS/cm}^2$, the voltage-dependent time constant of the X-gating variable of I_{K} is increased 5-fold ($\tau_X \to 5\tau_X$), and the steady-state curve of $y_{\text{to,f}}$ is shifted by 8 mV to more positive voltages.

We also use our recently developed iterated map model that incorporates memory from the slow K^+ channel recovery [LGWQ17, LQ18b] to investigate the efficacy of the different control methods. The model is described by the following

equations:

$$x_{n+1} = w(x_n, a_n, d_n) = \left[x_a - (x_a - x_n)e^{-\frac{a_n}{\tau_a}}\right] e^{-\frac{d_n}{\tau_d}} \tag{3.8}$$

$$a_n = g(x_n) \tag{3.9}$$

$$d_n = p(a_n) = mT - a_n, \tag{3.10}$$

where x_n is the variable describing the memory effect from the slow recovery of the K^+ channel, more specifically the X-gating variable of I_K in the LR1 model. The function g describes the dependence of APD on the memory variable X. In this manuscript we assume that $m = 1$, so there is always 1:1 capture. We call this model the *X-memory map model*. In our previous studies[LGWQ17, LQ18b], we determined parameter values $x_a = 0.6$, $\tau_a = 3000\,\text{ms}$, and $\tau_d = 1000\,\text{ms}$ to match closely with results seen in the LR1+I_{to} model. The function g was determined by simulating the LR1+I_{to} model at a fixed pacing period $T = 1500\,\text{ms}$, and at the time of the last stimulus the value of X is changed to a new value x_{init}. The APD of the resulting AP is then recorded for different values of x_{init}. The dependence of APD on x_{init} is shown in Fig. 3.1(f), and a linear interpolation of the data is used for g in the X-memory map model (Eq. (3.9)).

The second AP model we use is a much more complex one, a human ventricular AP model developed by ten Tusscher *et al.* [tTNNP04], denoted as the *TP04 model* in this study. I_{to} formulations (both slow and fast I_{to}) are present in the TP04 model, so for simplicity and consistency we remove the two original I_{to} formulations and add the I_{to} formulation in Eq. (3.7). In this model, the stimulus current is $I_{sti} = 52\,\mu\text{A/cm}^2$ for a 1 ms duration.

Since memory in the TP04 model is mainly caused by slow intracellular ion concentration accumulation, we previously developed another iterated map model to describe its memory effects and dynamics [LQ18b], which is described by the

following equations:

$$c_{n+1} = w(c_n, a_n, T) = c_n e^{\gamma_a a_n - \gamma_T T + \delta} \tag{3.11}$$

$$a_n = g(c_n) \tag{3.12}$$

$$d_n = mT - a_n, \tag{3.13}$$

where Eq. (3.11) is the iterated map describing the memory effect from the slow accumulation of the intracellular Ca^{2+} concentration. We refer to this model as the *Ca^{2+}-memory map model*. Note that under constant-T pacing with 1:1 capture ($m = 1$), $T = a_n + d_n$, so Eq. (3.11) becomes $c_{n+1} = w(c_n, a_n, d_n) = c_n e^{(\gamma_a - \gamma_t)a_n - \gamma_T d_n + \delta}$. Results from simulations of the TP04 model and of the Ca^{2+}-memory map model are in the Supplementary Material section. In our previous study[LQ18b], we determined parameter values $\gamma_a = 2 \times 10^{-4}\,\mathrm{ms}^{-1}$, $\gamma_T = 3.625 \times 10^{-6}\,\mathrm{ms}^{-1}$, and $\delta = -0.0275$.

Numerical simulations of the AP models are carried out using an adaptive forward-Euler method in which the time step $\Delta t = 0.05\,\mathrm{ms}$. If at any step the change in voltage would be greater than $0.1\,\mathrm{mV}$, i.e., $\Delta V > 0.1\,\mathrm{mV}$, the time step is then $\Delta t = 0.005\,\mathrm{ms}$. For every AP, the APD is calculated to be the duration of time such that $V > -75\,\mathrm{mV}$.

3.3 Results

3.3.1 Stability Analysis of a General Iterated Map Model

To analyze in general the APD stability of the system under different control methods, we consider the following general iterated map model, similar to the

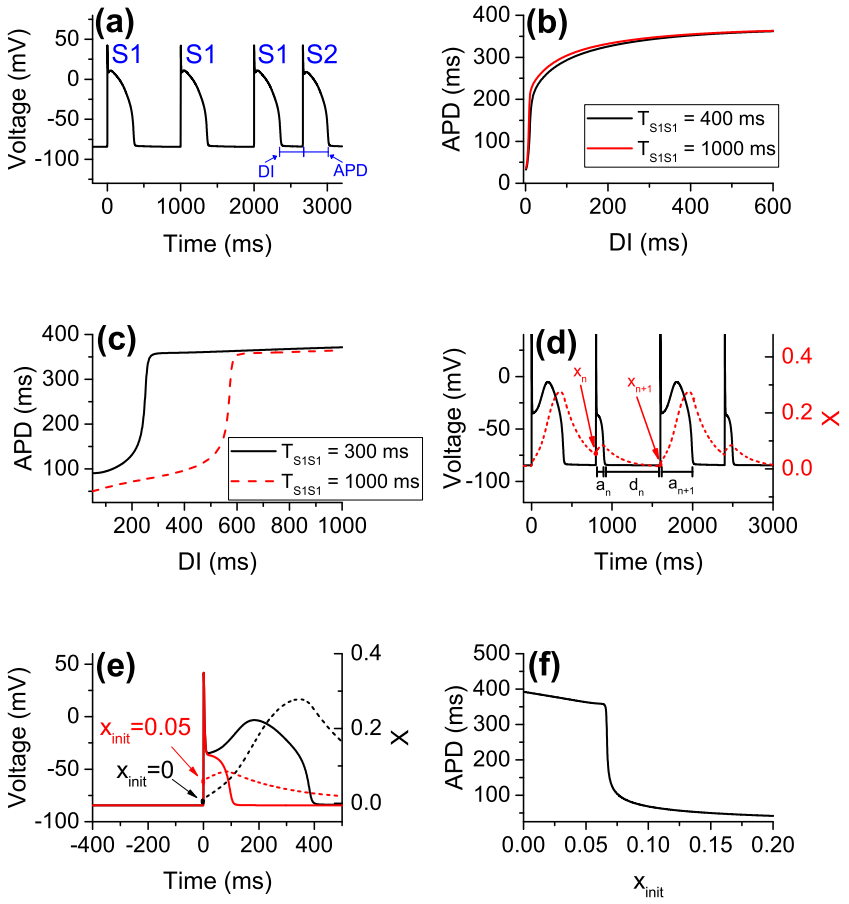

Figure 3.1: The S1S2 APD restitution and memory. **(a)**. Schematic plot of the S1S2 pacing protocol. A cell is paced with an S1-pacing period T, followed by a premature stimulus (S2) after a given DI, and the resulting APD is recorded. **(b)**. S1S2 APD restitutions of the LR1 model without I_{to} for S1-pacing periods $T = 400\,\text{ms}$ and $1000\,\text{ms}$. **(c)**. S1S2 APD restitutions of the LR1+I_{to} model for S1-pacing periods $T = 300\,\text{ms}$ and $1000\,\text{ms}$. **(d)**. Action potentials of the LR1+I_{to} model plotted against the gating variable X during APD alternans. **(e)**. Effects of initial X values, x_{init}, on APD. When $x_{\text{init}} = 0$, the resulting AP has a spike-and-dome with a prolonged APD. When $x_{\text{init}} = 0.05$, the resulting AP has a spike with a shortened APD. **(f)**. Plot of APD against x_{init}. The curve was generated by simulating the LR1+I_{to} model at a fixed pacing period $T = 1500\,\text{ms}$, and at the time of the next stimulus the value of X is changed, as illustrated in (e). The resulting APD is then recorded. This curve is used as the function g in the X-memory map model (Eq. (3.9)).

method used by Otani [Ota17]:

$$z_{n+1} = w(z_n, a_n, d_n) \tag{3.14}$$

$$a_n = g(z_n) \tag{3.15}$$

$$d_n = p(a_n, a_{n-1}, \dots). \tag{3.16}$$

Both the X-memory map model (Eqs.(3.8)-(3.10)) and the Ca^{2+}-memory map model (Eqs.(3.11)-(3.13)) are specific applications of the general iterated map model. The function $w = w(z, a, d)$ determines the growth or decay of the memory variable z dependent on the previous beat's APD (a) and DI (d). For example, in the LR1+I_{to} model, the memory variable X activates (increases) during the APD and deactivates (decreases) during the DI. The dotted-red curve in Fig. 3.1(d) shows that between x_n and x_{n+1}, the APD is short and the DI is long, resulting in a net decrease in X and thus $x_{n+1} < x_n$. Eqs.(3.8) and (3.11) provide explicit expressions for w in the X-memory map model and the Ca^{2+}-memory map model, respectively. For the X-memory map model, $z = x$, and for the Ca^{2+}-memory map model, $z = c$. The function g determines the dependence of APD on the memory variable.

The function p determines the method of "control," which is a constant for constant-DI control or a function of APD for the other control methods. In other words, p determines the period of time between repolarization of the previous AP and the next stimulus. Different control methods have p depend on a variable number of prior APDs. For example, in constant-DI control, $d_n = d_0$ so p is a constant independent of APD.

Together, Eqs.(3.14)-(3.16) simplify to

$$a_{n+1} = g(z_{n+1}) = g(w(g^{-1}(a_n), a_n, p(a_n, a_{n-1}, \dots)) \equiv H(a_n, a_{n-1}, \dots), \tag{3.17}$$

so a_{n+1} depends explicitly on prior APDs via the map H. The dimensionality of the iterated map depends on the control function p. If p is constant or depends

on only the previous APD a_n, then Eq. (3.17) is 1-dimensional. If, however, p depends on the previous $m > 1$ APDs so that $p = p(a_n, a_{n-1}, \ldots, a_{n-m+1})$, then Eq. (3.17) is an $(m-1)$-dimensional iterated map.

Under constant-T pacing, the n^{th} DI satisfies

$$d_n = p(a_n) = T - a_n. \tag{3.18}$$

Since $p = p(a_n)$ depends only on the prior APD, the return map H in Eq. (3.17) is 1-dimensional. Denoting the return map under constant-T pacing as H_T, the APD fixed point as a^*, and $z^* = g^{-1}(a^*)$ the corresponding memory fixed point, then the derivative of the iterated map at the fixed point is

$$H_T' \equiv H_T'(a^*) = \frac{\partial w}{\partial z} + g'(z^*)\left(\frac{\partial w}{\partial a} - \frac{\partial w}{\partial d}\right) = \rho - \sigma\left(\xi + \omega\right), \tag{3.19}$$

where

$$\sigma = -g'(z^*), \quad \rho = \frac{\partial w}{\partial z}, \quad \xi = \frac{\partial w}{\partial a}, \quad \omega = -\frac{\partial w}{\partial d}. \tag{3.20}$$

σ measures the dependence of APD on the memory variable z, and ω measures how slowly z changes during the DI. We make a number of constraints on the variables ρ, ξ, and ω to be physiologically realistic. Firstly, $\omega > 0$ (i.e. $\frac{\partial w}{\partial d} < 0$) since the memory variable decays during the DI. For example, the X-gating variable of I_{Ks} deactivates during the DI, and Ca^{2+} is effluxed out of the cytoplasm during the DI via the sodium-calcium exchanger (NCX). Similarly, $\xi > 0$ since the memory variable accumulates in the DI. For example, the X-gating variable activates during the AP, and Ca^{2+} accumulates in the cytoplasm via the calcium window current ($I_{\text{Ca,L}}$) and the SERCA pump during the AP. Finally, ρ must be constrained to $|\rho| < 1$, so that when the APD and DI are fixed, z stabilizes to z^*. In other words, restraining $|\rho| < 1$ assures that when voltage is stable, e.g. under voltage clamp conditions, memory is also stable. We are primarily interested in how σ and ω – the APD dependence on memory and the kinetics of memory – determine APD instability under constant-T pacing and under control. Thus, we

consider ρ and ξ as fixed constants. For the DNFC and NFC methods, we are also interested in α, which determines the strength of the two control schemes.

Under constant-T pacing, the APD fixed point is stable when $|H_T'(a^*)| < 1$, which leads to

$$\frac{\rho - 1}{\xi + \omega} < \sigma < \frac{\rho + 1}{\xi + \omega}. \tag{3.21}$$

For illustrative purposes, we provide an example stability region of σ and ω in Fig. 3.2(a) for fixed values of ρ and ξ. The stability boundary lines $\sigma = \frac{\rho \pm 1}{\xi + \omega}$ are plotted. The APD fixed point is stable under constant-T pacing provided σ is not too large (or too negative). A smaller ω tends to help stability, but only to an extent. In particular, if $\sigma > \frac{\rho+1}{\xi}$ then the fixed point will always be unstable, independent of ω.

Under constant-DI pacing, $d_n = d_0$, so the function p in Eq. (3.16) is a constant independent of prior APDs and the return map is 1-dimensional. Denoting the return map under constant-DI pacing as H_{DI}, then its derivative evaluated at the APD fixed point is

$$H_{DI}' \equiv H_{DI}'(a^*) = \rho - \sigma\xi. \tag{3.22}$$

Note that $H_{DI}' = H_T' + \sigma\omega$. Constant-DI pacing will stabilize the APD fixed point provided

$$\frac{\rho - 1}{\xi} < \sigma < \frac{\rho + 1}{\xi}. \tag{3.23}$$

This stability criterion is nearly identical to the constant-T pacing stability criterion (Eq. (3.21)), but the ω term in the denominators are absent here. The inequalities in Eq. (3.23) are independent of ω, and so stability depends solely on σ. Namely, if σ is too large (or too negative), constant-DI pacing will fail to stabilize the fixed point. In Fig. 3.2(b), the boundary lines $\sigma = \frac{\rho \pm 1}{\xi}$ are plotted. Compared to the stability region for constant-T pacing (Fig. 3.2(a)), constant-DI pacing is more stable, but the effectiveness of constant-DI pacing diminishes as ω gets smaller. More specifically, the upper stability limit of σ for constant-T pacing

is $\frac{\rho+1}{\xi+\omega}$ compared to $\frac{\rho+1}{\xi}$ for constant-DI pacing. In the region $\frac{\rho+1}{\xi+\omega} < \sigma < \frac{\rho+1}{\xi}$, constant-DI pacing will stabilize the fixed point where constant-T pacing fails, and this region shrinks as ω gets small. In the presence of memory, constant-DI pacing no longer stabilizes the fixed point unconditionally, and its efficacy of control may strongly depend on the memory effect, despite the fact that the APD instability is completely voltage driven.

Next, we consider the effectiveness of the DNFC method. Under the DNFC method, the pacing period T changes to a new pacing period T', as described in Eq. (3.1). Setting $d_n = T' - a_n$ in Eq. (3.1) gives

$$d_n = p(a_n, a_{n-1}) = T - a_n + \frac{\alpha}{2}(a_n - a_{n-1}). \tag{3.24}$$

Note that setting $\alpha = 0$ is equivalent to constant-T pacing. Under steady state $d_n = d^* = T - a^*$, so $T = a^* + d^*$ is the steady state pacing period.

Because $p = p(a_n, a_{n-1})$ depends on the prior two APDs, the iterated map in Eq. (3.17) is 2-dimensional such that a_{n+1} depends on both a_n and a_{n-1}. The Jacobian of the iterated map under DNFC is

$$J_{DNFC} \equiv \begin{pmatrix} \rho - \sigma\left[\xi + \frac{(2-\alpha)\omega}{2}\right] & -\frac{\alpha\sigma\omega}{2} \\ 1 & 0 \end{pmatrix}. \tag{3.25}$$

The fixed point is stable if and only if the two eigenvalues of J_{DNFC} have magnitude less than 1. This leads to the following stability criteria:

$$-2 < \sigma(\xi + \omega) - \rho - 1 < \alpha\sigma\omega < 2. \tag{3.26}$$

All three inequalities in Eq. (3.26) have to be met to guarantee stability. Fig. 3.2(c) and (d) show the boundaries of the stability region of the DNFC method for α fixed, varying σ and ω (panel (c)) and for ω fixed, varying σ and α (panel (d)). If σ is sufficiently large such that $\sigma > \frac{\rho+3}{\xi+\omega}$, the DNFC method will always fail to stabilize the APD fixed point. This condition is equivalent to $H'_T < -3$, so that if the derivative of the iterated map under constant-T pacing is sufficiently negative

(less than -3), the DNFC method will always fail to stabilize the fixed point. In Fig. 3.2(c), for a fixed α, the curves $\sigma(\xi+\omega)-\rho-1=\alpha\sigma\omega$ and $\alpha\sigma\omega=2$ meet at the point $(\sigma,\omega)=\left(\frac{\rho+3-\frac{2}{\alpha}}{\xi},\frac{2\xi}{\alpha(\rho+3)-2}\right)$, and choosing $\alpha=\frac{2\xi+2\omega}{\omega(\rho+3)}$ will maximize the range of σ that will stabilize the fixed point. This value of α is precisely the point of the cusp seen in Fig. 3.2(d), where the fixed point is stable up to $\sigma\approx 2\times 10^4$. However, despite the limitations of the DNFC method, the method is in general superior to constant-T and constant-DI pacing, as the region of stability increases (so long as α is chosen appropriately). For example, under constant-T pacing the fixed point is stable provided $\sigma<\frac{\rho+1}{\xi+\omega}$, whereas the DNFC method can stabilize the fixed point so long as $\sigma<\frac{\rho+3}{\xi+\omega}$.

Finally, we consider NFC. This is a new control method we propose in this study in which the pacing period T is perturbed by the following:

$$T'=T+\alpha(a_n-a^*), \tag{3.27}$$

where a^* is the APD fixed point under constant-T pacing. This is a form of negative feedback control. For example, under APD alternans, if $a_n>a^*$ so that a_{n+1} would be smaller than a^*, then the pacing period is lengthened to facilitate a_{n+1} to be closer to a^*. Conversely, if $a_n<a^*$ so that a_{n+1} would be larger than a^*, the pacing period is shortened to decrease a_{n+1} and be closer to a^*. Setting $d_n=T'-a_n$ gives

$$d_n=p(a_n)=T-a_n+\alpha(a_n-a^*). \tag{3.28}$$

Note that Eq. (3.28) is equivalent to $d_n=\kappa_0+(\alpha-1)a_n$ where $\kappa_0=T-\alpha a^*$. Although the APD fixed point a^* may not be known in advance in Eq. (3.28), κ_0 may be varied freely. Setting $\alpha=0$ is equivalent to constant-T pacing, and setting $\alpha=1$ is equivalent to constant-DI pacing (since $d_n=T-a_n+1\cdot(a_n-a^*)=T-a^*$ is a constant independent of a_n).

Because $p=p(a_n)$ depends only on the previous APD, the iterated map is 1-dimensional. Denoting H_{NFC} as the APD return map under NFC control, then

its derivative is

$$H'_{NFC} \equiv H'_{NFC}(a^*) = \rho - \sigma\left[\xi + (1-\alpha)\omega\right], \tag{3.29}$$

Stability of the fixed point is satisfied provided

$$\rho - 1 < \sigma\left[\xi + (1-\alpha)\omega\right] < \rho + 1. \tag{3.30}$$

See Fig. 3.2(e) and (f) for an example stability region under NFC. In contrast to the DNFC method, the NFC method can always stabilize the system provided a proper α is chosen. In particular, setting $\alpha = 1 + \frac{\xi}{\omega} - \frac{\rho}{\sigma\omega} \equiv \bar{\alpha}$ makes $H'_{NFC} = 0$ and the fixed point is stable regardless of how large or small σ and ω are. However, the range of α that stabilizes the fixed point may be very narrow so that stability is very sensitive to the exact choice of α. In particular, the fixed point is stable provided $|\alpha - \bar{\alpha}| < \frac{1}{\sigma\omega}$, and so when σ gets large the range of α that stabilizes the fixed point gets narrower.

We have estabilished stability criteria of the APD fixed point under constant-T pacing (Eq. (3.21)), constant-DI pacing (Eq. (3.23)), DNFC (Eq. (3.26)), and NFC (Eq. (3.30)). Among all control methods, NFC is most effective at stabilizing the APD fixed point, and in particular is the only method that can stabilize the fixed point regardless of the parameters of the iterated map. However, there are still limitations, namely that if σ is sufficiently large so that $\sigma >> \frac{1}{\omega}$, then the stability of the fixed point is very sensitive on the NFC parameter α. In other words, a small deviation from an optimal α that stabilizes the fixed point may destabilize the fixed point.

In the following sections, we carry out computer simulations using iterated map models and AP models to examine the general theoretical predictions of the efficacy of the three control methods.

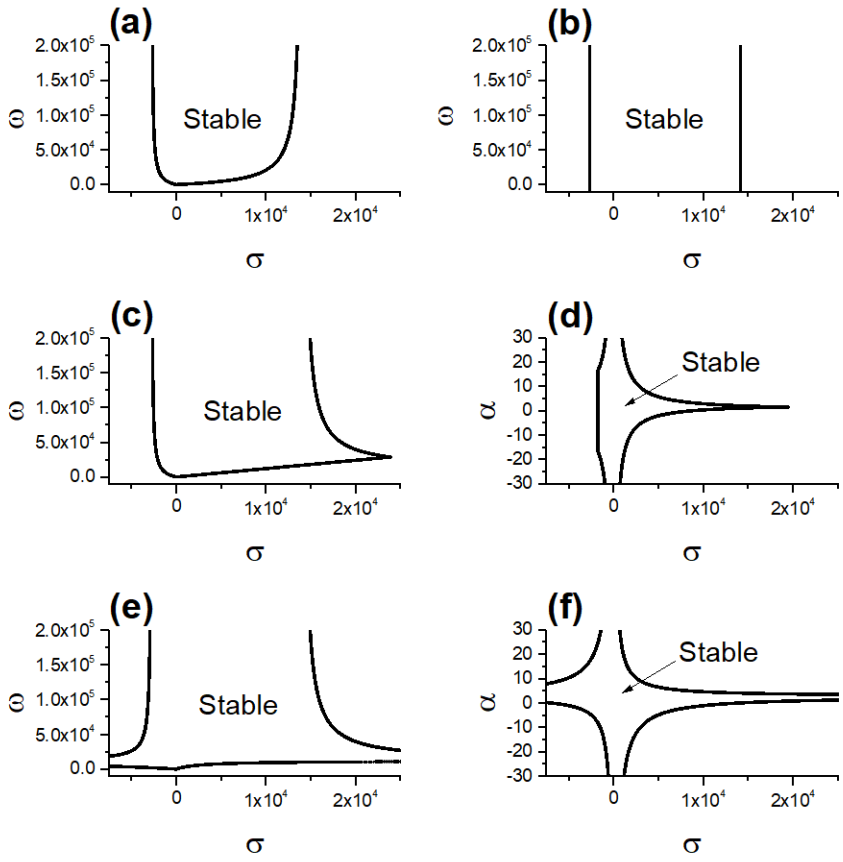

Figure 3.2: Stability of constant-T pacing **(a)**, constant-DI pacing **(b)**, DNFC **(c)** and **(d)**, and NFC **(e)** and **(f)** dependent on the parameters $\sigma = -g'(z^*)$, $\omega = -\frac{\partial w}{\partial d}$, and α. We set $\rho = 0.67368$ and $\xi = 1.190168 \times 10^{-4}$ fixed, which match closely to simulation results of the LR1+I_{to} model with $T = 515\,\text{ms}$. In panels (c) and (e), we fix $\alpha = 2.4$; in panels (d) and (f), we fix $\omega = 7 \times 10^{-5}$, which also matches closely to simulation results of the LR1+I_{to} model with $T = 515\,\text{ms}$.

3.3.2 Controlling Voltage-Driven Instabilities Due to Slow K^+ Channel Deactivation in the Presence of I_{to}

3.3.2.1 Constant-T vs. Constant-DI pacing

For both the LR1 and LR1+I_{to} models, we perform constant-T and constant-DI pacing under various pacing periods and DIs, and plot the corresponding APDs. Bifurcation diagrams are shown in Fig. 3.3. Without I_{to}, the system is unstable under very fast pacing ($T < 300\,\text{ms}$ – see Fig. 3.3(a)). The constant-DI method is able to completely stabilize the system (see Fig. 3.3(b)). This is because the S1S2 APD restitution of the LR1 model has minimal dependence on prior pacing periods, i.e. the memory effect is minimal so that APD depends mainly on the immediate preceding DI (see Fig. 3.1(b)).

In the LR1+I_{to} model, instability occurs at much slower pacing periods (see Fig. 3.3(c)), and there is a period-doubling bifurcation route to enter and exit chaos around pacing periods $T = 325\,\text{ms}$ and $T = 950\,\text{ms}$. In this scenario, constant-DI pacing fails to stabilize the system for most pacing periods (see Fig. 3.3(d)). The region of instability does shrink, as constant-DI control stabilizes APD instability around the pacing periods between $325-380\,\text{ms}$ and between $940-950\,\text{ms}$. However, the constant-DI method fails to stabilize the system for the pacing periods between $380-940\,\text{ms}$. This agrees with the general theoretical analysis above that constant-DI pacing can only stabilize a small range of parameters when the memory effect is large. Fig. 3.4 shows two examples, one in which constant-DI pacing does successfully stabilize APD dynamics ($T = 373\,\text{ms}$), and on which constant-DI pacing fails to stabilize ($T = 515\,\text{ms}$).

Findings from the X-memory map model are consistent with the simulation results of the LR1+I_{to} model. From Eqs.(3.8), we have

$$\sigma = -g'(x^*), \quad \omega = \frac{x^*}{\tau_d}. \tag{3.31}$$

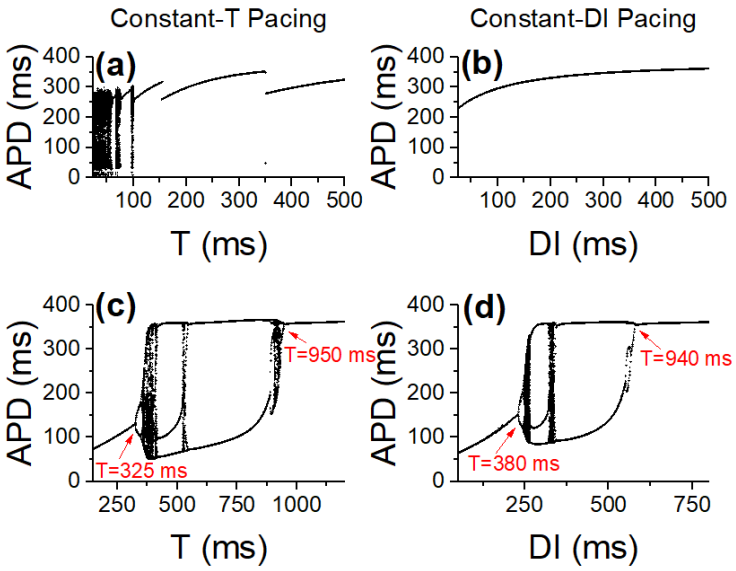

Figure 3.3: APD bifurcation diagrams of the LR1 (first row) and LR1+I_{to} (second row) models under constant-T pacing (left panels) and constant-DI pacing (right panels).

From the previous section, we have shown that in general, constant-DI pacing is more stable compared to constant-T pacing. However, the efficacy of constant-DI pacing depends on σ and ω. As we have shown, constant-T pacing is unstable if $\sigma > \frac{\rho+1}{\xi+\omega}$, while constant-DI pacing is stable when $\sigma < \frac{\rho+1}{\xi}$. Therefore, when APD has too steep of a dependence on memory (σ large) and/or the system has a long memory (ω small), constant-DI pacing control may fail.

Fig. 3.5 shows bifurcation diagrams of APD dynamics of the X-memory map model under both methods of pacing. We used a g-function that was measured from the LR1+I_{to} model using the same parameters as for Fig. 3.4 (i.e. the curve shown in Fig. 3.1(f)). For a narrow range of pacing periods ($396 - 438$ ms and $990 - 1000$ ms), constant-DI pacing stabilizes APD. However, for most pacing periods ($438 - 990$ ms), constant-DI pacing fails to stabilize APD. These results agree well with the simulation results of the LR1+I_{to} model shown in Fig. 3.4(c) and (d). The failure of constant-DI pacing in stabilizing the fixed point is because

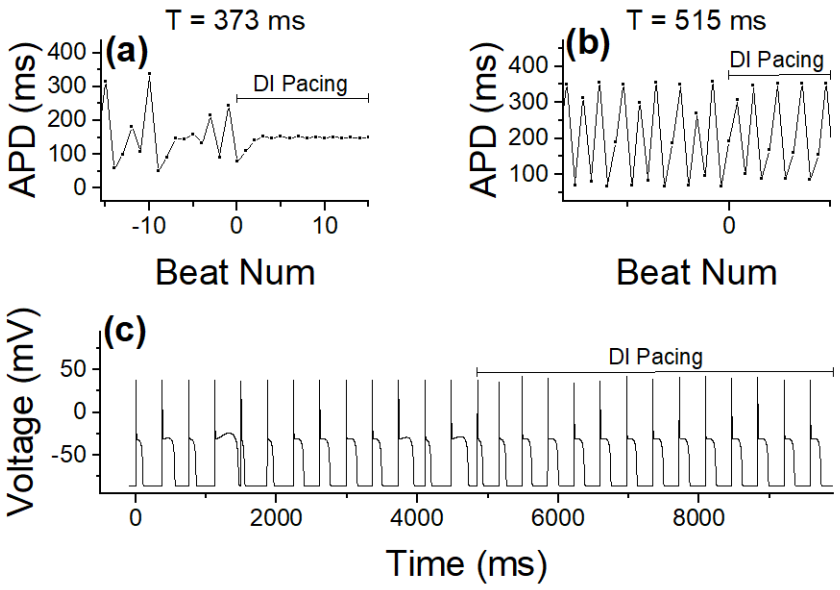

Figure 3.4: Dynamics of the LR1+I_{to} model when switching between constant-T pacing and constant-DI pacing. **(a)** APD vs. beat number for $T = 373\,\text{ms}$. At beat number 0, the system switches from constant-T pacing to constant-DI pacing. After about 5 beats, the APD is stabilized to about 150 ms. **(b)**. APD vs. beat number for $T = 515\,\text{ms}$. Constant-DI pacing switches the chaotic APD dynamics to period-3, failing to stabilize the system. **(c)**. APs before and after the switch from constant-T pacing to constant-DI pacing for $T = 373\,\text{ms}$, leading to stable APs.

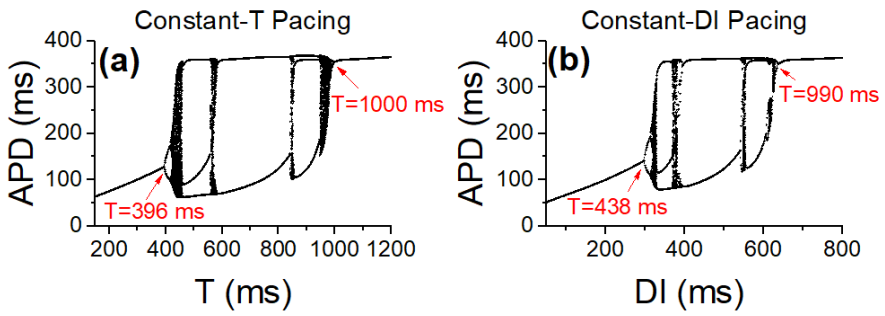

Figure 3.5: APD dynamics of the X-memory map model in Eqs.(3.8)-(3.10) under (a) constant-T pacing and (b) constant-DI pacing. Arrows point to the bifurcation points.

σ is too large. Based on Fig. 3.1(f), the maximum value of σ, i.e. the maximum slope of the curve in Fig. 3.1(f), is 1.5×10^5, which is much larger than the critical σ shown in Fig. 3.2(b).

3.3.2.2 The DNFC method

We next simulate the LR1+I_{to} model with the DNFC method, and the results are shown in Fig. 3.6. Fig. 3.6(a) shows the stability region of the model for various values of pacing period T and DNFC parameter α. The DNFC method can stabilize the model at some pacing periods, but for pacing periods in the range of $400 - 900$ ms the DNFC method fails to stabilize the fixed point. Fig. 3.6(b) shows a bifurcation diagram of the model when $\alpha = 1$, indicating that though the instability region has shrunk compared to constant-T pacing (as in Fig. 3.5(a)), there is still a period-doubling bifurcation route to enter and exit chaos. Fig. 3.6(c) shows an example of APD dynamics when the DNFC method does work at $T = 373$ ms, whereas Fig. 3.6(d) shows that the DNFC method fails when $T = 515$ ms.

Using the X-memory map model (Eqs.(3.8)-(3.10)), Fig. 3.7 shows the stability region of the DNFC method of the iterated map. For some pacing periods, the

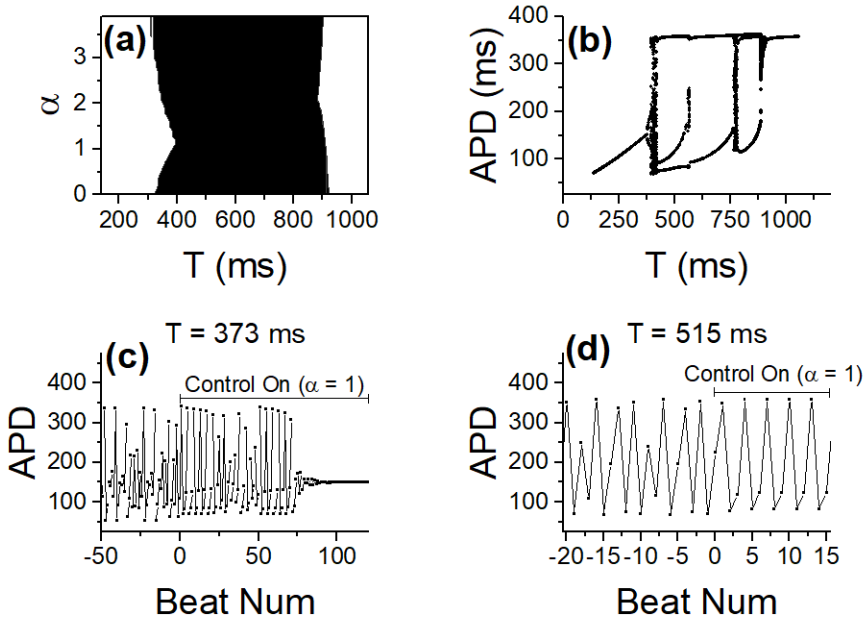

Figure 3.6: APD dynamics of the LR1+I_{to} model when implementing the DNFC method. **(a)**. Stability region of the model for different values of pacing period T and DNFC parameter α. **(b)**. Bifurcation diagram with $\alpha = 1$. **(c)**. APD vs. beat number setting $T = 373\,\text{ms}$. The DNFC method begins at beat number 0, and before that the model is paced with constant-T pacing. The model stabilizes to a fixed APD after about 100 APs. **(d)**. APD vs. beat number setting $T = 515\,\text{ms}$. The DNFC method fails to stabilize.

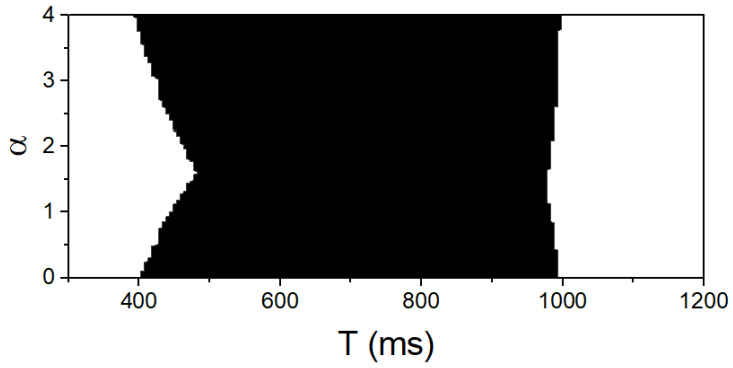

Figure 3.7: Stability region of the X-memory map model (Eqs.(3.8)-(3.10)) when implementing the DNFC method (Eq. (3.24)). The dark region is where the APD fixed point is unstable.

DNFC method can successfully stabilize APD dynamics. Up to $\alpha = 1.5$ the region of instability decreases to pacing periods between $500 - 980$ ms. For pacing periods between $396 - 500$ ms the DNFC method is effective and can stabilize APD dynamics. However, when α is too large, (e.g. $\alpha > 1.5$) the APD fixed point becomes unstable again. The shape of the instability region is very similar to that seen in the LR1+I_{to} model in Fig. 3.6(a). The iterated map model can well capture the behavior of the action potential model.

3.3.2.3 The NFC method

Finally, we perform simulations of the LR1+I_{to} model under the NFC method. The results are shown in Fig. 3.8. As shown in Fig. 3.8(a), APD dynamics can be stabilized for every pacing period by the NFC method for a sufficient choice of α. When α is too large the ionic model becomes unstable again. This is consistent with our prior stability analysis and criterion in Eq. (3.30). Fig. 3.8(b) shows APD dynamics before and after implementation of the NFC method with $T = 515$ ms. With constant-T pacing, the APDs are undergoing chaotic dynamics. When the NFC method is implemented with $\alpha = 2.4$, the APD slowly increases from one

beat to the next until the APD stabilizes to about 180 ms. The APs of this behavior is shown in the next panel, Fig. 3.8(c).

We next consider the regions of stability of the NFC method using the X-memory map model (Eqs.(3.8)-(3.10)). The results are shown in Fig. 3.9. Consistent with the stability criterion in Eq. (3.30), every pacing period T can be stabilized by the NFC method using some choice of α. In fact, there is a very narrow choice around $\alpha = 2.4$ which will stabilize APD dynamics for all pacing periods. For $\alpha > 2.4$, a new region of instability emerges. These results are consistent with our prior analysis that although the NFC method can successfully stabilize APD dynamics, the range of α can be quite narrow. As we have shown, this range depends on $\frac{1}{\sigma\omega}$, and so with σ sufficiently large the map is stable for only a narrow range of α.

3.3.3 Efficacy of Controlling Voltage Instabilities Due to Ion Concentration Accumulation

As shown in our previous work [LQ18b], in the TP04 model, slow Ca^{2+} concentration accumulation causes APD dynamics and instability. APD depends very sensitively on Ca^{2+}, and Ca^{2+} concentration equilibrates with a time constant on the order of several seconds. In contrast, the X-gating variable in the LR1+I_{to} model equilibrates with a time constant of about one second.

Controlling APD instability proves very difficult in the TP04 model and the Ca^{2+}-memory map model (Eqs.(3.11)-(3.13)). As we have shown previously [LQ18b], the Ca^{2+}-memory map model can accurately capture the bifurcations of the TP04 model. Here, we only evaluate the efficacy of the control methods using the iterated map model. Bifurcation diagrams and stability maps of the Ca^{2+}-memory map model under the different control methods are shown in Figs. S3-S5in the Supplementary Material section. Under constant-T pacing, APDs are unstable

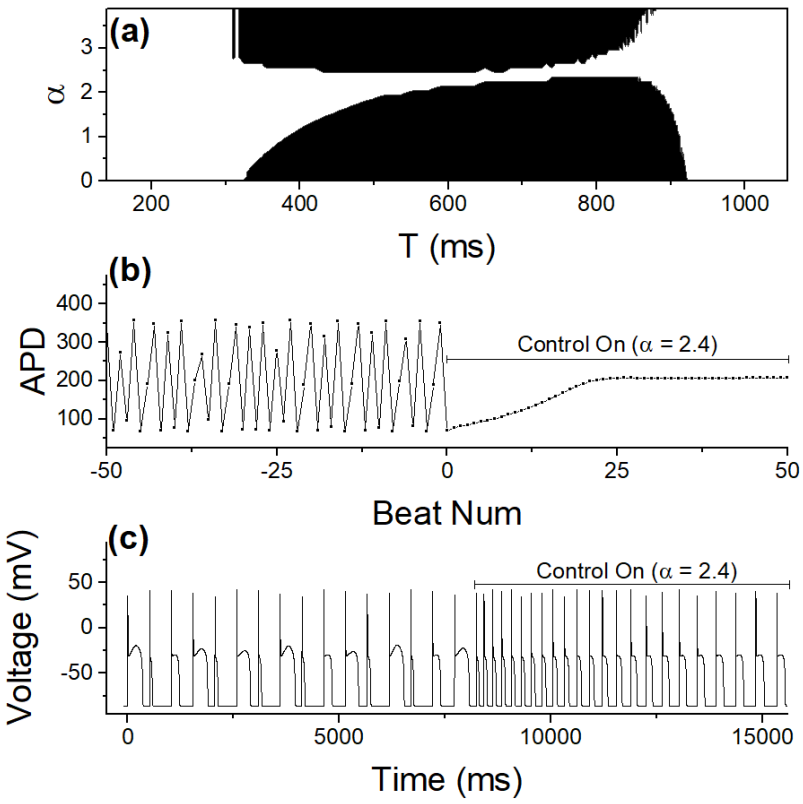

Figure 3.8: APD dynamics of the LR1+I_{to} model using the NFC method. **(a)**. Stability region for various values of pacing period T and NFC method parameter α. The dark region is where the APD fixed point is unstable. **(b)**. APD vs. beat number before and after the NFC method is implemented with $\alpha = 2.4$ and $T = 515$ ms. Once the control method is implemented, it takes about 25 APs before the APD stabilizes to 180 ms. **(c)**. APs before and after the NFC method is implemented, corresponding to the data shown in panel (b).

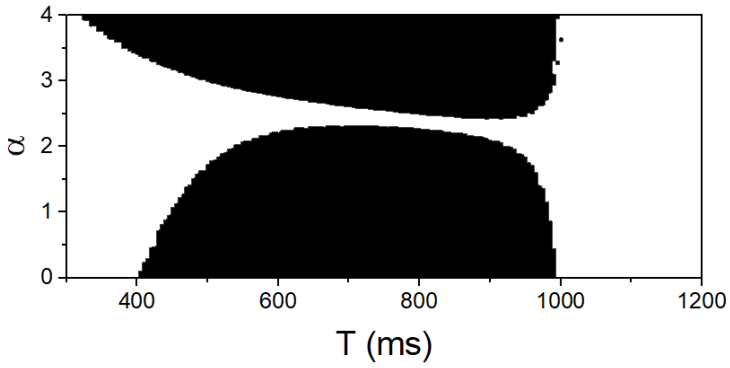

Figure 3.9: Stability region of the X-memory map model (Eqs.(3.8)-(3.10)) under the NFC method (Eq. (3.28)). The x-axis is the pacing period T, and the y-axis is the control parameter α. The dark region is where the APD fixed point is unstable.

for all pacing periods up to $T = 8420\,\text{ms}$. The constant-DI method fails to control instabilities for nearly all pacing periods, with the exception of a small range of pacing periods between $8410 - 8420\,\text{ms}$ (Fig. 3.12). This is due to the fact that in the model, ω is very large and so constant-DI pacing is only effective in a very narrow range.

The DNFC method also has limited efficacy, only successfully stabilizing APD dynamics under rapid pacing (Fig. 3.13). The NFC method is able to successfully stabilize APDs, but only when the NFC control parameter is in a very narrow range around $\alpha = 55.1$ (Fig. 3.14) The controllability of APD dynamics under the Ca^{2+}-memory map model is incredibly sensitive to changes in α; for example, setting $\alpha = 55$ instead of 55.1 fails to stabilize APD dynamics for most pacing periods (Fig. 3.14(b)). The range of α that stabilizes the iterated map depends on $\frac{1}{\sigma\omega}$, and since σ is very large, stability is very sensitive on α.

3.3.4 Efficacy of Controlling Voltage Instabilities Induced by EADs

As shown previously [LGWQ17, LQ18b], we use the LR1 model and modify I_{K} by increasing the voltage-dependent time constant of the X-gating variable 10-fold ($\tau_X \to 10\tau_X$) to promote EADs. Using our X-memory map model in Eqs.(3.8)-(3.10), with parameter values $x_a = 0.6, \tau_a = 6000\,\mathrm{ms}$, and $\tau_d = 2000\,\mathrm{ms}$, we can well capture the bifurcations of the LR1 model in the presence of EADs. Again, we can use this iterated map to evaluate the efficacy of the different control methods on stabilizing the fixed point.The function g was determined in exactly the same fashion as the function g was determined using the LR1+I_{to} model, but instead using the LR1 model in the presence of EADs.

Bifurcation diagrams and stability maps of the iterated map model under the different control methods are provided in Figs. 3.15 and 3.16. Under constant-T pacing at $T = 1250\,\mathrm{ms}$, a period-doubling bifurcation point occurs where the APs are stable with 0 EADs ($T < 1250\,\mathrm{ms}$) to complex APD alternans ($T > 1250\,\mathrm{ms}$) soon leading to complex APD dynamics with EADs (Fig. 3.15(a)). Under constant-DI pacing (Fig. 3.15(b)), the bifurcation point shifts slightly to $T = 1280\,\mathrm{ms}$, and so constant-DI pacing successfully stabilizes APD dynamics for pacing periods between $1250 - 1280\,\mathrm{ms}$. However, the method fails to control APD dynamics under all pacing periods greater than 1280 ms.

The DNFC and NFC methods have little success in controlling APD instability (Fig. 3.16). As shown in Fig. 3.16(a), the DNFC method has limited success to control instability up to $\alpha = 1$ near the bifurcation point around $T = 1250\,\mathrm{ms}$ and at the bifurcation points corresponding to transitions from 1 EAD to 2 EADs ($T = 1750\,\mathrm{ms}$) and from 2 EADs to 3 EADs ($T = 2050\,\mathrm{ms}$). As expected, the NFC method (Fig. 3.16(b)) does successfully stabilize APD dynamics, but under very narrow choices of α around $\alpha = 1.6$.

3.4 Discussion and Conclusions

In this study, we investigated the efficacy of three pacing control methods in stabilizing voltage-driven instabilities in ventricular myocytes under two diseased conditions. The three control methods include two previous widely studied methods [HG02, HCT+97, JC04] and a new one proposed in this study. We show that under the normal condition in which there is no or little memory effect, all three methods can successfully stabilize the voltage-driven instabilities caused by steep APD restitution curves. However, under the two diseased conditions, constant-DI pacing almost completely fails to stabilize the voltage-driven instabilities, while the other two methods can suppress the instabilities with the simple feedback pacing being the most effective. Note that in the absence of the memory effect (Eq. (3.2)), under constant-DI pacing, the system is unconditionally controllable, while under the other two methods, the system is conditionally controllable. The failure of constant-DI pacing in stabilizing voltage-driven instabilities agrees with the prediction by Otani [Ota17] using a generic iterated map model. The controllability of the system depends on the strength of the memory effect and the steepness of the APD dependence on the memory variables. As shown by Hall *et al.* [HCT+97] who used an experimental model in which alternans was likely promoted by the memory effect [SAGB95], alternans can be controlled by the time-delayed feedback pacing algorithm. As shown in this study, under the diseased conditions, the strong memory effect and the all-or-none behaviors make the controlling to be difficult. Moreover, the instabilities tend to occur at multiple scales with multiple causes and mechanisms [QW15], one would expect that more sophisticated controlling methods are needed to control the instabilities under the diseased conditions. In addition, since the instabilities shown in our models are purely voltage-driven, constant-DI pacing may not be appropriate in differentiating voltage-driven instabilities from Ca^{2+}-driven instabilities as suggested by Cherry [Che17].

Finally, we would like to point out that we only studied two sources of memory: the slow recovery of the K^+ channel and the slow accumulation of intracellular Ca^{2+} concentration. However, there are many sources of memory in the heart, from seconds to minutes. Memory from the K^+ channel is due to the slow component of the delayed K^+ current I_{Ks} [SJ90, ZLRR95, SR05], which activates and recovers slowly on the order of several hundred milliseconds to a couple of seconds. The memory effect in the LR1 model is mainly caused by the K^+ current, which only takes a couple of beats to recover after a sudden change in pacing period (Fig. 3.10). Another major source of memory is from the slow accumulation of intracellular ion (Na^+, K^+, and Ca^{2+}) concentrations, which can take minutes to re-equilibrate after a sudden change in heart rate [FR00]. In our study of the TP04 model, since we set Na^+ to be a constant, the memory effect is caused only by Ca^{2+} accumulation which takes 10 to 20 beats (i.e. 10 to 20 s) to reach steady state after a sudden change in pacing period (Fig. 3.11) In the experimental study by Franz *et al.* [FSLS88], it took about 120 s for the APD to reach a new steady state after a sudden change in pacing period. In a series of experimental studies by Kunsyz *et al.* [KGS95, KMS95, KSG97], they showed that in spontaneous beating chicken heart aggrevates, it took tens of seconds for the aggregates to go back to steady state after overdrive pacing. The memory time constant in the TP04 model is in the same order of magnitude as in the experiments despite the exclusion of memory from Na^+ accumulation. If Na^+ is not clamped in the TP04 model, the time constant of memory will be significantly longer. Recent studies have shown that slow accumulation may also promote interesting action potential dynamics [XLG+15, KMC17]. As shown in our general iterated map analyses, it will be more difficult to control the instabilities for a longer memory time constant. Although in theory the NFC method that we propose in this study is able to control the instabilities when the memory effect is strong, it may depend too sensitively on the strength of control signal to be practically useful (see Fig. 3.14)

Therefore, better control algorithms are needed for the control of the instabilities under the diseased conditions in which strong memory effects exist.

3.5 Supplementary Material

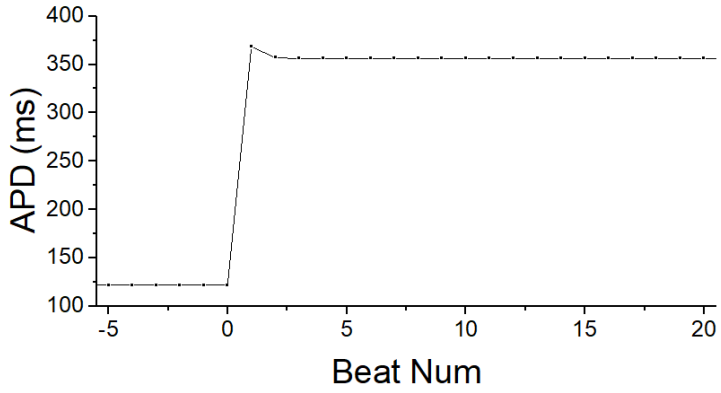

Figure 3.10: APDs of the LR1+I_{to} model before and after switching from rapid pacing, $T = 300\,\text{ms}$, and slow pacing, $T = 1000\,\text{ms}$. Before the switch at beat number 0, APDs are stable at 122 ms. After the switch, it takes about 5 beats to reach a steady state APD of 356 ms.

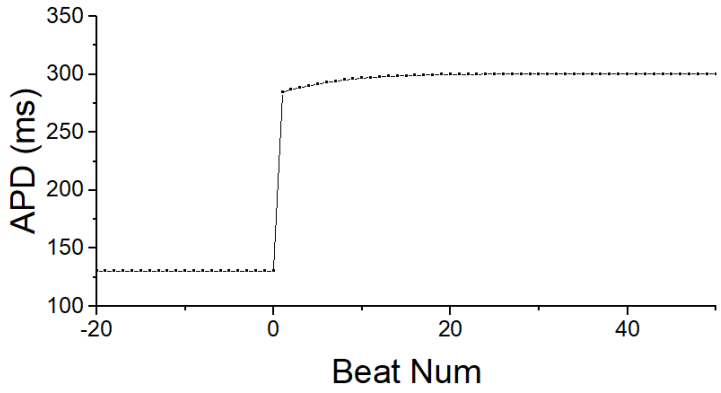

Figure 3.11: APDs of the TP04 model before and after switching from rapid pacing, $T = 300\,\text{ms}$, and slow pacing, $T = 9000\,\text{ms}$.

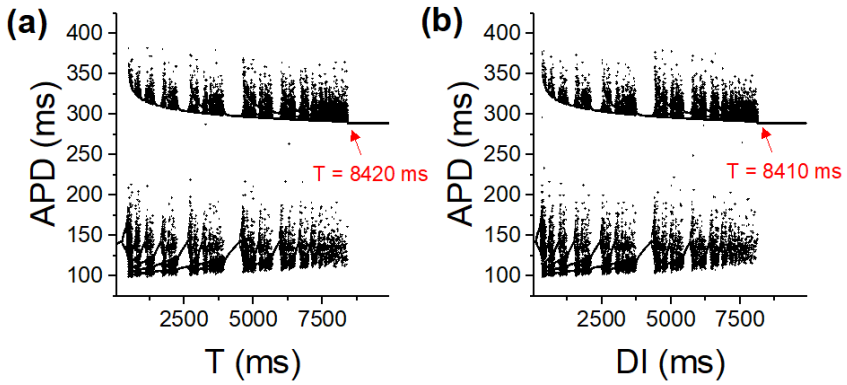

Figure 3.12: APD bifurcation diagrams of the Ca^{2+}-memory map model under **(a)** constant-T pacing and **(b)** constant-DI pacing.

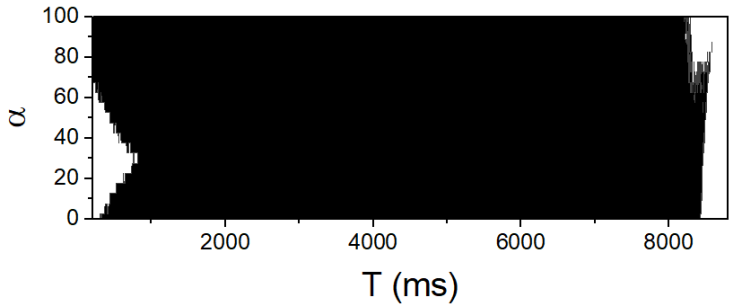

Figure 3.13: Stability of the Ca^{2+}-memory map model under the DNFC method. The x-axis is the pacing period T, and the y-axis is the control parameter α. The dark area is where the APD is unstable.

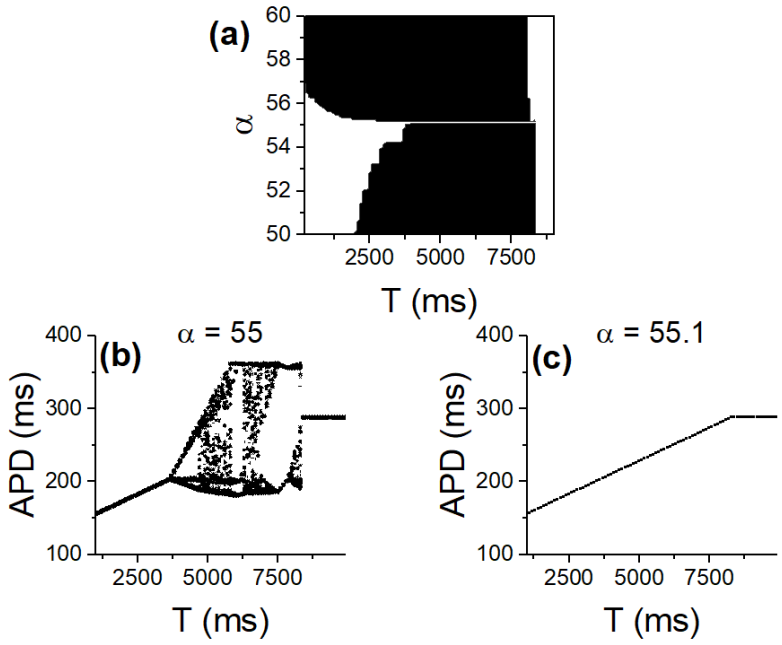

Figure 3.14: Dynamics of the Ca^{2+}-memory map model under the NFC method. **(a)**. APD stability region for different pacing cycles T and control parameters α. The dark region is where the APD is unstable. **(b)**. APD bifurcation diagram with $\alpha = 55$. **(c)**. APD bifurcation diagram with $\alpha = 55.1$.

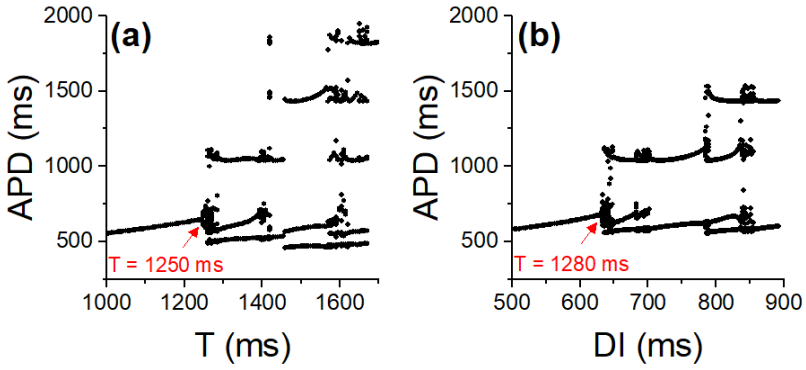

Figure 3.15: APD bifurcation diagrams of the LR1 EAD model under **(a)** constant-T pacing and **(b)** constant-DI pacing.

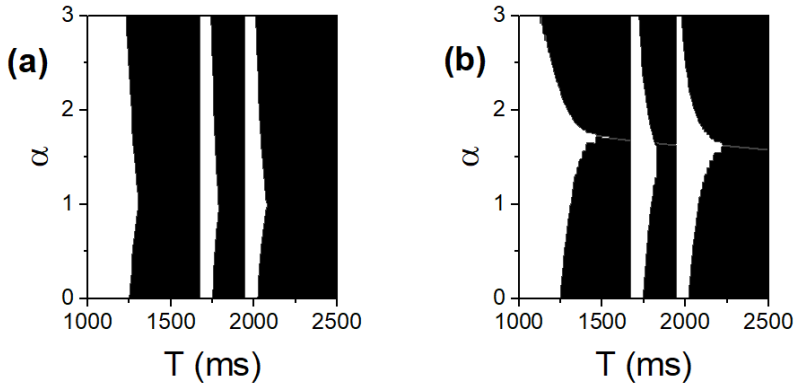

Figure 3.16: Stability of the LR1 EAD model under **(a)** the DNFC method and **(b)** the NFC Method.

CHAPTER 4

Induction of Action Potential Dynamics by the Accumulation of Calcium and Sodium in Cardiac Myocytes

4.1 Introduction

Many biological systems exhibit complex oscillatory behaviors, such as bursting dynamics in neurons [DNHCG98, KS98, Izh00, SCC05, TSY+09, Rul02] and in pancreatic β-cells [KS98]. These complex behaviors emerge as a result of interactions between fast variables, which undergo rapid responses to stimuli, and slow variables or *memory*, which undergo slow changes over larger time windows. The role of memory itself in inducing complex dynamics has been widely studied in many scientific fields of research in biology, chemistry, and physics [Kan01, ASR98, YBS95, XFJ03].

In cardiac myocytes, fast and slow time scales can give rise to early afterdepolarizations (EADs) from a similar Hopf-homoclinic bifurcation mechanism as in neurons and β-cells [TSY+09]. Simplified iterated maps of action potential (AP) dynamics have been used and studied to reveal underlying mechanisms. The AP duration (APD) restitution is perhaps the simplest iterated map model used, in which

$$a_{n+1} = f(d_n), \tag{4.1}$$

where a_{n+1} is the APD of the $(n+1)^{\text{st}}$ AP, and d_n is the diastolic interval (DI)

of the preceding beat, defined to be the duration of time between the end of the previous AP and the initiation of the next AP. For a periodically driven cell with period T, $T = a_n + d_n$, and so

$$a_{n+1} = f(T - a_n). \tag{4.2}$$

Eq. (4.2) has been widely used to investigate APD dynamics under periodic stimulation [CGJJ90, VCMJ90, WOGJ95, GWSG84, Kar94, QSW07]. However, this model neglects the effects of short- and long-term memory effects. The effects of memory on cardiac alternans have been investigated in previous studies, which have shown that memory can suppress alternans [OGJ97, FBGJ02, KTS+05, TSGK03, FRD+03, TRGG04, CF04, BQK+07, GCGJ+13, MJT08, WMT15]. In recent studies, we have shown that memory can actually promote instabilities [LGWQ17, LQ18b, LQ18a].

Experiments [SXN+10, PC90] and simulations [SXN+10, LKMGG07] have demonstrated that APs can have spontaneous fluctuations of EADs and no EADs. In these demonstrations, a sequence of consecutive APs will have EADs for a certain number of beats, followed by consecutive APs without EADs for another number of beats. A study by Xie *et al.* [XLG+15] proposes a mechanism by which this so-called *intermittent EAD behavior* can occur. Namely, positive feedback between APD and intracellular calcium concentration ($[Ca^{2+}]_i$) results in two stable states - one state with stable APs without EADs, and the other with stable EADs. Simultaneously, negative feedback between APD and intracellular sodium concentration ($[Na^+]_i$) acts as a bistable on-off switch, transitioning the system from one stable state to the other. It is postulated that intermittent EAD behavior occurs since $[Na^+]_i$ changes very slowly on a much longer time scale compared to changes in $[Ca^{2+}]_i$. A study by Krogh-Madsen *et al.* [KMC17] show that intermittent EAD behavior due to slow $[Na^+]_i$ accumulation can lead to spiral wave reentry and arrhythmogenesis.

In this study, we analyze complex excitation patterns in a cardiac AP model with EADs, demonstrating intermittent EAD behavior. We develop a simplified two-dimensional iterated map model of $[Ca^{2+}]_i$ and $[Na^+]_i$ that well captures the behaviors from the AP model. Stability analyses show that the degree of APD-to-Ca^{2+} feedback and the time constant of $[Na^+]_i$ accumulation dictate the complex dynamics of the model via a Hopf bifurcation. Finally, we show that a key mitigator in controlling feedback with $[Ca^{2+}]_i$ is the sodium/calcium exchanger, I_{NCX}, and controlling the degree of I_{NCX} will modify EAD dynamics. Reduction of I_{NCX} activity can lead to negative APD-to-Ca^{2+} feedback and result in a period-2 doubling bifurcation.

4.2 Methods

Simulations of APs were carried out in a single cell with the equation of voltage (V) as

$$C_m \frac{dV}{dt} = -I_{\mathrm{ion}} + I_{\mathrm{sti}}, \tag{4.3}$$

where $C_m = 1\,\mu\mathrm{F/cm^2}$ is the membrane capacitance, I_{ion} is the total ionic current density, and I_{sti} is the stimulus current density, which is a 2 ms square pulse of amplitude $-52\,\mu\mathrm{A/cm^2}$. $I_{\mathrm{ion}} = I_{\mathrm{Na}} + I_{\mathrm{K1}} + I_{\mathrm{to}} + I_{\mathrm{Kr}} + I_{\mathrm{Ks}} + I_{\mathrm{Ca,L}} + I_{\mathrm{NCX}} + I_{\mathrm{NaK}} + I_{\mathrm{pCa}} + I_{\mathrm{pK}} + I_{\mathrm{bCa}} + I_{\mathrm{bNa}}$, in which the formulations of the currents are from the 2004 ten Tusscher *et al.* (TP04) model [tTNNP04]. We made a number of changes to the TP04 model in order to induce EADs. We remove I_{to} and I_{Kr} (i.e. by setting the maximum conductances $G_{\mathrm{to}} = G_{\mathrm{Kr}} = 0\,\mathrm{mS/cm^2}$) and reduce the maximum conductance of I_{Ks} to $G_{\mathrm{Ks}} = 0.125\,\mathrm{mS/cm^2}$. The formulation of $I_{\mathrm{Ca,L}}$ is substituted by the formulation described by Huang *et al.* [HKK+16], in which

$$I_{\mathrm{Ca,L}} = G_{\mathrm{Ca,L}} \cdot d \cdot f \cdot f_{\mathrm{Ca}} \cdot i_{\mathrm{Ca,L}}, \tag{4.4}$$

where $G_{\mathrm{Ca,L}} = 0.000\,14\,\mathrm{mS/cm^2}$, $f_{\mathrm{Ca}} = \frac{1}{1+\frac{c_i}{0.6}}$ is the intracellular Ca^{2+}-dependent inactivation gating variable taken from Zeng *et al.* [ZLRR95], and $i_{\mathrm{Ca,L}}$ is the

unitary current of the channel. Intracellular potassium concentration $[K^+]_i$ is set and clamped at 138 mM. The maximum conductance of I_{NCX} is set to $k_{NCX} = 5\,\text{nA/pF}$.

Single cell simulations were performed using a custom-made integration solver in C++ using a time-adaptive forward Euler method. The time step is $\Delta t = 0.05\,\text{ms}$ if the change in voltage $\Delta V < 0.1\,\text{mV}$, otherwise the time step is $\Delta t = 0.005\,\text{ms}$. APD is defined numerically as the duration of time an AP's voltage $V > -75\,\text{mV}$. Cells are paced periodically with period T, so that I_{sti} is applied every T s.

4.3 Results

At a pacing period of $T = 2.4\,\text{s}$, the AP model undergoes intermittant EAD behavior. Fig. 4.1(a) shows APD as a function of the beat number. APD cycles about every 75 beats, where 25 of those beats are consecutive APs with EADs (APD $> 0.8\,\text{s}$) and the other 50 are consecutive APs without EADs (APD $< 0.8\,\text{s}$). The inlets in Fig. 4.1(a) show representative APs with and without EADs.

Fig. 4.1(b) is a bifurcation diagram of the AP model, with the x-axis the pacing period T and the y-axis is APD. Pacing periods $T < 2.35\,\text{s}$ give rise to stable APs without EADs, whereas $T > 3.4\,\text{ms}$ give rise to stable APs with EADs. In the intermediate range $2.35\,\text{ms} < T < 3.4\,\text{s}$, the AP model is unstable and undergoes intermittant EAD behavior. Instability arises via a subcritical Hopf bifurcation.

Based on our earlier work [LQ18b], we deduced that APDs in the $[Na^+]_i-$clamped TP04 model depend on diastolic $[Ca^{2+}]_i$ in which

$$a_n = g(c_n), \tag{4.5}$$

where a_n is the APD of the n^{th} beat, and c_n is diastolic $[Ca^{2+}]_i$ immediately preceding the n^{th} AP. Here, $[Na^+]_i$ is unclamped, so we consider the dependence

of APD on $[Na^+]_i$ in addition to $[Ca^{2+}]_i$, i.e.,

$$a_n = g(c_n, s_n), \tag{4.6}$$

where a_n and c_n are as before, and s_n is diastolic $[Na^+]_i$ immediately preceding the n^{th} AP.

We determine the dependence of APD on $[Ca^{2+}]_i$ and $[Na^+]_i$ based on results from the AP model. Fig. 4.1(c) shows a contour plot illustrating the dependence of APD on diastolic $[Ca^{2+}]_i$ and $[Na^+]_i$. $[Na^+]_i$, in mM, is on the x-axis, and $[Ca^+]_i$, in nM, is on the y-axis. Colors closer to yellow/red indicate larger APDs, and the contours indicate curves of equal APDs. Four equi-APD curves are highlighted: 0.62, 0.65, 0.70, and 0.75 s. Since the equi-APD curves are nearly straight lines (with some small deviations), we consider APD to be dependent on a variable Z that is a linear combination of $[Ca^{2+}]_i$ and $[Na^+]_i$:

$$Z = [Na^+]_i - \alpha[Ca^{2+}]_i, \tag{4.7}$$

where Z is a constant that uniquely determines each equi-APD curve. Based on the data, we approximate $\alpha = 0.013$, and suppose there is a function g such that

$$\text{APD} = g(Z) = g\left([Na^+]_i - \alpha[Ca^{2+}]_i\right). \tag{4.8}$$

Fig. 4.1(d) shows the dependence of APD on Z. The data from the AP model is nearly one-to-one, showing that nearly every unique value of Z corresponds to one APD. In addition, at around $Z = 10.9$, there is a sharp transition from longer APDs ($Z < 10.9$) to shorter APDs ($Z > 10.9$). Since APD is nearly everywhere a decreasing function of Z, when $\alpha > 0$, an increase in $[Ca^{2+}]_i$ causes APD to increase. Conversely, when $\alpha < 0$, an increase in $[Ca^{2+}]_i$ causes APD to decrease. In other words, α determines the feedback between APD and Ca^{2+}: $\alpha > 0$ models positive feedback and $\alpha < 0$ models negative feedback.

Next we determine how $[Ca^{2+}]_i$ and $[Na^{2+}]_i$ accumulate or decay from one AP to the next. Generally, $[Ca^{2+}]_i$ and $[Na^+]_i$ tend to accumulate during the AP

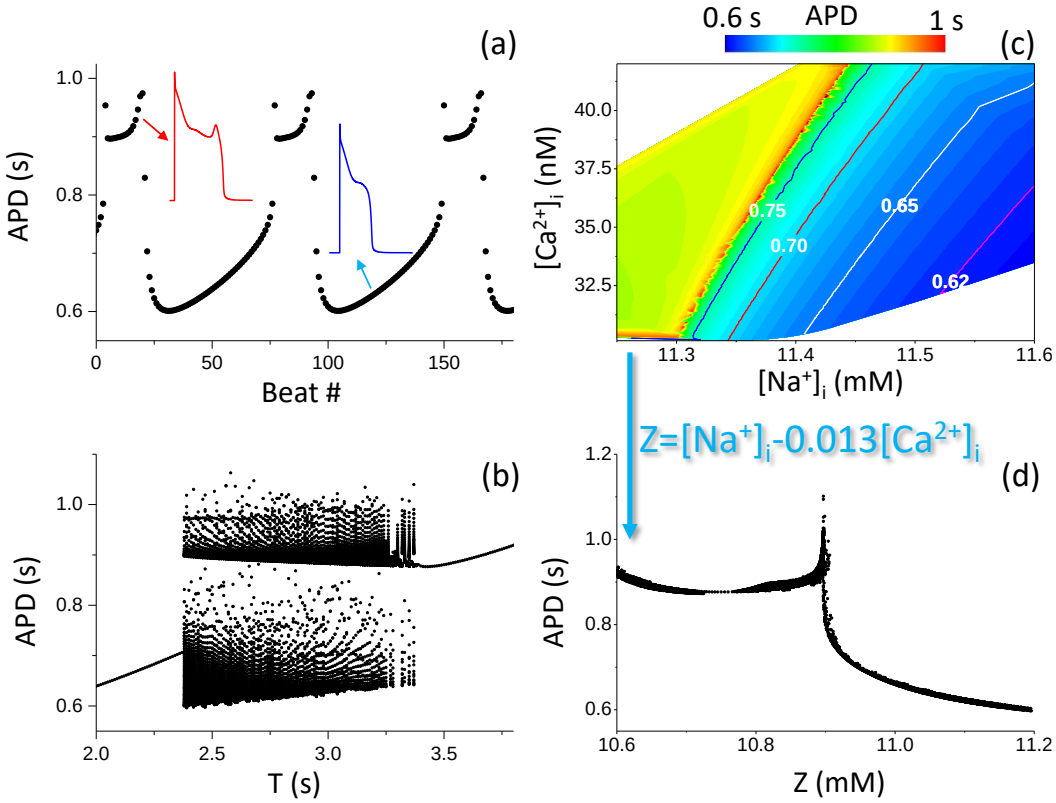

Figure 4.1: Dynamics and properties of the AP model undergoing EADs. **(a)**. APD series under constant pacing with period $T = 2.4\,\mathrm{s}$. APs cycle between a series of 25 consecutive EADs (APD $> 0.8\,\mathrm{s}$) followed by a series of 50 APs without EADs (APD $< 0.8\,\mathrm{s}$). **(b)**. APD bifurcation diagram. **(c)**. Contour plot showing the dependence of APD on diastolic $[\mathrm{Na}^+]_i$ and $[\mathrm{Ca}^{2+}]_i$. Contours are equi-APD curves where the APD is constant. Equi-APD curves at 0.62, 0.65, 0.70, and 0.75 s are highlighted. **(d)**. Dependence of APD on $Z = [\mathrm{Na}^+]_i - \alpha[\mathrm{Ca}^{2+}]_i$ with $\alpha = 0.013$. There is a nearly one-to-one correspondence between APD and Z.

and decay during the DI, so we assume that longer APDs will tend to increase the concentrations. Furthermore, as had been demonstrated previously [LQ18b], a sudden switch from a small APD to a large APD will cause the ionic concentrations to increase exponentially towards a larger steady state. We model this in the following form:

$$c_{n+1} - \bar{c}(a_n) = (1 - \beta_c)(c_n - \bar{c}(a_n)), \tag{4.9}$$

$$s_{n+1} - \bar{s}(a_n) = (1 - \beta_s)(s_n - \bar{s}(a_n)), \tag{4.10}$$

where $\bar{c}(\text{APD})$ and $\bar{s}(\text{APD})$ are steady state $[Ca^{2+}]_i$ and $[Na^+]_i$ levels for a given APD, and β_c and β_s are rate parameters which determine how rapidly or slowly $[Ca^{2+}]_i$ and $[Na^+]_i$ accumulate (or decay) towards steady state concentrations. As β_c or β_s approaches zero, the accumulation rate decreases. Setting β_c or β_s to zero is equivalent to the corresponding concentration being held constant, or clamped. In general we assume $1 > \beta_c \gg \beta_c > 0$ since $[Ca^{2+}]_i$ change is much faster than $[Na^+]_i$ change. We approximate $\bar{c}$ and $\bar{s}$ to be linearly dependent on APD, so that

$$\bar{c}(\text{APD}) = c_1 \text{APD} + c_0 \tag{4.11}$$

$$\bar{s}(\text{APD}) = s_1 \text{APD} + s_0, . \tag{4.12}$$

Based on results from the AP model, we set parameter values to

$$c_1 = \frac{0.2}{T + 2.1},\ c_0 = 0, s_1 = \frac{0.03}{T + 2.8},\ s_0 = 7,$$
$$\beta_c = 0.32,\ \beta_s = 0.01,\ \alpha = 0.13, \tag{4.13}$$

where T is the pacing period (in seconds). The inverse relations between T and s_1 or c_1 are consistent with a larger pacing period decreasing ionic concentrations due to there being a larger DI. It is worthwhile to also denote

$$\tau_s \equiv \frac{1}{\beta_s}. \tag{4.14}$$

In τ_s beats, if τ_s is large enough, then $[Na^+]_i$ is approximately $\frac{1}{e} = 36.79\%$ closer to steady state. In the model, $\tau_s = \frac{1}{0.01} = 100$.

Putting everything together, we have the following two-dimensional iterated map of APD, $[Ca^{2+}]_i$, and $[Na^+]_i$:

$$Z = s_n - \alpha c_n \tag{4.15}$$

$$\bar{c} = c_1 a_n + c_0 \tag{4.16}$$

$$\bar{s} = s_1 a_n + s_0 \tag{4.17}$$

$$a_n = g(Z) \tag{4.18}$$

$$c_{n+1} - \bar{c} = (1 - \beta_c)(c_n - \bar{c}) \tag{4.19}$$

$$s_{n+1} - \bar{s} = (1 - \beta_s)(s_n - \bar{s}). \tag{4.20}$$

We first use a function g that matches the data in Fig. 4.1(d) by choosing a linear interpolation of points manually chosen in the data set to assure a one-to-one correspondence between APD and Z. Fig. 4.2 shows results of the iterated map model (Eqs. (4.15)-(4.20)). Fig. 4.2(a) shows a bifurcation diagram of APD against T, which closely resembles the bifurcation diagram from the AP model (Fig. 4.1(b)). Setting $T = 2.5\,\mathrm{s}$, we plot APD, $[Ca^{2+}]_i$, and $[Na^+]_i$ against beat number from the iterated map model (Fig. 4.2(b)), and compare with results from the AP model with the same T (Fig. 4.2(c)). In both cases, APD cycles between large values (APs with EADs) and smaller values (APs without EADs). Both APD and $[Ca^{2+}]_i$ increase or decrease together, confirming positive APD-to-Ca^{2+} feedback. Concurrently, $[Na^+]_i$ increases with larger APDs and decrease with smaller APDs, changing directions precisely when APD switches from low to high or high to low. This suggests that, indeed, $[Na^+]_i$ acts a "switch" that modulates when APD goes from the high APD region to the low one, and vice versa. When EADs are occurring, $[Na^+]_i$ slowly accumulates until some point when the larger $[Na^+]_i$ causes the APs to lose EADs and have smaller APDs. With the reduction in APD, $[Na^+]_i$ now slowly decays, until another point when the smaller $[Na^+]_i$ causes the APs to have EADs again and have larger APDs. This cycle continues indefinitely.

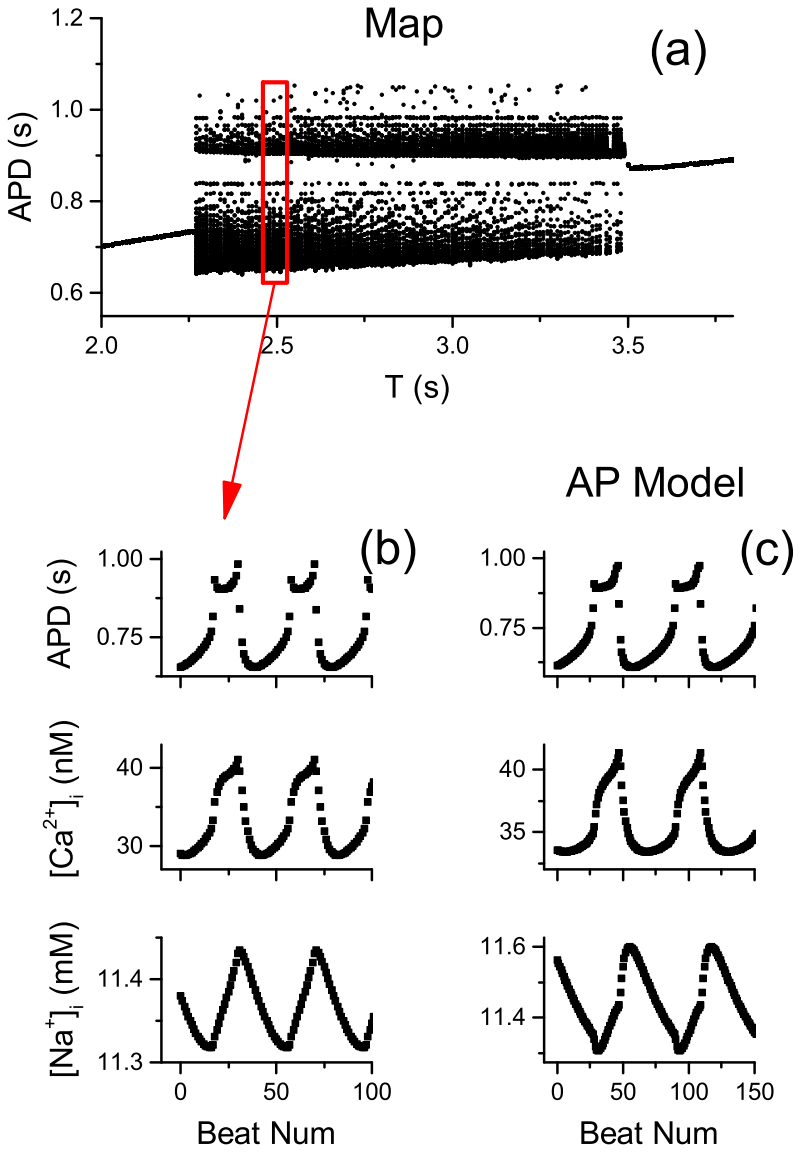

Figure 4.2: Dynamics of the iterated map model in Eqs. (4.15)-(4.20), compared to the AP model. The function g is derived from the curve in Fig. 4.1(d). **(a)**. APD bifurcation diagram. **(b)**. APD, $[Ca^{2+}]_i$, and $[Na^+]_i$ vs. beat number of the iterated map model, with $T = 2.5\,\text{s}$. **(c)**. APD, $[Ca^{2+}]_i$, and $[Na^+]_i$ vs. beat number of the AP model, with $T = 2.5\,\text{s}$.

We next perform a stability analysis of the iterated map model to understand how interactions between APD and the ionic concentrations can give rise to intermittent EAD behavior. For simplicity, we model g in Eq. (4.8) as a Hill function:

$$g(Z) = a_{\min} + \frac{a_{\max} - a_{\min}}{1 + \left(\frac{Z}{K_d}\right)^h}, \tag{4.21}$$

where $a_{\min}$ and $a_{\max}$ are values of the minimum and maximum values of APD, and K_d is the half-max value for Z, and h is the Hill coefficient. Based on Fig. 4.1(d), we approximate $a_{\min} = 0.6\,\text{s}$, $a_{\max} = 1.0\,\text{s}$, and $K_d = 10.9$, and initially set $h = 500$.

The Jacobian of the iterated map at steady state is

$$J = \begin{pmatrix} 1 - \beta_c - c_1\alpha\beta_c g' & c_1\beta_c g' \\ -s_1\alpha\beta_s g' & 1 - \beta_s + s_1\beta_s g' \end{pmatrix} \tag{4.22}$$

where $g' = g'(s^* - \alpha c^*)$ is the slope of g evaluated at the fixed point. The trace and determinant are

$$\tau = \text{tr } J = 2 - \beta_c - \beta_s + [s_1\beta_s - c_1\alpha\beta_c]\, g' \tag{4.23}$$

$$\Delta = \det J = (1 - \beta_c)(1 - \beta_s) + [s_1(1 - \beta_c)\beta_s - c_1\alpha(1 - \beta_s)\beta_c]\, g', \tag{4.24}$$

and the eigenvalues of J satisfy $\lambda = \frac{\tau}{2} \pm \sqrt{\left(\frac{\tau}{2}\right)^2 - \Delta}$. The iterated map is stable at the fixed point provided $|\lambda| < 1$ for both eigenvalues.

Fig. 4.3(a) shows bifurcation diagrams of the iterated map model (left panel) compared with the AP model (right panel) of APD versus $[\text{Na}^+]_i$. For the iterated map, $[\text{Na}^+]_i$ was fixed at different values and "clamped" by setting $\beta_s = 0$. Fixed points were calculated, and stability of the fixed points were determined by computing the eigenvalues.

Results indicate the existance of a supercritical Hopf bifurcation. In the range of $[\text{Na}^+]_i$ values between 11.32 and 11.4 mM, the map has 2 stable fixed points

(black line) and 1 unstable fixed point (blue dotted line). Outside that range, the map has 1 stable fixed point. This agrees with results from the AP model (right panel of Fig. 4.3(a)), showing that APDs are also bistable for a certain range of $[Na^+]_i$ values. The curves were generated by setting and clamping $[Na^+]_i$ in the AP model first at 11 mM and slowly increasing the concentration 0.01 mM every 100 beats, then setting $[Na^+]_i$ at 11.5 mM and slowly decreasing the concentration 0.01 mM every 100 beats.

Because the model is undergoing a Hopf bifurcation, at the bifurcation point the eigenvalues have complex eigenvalues of the form $\lambda = a \pm bi$ with $|\lambda| = 1$. Since the map is two-dimensional, the determinant Δ is 1 at the bifurcation point, and thus

$$\lambda_{\text{crit}} = \frac{\tau}{2} \pm i\sqrt{1 - \left(\frac{\tau}{2}\right)^2}. \tag{4.25}$$

From Eq. (4.24) $\Delta = 1$ also gives the relation

$$-g' = S \equiv \frac{\beta_c + \beta_s - \beta_c\beta_s}{c_1\alpha(1-\beta_s)\beta_c - s_1(1-\beta_c)\beta_s}. \tag{4.26}$$

Fig. 4.3(b) plots the stability of the iterated map model dependent on $-g'$ and τ_s. The red curve is from Eq. (4.26), which is the Hopf bifurcation curve. Since $g' < 0$, when $-g' \geq S$ the map is unstable. Along the bifurcation curve,

$$\frac{\tau}{2} = 1 - \frac{\beta_c}{2} - \frac{\beta_s}{2} + \frac{s_1\beta_s - c_1\alpha\beta_c}{s_1\beta_s(1-\beta_c) - c_1\alpha\beta_c(1-\beta_s)} \frac{\beta_c + \beta_s - \beta_c\beta_s}{2}. \tag{4.27}$$

Taking λ_{crit} in the form $\lambda_{\text{crit}} = e^{\pm i\theta}$, then $\theta = \cos^{-1}\left(\frac{\tau}{2}\right)$. At the bifurcation point, θ is the frequency of oscillation, and so

$$P_{\text{crit}} = \frac{2\pi}{\cos^{-1}\left(\frac{\tau}{2}\right)} \tag{4.28}$$

is the period of oscillations at the Hopf bifurcation point.

We also calculate the period of the iterated map (Eqs. (4.15)-(4.20)) under the assumption that g is a step function, when $h \to \infty$ in Eq. (4.21). In this scenario, $-g' \to \infty$ at the fixed point when it is unstable. Here, $g(Z) = a_{\max}$

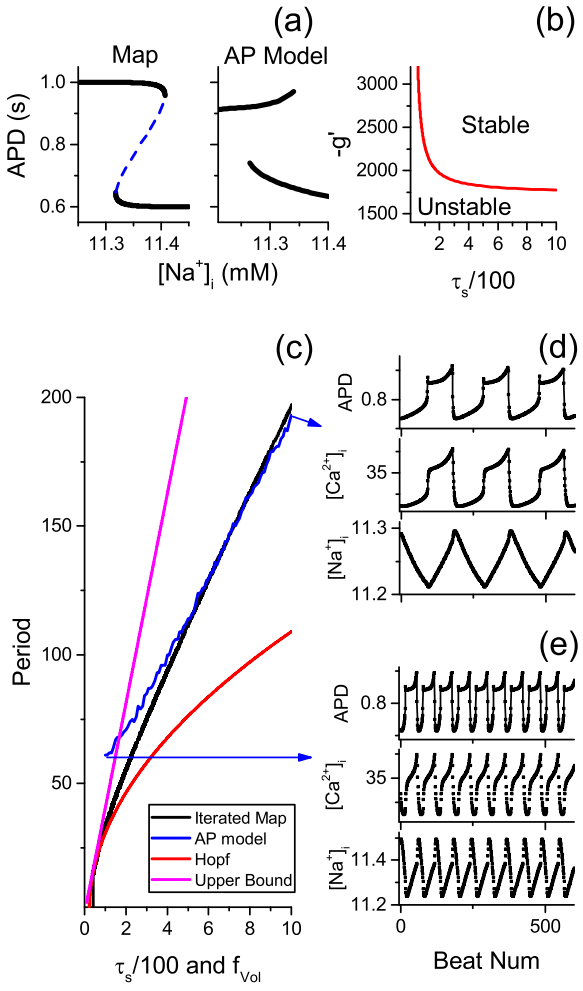

Figure 4.3: Properties of the iterated map model and AP model under positive APD-to-Ca^{2+} feedback. **(a)**. APD bifurcation diagrams of the iterated map model (left panel) and AP model (right panel) under clamped $[Na^+]_i$ values. In both cases, bistable APD regions emerge for a certain range of $[Na^+]_i$. **(b)**. Stability of the iterated map model dependent on $-g'$ and $\frac{\tau_s}{100}$. The red curve is the Hopf bifurcation curve, from Eq. (4.26). **(c)**. Period of APD oscillations of the iterated map model (blue line) and AP model (blue curve), and from theoretical calculations of the Hopf bifurcation in Eq. (4.28) (red curve) and from Eq. (4.31) (purple curve). For the AP model, the period is plotted against f_{Vol}, the factor controlling the volume of the cell (see Eq. (4.32)). For the other curves, the period is plotted again $\frac{\tau_s}{100}$. At control, $\frac{\tau_s}{100} = f_{\text{Vol}} = 1$. **(d)**. APD, $[Ca^{2+}]_i$, and $[Na^+]_i$ versus beat number of the AP model with $f_{\text{Vol}} = 10$ (10x volume in the control model). **(e)**. Same conditions as (d), but $f_{\text{Vol}} = 1$ (volume in the control model).

when $Z < K_d$, and $g(Z) = a_{\min}$ when $Z > K_d$. Assuming the map is undergoing oscillations between high APDs at $a_{\max}$ and low APDs at $a_{\min}$, we denote N_1 to be the number of iterations with high APDs and N_2 the number of iterations at low APDs. We also assume that at the transition from high APDs to low APDs, $Z = K_d$, and $[Ca^{2+}]_i$ has reached steady state at $\bar{c}(a_{\max})$, since $[Ca^{2+}]_i$ dynamics are much faster than that for $[Na^+]_i$. Similarly, $Z = K_d$ and $[Ca^{2+}]_i = \bar{c}(a_{\min})$ at the transition from low APDs to high APDs.

Based on these assumptions, the values of N_1 and N_2 are

$$N_1 = \frac{1}{\ln\left(\frac{\tau_s}{\tau_s - 1}\right)} \ln\left[\frac{1 - \frac{s_{\min} - \alpha c_{\max}}{K_d}}{1 - \frac{s_{\min} - \alpha c_{\min}}{K_d}}\right] \tag{4.29}$$

$$N_2 = \frac{1}{\ln\left(\frac{\tau_s}{\tau_s - 1}\right)} \ln\left[\frac{\frac{s_{\max} - \alpha c_{\min}}{K_d} - 1}{\frac{s_{\max} - \alpha c_{\max}}{K_d} - 1}\right], \tag{4.30}$$

where $c_{\min} = \bar{c}(a_{\min})$, $c_{\max} = \bar{c}(a_{\max})$, $s_{\min} = \bar{s}(a_{\min})$, and $s_{\max} = \bar{s}(a_{\max})$. Summing N_1 and N_2 gives the period under the condition that g is a step function: of oscillations:

$$P_{\text{step}} = \frac{1}{\ln\left(\frac{\tau_s}{\tau_s - 1}\right)} \ln\left[\frac{\left(1 - \frac{s_{\min} - \alpha c_{\max}}{K_d}\right)\left(\frac{s_{\max} - \alpha c_{\min}}{K_d} - 1\right)}{\left(1 - \frac{s_{\min} - \alpha c_{\min}}{K_d}\right)\left(\frac{s_{\max} - \alpha c_{\max}}{K_d} - 1\right)}\right] \tag{4.31}$$

Fig. 4.3(c) plots the period of oscillations in the iterated map model (black curve) with the theoretical predictions in Eq. (4.28) (red curve) and Eq. (4.31) (purple curve) as a function of τ_s. To test how $[Na^+]_i$ accumulation rates determine oscillations in the AP model, we modify the differential equation in the TP04 model by adding a parameter f_{Vol}:

$$\frac{d[Na^+]_i}{dt} = -C\frac{I_{\text{Na}} + I_{\text{bNa}} + 3I_{\text{NaK}} + 3I_{\text{NCX}}}{(f_{\text{Vol}} V_{\text{c}})F}, \tag{4.32}$$

where C is the membrane capacitance, V_{c} is the volume of the cell, and F is Faraday's constant. Setting $f_{\text{Vol}} = 1$ is equivalent to the original model. Increasing f_{Vol} has the effect of increasing the volume of the cell, and the absolute rate of

change of $[Na^+]_i$ decreases. This is analogous to increasing τ_s (or decreasing β_s) in the iterated map model, since increasing τ_s will slow the rate of accumulation of $[Na^+]_i$.

We plot the periods of APD oscillation in the AP model with f_{Vol} in the red curve of Fig. 4.3(c). Indeed, increasing f_{Vol} increases the period of oscillations roughly linearly. The plots of the period vs. τ_s in the iterated map model match fairly closely with the period vs. f_{Vol} in the AP model, especially when $\frac{\tau_s}{100}$ and f_{Vol} are greater than 5. Fig. 4.3(d) and (e) show APD versus beat number of the AP model with $f_{\text{Vol}} = 10$ (panel (d)) and $f_{\text{Vol}} = 1$ (panel (e)). The period of oscillations is about 190 when $f_{\text{Vol}} = 10$ and about 60 when $f_{\text{Vol}} = 1$. As predicted by the iterated map model, the accumulation and decay rate of $[Na^+]_i$ affect the period of oscillations, and therefore $[Na^+]_i$ accumulation is critical in APD dynamics. The theoretical predictions in Eq. (4.28) and (4.31) provide a lower and upper bound of the oscillation periods.

Our analysis thus far has assumed positive APD-to-Ca^{2+} feedback. We have demonstrated that in this setting, APD is bistable, and $[Na^+]_i$ accumulation can cause APD to oscillate between the two locally stable regimes. We next investigate how changing the feedback between APD and $[Ca^{2+}]_i$. In the iterated map, feedback is controlled by α. Fig. 4.4 (a)-(c) demonstrate the effects of changing α. Fig. 4.4(a) shows a stability phase plot of α against T, where the black regions indicate the iterated map is unstable. Two unstable regions emerge: the top region where $\alpha > 0.008$, and the bottom region where $\alpha < -0.025$.

The top region, where $\alpha > 0$, is the positive feedback regime, and APD undergoes oscillations (Fig. 4.4(b)) in a similar manner as the AP model in Fig. 4.3(d) and (e). In the bottom region, $\alpha < 0$, so APD is negatively coupled with $[Ca^{2+}]_i$. In this region, APD and $[Ca^{2+}]_i$ undergo rapid beat-to-beat oscillations. In contrast to the Hopf bifurcation occurring in the positive feedback scenario, here the map is undergoing a period-2 doubling bifurcation, as seen in simulations of the

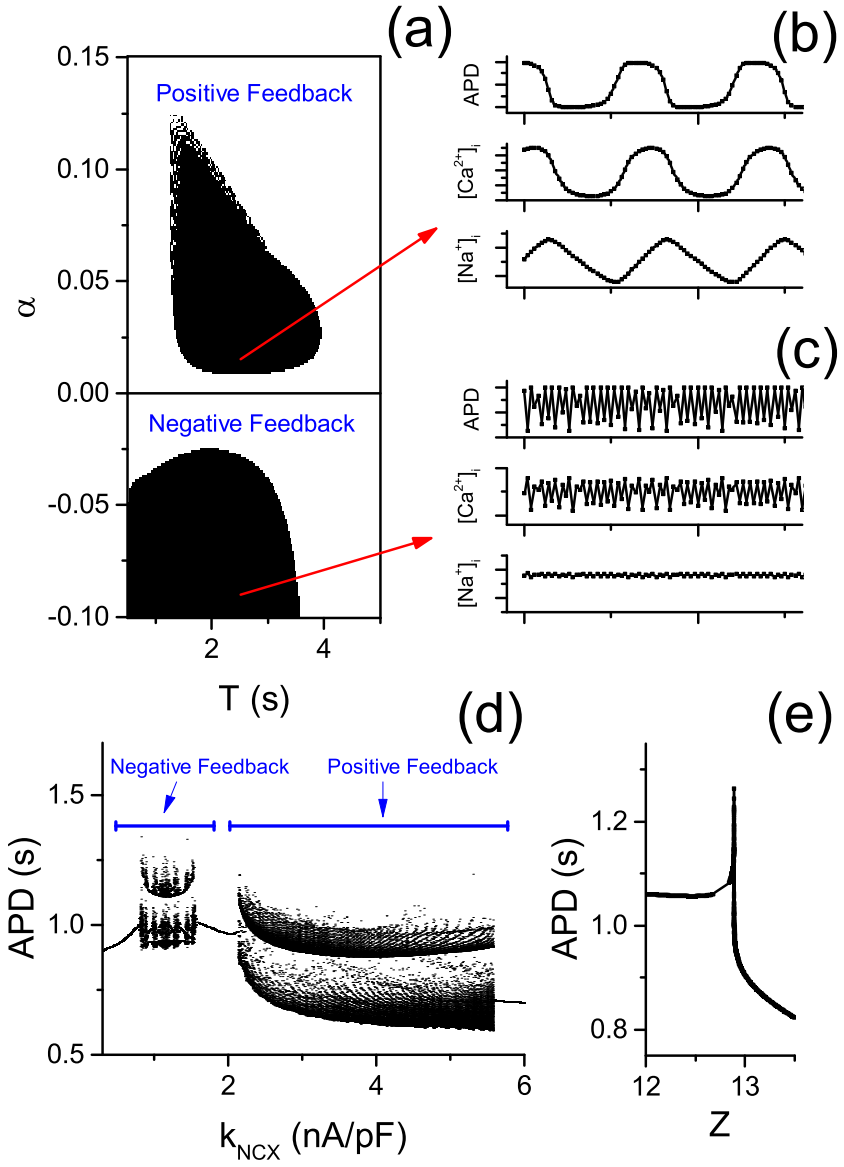

Figure 4.4: Dynamics under positive versus negative feedback. **(a)**. Stability of the iterated map model (Eqs. (4.15)-(4.20)) dependent on the feedback parameter α and T. **(b)**. APD, $[Ca^{2+}]_i$, and [Na+]$_i$ versus beat number with $\alpha = 0.013$ and $T = 2.5\,\mathrm{s}$. **(c)**. Same as (b) but with $\alpha = -0.08$. **(d)**. APD bifurcation diagram of the AP model with k_{NCX} varied. k_{NCX} is the maximum conductance of I_{NCX}. **(e)**. APD versus $Z = [\mathrm{Na}^+]_i - \alpha[\mathrm{Ca}^{2+}]_i$ with $\alpha = -0.025$ from the AP model with $k_{\mathrm{NCX}} = 1\,\mathrm{nA/pF}$. There is a fairly good one-to-one mapping of APD on Z. Since $\alpha < 0$, there is negative APD-to-Ca^{2+} feedback.

TP04 model with $[Na^+]_i$ clamped [LQ18b].

We now test the effects of APD-to-Ca^{2+} coupling on APD dynamics in the AP model. The degree of feedback between APD and $[Ca^{2+}]_i$ can be controlled by modifying the maximum conductance of I_{NCX}, k_{NCX}. Larger values of k_{NCX} increase the activity of I_{NCX} and increase APD-to-Ca^{2+} coupling. And conversely, decreasing k_{NCX} will decrease coupling. We vary k_{NCX} from 0 to 6 nA/pF in the AP model and plot APD, with $T = 2.5$ s. A bifurcation diagram of APD versus k_{NCX} is shown in Fig. 4.4(d). Two unstable regions emerge, one with $k_{NCX} > 2$ nA/pF, and the other with $k_{NCX} < 1.8$ nA/pF. The right region corresponds to intermittent EAD behavior, in which slow $[Na^+]_i$ accumulation causes a switch in APD from one bistable region to another, just as in Fig. 4.4(b). In the left region, APD undergoes rapid oscillations via a period-2 doubling bifurcation. With $k_{NCX} = 1$ nA/pF, APD is plotted against $Z = [Na^+]_i - \alpha[Ca^{2+}]_i$ with $\alpha = -0.025$ in Fig. 4.4(e). There is a nice one-to-one mapping between APD and Z, and $\alpha < 0$ suggests that indeed there is negative APD-to-Ca^{2+} feedback.

4.4 Discussion

In this study, we investigated the roles of Ca^{2+} and Na^+ concentration accumulation on action potential dynamics in cardiac myocytes under the condition of EADs. We confirm previous experimental and computational studies suggesting that intermittent EAD behavior, in which APs cycle between having EADs for a period of time followed by having no EADs, may be modulated by positive APD-to-Ca^{2+} feedback in conjunction with slow accumulation of $[Na^+]_i$ acting as a bistable switch. Recent studies have shown that slow $[Na^+]_i$ accumulation may also promote complex action potential dynamics and arrhythmias [XLG+15, KMC17].

From a simplified iterated map model that well capitulates findings in a dif-

ferential equation model of APs, we demonstrated that intermittent EAD behavior arises due to a supercritical Hopf bifurcation, in which the APD fixed point becomes unstable, and a limit cycle arises with oscillations in $[Ca^{2+}]_i$ and $[Na^+]_i$. The rate constant of $[Na^+]_i$ accumulation determines the frequency of oscillations, i.e., if $[Na^+]_i$ more slowly, then the series of consecutive APs having EADs (or lacking EADs) is larger. Finally, removing positive APD-to-Ca^{2+} feedback makes intermittent EAD behavior impossible, and negative APD-to-Ca^{2+} feedback can cause period-2 doubling bifurcations. Under negative APD-to-Ca^{2+} coupling, $[Na^+]_i$ plays no role, and complex APD dynamics can be explained by a simple 1-dimensional map model of Ca^{2+} and APD [LQ18b].

CHAPTER 5

Small-Conductance Ca^{2+}-Activated K^+ Channels Promote J-wave Syndrome and Phase 2 Reentry

5.1 Abstract

Background: Small-conductance calcium (Ca^{2+})-activated potassium (SK) channels play complex roles in cardiac repolarization and arrhythmogenesis under both physiological and pathophysiological conditions. However, the underlying mechanisms are not well understood. As SK channels are gated by intracellular Ca^{2+} only, we hypothesize that the conductance of SK channels tracks the intracellular Ca^{2+} transient, and thus the SK current (I_{SK}) behaves functionally like a transient outward K^+ current (I_{to}) to promote J-wave syndromes and arrhythmias.

Methods: Computer simulations of single cell and tissue models were used to investigate the role I_{SK} in promoting arrhythmias relevant to J-wave syndromes

Results: We show that if I_{SK} rises and decays rapidly during an action potential in a spike-like pattern in response to the intracellular Ca^{2+} transient (either because the whole-cell Ca^{2+} transient is inherently spike-like or because SK channels partially sense submembrane Ca^{2+}), it can mimic the functional behaviors of I_{to} to promote J-wave syndromes and related arrhythmias. Specifically, under the right conditions, I_{SK} can cause the all-or-none spike-and-dome action potential morphology and promote action potential duration alternans and complex chaotic dynamics in single cells. At the tissue-scale, I_{SK} can promote phase 2 reentry ei-

ther in the absence or presence of I_{to}. Our simulation results can account for the recent experimental finding that pharmacological activation of I_{SK} induced a J-wave syndrome and its arrhythmogenic consequences in rabbit hearts, and raise the possibility that I_{SK} may contribute to arrhythmogenesis in other forms of J-wave syndromes as well.

Conclusions: When the intracellular Ca^{2+} transient waveform sensed by SK channels is spike-like, I_{SK} can play functionally the role of I_{to}, which alone or combined with I_{to} can promote J-wave syndromes and the related arrhythmias, such as T-wave alternans and phase 2 reentry.

5.2 Introduction

Small-conductance Ca^{2+}-activated K^+ (SK) channels are widely expressed in a variety of cell types and play multiple biological roles, particularly in the nervous system where they regulate neuronal firing [FS03, AMS12]. The SK current (I_{SK}) is also present in atrial and ventricular myocytes under normal and diseased conditions [TXT+05, SPD+14, CCM+11, CTL+13, CHH+13, ZLC15, QDB+14]. Depending on experimental conditions [QDB+14], both proarrhythmic and antiarrhythmic effects of I_{SK} have been identified in experiments using apamin, a selective SK channel blocker. However, the underlying mechanisms are not well understood.

I_{SK} is activated by Ca^{2+} with a fast time constant on the order of a few milliseconds [HMAM98, XFR+98, BST+04, PMR+01], and thus its activation and deactivation time course tracks the intracellular Ca^{2+} transient. Depending on the profile of the Ca^{2+} transient, I_{SK} can rise and then decreases rapidly during the action potential (AP), making it behave functionally like a transient outward K^+ current (I_{to}). As shown in many previous studies, I_{to} can promote all-or-none early repolarization [GWP+00], complex arrhythmogenic AP dynamics such as

AP duration (APD) alternans and chaos [CR02, QXGW10, LGWQ17, LQ18b, LA93, MZL+06], and phase 2 reentry (P2R) [MCKM14, MKMC09, CPM+09, PCE10, BOCEF15] that are hallmarks of J-wave syndromes such as Brugada syndrome [AY15]. I_{to} can also facilitate the genesis of early afterdepolarizations when repolarization reserve is reduced [ZXW+12, CLT+18, NSX+15]. In a recent experimental study, Chen *et al.* [CXW+18] discovered that rabbit hearts exposed to a drug that activates I_{SK} while simultaneously inhibit the I_{Na} developed a J-wave syndrome leading to P2R and ventricular arrhythmias. Since I_{to} is very small in rabbits at normal heart rates, we hypothesized that this arrhythmogenic J-wave syndrome was related to the I_{to}-like properties of the activated I_{SK} current. In this study, we used computer simulations to test this hypothesis. We carried out simulations in single myocyte and one-dimensional (1D) cable models. In single myocytes, we investigated how the features of the intracellular Ca^{2+} transient impact the ability of I_{SK} to influence AP morphology and produce complex AP dynamics. In 1D cable simulations, we defined the conditions under which I_{SK} can either substitute for or synergize with I_{to} to produce complex APD dynamics leading to P2R. Our major conclusion is that when the Ca^{2+} transient is inherently spike-like or SK channels predominantly sense the spike-like submembrane Ca^{2+} transient waveform, the resulting rapid activation and deactivation of I_{SK} plays a comparable role to I_{to} in promoting complex AP dynamics and P2R. However, when I_{SK} is not spike-like and inactivates slowly, it influences repolarization in a manner similar to other time- and voltage-dependent K^+ currents such as I_{Kr}.

5.3 Methods

5.3.1 Action Potential Models

Simulations of single cells were carried out using the following differential equation:

$$C_m \frac{dV}{dt} = -I_{\text{ion}} + I_{\text{sti}}, \tag{5.1}$$

where V is the voltage and $C_m = 1\,\mu\text{F/cm}^2$ is the membrane capacitance. We used two AP models in this study: the human ventricular model by O'Hara *et al.* [OVVR11] (the ORd model) and the guinea pig ventricular AP model (a later version of the LRd model) by Faber and Rudy [FR00]. An I_{SK} current model was added to both AP models, described below. In addition, for P2R to occur in tissue, we followed Maoz *et al.* [MKMC09] to modify the LRd model by using the I_{to} formulation from Dumaine *et al.* [DTB+99], and the $I_{\text{Ca,L}}$ formulation from Miyoshi *et al.* [MMF+03] with the control p_{Ca} value 0.000 54 cm/s. Since replacing $I_{\text{Ca,L}}$ in the ORd model causes a big change in the AP morphology and APD, we only replaced the I_{to} formulation by the formulation from Dumaine *et al.* [DTB+99]. However, we were not able to observe P2R in tissue using the ROd model, and therefore, we only used LRd to simulate P2R in this study. The stimulus current I_{sti} was a $-34\,\mu\text{A/cm}^2$ square pulse for a duration of 2 ms in the ORd model, and a $-38\,\mu\text{A/cm}^2$ square pulse for a duration of 2 ms in the LRd model.

5.3.2 Modeling I_{SK}

Komendantov *et al.* [KKJC04] used a I_{SK} formulation to study neuronal firing as follows:

$$I_{\text{SK}} = G_{\text{SK}} \frac{1}{1 + \left(\frac{K_d}{[\text{Ca}^{2+}]}\right)^4} (V - E_{\text{K}}). \tag{5.2}$$

Here we modified the I_{SK} formulation fo Komendantov *et al.* to include a time-dependent gating variable, i.e.,

$$I_{\mathrm{SK}} = G_{\mathrm{SK}} x_{\mathrm{SK}} (V - E_{\mathrm{K}}) \tag{5.3}$$

where G_{SK} is the maximum conductance and E_{K} is the reversal potential. x_{SK} is the time-dependent gating variable, satisfying

$$\frac{dx_{\mathrm{SK}}}{dt} = \frac{x_{\mathrm{SK},\infty} - x_{\mathrm{SK}}}{\tau_{\mathrm{SK}}} \tag{5.4}$$

where $x_{\mathrm{SK},\infty}$ is a Hill function of Ca^{2+}, i.e.,

$$x_{\mathrm{SK},\infty} = \frac{1}{1 + \left(\frac{K_d}{[\mathrm{Ca}^{2+}]_{\mathrm{SK}}}\right)^n} \tag{5.5}$$

where $[Ca^{2+}]_{\mathrm{SK}}$ is the Ca^{2+} concentration sensed by SK channels. In the ORd model, we used

$$[\mathrm{Ca}^{2+}]_{\mathrm{SK}} = \alpha [\mathrm{Ca}^{2+}]_s + (1 - \alpha)[\mathrm{Ca}^{2+}]_i \tag{5.6}$$

where $[Ca^{2+}]_s$ is the submembrane Ca^{2+} concentration and $[Ca^{2+}]_i$ is the intracellular Ca^{2+} concentration. α is a parameter that determines a weighted contribution of the two concentrations. In the LRd model, we set $[Ca^{2+}]_{\mathrm{SK}} = [Ca^{2+}]_i$ since the model does not contain a submembrane Ca^{2+} compartment. In Eq. (5.5), n is the Hill coefficient, which we set at $n = 4$, in the range from 2 to 6 measured in experiments [CCM+11, HMAM98, XFR+98, BST+04, PMR+01, HMAM99]. Thus when $\tau_{\mathrm{SK}} = 0$, Eq. (5.3) is identical to Eq. (5.2). Based on experiments [CCM+11, HMAM98, XFR+98, BST+04, PMR+01, HMAM99], K_d is in the sub-μM range. For example, Chua *et al.* [CCM+11] found $K_d = 0.5\,\mu\mathrm{M}$ for normal ventricles and $K_d = 0.3\,\mu\mathrm{M}$ for failing ventricles. In this study, we used $K_d = 1\,\mu\mathrm{M}$ when implemented in the ORd model and $2\,\mu\mathrm{M}$ in the LRd model (see Discussion for the higher than experimentally observed K_d used in this study).

As for τ_{SK}, we plotted experimental data in Fig. 5.1 from different experiments (in different symbols) [HMAM98, XFR+98, BST+04, PMR+01]. Using their multi-state Markovian SK channel model, Hirschberg *et al.* [HMAM98] showed that τ_{SK}

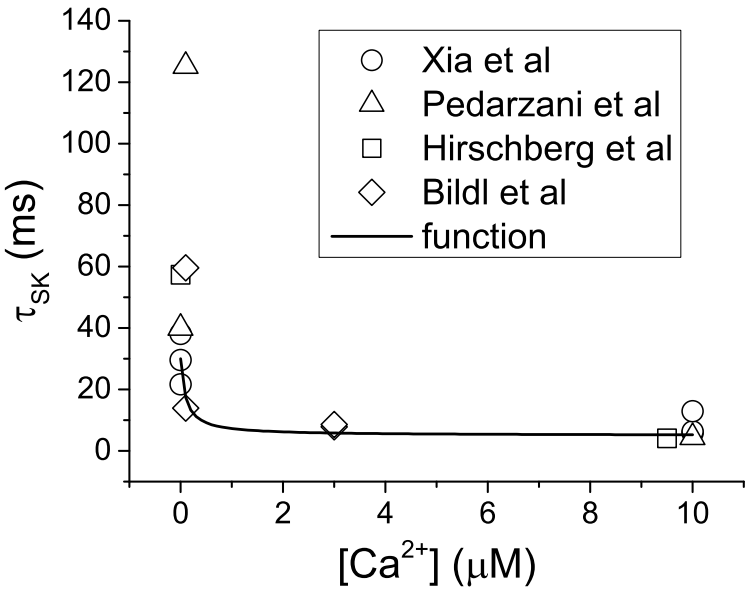

Figure 5.1: τ_{SK} versus intracellular Ca^{2+} concentration from different experiments and the mathematical model. Different symbols are data from different experiments [HMAM98, XFR+98, BST+04, PMR+01]. The line is a plot of the mathematical model of Eq. (5.7) with $\tau_0 = 5\,\mathrm{ms}$ and $\tau_1 = 25\,\mathrm{ms}$.

exhibits and inverse linear relationship with $[Ca^{2+}]$. In other words, τ_{SK} can be represented by a Hill function with a Hill coefficient of 1. Based on this observation, we formulated τ_{SK} as:

$$\tau_{\mathrm{SK}} = \tau_0 + \frac{\tau_1}{1 + \frac{[Ca^{2+}]_{\mathrm{SK}}}{0.1}}. \tag{5.7}$$

A plot of this function for $\tau_0 = 5$ and $\tau_1 = 25$ is shown in Fig. 5.1, which is well within the range of the experimental data.

5.3.3 1D Cable Model

1D cables were described by the following partial differential equation for voltage:

$$\frac{\partial V}{\partial t} = -\frac{I_{\mathrm{ion}}}{C_m} + D\frac{\partial^2 V}{\partial x^2}, \tag{5.8}$$

where $D = 0.001\,\mathrm{cm}^2/\mathrm{ms}$ is the diffusion constant describing the strength of gap junction coupling. The pseudo-ECG was calculated as:

$$\mathrm{ECG} = \int_0^{3.75\,\mathrm{cm}} D\nabla V \cdot \nabla \left(\frac{1}{r}\right) dx, \tag{5.9}$$

where $r = \sqrt{(x - x_p)^2 + y_p^2}$, x is a point in the cable, and $(x_p, y_p) = (3\,\mathrm{cm}, 0.9375\,\mathrm{cm})$ is the location of the pseudo-ECG electrode.

5.3.4 Numerical Methods

Single cell siulations were performed using a custom-made integration solver in C++ using a time-adaptive forward Euler method. The time step is $\Delta t = 0.05\,\mathrm{ms}$ if the change in voltage $\Delta V < 0.1\,\mathrm{mV}$, otherwise the time step is $\Delta t = 0.005\,\mathrm{ms}$.

Cable simulations were performed using a custom-made integration solver in CUDA, a programming language designed for graphical processing units (GPUs), using a time-adaptive forward Euler method. For each cell, the time step is $\Delta t = 0.025\,\mathrm{ms}$ if the change in voltage $\Delta V < 0.1\,\mathrm{mV}$, otherwise the time step is $\Delta t = 0.0025\,\mathrm{ms}$. Each cable consists of 300 cells, and the cell length corresponding to the spatial step is $\Delta x = 0.0125\,\mathrm{cm}$. No-flux boundary conditions are imposed.

5.4 Results

5.4.1 Ca^{2+}-Dependent I_{SK} Properties

The ORd model consists of both submembrane and cytosolic Ca^{2+} compartments. During an AP at a pacing cycle length (PCL) 1000 ms (Fig. 5.2(a)), the cytosolic Ca^{2+} concentration ($\approx 0.25\,\mu\mathrm{M}$, Fig. 5.2(b)) is much lower than the submembrane Ca^{2+} concentration ($\approx 7\,\mu\mathrm{M}$, Fig. 5.2(c)). When I_{SK} depends on $[Ca^{2+}]_i$ alone ($\alpha = 0$), the current amplitude is low and the duration is relatively broad (Fig. 5.2(d)). The Ca^{2+}-dependent activation time constant (τ_{SK}) has a

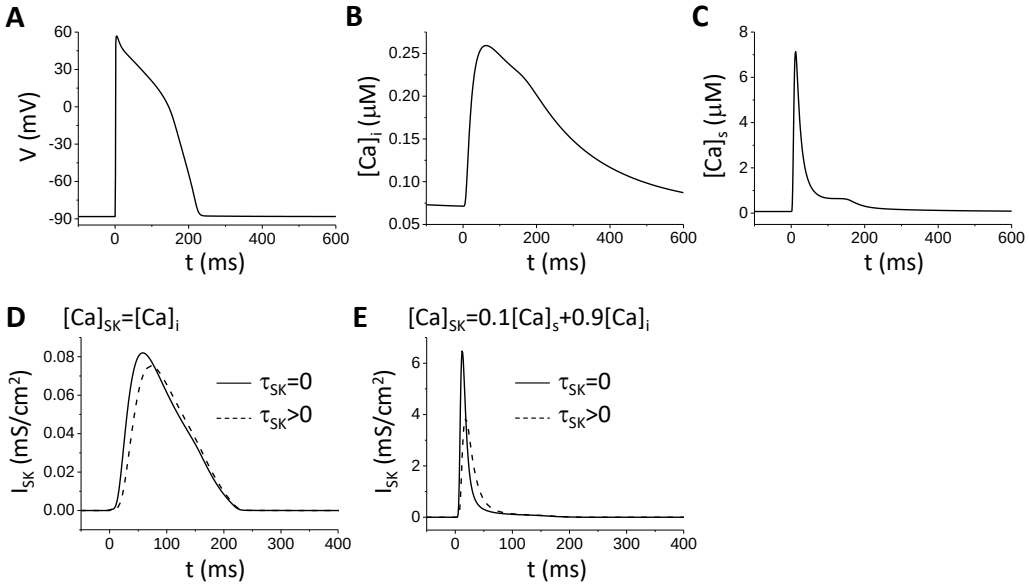

Figure 5.2: Ca-dependence of I_{SK} properties in the ORd model. **(a)**. Action potential of the ORd model at PCL = 1000 ms. **(b)**. Cytosolic Ca concentration versus time. **(c)**. Submembrane Ca concentration versus time. **(d)**. I_{SK} under AP clamp using the AP in (a) for $\tau_{\mathrm{SK}} = 0$ and τ_{SK} using Eq. (5.7). **(e)**. I_{SK} under AP clamp using the AP in (a) for $\tau_{\mathrm{SK}} = 0$ and τ_{SK} using Eq. (5.7).

small effect. If a fraction of the SK channels are assumed to be located near L-type Ca^{2+} channels in the membrane ($\alpha = 0.1$, equivalent to 10% of SK channels sensing submembrane rather than cytoplasmic Ca^{2+}), I_{SK} becomes much larger in amplitude and narrower (Fig. 5.2(e)), exhibiting a profile very similar to I_{to}. The Ca^{2+}-dependent activation time constant also has a much larger effect on reducing the current amplitude.

The LRd model does not consist of a submembrane Ca^{2+} compartment but an intracellular Ca^{2+} compartment. In the original model (thick lines in Fig. 5.3(a) and (b)), the intracellular Ca^{2+} transient has a relatively low amplitude and broad duration. If we increased the SERCA pump activity three-fold to mimic

β-adrenergic stimulation, however, the Ca^{2+} transient increased in amplitude and became much narrower and spike-like in appearance (thick lines in Fig. 5.3(a) and (b)), consistent with experimental observations [CZZ+10, BRK+04, KMS+16, AS14]. APD also lengthened slightly. Similarly, I_{SK} had a low amplitude and broad duration for the 1 × SERCA case (Fig. 5.3(c)), but became much larger and narrower when SERCA activity was tripled (Fig. 5.3(d)), resembling the I_{SK} properties in the ORd model shown in Fig. 5.2.

5.4.2 Effects of I_{SK} on Action Potential Morphology and Duration

We next carried out simulations to show how I_{SK} properties affect the AP morphology and duration for both the ORd model and the LRd model (Fig. 5.4). In the ORd model (Fig. 5.4(a)), APD decreased gradually as G_{SK} increased for the case in which I_{SK} depended solely on the cytoplasmic Ca^{2+} compartment (i.e. $\alpha = 0$). However, when 10% of I_{SK} sensed the submembrane Ca^{2+} ($\alpha = 0.1$), increasing I_{SK} initially increased APD and then abruptly decreased APD to very short values. This all-or-none early repolarization behavior was associated with a spike-and-dome AP morphology induced by I_{SK}, similar to the well-known effects of I_{to}. In the LRd model (Fig. 5.4(b)), comparable findings were obtained, with I_{SK} activation causing gradual APD shortening for the control SERCA value, but all-or-none repolarization when SERCA activity was increased 3-fold.

5.4.3 I_{SK} Promotes APD Alternans and Chaos

When I_{SK} was spike-like, it promoted APD alternans and more complex APD dynamics in the AP models, in the same way as previously demonstrated for I_{to} [QXGW10, LGWQ17, LQ18b, LA93]. Fig. 5.5 shows the simulation results from the ORd model. When I_{SK} was not spike-like (the $\alpha = 0$ case), no APD alternans occurred, and APD decreased gradually as G_{SK} increased (Fig. 5.5(a)).

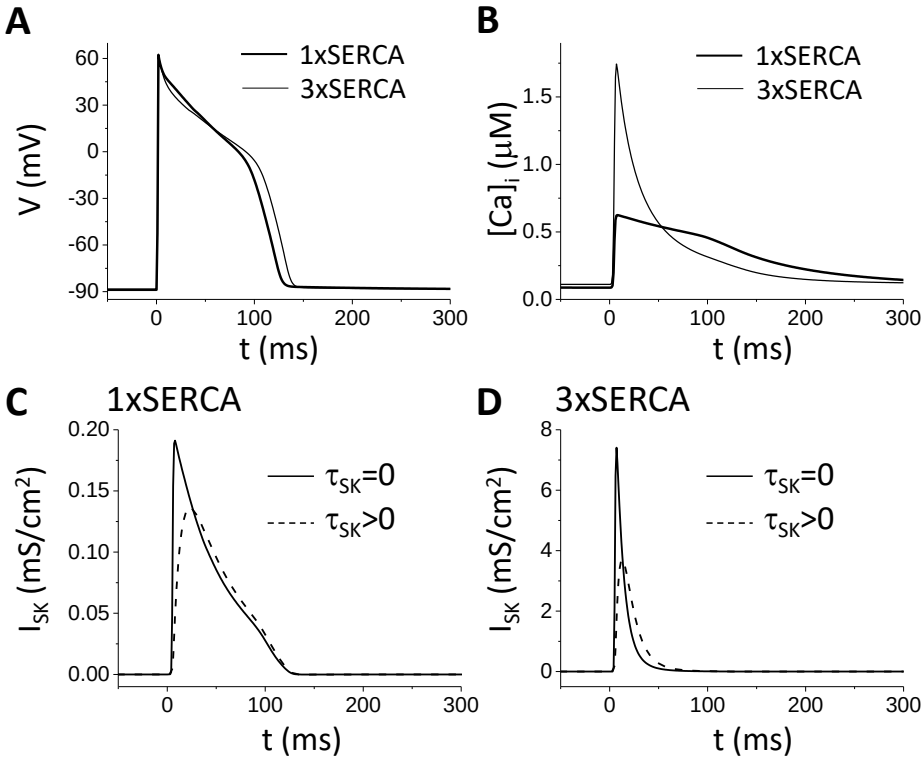

Figure 5.3: Ca-dependence of I_{SK} properties in the LRd model. **(a)**. Action potential of the LRd model at PCL = 1000 ms for control and 3 × SERCA. **(b)**. Cytosolic Ca concentrations versus time. **(c)**. I_{SK} under AP clamp using the AP in (a) for control SERCA with $\tau_{\mathrm{SK}} = 0$ and τ_{SK} using Eq. (5.7). **(d)**. I_{SK} under AP clamp using the AP in (a) for 3 × SERCA with $\tau_{\mathrm{SK}} = 0$ and τ_{SK} using Eq. (5.7).

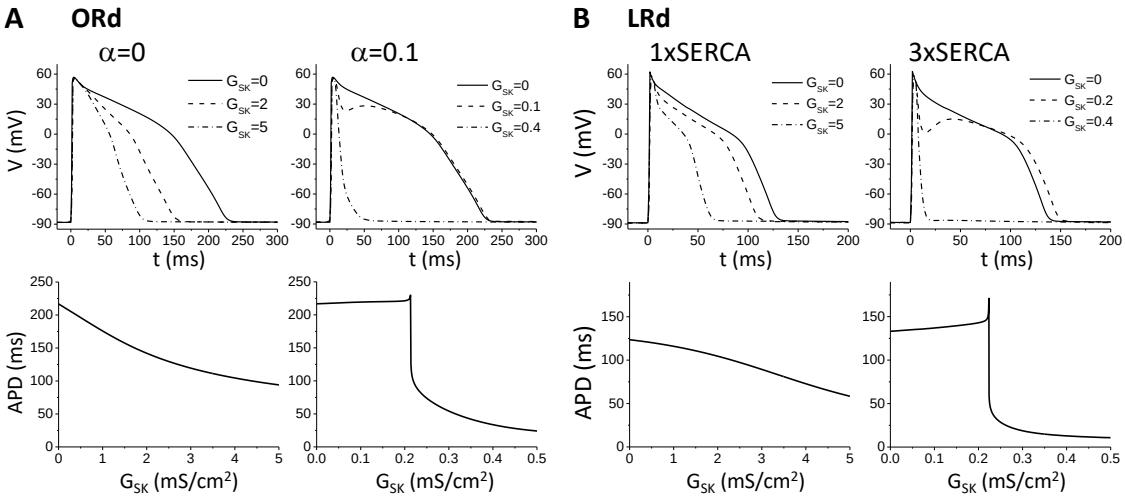

Figure 5.4: Effects of I_{SK} on AP morphology and APD. Upper panels are example APs for different levels of G_{SK} and lower panels are plots of APD versus G_{SK}. **(a)**. The ORd model with $\alpha = 0$ (left) and $\alpha = 0.1$ (right). **(b)**. The LRd model with the control SERCA activity (left) and $3 \times$ SERCA activity (right).

When I_{SK} was spike-like (the $\alpha = 0.1$ case), however, APD alternans as well as chaos occurred over a wide range of G_{SK}, from 0.05 to 0.55 $\mathrm{mS/cm^2}$ (Fig. 5.5(b)). As a reference, Fig. 5.5(c) compares the APD dynamics induced by I_{to} in the ORd model in the absence of I_{SK}. To systematically evaluate the roles of I_{SK} in promoting the APD dynamics, we scanned the parameter combinations of G_{SK} and G_{to} for complex APD dynamics under different conditions: $\alpha = 0$ (Fig. 5.5(d)), $\alpha = 0.1$ and $\tau_{\mathrm{SK}} = 0$ (Fig. 5.5(e)), and $\alpha = 0.1$ and $\tau_{\mathrm{SK}} > 0$ (Fig. 5.5(f)). When I_{SK} was not spike-like ($\alpha = 0$), no complex APD dynamics could be induced by I_{SK} in the absence of I_{to}. Moreover, I_{SK} suppressed the complex APD dynamics induced by I_{to} since the black region in Fig. 5.5(e) became smaller as G_{SK} increased. In contrast, when I_{SK} was spike-like ($\alpha = 0.1$), complex APD dynamics could be induced in the absence of I_{to}. In general, I_{SK} and I_{to} played complementary roles in promoting complex AP dynamics, such that when the sum of the two

currents was in the proper range, complex APD dynamics occurred. When the sum was too small or too large, APD was stable. To exclude the possibility that other K^+ currents could substitute for I_{SK}, we carried out the same simulations for parameter combinations of G_{to} and ΔG_{Kr} (Fig. 5.5(g)), where ΔG_{Kr} is the increase in the maximum conductance of I_{Kr} from its control value in the original model. In this case, no complex APD dynamics occurred in the absence of I_{to}.

We repeated the same simulations in the modified LRd model and observed the same behaviors (Fig. 5.6): I_{SK} did not promote complex APD dynamics for the control value of SERCA activity in which the Ca^{2+} transient and I_{SK} was not spike-like, but promoted complex dynamics when SERCA was increased 3-fold to produce a spike-like Ca^{2+} transient and I_{SK}.

Based on these simulations, we conclude that when I_{SK} is not spike-like, I_{SK} does not promote complex APD dynamics. In contrast, when I_{SK} is spike-like, APD alternans and more complex APD dynamics can occur even in the absence of I_{to}.

5.4.4 I_{SK} Promotes J-wave Syndromes and P2R

To examine whether the all-or-none early repolarization and complex APD dynamics induced by I_{SK} in isolated cells could result in P2R in tissue, we simulated 1D cables of 300 cells. We used both the ORd and LRd models, but since we could not induce P2R in the ORd model using either I_{to} or I_{SK}, we only show our results from the LRd model. We simulated two types of 1D cables: a cable consisting of cells mimicking ventricular transmural heterogeneity and a cable consisting of ventricular epicardial cells only.

In the cable simulating transmural heterogeneity, we reduced IKs by 50% in top half of the cable to mimic the mid-myocardial/endocardial cell layer. I_{to} or I_{SK} was added only to the bottom half of the cable to mimic the epicardial layer. The cable

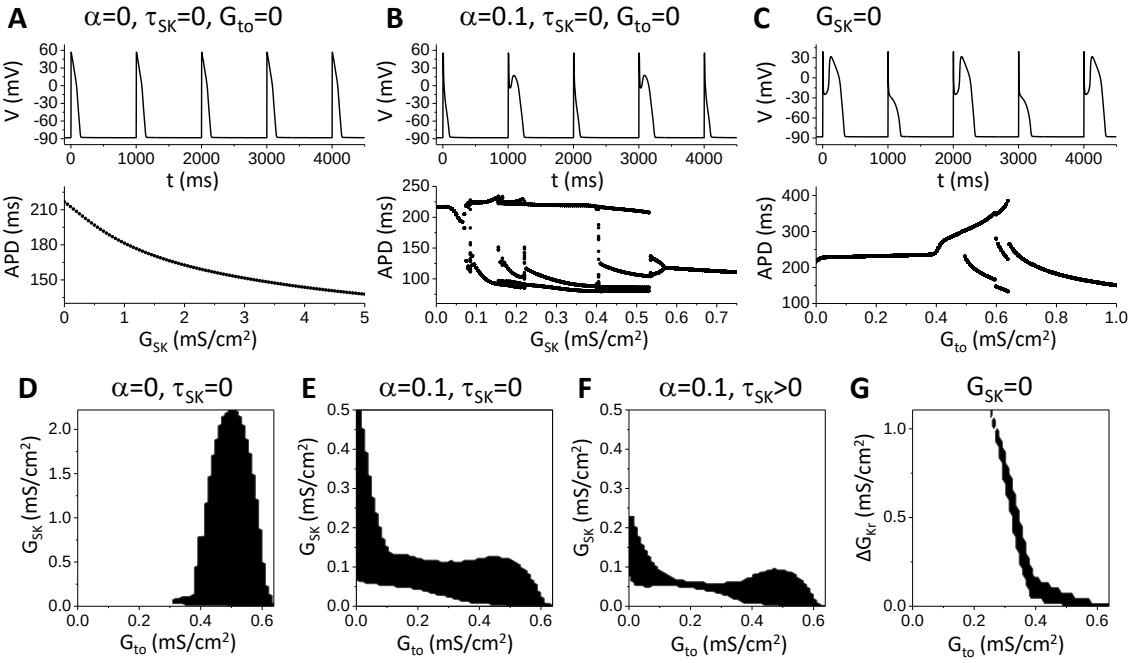

Figure 5.5: I_{SK} promotes complex APD dynamics in the ORd model. **(a)**. An example voltage trace (upper panel, $G_{\mathrm{SK}} = 5\,\mathrm{mS/cm^2}$) and APD versus G_{SK} (lower panel) for $\alpha = 0$ and $\tau_{\mathrm{SK}} = 0$. $G_{\mathrm{to}} = 0$. For each G_{SK} value, APDs from 50 beats are plotted. Since this case, no APD alternans and other complex APD dynamics, all 50 APDs are identical. **(b)**. Same as (a) but for $\alpha = 0.1$ and $\tau_{\mathrm{SK}} = 0$ (upper panel, $G_{\mathrm{SK}} = 0.15\,\mathrm{mS/cm^2}$). **(c)**. An example voltage trace (upper panel, $G_{\mathrm{to}} = 0.55\,\mathrm{mS/cm^2}$) and APD versus G_{to} (lower panel) in the absence of I_{SK}, i.e., $G_{\mathrm{SK}} = 0$. **(d)**. APD dynamics versus G_{SK} and G_{to} for $\alpha = 0$ and $\tau_{\mathrm{SK}} = 0$. The black region is where APD alternans and other complex dynamics occur. **(e)**. Same as (d) but $\alpha = 0.1$ and $\tau_{\mathrm{SK}} = 0$. **(f)**. Same as (d) but for $\alpha = 0.1$ and $\tau_{\mathrm{SK}} > 0$ (Eq. (5.7)). **(g)**. APD dynamics versus ΔG_{Kr} and G_{to} for $G_{\mathrm{SK}} = 0$. ΔG_{Kr} is the increase from the control G_{Kr} in the model. PCL = 1000 ms.

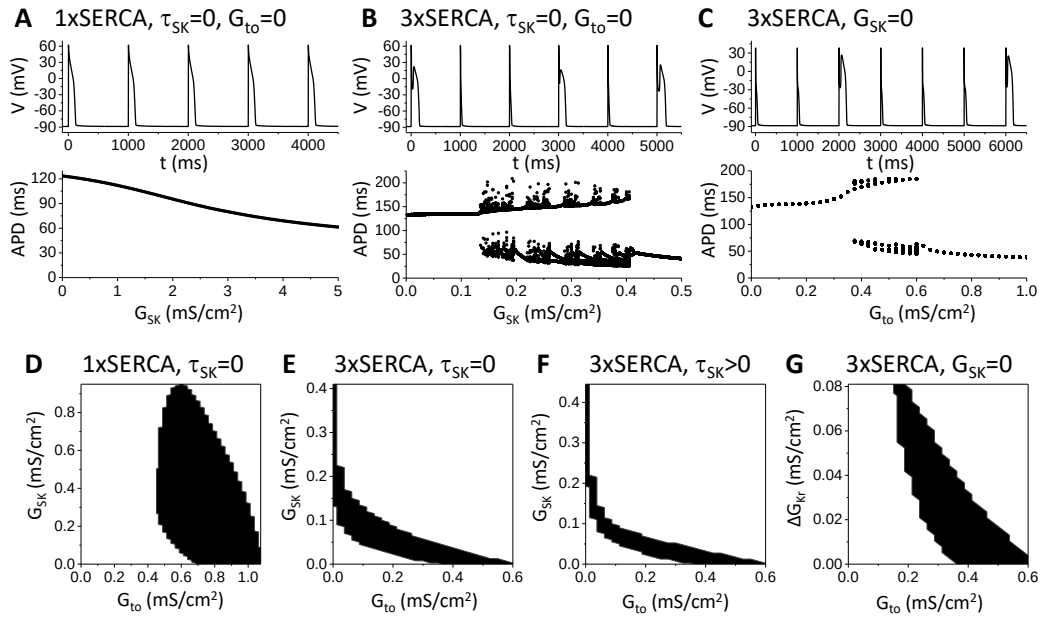

Figure 5.6: I_{SK} promotes complex APD dynamics in the LRd model. **(a)**. An example voltage trace (upper panel, $G_{\mathrm{SK}} = 0.5\,\mathrm{mS/cm^2}$) and APD versus G_{SK} (lower panel) for $1\times$ SERCA. $\tau_{\mathrm{SK}} = 0$, and $G_{\mathrm{to}} = 0$. **(b)**. Same as (a) but for $3\times$ SERCA. $G_{\mathrm{SK}} = 0.25\,\mathrm{mS/cm^2}$ for the upper panel. **(c)**. An example voltage trace (upper panel, $G_{\mathrm{to}} = 0.5\,\mathrm{mS/cm^2}$) and APD versus G_{to} in the absence of I_{SK}, i.e., $G_{\mathrm{SK}} = 0$. **(d)**. APD dynamics versus G_{SK} and G_{to} for $1\times$ SERCA and $\tau_{\mathrm{SK}} = 0$. The black region is where APD alternans and other complex dynamics occur. **(e)**. Same as (d) but for $3\times$ SERCA and $\tau_{\mathrm{SK}} = 0$. **(f)**. Same as (d) but for $3\times$ SERCA and $\tau_{\mathrm{SK}} > 0$ (Eq. (5.7)). **(g)**. APD dynamics versus ΔG_{Kr} and G_{to} for $G_{\mathrm{SK}} = 0$. ΔG_{Kr} is the increase from the control G_{Kr} in the model. PCL = 1000 ms.

was paced from the endocardial side (top) and pseudo-ECGs were recorded in the epicardial side (bottom). The left panel in Fig. 5.7(a) shows ECGs for three I_{to} levels in the epicardial region. As the maximum conductance of I_{to} increased, the J-point in the ECG became elevated due to the spike-and-dome AP morphology in the epicardial region (see middle panel). When the maximum conductance reached a threshold value ($G_{\text{to}} > 0.4\,\text{mS/cm}^2$), all-or-none early repolarization occurred in the epicardial region, resulting in P2R (right panel). P2R occurred for G_{to} from 0.4 to $1.5\,\text{mS/cm}^2$. For larger G_{to}, no P2R occurred even though the APD gradient was even larger. When we replaced I_{to} in the epicardial region by I_{SK}, we observed nearly identical behaviors (Fig. 5.7(b)) for the $3\times$ SERCA case. P2R occurred for G_{SK} from 0.1 to $0.2\,\text{mS/cm}^2$. However, when the SERCA activity was not enhanced (i.e., the control $1\times$SERCA case), the J-point elevation is only modest as G_{SK} increased (Fig. 5.7(c)). As the APD in the epicardial region became much shorter, a large upright T-wave occurred in the ECG. Despite the large APD gradient, however, no P2R occurred in this case. The same behavior was observed when I_{Kr} was increased in the epicardial region (Fig. 5.7(d)).

In the cable simulating epicardial cells only, we varied the maximal conductance of $I_{\text{Ca,L}}$ along the cable from the control value to 1.2 times the control value. All other currents, including I_{SK} or I_{to}, were uniform throughout the cable. We paced all cells in the cable simultaneously, mimicking the simultaneous activation of the epicardium during a sinus beat. This results in an APD difference of 10 ms at 1 s pacing in the absence of I_{to} and I_{SK}. The purpose of simulating this type of cable is two-fold. First, in an experimental study by Lukas and Antzelevitch [LA96], P2R occurs in the epicardium, indicating that transmural heterogeneity may not be necessary for P2R. Second, since we only added a small heterogeneity in the cable, the large APD gradient inducing P2R is mainly caused by the APD dynamics facilitated by the small heterogeneity. Fig. 5.8(a) shows an example in the LRd model of P2R induced by I_{to} without I_{SK}, while Fig. 5.8(b) shows

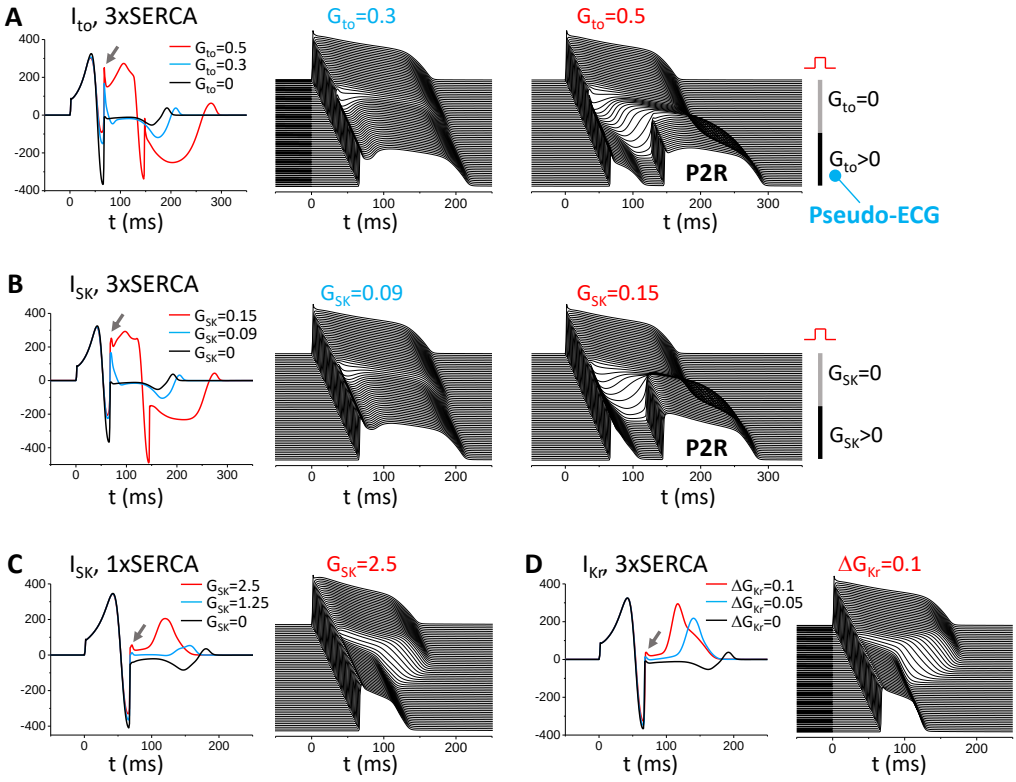

Figure 5.7: I_{SK} promotes J-wave elevation and P2R in 1D cable with transmural heterogeneities. The LRd model with $3 \times$ SERCA was used. The cable length is 300 cells. IKs was reduced by 50% in the top half of 150 cells to mimic the mid-myocardium/endocardial cells. I_{to} or I_{SK} was added only to the 150 cells in the bottom half of the cable. The pacing stimulus was applied to the endocardial end and the pseudo-ECG electrode was placed at the epicardial side as indicated in (a). **(a)**. I_{to} induced J-point elevation and P2R Left panel: Pseudo-ECG traces for three different G_{to} values as indicated. Arrow marks the J-point. Middle and right panels: 3D (V-space-time) plots for $G_{\mathrm{to}} = 0.3\,\mathrm{mS/cm^2}$ and $G_{\mathrm{to}} = 0.5\,\mathrm{mS/cm^2}$. **(b)**. I_{SK} induced J-point elevation and P2R. Left panel: Pseudo-ECG traces for three different G_{SK} values as indicated. Middle and right panels: 3D (V-space-time) plots for $G_{\mathrm{to}} = 0.3\,\mathrm{mS/cm^2}$ and $G_{\mathrm{to}} = 0.5\,\mathrm{mS/cm^2}$. **(c)**. Effects of I_{SK} on ECG when I_{SK} is not spiky, i.e., the $1 \times$ SERCA case. **(d)**. Effects of increasing I_{Kr} in the epicardial region on ECG. Note: Reentry cannot occur in a 1D cable. The extra-excitations labeled as P2R in (a) and (b) are PVCs. As shown in computer simulations, this type of PVC can degenerate into phase 2 reentry in heterogeneous tissue [MCKM14, CPM+09, BOCEF15], so we still label it as P2R.

an example of P2R induced by I_{SK} without I_{to}. To systematically evaluate the role of I_{SK} in promoting P2R, we scanned the parameter combinations for P2R in the same manner that we systematically evaluated the role of I_{SK} in promoting complex APD dynamics in single cells. Since the AP changes are very dynamic, P2R did not reliably occur after all beats for a given parameter set. Therefore, we paced 100 beats for each parameter set, and if P2R occurred in any of the 100 beats, we denoted the case as P2R. The results are shown in Figs. 5.8(c)-(f), demonstrating that when I_{SK} was spike-like (Figs. 5.8(d) and (e)), P2R could be induced by I_{SK} without the presence of I_{to}. I_{SK} and I_{to} again played complementary roles in promoting P2R. When I_{SK} was not spike-like (Fig. 5.8(c)), however, no P2R could be induced by I_{SK} in the absence of I_{to}. In this case, the effect of I_{SK} on P2R was similar to that of I_{Kr} (Fig. 5.8(f)). Note that the parameter regions of P2R are very similar to those that exhibited complex APD dynamics in the single cell simulations shown in Fig. 5.6, indicating that the complex APD dynamics play an important role in the genesis of P2R. Since the baseline APD heterogeneity was small and since I_{to} or I_{SK} were uniform throughout the cable, the large APD gradients during APD alternans and more complex APD dynamics induced by I_{to} or I_{SK} indicate that a large pre-existing heterogeneity is not needed. This agrees with the observation by Maoz *et al.* [MKMC09] that P2R can occur in a homogeneous 1D cable.

5.5 Discussion

The SK current (I_{SK}) is present in both atrial and ventricular myocytes under normal and diseased conditions [TXT+05, SPD+14, CCM+11, CTL+13, CHH+13, ZLC15, QDB+14] and has been shown to be proarrhythmic in some settings and antiarrhythmic in others [QDB+14]. Recently, pharmacologic I_{SK} activation with simultaneous I_{Na} suppression was shown to induce a J-wave syndrome leading

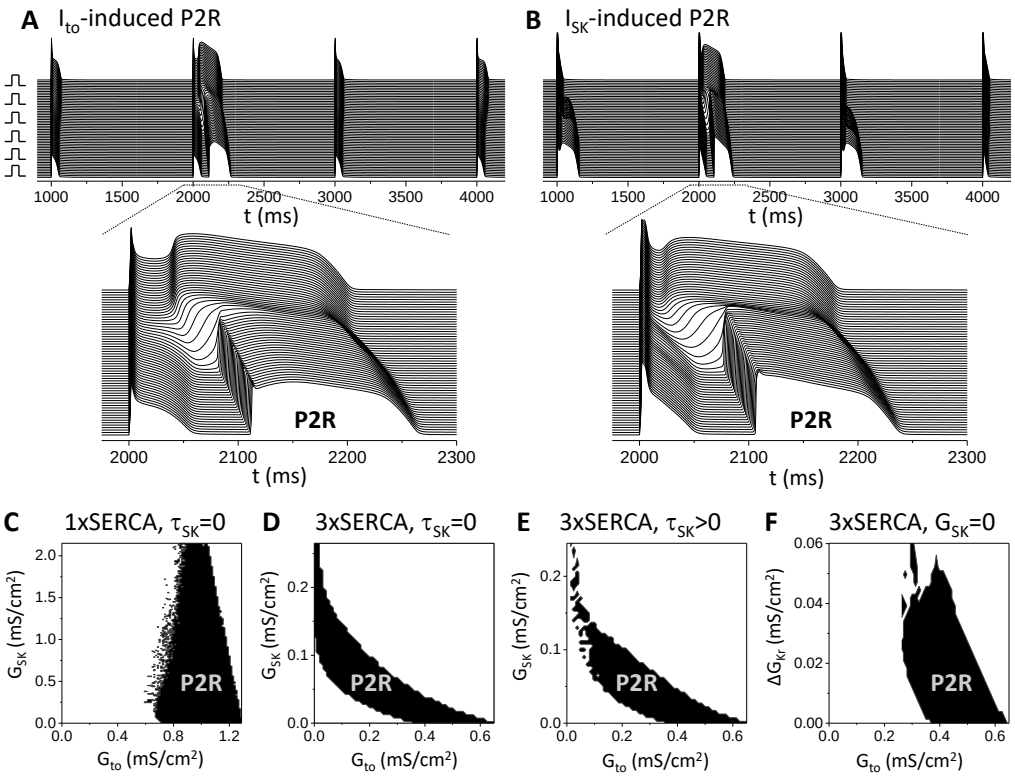

Figure 5.8: I_{SK} promotes phase 2 reentry in a cable consisting of epicardial cells only. The LRd model with $3 \times$ SERCA was used. The cable length is 300 cells and the cells were paced simultaneously at PCL = 1000 ms. The $I_{\mathrm{Ca,L}}$ heterogeneity was modeled by altering p_{Ca} as follows: $p_{Ca}(i) = 0.00054\left[1 + \frac{0.2}{1+e^{-(i-150)/5}}\right]$ in which $i = 1$ to 300 is the index of cells, which resulted in 10 ms difference in APD across the cable in the absence of I_{to} and I_{SK}. **(a)**. 3D (V-space-time) plots showing P2R induced by I_{to} in the absence of I_{SK}. $G_{\mathrm{to}} = 0.5\,\mathrm{mS/cm^2}$ and $G_{\mathrm{SK}} = 0$. Blowup is the beat with P2R. **(b)**. 3D (V-space-time) plots showing P2R induced by I_{SK} in the absence of I_{to}. $G_{\mathrm{to}} = 0$ and $G_{\mathrm{SK}} = 0.25\,\mathrm{mS/cm^2}$ and $\tau_{\mathrm{SK}} = 0$. Blowup is the beat with P2R. **(c)**. The window of P2R versus G_{SK} and G_{to}. The black region is where P2R occurs as indicated. Since the AP is very dynamic in both space and time, P2R does not occur at every beat of pacing. We record 100 beats for each parameter set, and if P2R occurs in any of the 100 beats, we label this parameter set as P2R in the parameter space. Because of this dynamic nature and the finite time intervals of simulation, the boundary between no P2R and P2R may not be smooth. For example, the left boundary in this plot would be smoother (more black dots will show up) if we run our simulations longer. **(d)**. Same as (c) but for $3 \times$ SERCA and $\tau_{\mathrm{SK}} = 0$. **(e)**. Same as (c) but for $3 \times$ SERCA and $\tau_{\mathrm{SK}} > 0$ (Eq. (5.7)). **(f)**. The window of P2R versus ΔG_{Kr} and G_{to} for $G_{\mathrm{SK}} = 0$.

to ventricular arrhythmias in isolated rabbit hearts [CXW+18]. Although I_{to} is thought to play a key role in most J-wave syndromes [AYA+16], rabbits have almost no I_{to} at physiological heart rates due to its slow recovery kinetics from inactivation. This suggests that I_{SK} may have substituted for I_{to} due to its similar transient behavior as it tracks the intracellular Ca^{2+} transient. In this study, we used computer modeling to investigate the conditions under which I_{SK} may substitute for I_{to} to produce I_{to}'s hallmark arrhythmogenic features of spike-and-dome AP morphologies, APD alternans and more complex APD dynamics in isolated cells and P2R in cardiac tissue. We show that when the intracellular Ca^{2+} transient is sufficiently spike-like to generate an I_{SK} that rises and decays rapidly like I_{to}, I_{SK} can generate all of these behaviors, either alone or in combination with I_{to}.

Thus, our results support the experimental findings reported in isolated rabbit hearts that I_{SK} induced an arrhythmogenic J-wave syndrome, despite the functional absence of significant I_{to}, provided that the Ca^{2+} transient sensed by the pharmacologically-activated rabbit SK channels has a spike-like waveform. We simulated this situation in the ORd model by assigning 10% of I_{SK} to sense the submembrane Ca^{2+} compartment and 90% to sense the bulk cytoplasmic Ca^{2+} compartment. The bulk cytoplasmic Ca^{2+} transient waveform can also vary depending on the state of SR Ca^{2+} loading of the cell. For example, experiments [CZZ+10, BRK+04, KMS+16, AS14] have shown that Ca^{2+} transients become much spikier after isoproterenol. We simulated this situation in the LRd model by increasing the SERCA pump three-fold to mimic the effects of β-adrenergic stimulation. In both models simulated in this study, I_{SK} became sufficiently spiky to induce all-or-none early repolarization, APD alternans and complex APD dynamics. Which scenario best explains the experimental observations in the isolated rabbit hearts? Those experiments were performed in the absence of beta-adrenergic stimulation, and isoproterenol suppressed the arrhythmias induced by

pharmacological activation of I_{SK}. Thus, it seems more likely that a portion of SK channels in rabbit hearts sense a spike-like Ca^{2+} transient in the submembrane space rather than the bulk cytoplasmic Ca^{2+} transient. This is supported by previous observations that SK channels are located in close proximity to L-type Ca^{2+} channels in the sarcolemma [ZCC+18] such that they may be transiently exposed to much higher $[Ca^{2+}]$ in the submembrane space when L-type Ca^{2+} channels open.

Finally, our study raises the possibility that I_{SK} may synergize with I_{to} to cause all-or-none early repolarization and its arrhythmogenic consequences in human early repolarization syndromes such as the Brugada syndrome. Most of the experimental studies of P2R have been carried out in canine hearts [LA96, DDA94, ASH+06, PYA17] which have an unusually high I_{to} density in the right ventricular epicardium [LA88, ZXS+04]. Experimentally, P2R has been much more difficult to induce in other species. For example, Park *et al.* [PCM+15] attempted unsuccessfully to create a pig model of Brugada syndrome by engineering a human-homologous loss-of-function SCN5A mutation, suggesting that I_{to} density in the pig was not high enough to recapitulate the Brugada syndrome phenotype. Therefore, in the setting of low or reduced I_{to}, activation of I_{SK} can promote J-wave syndrome and arrhythmias, as in the rabbit experiments by Chen *et al.* [CXW+18].

There are several limitations in the current study. First, although SK channels have been widely investigated, their kinetics and localizations in cardiac myocytes are still largely unknown, and therefore, the relatively simple I_{SK} model may not accurately describe the I_{SK} behaviors in the ventricular myocytes. Second, since SK channels are activated by Ca^{2+}, the Ca^{2+} sensed by the channels and thus I_{SK} profile may strongly depend on the localization of the SK channels. As shown in our simulations of the ORd model, a small portion of the channels sense the submembrane Ca^{2+} can result in a much spiker current profile. Third, in the

ventricular AP models, the Ca^{2+} transient behaviors are very different from model to model, and thus the I_{SK} profile can be very model-dependent. For example, the AP model by ten Tusscher *et al.* [tTNNP04] exhibits a very spiky intracellular Ca^{2+} transient, while the LRd and ORd models used in this study exhibit much broader Ca^{2+} transients. Thus, in this study, to result in a spiky I_{SK}, we sped up SERCA in the LRd model while letting a small portion of the SK channels sense the submembrane Ca^{2+} in the ORd model. Fourth, in our simulations, we used larger K_d's than experimentally observed ones. The reason was that for the two models we used, a smaller K_d makes it more difficult to induce APD alternans and P2R by I_{SK} alone. Since I_{SK} depends on the Ca^{2+} transient profile which are very different in different models, this could be a model-dependent requirement. It is also possible that since SK channels may colocalize with the L-type Ca^{2+} channels where Ca^{2+} is much higher than bulk cytosolic Ca^{2+} concentration, their K_d for half-activation is indeed larger than the ones determined experimentally based on measurements of the bulk cytosolic Ca^{2+} concentration. Nevertheless, even if the K_d is lower than what used in our model, due to its spiky behavior, I_{SK} can still function in synergy with I_{to} to promote J-wave syndromes and arrhythmias.

In conclusion, when the intracellular Ca^{2+} transient waveform sensed by SK channels is spike-like, I_{SK} can play functionally the role of I_{to}, which alone or combined with I_{to} can promote J-wave syndromes and the related arrhythmias, such as T-wave alternans and phase 2 reentry.

CHAPTER 6

The Transient Outward Potassium Current ($I_{\mathbf{to}}$) Plays a Critical Role in Spiral Wave Breakup

6.1 Introduction

The leading cause of sudden cardiac death is ventricular arrhythmias. The main abnormal electrical activities in cardiac ventricular muscle are focal excitations and [ZW98, QW15]. Spiral waves (also called "rotors") as a form of functional reentry have been widely shown in experiments of animal hearts [DPS+92, GPJ98, GKV+00, CMB+00, WGB+03, PWM+10, PG15, KWG+06, WLB+04, VYO+02] and recordings in human hearts [NMC+06, NUF+11, MDC+07]. In most cases, arrhythmias are manifested by multiple spiral waves. Moreover, the number of spiral waves does not remain constant but is highly variable over time and the spiral waves are usually short-lived [CMB+00, KWG+06, CNLS02]. Because of the spatiotemporal irregularity in spiral wave dynamics, electrocardiogram (ECG) signaling is also highly irregular. In human cardiac arrhythmias, polymorphic ventricular tachycardia (VT) and ventricular fibrillation (VF), two most dangerous forms of arrhythmias, also exhibit irregular ECG signals, indicating that unstable spatiotemporal spiral wave dynamics may indeed be responsible for these lethal forms of human arrhythmias.

It has been well-known that the genesis of complex spatiotemporal spiral wave dynamics can be caused by tissue heterogeneities or by dynamical instabilities, or the interactions of both [QHGW14]. In the last three decades, a large

number of computer simulations have been carried out on spiral wave stability and breakup in cardiac tissue models [Kar93, Kar94, Pan98, QXGW00, QWG99, QKX+00, QWG00, XQGW01, XQGW02], which investigated the roles of dynamical instabilities and tissue heterogeneities, as well as excitability in spiral wave dynamics. In the early simulations using the Noble model [Kar93, Kar94], the Beeler-Reuter model [LRV94, Cou96, CW91, FK98], and the 1991 Luo-Rudy (LR1) model [QXGW00, QWG99, QKX+00, QWG00], or other simplified models [Pan98, FCHE02, PP01, BWZ+02], it has been shown that the slope of APD restitution is a major determent of spiral wave stability. One can change the slope of the APD restitution curve, and thus the spiral wave stability, by adjusting the maximum conductance of some ionic currents, in particular the maximum conductance of the calcium (Ca^{2+}) or the potassium (K^+) current [QWG00]. However, in many of the later action potential models [LR94, OVVR11, tTNNP04, tTP06], spiral waves are stable [SNP09, EC14, CF07, CF08].

Since the spiral waves are highly variable and short-lived as demonstrated in the mapping studies, dynamical instabilities may play a critical role, and therefore, it is important to understand the dynamical mechanisms of spiral wave stability and pinpoint the major biophysical and physiological causes for therapeutic purpose. A key question is which ionic current to target in therapy if one wants to prevent breakup. Which ionic current plays the primary role in spiral wave breakup.

6.2 Methods

6.2.1 Action Potential Models

Single cell action potentials follow the following differential equation:

$$C_m \frac{dV}{dt} = -I_{\text{ion}} + I_{\text{sti}}, \tag{6.1}$$

where V is the voltage and C_m is the membrane capacitance. Here, we use five different models: the guinea pig ventricular AP model (a later version fo the LRd model) by Faber and Rudy [FR00], the rabbit ventricular model by Mahajan *et al.* [MSS+08], the ORd human ventricular myocyte model [OVVR11], the TP04 human ventricular myocyte model [tTNNP04], and the TP06 human ventricular myocyte model (a later modification of the TP04 model) [tTP06]. In the TP06 model, $C_m = 2\,\mu\text{F/cm}^2$; in all other models, $C_m = 1\,\mu\text{F/cm}^2$.

For every model, we test the effects of changes in the maximum conductance I_{to}. Each model has a different formulation for I_{to}, but in general satisfies

$$I_{\text{to}} = \bar{G}_{\text{to}} Z (V - E_{\text{K}}), \tag{6.2}$$

where $\bar{G}_{\text{to}}$ is the maximum conductance, E_{K} is the Nernst potential for K^+, and Z is the product of certain gating variables (different models have different formulations for the gating variables). Each model has a given value for $\bar{G}_{\text{to}}$, which we call the "control." We increase or decrease $\bar{G}_{\text{to}}$ by multiplying the control value a certain amount. We also do the same for other currents: I_{Kr}, I_{Ks}, $I_{\text{Ca,L}}$, and I_{K1}.

6.2.2 2D Tissue Model of Spiral Waves

Cardiac myocytes are coupled together in a 2-dimensional square lattice. The voltage of each cell follows the following partial differential equation:

$$\frac{\partial V}{\partial t} = -\frac{I_{\text{ion}}}{C_m} + D\Delta V, \tag{6.3}$$

where $\Delta = \frac{\partial^2}{\partial x^2} + \frac{\partial^2}{\partial y^2}$ is the 2-dimensional Laplacian operator, and D is the diffusion constant describing the strength of gap junction coupling. For the LRd and OHara models we set the cell lengths dx and dy to be 0.0125 cm, and 0.025 cm in the other models. The diffusion constant D is $0.001\,\text{cm}^2/\text{ms}$ in the LRd and OHara models, and $0.001\,54\,\text{cm}^2/\text{ms}$ in the other models. No flux boundary conditions are imposed on the boundary.

To generate spiral waves, we perform the cross-field protocol. Each cell's initial condition is determined by pacing a single cell at a pacing period of $T = 500\,\text{ms}$ for 1000 beats, to remove transient behavior. The entire left boundary of cells in the tissue is then paced, triggering propagation moving to the right towards the center of the tissue. Once the propagated wave hits the center of the tissue, all cells in the bottom half of the tissue are depolarized by fixing their voltages to $-30\,\text{mV}$ for $2\,\text{ms}$. Afterwards, Eq. (6.3) is integrated for $5 - 10\,\text{s}$. In each simulation, breakup or stability was determined. APD and cycle length (CL) were both determined from cells reasonably far away from the spiral tip. To calculate APD and CL, depolarization of a cell was determined to be when the voltage V rises past $-75\,\text{mV}$, and repolarization the time the voltage falls below $-75\,\text{mV}$. APD is the difference in time between repolarization and depolarization, and CL is the difference between two successive depolarizations.

6.2.3 Numerical Methods

Spiral wave simulations were performed using a custom-made integration solver in CUDA, a programming language designed for graphical processing units (GPUs), using a time-adaptive forward Euler method. For each cell, the time step is $\Delta t = 0.025\,\text{ms}$ if the change in voltage $\Delta V < 0.1\,\text{mV}$, otherwise the time step is $\Delta t = 0.0025\,\text{ms}$.

6.3 Results

6.3.1 I_{to} Promotes Spiral Wave Breakup in the LRd Model

We first simulated spiral wave dynamics in the LRd model using different I_{to} levels. Spiral waves in the original LRd model are stable with small variations in CL ($\approx 85\,\text{ms}$) and APD ($\approx 65\,\text{ms}$) over time (Fig. 6.1(a)). In this case, the max-

imum conductance (G_{to}) of I_{to} is $0.5\,\text{mS/cm}^2$, which was set as the control value (G_{to}, Control). When G_{to} was 2 times the control value (Fig. 6.1(b)), spiral wave breakup occurred with CL ($\approx 70-150\,\text{ms}$) and APD ($\approx 45-100\,\text{ms}$) varying in large ranges and irregularly. When G_{to} was 5 times the control value (Fig. 6.1(c)), spiral wave breakup still occurred but the wavelength became apparently shorter. APD remains below 40 ms and CL around 60 ms but can occasionally be very large (APD $\approx 100\,\text{ms}$ and CL $\approx 150\,\text{ms}$). When G_{to} was 6.5 times the control value, spiral wave breakup occurred initially with large CL and small APD variances, but eventually became stable (Fig. 6.1(d)). In this case, after the initial chaotic spiral wave breakup phase, the spiral waves are all stable, and thus the spiral wave pattern became temporally periodic. When G_{to} was 10 times the control value (Fig. 6.1(e)), no breakup occurred. The spiral wave became stable with a much shorter APD and CL than in control.

We systematically explored the spiral wave behaviors using different combinations of the maximum conductance of $I_{\text{Ca,L}}$ and I_{to} while maintaining other parameters at their control values, summarized in Fig. 6.1(f). Varying the conductances of both I_{to} and $I_{\text{Ca,L}}$ was done for two reasons. First, it is known that $I_{\text{Ca,L}}$ plays a role in inducing spiral wave breakup by affecting APD restitution properties [QWG99]. Secondly, we wish to see whether I_{to}'s effects on spiral wave breakup change if $I_{\text{Ca,L}}$ changes as well. We used the cross-field protocol to induce a single spiral wave in the tissue. If this spiral wave remains intact without breakup, we label the point as "no breakup" (open circles). If the spiral wave cannot remain intact, multiple spiral waves occur, whether they finally become stable (such as the case in Fig. 6.1(d)) or unstable (such as the cases in Figs. 6.1(b) and (c)), we label the point as "breakup" (solid circles). As shown in Fig. 6.1(f), spiral wave breakup occurs in a wide range of parameters.

As shown in Fig. 6.1, I_{to} plays a critical role in spiral wave breakup in the LRd model. We then ask the question whether spiral wave breakup can occur

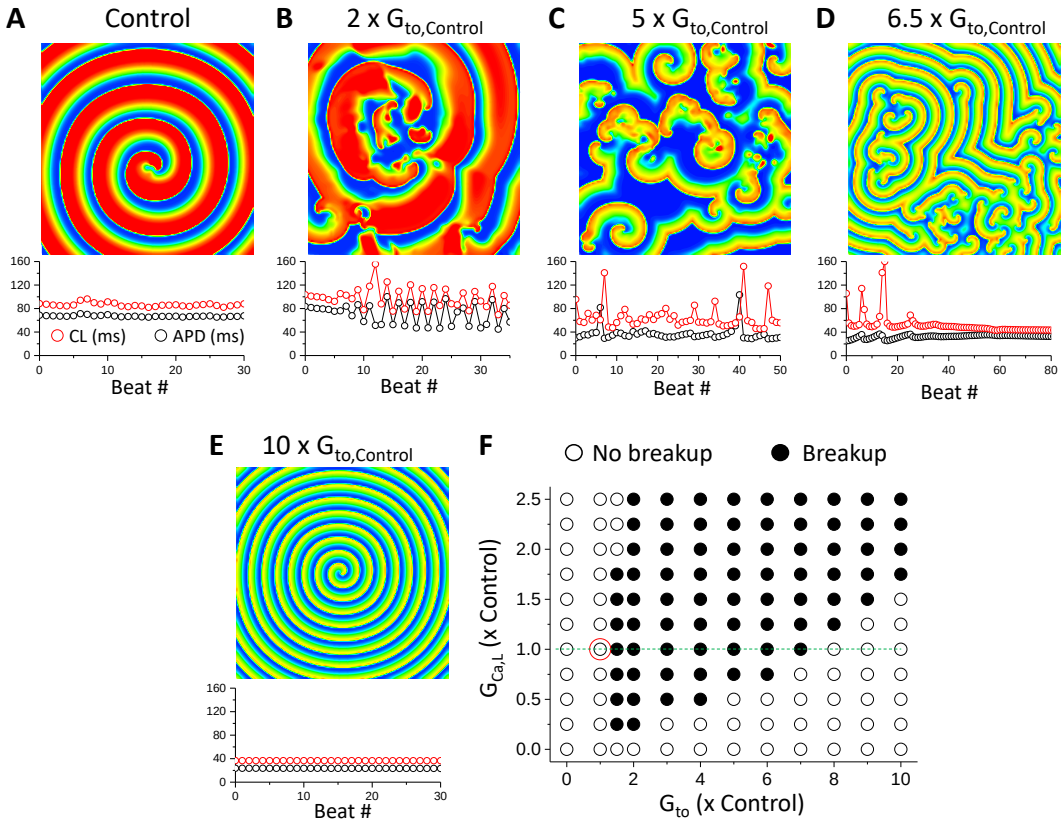

Figure 6.1: Effects of I_{to} on spiral wave dynamics in the LRd model. **(a)-(e)**. Voltage snapshots (upper) and cycle length (CL) and APD versus beat number (lower) for the original (Control) LRd model (a), 2 times control G_{to} (b), 5 times control G_{to} (c), 6.5 times control G_{to} (d), and 10 times control G_{to} (e). **(f)**. Spiral wave behaviors versus $G_{\text{Ca,L}}$ and G_{to}. The red circles marks the parameter set of the original LRd model (Control).

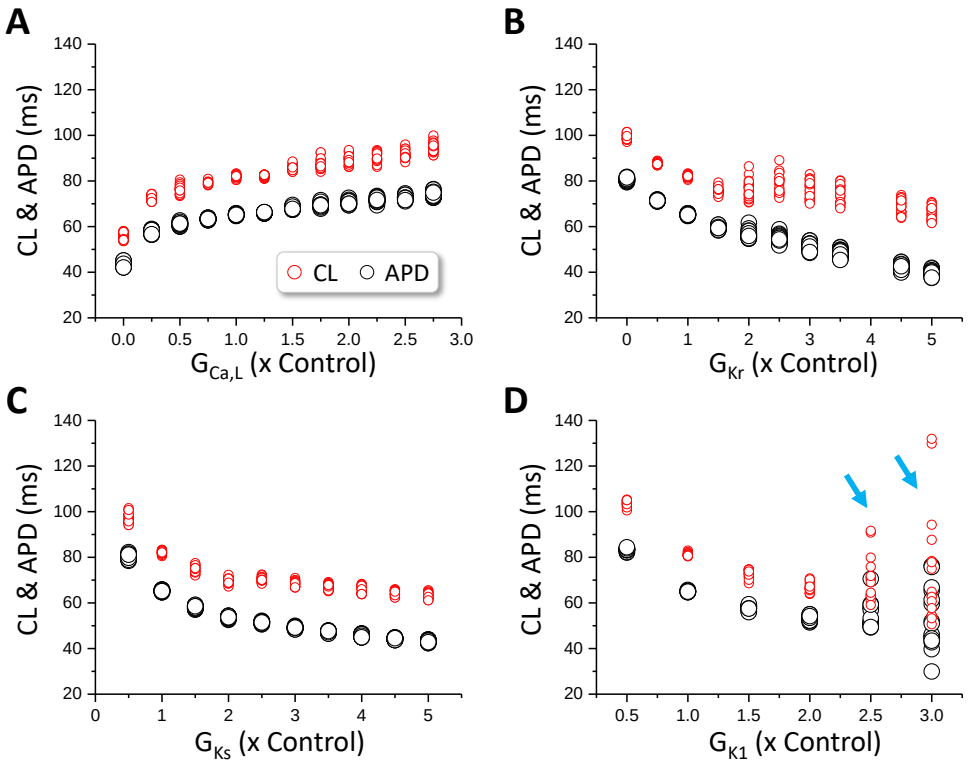

Figure 6.2: Spiral wave dynamics in the LRd model in the absence of I_{to}. CL and APD versus the maximum conductance for $G_{\text{Ca,L}}$ **(a)**, G_{Kr} **(b)**, G_{Ks} **(c)**, and G_{K1} **(d)**. Arrows mark the cases of spiral wave breakup.

in the LRd model by varying the maximum conductance of other ionic currents in the absence of I_{to} ($G_{\text{to}} = 0$). Fig. 6.2 plots APD and CL for different times of the control maximum conductance of $I_{\text{Ca,L}}$ (Fig. 6.2(a)), I_{Kr} (Fig. 6.2(b)), I_{Ks} (Fig. 6.2(c)), and I_{K1} (Fig. 6.2(d)). We also plotted in each case the action potentials for the smallest, the control, and the largest value of the maximum conductance of an ionic current for reference. We did not observe spiral wave breakup for $G_{\text{Ca,L}}$ from 0 to 3 times its control value, for G_{Kr} from 0 to 5 times its control value, and for G_{Ks} from 0.5 to 5 times its control value. However, when increased G_{K1} to 2.5 times its control value, spiral wave breakup occurred (arrows in Fig. 6.2(d)).

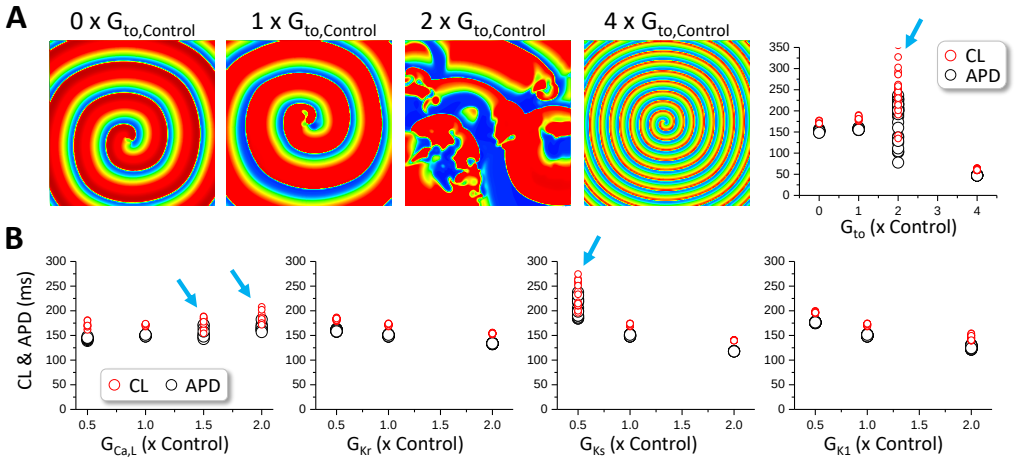

Figure 6.3: Effects of I_{to} on spiral wave dynamics in the UCLA model [MSS+08]. **(a)**. From left to right, voltage snapshots with $0\times$, $1\times$, $2\times$, and $4 \times G_{\text{to,Control}}$. The spiral wave breaks up with $2 \times G_{\text{to,Control}}$. In the right most panel, APD and CL are plotted against G_{to} ($\times$ control). **(b)**. CL and APD versus the maximum conductance of, from left to right, $G_{\text{Ca,L}}$, G_{Kr}, G_{Ks}, and G_{K1}.

6.3.2 I_{to} Promotes Spiral Wave Breakup in Other Ventricular AP Models

We simulated four other models for spiral wave stability: the rabbit ventricular myocyte model by Mahajan *et al.* (Fig. 6.3) [MSS+08], the ORd human ventricular myocyte model (Fig. 6.4) [OVVR11], the TP04 human ventricular myocyte model (Fig. 6.5) [tTNNP04], and the TP06 human ventricular myocyte model (Fig. 6.6) [tTP06]. In all 4 models, no spiral wave breakup occurs in their control conditions. Increasing I_{to} promoted spiral waves breakup. When I_{to} is very large, stable spiral waves occurred.

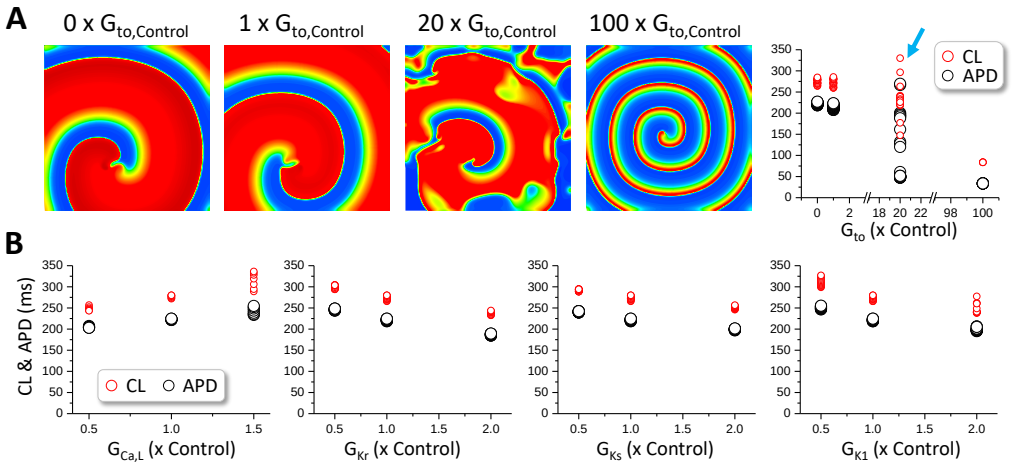

Figure 6.4: Effects of I_{to} on spiral wave dynamics in the ORd model [OVVR11]. **(a)**. From left to right, voltage snapshots with $0\times$, $1\times$, $20\times$, and $100 \times G_{\text{to,Control}}$. The spiral wave breaks up with $20 \times G_{\text{to,Control}}$. In the right most panel, APD and CL are plotted against G_{to} ($\times$ control). **(b)**. CL and APD versus the maximum conductance of, from left to right, $G_{\text{Ca,L}}$, G_{Kr}, G_{Ks}, and G_{K1}.

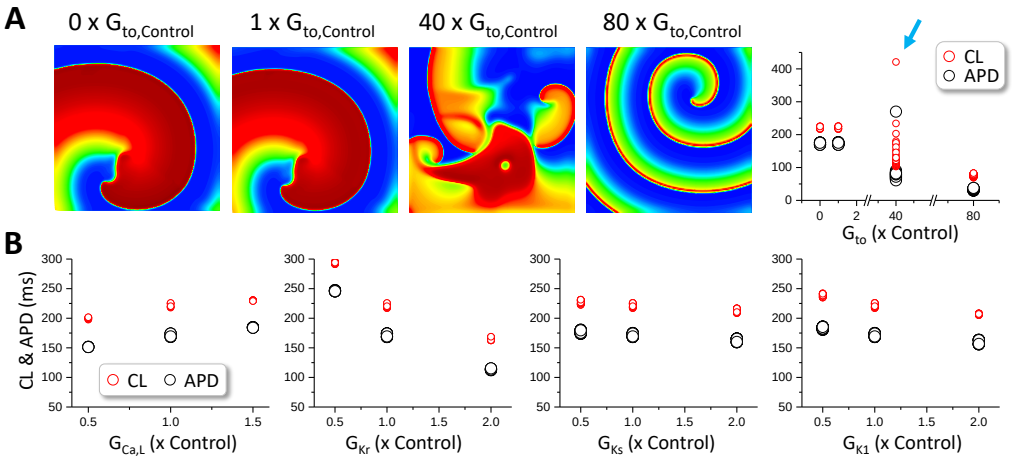

Figure 6.5: Effects of I_{to} on spiral wave dynamics in the TP04 model [tTNNP04]. **(a)**. From left to right, voltage snapshots with $0\times$, $1\times$, $40\times$, and $80 \times G_{\text{to,Control}}$. The spiral wave breaks up with $40 \times G_{\text{to,Control}}$. In the right most panel, APD and CL are plotted against G_{to} ($\times$ control). **(b)**. CL and APD versus the maximum conductance of, from left to right, $G_{\text{Ca,L}}$, G_{Kr}, G_{Ks}, and G_{K1}.

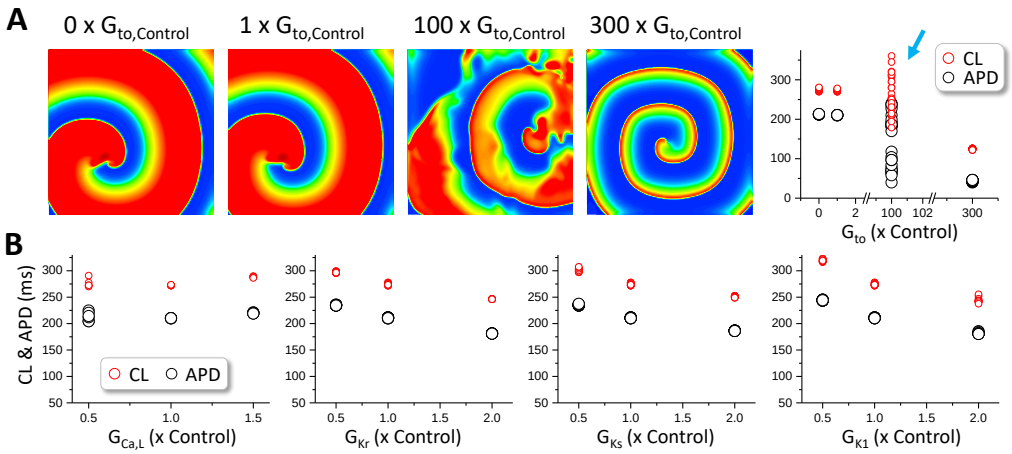

Figure 6.6: Effects of I_{to} on spiral wave dynamics in the TP06 model [tTP06]. **(a)**. From left to right, voltage snapshots with 0×, 1×, 100×, and 300 × $G_{\text{to,Control}}$. The spiral wave breaks up with 100 × $G_{\text{to,Control}}$. In the right most panel, APD and CL are plotted against G_{to} (× control). **(b)**. CL and APD versus the maximum conductance of, from left to right, $G_{\text{Ca,L}}$, G_{Kr}, G_{Ks}, and G_{K1}.

6.4 Discussion

Action potential instabilities at the cellular level can manifest as arrhythmias at the whole organ level. Previous studies have suggested the importance of I_{to} in inducing action potential dynamics and arrhythmias [LGWQ17, LQ18b, CLT+18, GYT+11]. Here, we demonstrate that I_{to} can also play a critical role in inducing spiral wave breakup. Namely, under a certain regime of I_{to} intensity, spiral waves breakup due to APD and CL instabilities.

CHAPTER 7

Conclusions

This body of work focuses on the role of short-term cardiac memory and its effects on action potential instability at the single-cell level to arrhythmogenesis at the tissue-scale level. Early repolarization syndrome causes spike-and-dome action potential morphology, and long QT syndrome causes early afterdeploarizations (EADs). In these two diseased syndromes, the action potential abnormalities cause a sensitive dependence of action potential duration (APD) on the effects of memory, resulting in APD instability and alternans.

Our findings suggest that cardiac memory promotes, rather than suppresses, arrhythmogenesis under diseased conditions in cardiac ventricular tissue. Here, we analyzed two scenarios of early repolarization syndrome inducing phase 2 reentry (via activation of the SK channels) and spiral wave breakup (via enhanced I_{to}). Memory-induced alternans and chaos of APD may be the underlying mechanism of T-wave alternans, shown to be arrhythmogenic in cardiac diseases including early repolarization syndromes like Brugada syndrome and in long QT syndrome [QXGW10, MZL+06, TKN+08, FA08]. In addition, memory-induced chaos of action potentials may be the underlying mechanism of synchronization of chaotic early afterdeploarizations, which has been shown to induce reentry and arrhythmias [XHS+07, SXS+09]. Understanding the roles of memory may provide insights in future clinical targets for suppressing arrhythmogenesis in cardiac diseases.

References

[AC09] Srisairam Achuthan and Carmen C. Canavier. Phase-resetting curves determine synchronization, phase locking, and clustering in networks of neural oscillators. *Journal of Neuroscience*, 29(16):5218–5233, 2009.

[AKSA+18] Sana M. Al-Khatib, William G. Stevenson, Michael J. Ackerman, William J. Bryant, David J. Callans, Anne B. Curtis, Barbara J. Deal, Timm Dickfeld, Michael E. Field, Gregg C. Fonarow, et al. 2017 AHA/ACC/HRS guideline for management of patients with ventricular arrhythmias and the prevention of sudden cardiac death: A report of the American College of Cardiology/American Heart Association Task Force on Clinical Practice Guidelines and the Heart Rhythm Society. *Journal of the American College of Cardiology*, 72(14):e91–e220, 2018.

[AMS12] John P. Adelman, James Maylie, and Pankaj Sah. Small-conductance Ca^{2+}-activated K^+ channels: Form and function. *Annual Review of Physiology*, 74:245–269, 2012.

[AS14] Robert K. Amanfu and Jeffrey J. Saucerman. Modeling the effects of β_1-adrenergic receptor blockers and polymorphisms on cardiac myocyte Ca^{2+} handling. *Molecular Pharmacology*, 86(2):222–230, 2014.

[ASH+06] Takeshi Aiba, Wataru Shimizu, Ichiro Hidaka, Kazunori Uemura, Takashi Noda, Can Zheng, Atsunori Kamiya, Masashi Inagaki, Masaru Sugimachi, and Kenji Sunagawa. Cellular basis for trigger and maintenance of ventricular fibrillation in the Brugada syndrome model: High-resolution optical mapping study. *Journal of the American College of Cardiology*, 47(10):2074–2085, 2006.

[ASK+09] Gary L. Aistrup, Yohannes Shiferaw, Sunil Kapur, Alan H. Kadish, and J. Andrew Wasserstrom. Mechanisms underlying the formation and dynamics of subcellular calcium alternans in the intact rat heart. *Circulation Research*, 104(5):639–649, 2009.

[ASR98] Orlando Auciello, James F. Scott, and Ramamoorthy Ramesh. The physics of ferroelectric memories. *Physics Today*, 51(7):22–27, 1998.

[AWS+13] Antonis A. Armoundas, Eric H. Weiss, Omid Sayadi, Shawna Laferriere, Naveen Sajja, Theofanie Mela, Jagmeet P. Singh, Conor D. Barrett, E. Kevin Heist, and Faisal M. Merchant. A novel pacing method to suppress repolarization alternans in vivo: Implications for arrhythmia prevention. *Heart Rhythm*, 10(4):564–572, 2013.

[AY15] Charles Antzelevitch and Gan-Xin Yan. J-wave syndromes: Brugada and early repolarization syndromes. *Heart Rhythm*, 12(8):1852–1866, 2015.

[AYA+16] Charles Antzelevitch, Gan-Xin Yan, Michael J. Ackerman, Martin Borggrefe, Domenico Corrado, Jihong Guo, Ihor Gussak, Can Hasdemir, Minoru Horie, Heikki Huikuri, et al. J-wave syndromes expert consensus conference report: Emerging concepts and gaps in knowledge. *Journal of Arrhythmia*, 32(5):315–339, 2016.

[Ber02] Julius Bernstein. Untersuchungen zur thermodynamik der bioelektrischen ströme. *Archiv für die Gesamte Physiologie des Menschen und der Tiere*, 92(10):521–562, Nov 1902.

[Ber08] Donald M. Bers. Calcium cycling and signaling in cardiac myocytes. *Annual Review of Physiology*, 70(1):23–49, 2008. PMID: 17988210.

[BOCEF15] Alfonso Bueno-Orovio, Elizabeth M. Cherry, Steven J. Evans, and Flavio H. Fenton. Basis for the induction of tissue-level phase-2 reentry as a repolarization disorder in the Brugada syndrome. *BioMed Research International*, 2015, 2015.

[BQK+07] Ali Baher, Zhilin Qu, Ashkan Kayatdavoudi, Scott T. Lamp, Ming-Jim. Yang, Fagen Xie, Stephen Turner, Alan Garfinkel, and James N. Weiss. Short-term cardiac memory and mother rotor fibrillation. *American Journal of Physiology - Heart and Circulatory Physiology*, 292(1):H180–H189, 2007.

[BRK+04] F. Brette, P. Rodriguez, K. Komukai, J. Colyer, and C. H. Orchard. β-adrenergic stimulation restores the Ca transient of ventricular myocytes lacking t-tubules. *Journal of Molecular and Cellular Cardiology*, 36(2):265–275, 2004.

[BST+04] Wolfgang Bildl, Tim Strassmaier, Henrike Thurm, Jens Andersen, Silke Eble, Dominik Oliver, Marlies Knipper, Matthias Mann, Uwe Schulte, John P. Adelman, et al. Protein kinase CK2 is coassembled with small conductance Ca^{2+}-activated K^+ channels and regulates channel gating. *Neuron*, 43(6):847–858, 2004.

[BTN89] Kurt G. Beam, Tsutomu Tanabe, and Shosaku Numa. Structure, function, and regulation of the skeletal muscle dihydropyridine receptor. *Annals of the New York Academy of Sciences*, 560(1):127–137, 1989.

[BWZ+02] Olivier Bernus, Ronald Wilders, Christian W. Zemlin, Henri Verschelde, and Alexander V. Panfilov. A computationally efficient electrophysiological model of human ventricular cells. *American Jour-*

nal of Physiology - Heart and Circulatory Physiology, 282(6):H2296–H2308, 2002.

[CC96] David J. Christini and James J. Collins. Using chaos control and tracking to suppress a pathological nonchaotic rhythm in a cardiac model. *Physical Review E*, 53(1):R49, 1996.

[CCM+11] Su-Kiat Chua, Po-Cheng Chang, Mitsunori Maruyama, Isik Turker, Tetsuji Shinohara, Mark J. Shen, Zhenhui Chen, Changyu Shen, Michael Rubart-Von Der Lohe, John C. Lopshire, et al. Small-conductance calcium-activated potassium channel and recurrent ventricular fibrillation in failing rabbit ventricles. *Circulation Research*, pages 971–979, 2011.

[CF04] Elizabeth M. Cherry and Flavio H. Fenton. Suppression of alternans and conduction blocks despite steep APD restitution: Electrotonic, memory, and conduction velocity restitution effects. *American Journal of Physiology*, 286(6):H2332–H2341, 2004.

[CF07] Elizabeth M. Cherry and Flavio H. Fenton. A tale of two dogs: Analyzing two models of canine ventricular electrophysiology. *American Journal of Physiology - Heart and Circulatory Physiology*, 2007.

[CF08] Elizabeth M. Cherry and Flavio H. Fenton. Visualization of spiral and scroll waves in simulated and experimental cardiac tissue. *New Journal of Physics*, 10(12):125016, 2008.

[CGG+99] E. Chudin, J. Goldhaber, A. Garfinkel, J. Weiss, and B. Kogan. Intracellular Ca^{2+} dynamics and the stability of ventricular tachycardia. *Biophysical Journal*, 77(6):2930–2941, 1999.

[CGJJ90] Dante R. Chialvo, Robert F. Gilmour Jr, and José Jalife. Low dimensional chaos in cardiac tissue. *Nature*, 343(6259):653–657, 1990.

[Che17] Elizabeth M. Cherry. Distinguishing mechanisms for alternans in cardiac cells using constant-diastolic-interval pacing. *Chaos: An Interdisciplinary Journal of Nonlinear Science*, 27(9):093902, 2017.

[CHH+13] Po-Cheng Chang, Yu-Cheng Hsieh, Chia-Hsiang Hsueh, James N. Weiss, Shien-Fong Lin, and Peng-Sheng Chen. Apamin induces early afterdepolarizations and torsades de pointes ventricular arrhythmia from failing rabbit ventricles exhibiting secondary rises in intracellular calcium. *Heart Rhythm*, 10(10):1516–1524, 2013.

[CLS04] Bum-Rak Choi, Tong Liu, and Guy Salama. Adaptation of cardiac action potential durations to stimulation history with random diastolic intervals. *Journal of Cardiovascular Electrophysiology*, 15(10):1188–1197, 2004.

[CLT+18] Bum-Rak Choi, Weiyan Li, Dmitry Terentyev, Anatoli Y. Kabakov, Mingwang Zhong, Colin M. Rees, Radmila Terentyeva, Tae Yun Kim, Zhilin Qu, Xuwen Peng, et al. Transient outward K^+ current (I_{to}) underlies the right ventricular initiation of polymorphic ventricular tachycardia in a transgenic rabbit model of long-QT syndrome type 1. *Circulation: Arrhythmia and Electrophysiology*, 11(6):e005414, 2018.

[CMB+00] Jay Chen, Ravi Mandapati, Omer Berenfeld, Allan C. Skanes, and José Jalife. High-frequency periodic sources underlie ventricular fibrillation in the isolated rabbit heart. *Circulation Research*, 86(1):86–93, 2000.

[CMJ90] Dante R. Chialvo, Donald C. Michaels, and José Jalife. Supernormal excitability as a mechanism of chaotic dynamics of activation in cardiac Purkinje fibers. *Circulation Research*, 66(2):525–545, 1990.

[CNLS02] Bum-Rak Choi, Wonchul Nho, Tong Liu, and Guy Salama. Life span of ventricular fibrillation frequencies. *Circulation Research*, 91(4):339–345, 2002.

[Cou96] Marc Courtemanche. Complex spiral wave dynamics in a spatially distributed ionic model of cardiac electrical activity. *Chaos: An Interdisciplinary Journal of Nonlinear Science*, 6(4):579–600, 1996.

[CPM+09] Inma R. Cantalapiedra, Angelina Penaranda, Lluis Mont, Josep Brugada, and Blas Echebarria. Reexcitation mechanisms in epicardial tissue: Role of I_{to} density heterogeneities and I_{Na} inactivation kinetics. *Journal of Theoretical Biology*, 259(4):850–859, 2009.

[CR01] Colleen E. Clancy and Yoram Rudy. Cellular consequences of HERG mutations in the long QT syndrome: Precursors to sudden cardiac death. *Cardiovascular Research*, 50(2):301–313, 2001.

[CR02] Colleen E. Clancy and Yoram Rudy. Na^+ channel mutation that causes both Brugada and long-QT syndrome phenotypes: A simulation study of mechanism. *Circulation*, 105(10):1208–1213, 2002.

[CRC+06] David J. Christini, Mark L. Riccio, Calin A. Culianu, Jeffrey J. Fox, Alain Karma, and Robert F. Gilmour Jr. Control of electrical alternans in canine cardiac Purkinje fibers. *Physical Review Letters*, 96(10):104101, 2006.

[CSM+01] David J. Christini, Kenneth M. Stein, Steven M. Markowitz, Suneet Mittal, David J. Slotwiner, Marc A. Scheiner, Sei Iwai, and Bruce B.

Lerman. Nonlinear-dynamical arrhythmia control in humans. *Proceedings of the National Academy of Sciences*, 98(10):5827–5832, 2001.

[CTL+13] Po-Cheng Chang, Isik Turker, John C. Lopshire, Saqib Masroor, Bich-Lien Nguyen, Wen Tao, Michael Rubart, Peng-Sheng Chen, Zhenhui Chen, and Tomohiko Ai. Heterogeneous upregulation of apamin-sensitive potassium currents in failing human ventricles. *Journal of the American Heart Association*, 2(1):e004713, 2013.

[CW91] Marc Courtemanche and Arthur T. Winfree. Re-entrant rotating waves in a Beeler–Reuter based model of two-dimensional cardiac electrical activity. *International Journal of Bifurcation and Chaos*, 1(02):431–444, 1991.

[CXW+18] Mu Chen, Dong-Zhu Xu, Adonis Z. Wu, Shuai Guo, Juyi Wan, Dechun Yin, Shien-Fong Lin, Zhenhui Chen, Michael Rubart-von der Lohe, Thomas H Everett IV, et al. Concomitant SK current activation and sodium current inhibition cause J wave syndrome. *JCI insight*, 3(22), 2018.

[CZZ+10] Yan Cui, Shu-Miao Zhang, Quan-Yu Zhang, Rong Fan, Juan Li, Hai-Tao Guo, Hui Bi, Yue-Min Wang, Yu-Zhen Hu, Qi-Jun Zheng, et al. Modulation of intracellular calcium transient in response to β-adrenoceptor stimulation in the hearts of 4-wk-old rats during simulated weightlessness. *Journal of Applied Physiology*, 108(4):838–844, 2010.

[DDA94] Jose M. Di Diego and Charles Antzelevitch. High $[Ca^{2+}]_o$-induced electrical heterogeneity and extrasystolic activity in isolated canine ventricular epicardium. Phase 2 reentry. *Circulation*, 89(4):1839–1850, 1994.

[DEO02] M. E. Diaz, D. A. Eisner, and S. C. O'neill. Depressed ryanodine receptor activity increases variability and duration of the systolic Ca^{2+} transient in rat ventricular myocytes. *Circulation Research*, 91(7):585–593, 2002.

[DL88] Stephen G. Dilly and Max J. Lab. Electrophysiological alternans and restitution during acute regional ischaemia in myocardium of anaesthetized pig. *The Journal of Physiology*, 402(1):315–333, 1988.

[DNHCG98] Christopher A. Del Negro, Chie-Fang Hsiao, Scott H. Chandler, and Alan Garfinkel. Evidence for a novel bursting mechanism in rodent trigeminal neurons. *Biophysical Journal*, 75(1):174–182, 1998.

[DOE04] Mary E. Diaz, Stephen C. O'neill, and David A. Eisner. Sarcoplasmic reticulum calcium content fluctuation is the key to cardiac alternans. *Circulation Research*, 94(5):650–656, 2004.

[DPS+92] Jorge M. Davidenko, Arcady V. Pertsov, Remy Salomonsz, William Baxter, and José Jalife. Stationary and drifting spiral waves of excitation in isolated cardiac muscle. *Nature*, 355(6358):349, 1992.

[DSI+00] William L. Ditto, Mark L. Spano, Visarath In, J. Neff, B. Meadows, J. J. Langberg, A. Bolmann, and K. McTeague. Control of human atrial fibrillation. *International Journal of Bifurcation and Chaos*, 10(03):593–601, 2000.

[DSPW06] Min Dong, Xiaoyin Sun, Astrid A. Prinz, and Hong-Sheng Wang. Effect of simulated I_{to} on guinea pig and canine ventricular action potential morphology. *American Journal of Physiology - Heart and Circulatory Physiology*, 291(2):H631–H637, 2006.

[DTB+99] Robert Dumaine, Jeffrey A. Towbin, Pedro Brugada, Matteo Vatta, Dmitri V. Nesterenko, Vladislav V. Nesterenko, Josep Brugada, Ramon Brugada, and Charles Antzelevitch. Ionic mechanisms responsible for the electrocardiographic phenotype of the Brugada syndrome are temperature dependent. *Circulation Research*, 85(9):803–809, 1999.

[EC14] Mohamed M. Elshrif and Elizabeth M. Cherry. A quantitative comparison of the behavior of human ventricular cardiac electrophysiology models in tissue. *PLoS One*, 9(1):e84401, 2014.

[ECD+00] D. A. Eisner, H. S. Choi, M. E. Diaz, S. C. O'Neill, and A. W. Trafford. Integrative analysis of calcium cycling in cardiac muscle. *Circulation Research*, 87(12):1087–1094, 2000.

[EK02] Blas Echebarria and Alain Karma. Spatiotemporal control of cardiac alternans. *Chaos: An Interdisciplinary Journal of Nonlinear Science*, 12(3):923–930, 2002.

[ES83] Victor Elharrar and Borys Surawicz. Cycle length effect on restitution of action potential duration in dog cardiac fibers. *American Journal of Physiology - Heart and Circulatory Physiology*, 244(6):H782–H792, 1983.

[FA08] Jeffrey M. Fish and Charles Antzelevitch. Cellular mechanism and arrhythmogenic potential of T-wave alternans in the Brugada syndrome. *Journal of Cardiovascular Electrophysiology*, 19(3):301–308, 2008.

[FAP97] Clara Franzini-Armstrong and Feliciano Protasi. Ryanodine receptors of striated muscles: A complex channel capable of multiple interactions. *Physiological Reviews*, 77(3):699–729, 1997.

[FBGJ02] Jeffrey J. Fox, Eberhard Bodenschatz, and Robert F. Gilmour Jr. Period-doubling instability and memory in cardiac tissue. *Physical Review Letters*, 89(13):138101, 2002.

[FCHE02] Flavio H. Fenton, Elizabeth M. Cherry, Harold M. Hastings, and Steven J. Evans. Multiple mechanisms of spiral wave breakup in a model of cardiac electrical activity. *Chaos: An Interdisciplinary Journal of Nonlinear Science*, 12(3):852–892, 2002.

[FK98] Flavio Fenton and Alain Karma. Vortex dynamics in three-dimensional continuous myocardium with fiber rotation: Filament instability and fibrillation. *Chaos: An Interdisciplinary Journal of Nonlinear Science*, 8(1):20–47, 1998.

[FR00] Gregory M. Faber and Yoram Rudy. Action potential and contractility changes in $[Na^+]_i$ overloaded cardiac myocytes: A simulation study. *Biophysical Journal*, 78(5):2392–2404, 2000.

[FRD+03] Jeffrey J. Fox, Mark L. Riccio, Paul Drury, Amanda Werthman, and Robert F. Gilmour Jr. Dynamic mechanism for conduction block in heart tissue. *New Journal of Physics*, 5(1):101, 2003.

[FS03] E. S. Louise Faber and Pankaj Sah. Calcium-activated potassium channels: Multiple contributions to neuronal function. *The Neuroscientist*, 9(3):181–194, 2003.

[FSLS88] Michael R. Franz, Charles D. Swerdlow, L. Bing Liem, and Jochen Schaefer. Cycle length dependence of human action potential duration in vivo. Effects of single extrastimuli, sudden sustained rate acceleration and deceleration, and different steady-state frequencies. *Journal of Clinical Investigation*, 82(3):972–979, 1988.

[FSS+83] Michael R. Franz, Jochen Schaefer, Michael Schöttler, W. Anthony Seed, and Mark I. M. Noble. Electrical and mechanical restitution of the human heart at different rates of stimulation. *Circulation Research*, 53(6):815–822, 1983.

[GBAC09] Stephen A. Gaeta, Gil Bub, Geoffrey W. Abbott, and David J. Christini. Dynamical mechanism for subcellular alternans in cardiac myocytes. *Circulation Research*, 105(4):335–342, 2009.

[GBC+11] Jeffery J. Goldberger, Alfred E. Buxton, Michael Cain, Otto Costantini, Derek V. Exner, Bradley P. Knight, Donald Lloyd-Jones,

Alah H. Kadish, Byron Lee, Arthur Moss, Robert Myerburg, Jeffrey Olgin, Rod Passman, David Rosenbaum, William Stevenson, Wojciech Zareba, and Douglas P. Zipes. Risk stratification for arrhythmic sudden cardiac death. *Circulation*, 123(21):2423–2430, 2011.

[GCGJ+13] Alessio Gizzi, Elizabeth Cherry, Robert F. Gilmour Jr, Stefan Luther, Simonetta Filippi, and Flavio H. Fenton. Effects of pacing site and stimulation history on alternans dynamics and the development of complex spatiotemporal patterns in cardiac tissue. *Frontiers in Physiology*, 4:71, 2013.

[GGS81] Michael R. Guevara, Leon Glass, and Alvin Shrier. Phase locking, period-doubling bifurcations, and irregular dynamics in periodically stimulated cardiac cells. *Science*, 214:1350–1353, 1981.

[GKV+00] Alan Garfinkel, Young-Hoon Kim, Olga Voroshilovsky, Zhilin Qu, Jong R. Kil, Moon-Hyoung Lee, Hrayr S. Karagueuzian, James N. Weiss, and Peng-Sheng Chen. Preventing ventricular fibrillation by flattening cardiac restitution. *Proceedings of the National Academy of Sciences*, 97(11):6061–6066, 2000.

[Gla96] Leon Glass. Dynamics of cardiac arrhythmias. *Physics Today*, 49(8):40–45, 1996.

[GPJ98] Richard A. Gray, Arkady M. Pertsov, and José Jalife. Spatial and temporal organization during cardiac fibrillation. *Nature*, 392(6671):75, 1998.

[GSDW92] Alan Garfinkel, Mark L. Spano, William L. Ditto, and James N. Weiss. Controlling cardiac chaos. *Science*, 257(5074):1230–1235, 1992.

[GWP+00] Joseph L. Greenstein, Richard Wu, Sunny Po, Gordon F. Tomaselli, and Raimond L. Winslow. Role of the calcium-independent transient outward current I_{to1} in shaping action potential morphology and duration. *Circulation Research*, 87(11):1026–1033, 2000.

[GWSG84] M. R. Guevara, G. Ward, A. Shrier, and L. Glass. Electrical alternans and period doubling bifurcations. *IEEE Computational Cardiology*, 562:167–170, 1984.

[GXD+05] Joshua I. Goldhaber, Lai-Hua Xie, Tan Duong, Christi Motter, Kien Khuu, and James N. Weiss. Action potential duration restitution and alternans in rabbit ventricular myocytes: The key role of intracellular calcium cycling. *Circulation Research*, 96(4):459–466, 2005.

[GYT+11] John R. Giudicessi, Dan Ye, David J. Tester, Lia Crotti, Alessandra Mugione, Vladislav V. Nesterenko, Richard M. Albertson, Charles Antzelevitch, Peter J. Schwartz, and Michael J. Ackerman. Transient outward current (I_{to}) gain-of-function mutations in the KCND3-encoded Kv4.3 potassium channel and Brugada syndrome. *Heart Rhythm*, 8(7):1024–1032, 2011.

[GZM08] Ilan Goldenberg, Wojciech Zareba, and Arthur J. Moss. Long QT syndrome. *Current Problems in Cardiology*, 33(11):629–694, 2008.

[HCT+97] Kevin Hall, David J. Christini, Maurice Tremblay, James J. Collins, Leon Glass, and Jacques Billette. Dynamic control of cardiac alternans. *Physical Review Letters*, 78(23):4518, 1997.

[HG02] G. Martin Hall and Daniel J. Gauthier. Experimental control of cardiac muscle alternans. *Physical Review Letters*, 88(19):198102, 2002.

[HH52] Alan L. Hodgkin and Andrew F. Huxley. A quantitative description of membrane current and its application to conduction and excitation in nerve. *The Journal of Physiology*, 117(4):500, 1952.

[HKK+16] Xiaodong Huang, Tae Yun Kim, Gideon Koren, Bum-Rak Choi, and Zhilin Qu. Spontaneous initiation of premature ventricular complexes and arrhythmias in type 2 long QT syndrome. *American Journal of Physiology - Heart and Circulatory Physiology*, 311(6):H1470–H1484, 2016.

[HMAM98] Birgit Hirschberg, James Maylie, John P. Adelman, and Neil V. Marrion. Gating of recombinant small-conductance Ca-activated K^+ channels by calcium. *The Journal of General Physiology*, 111(4):565–581, 1998.

[HMAM99] Birgit Hirschberg, James Maylie, John P. Adelman, and Neil V. Marrion. Gating properties of single SK channels in hippocampal CA1 pyramidal neurons. *Biophysical Journal*, 77(4):1905–1913, 1999.

[Hop06] Bruce Hopenfeld. Mechanism for action potential alternans: The interplay between L-type calcium current and transient outward current. *Heart Rhythm*, 3(3):345–352, 2006.

[Izh00] Eugene M. Izhikevich. Neural excitability, spiking and bursting. *International Journal of Bifurcation and Chaos*, 10(06):1171–1266, 2000.

[JC04] Peter N. Jordan and David J. Christini. Adaptive diastolic interval control of cardiac action potential duration alternans. *Journal of Cardiovascular Electrophysiology*, 15(10):1177–1185, 2004.

[JM92] Craig T. January and Adriana Moscucci. Cellular mechanisms of early afterdepolarizations. *Annals of the New York Academy of Sciences*, 644(1):23–32, 1992.

[JPV07] Norbert Jost, Julius Gy Papp, and András Varró. Slow delayed rectifier potassium current (I_{Ks}) and the repolarization reserve. *Annals of Noninvasive Electrocardiology*, 12(1):64–78, 2007.

[Kan01] Eric R. Kandel. The molecular biology of memory storage: A dialogue between genes and synapses. *Science*, 294(5544):1030–1038, 2001.

[Kar93] Alain Karma. Spiral breakup in model equations of action potential propagation in cardiac tissue. *Physical Review Letters*, 71(7):1103, 1993.

[Kar94] Alain Karma. Electrical alternans and spiral wave breakup in cardiac tissue. *Chaos: An Interdisciplinary Journal of Nonlinear Science*, 4(3):461–472, 1994.

[Kar13] Alain Karma. Physics of cardiac arrhythmogenesis. *Annual Review of Condensed Matter Physics*, 4(1):313–337, 2013.

[KB02] Jens Kockskämper and Lothar A. Blatter. Subcellular Ca^{2+} alternans represents a novel mechanism for the generation of arrhythmogenic Ca^{2+} waves in cat atrial myocytes. *The Journal of Physiology*, 545(1):65–79, 2002.

[KDT+04] Soma S. Kalb, Hana M. Dobrovolny, Elena G. Tolkacheva, Salim F. Idriss, Wanda Krassowska, and Daniel J. Gauthier. The restitution portrait: A new method for investigating rate-dependent restitution. *Journal of Cardiovascular Electrophysiology*, 15(6):698–709, 2004.

[KGS95] Arkady M. Kunysz, Leon Glass, and Alvin Shrier. Overdrive suppression of spontaneously beating chick heart cell aggregates: Experiment and theory. *American Journal of Physiology - Heart and Circulatory Physiology*, 269(3):H1153–H1164, 1995.

[KKH+93] Hrayr S. Karagueuzian, Steven S. Khan, Kichol Hong, Yoshinori Kobayashi, Timothy Denton, William J. Mandel, and George A. Diamond. Action potential alternans and irregular dynamics in quinidine-intoxicated ventricular muscle cells. Implications for ventricular proarrhythmia. *Circulation*, 87(5):1661–1672, 1993.

[KKJC04] Alexander O. Komendantov, Olena G. Komendantova, Steven W. Johnson, and Carmen C. Canavier. A modeling study suggests complementary roles for GABAA and NMDA receptors and the SK chan-

nel in regulating the firing pattern in midbrain dopamine neurons. *Journal of Neurophysiology*, 91(1):346–357, 2004.

[KMC12] Trine Krogh-Madsen and David J. Christini. Nonlinear dynamics in cardiology. *Annual Review of Biomedical Engineering*, 14:179–203, 2012.

[KMC17] Trine Krogh-Madsen and David J. Christini. Slow $[Na^+]_i$ dynamics impacts arrhythmogenesis and spiral wave reentry in cardiac myocyte ionic model. *Chaos: An Interdisciplinary Journal of Nonlinear Science*, 27(9):093907, 2017.

[KMKR+10] Trine Krogh-Madsen, Alain Karma, Mark L. Riccio, Peter N. Jordan, David J. Christini, and Robert F. Gilmour Jr. Off-site control of repolarization alternans in cardiac fibers. *Physical Review E*, 81(1):011915, 2010.

[KMS95] Arkady M. Kunysz, Andrew A. Munk, and Alvin Shrier. Phase resetting and dynamics in isolated atrioventricular nodal cell clusters. *Chaos: An Interdisciplinary Journal of Nonlinear Science*, 5(1):184–192, 1995.

[KMS+16] Tijana Knezevic, Valerie D. Myers, Feifei Su, JuFang Wang, Jianliang Song, Xue-Qian Zhang, Erhe Gao, Guofeng Gao, Muniswamy Madesh, Manish K. Gupta, et al. Adeno-associated virus serotype 9–driven expression of BAG3 improves left ventricular function in murine hearts with left ventricular dysfunction secondary to a myocardial infarction. *JACC: Basic to Translational Science*, 1(7):647–656, 2016.

[KS98] J. P. Keener and J. Sneyd. *Mathematical Physiology*. Springer, New York, 1998.

[KSG97] Arkady M. Kunysz, Alvin Shrier, and Leon Glass. Bursting behavior during fixed-delay stimulation of spontaneously beating chick heart cell aggregates. *American Journal of Physiology - Cell Physiology*, 273(1):C331–C346, 1997.

[KTS+05] Soma S. Kalb, Elena G. Tolkacheva, David G. Schaeffer, Daniel J. Gauthier, and Wanda Krassowska. Restitution in mapping models with an arbitrary amount of memory. *Chaos*, 15(2):023701, 2005.

[KWG+06] Matthew W. Kay, Gregory P. Walcott, James D. Gladden, Sharon B. Melnick, and Jack M. Rogers. Lifetimes of epicardial rotors in panoramic optical maps of fibrillating swine ventricles. *American Journal of Physiology - Heart and Circulatory Physiology*, 291(4):H1935–H1941, 2006.

[LA88] Silvio H. Litovsky and Charles Antzelevitch. Transient outward current prominent in canine ventricular epicardium but not endocardium. *Circulation Research*, 62(1):116–126, 1988.

[LA93] Anton Lukas and Charles Antzelevitch. Differences in the electrophysiological response of canine ventricular epicardium and endocardium to ischemia. Role of the transient outward current. *Circulation*, 88(6):2903–2915, 1993.

[LA96] Anton Lukas and Charles Antzelevitch. Phase 2 reentry as a mechanism of initiation of circus movement reentry in canine epicardium exposed to simulated ischemia. *Cardiovascular Research*, 32(3):593–603, 1996.

[LGWQ17] Julian Landaw, Alan Garfinkel, James N. Weiss, and Zhilin Qu. Memory-induced chaos in cardiac excitation. *Physical Review Letters*, 118(13):138101, 2017.

[LHX04] Diane Lipscombe, Thomas D. Helton, and Weifeng Xu. L-type calcium channels: The low down. *Journal of Neurophysiology*, 92(5):2633–2641, 2004. PMID: 15486420.

[LKMGG07] Claudia Lerma, Trine Krogh-Madsen, Michael Guevara, and Leon Glass. Stochastic aspects of cardiac arrhythmias. *Journal of Statistical Physics*, 128(1-2):347–374, 2007.

[LLD+02] Gui-Rong Li, Chu-Pak Lau, Anique Ducharme, Jean-Claude Tardif, and Stanley Nattel. Transmural action potential and ionic current remodeling in ventricles of failing canine hearts. *American Journal of Physiology - Heart and Circulatory Physiology*, 283(3):H1031–H1041, 2002.

[LLLN04] Gui-Rong Li, Chu-Pak Lau, Tack-Ki Leung, and Stanley Nattel. Ionic current abnormalities associated with prolonged action potentials in cardiomyocytes from diseased human right ventricles. *Heart Rhythm*, 1(4):460–468, 2004.

[LQ18a] Julian Landaw and Zhilin Qu. Control of voltage-driven instabilities in cardiac myocytes with memory. *Chaos: An Interdisciplinary Journal of Nonlinear Science*, 28(11):113122, 2018.

[LQ18b] Julian Landaw and Zhilin Qu. Memory-induced nonlinear dynamics of excitation in cardiac diseases. *Physical Review E*, 97(4):042414, 2018.

[LR91] Ching-Hsing Luo and Yoram Rudy. A model of the ventricular cardiac action potential. Depolarization, repolarization, and their interaction. *Circulation Research*, 68(6):1501–1526, 1991.

[LR94] Ching-hsing Luo and Yoram Rudy. A dynamic model of the cardiac ventricular action potential. I. Simulations of ionic currents and concentration changes. *Circulation Research*, 74(6):1071–1096, 1994.

[LRV94] L. J. Leon, F. A. Roberge, and A. Vinet. Simulation of two-dimensional anisotropic cardiac reentry: Effects of the wavelength on the reentry characteristics. *Annals of Biomedical Engineering*, 22(6):592–609, 1994.

[Lüd09] Berndt Lüderitz. Historical perspectives of cardiac electrophysiology. *Hellenic Journal of Cardiology*, 50(1):3–16, 2009.

[MCKM14] Anat Maoz, David J. Christini, and Trine Krogh-Madsen. Dependence of phase-2 reentry and repolarization dispersion on epicardial and transmural ionic heterogeneity: A simulation study. *EP Europace*, 16(3):458–465, 2014.

[MCR92] John M. Morgan, David Cunningham, and Edward Rowland. Electrical restitution in the endocardium of the intact human right ventricle. *British Heart Journal*, 67(1):42–46, 1992.

[MDC+07] Stephane Masse, Eugene Downar, Vijay Chauhan, Elias Sevaptsidis, and Kumaraswamy Nanthakumar. Ventricular fibrillation in myopathic human hearts: Mechanistic insights from in vivo global endocardial and epicardial mapping. *American Journal of Physiology - Heart and Circulatory Physiology*, 292(6):H2589–H2597, 2007.

[MJ12] Robert J. Myerburg and M. Juhani Junttila. Sudden cardiac death caused by coronary heart disease. *Circulation*, 125(8):1043–1052, 2012.

[MJT08] Sergey Mironov, José Jalife, and Elena G. Tolkacheva. Role of conduction velocity restitution and short-term memory in the development of action potential duration alternans in isolated rabbit hearts. *Circulation*, 118(1):17–25, 2008.

[MKMC09] Anat Maoz, Trine Krogh-Madsen, and David J. Christini. Instability in action potential morphology underlies phase 2 reentry: A mathematical modeling study. *Heart Rhythm*, 6(6):813–822, 2009.

[MKMT14] Stephen D. McIntyre, Virendra Kakade, Yoichiro Mori, and Elena G. Tolkacheva. Heart rate variability and alternans formation in the heart: The role of feedback in cardiac dynamics. *Journal of Theoretical Biology*, 350:90–97, 2014.

[MMF+03] Shunichiro Miyoshi, Hideo Mitamura, Kana Fujikura, Yukiko Fukuda, Kojiro Tanimoto, Yoko Hagiwara, Makoto Ita, and Satoshi

Ogawa. A mathematical model of phase 2 reentry: Role of L-type Ca current. *American Journal of Physiology - Heart and Circulatory Physiology*, 284(4):H1285–H1294, 2003.

[MSS+08] Aman Mahajan, Yohannes Shiferaw, Daisuke Sato, Ali Baher, Riccardo Olcese, Lai-Hua Xie, Ming-Jim Yang, Peng-Sheng Chen, Juan G. Restrepo, Alain Karma, et al. A rabbit ventricular action potential model replicating cardiac dynamics at rapid heart rates. *Biophysical Journal*, 94(2):392–410, 2008.

[MZL+06] Hiroshi Morita, Douglas P. Zipes, John Lopshire, Shiho T. Morita, and Jiashin Wu. T wave alternans in an in vitro canine tissue model of Brugada syndrome. *American Journal of Physiology - Heart and Circulatory Physiology*, 291(1):H421–H428, 2006.

[NC13] NCHS and CDC. Underlying cause of death 1999-2013 on CDC WONDER online database. 2013.

[ND68] J. B. Nolasco and R. W. Dahlen. A graphic method for the study of alternation in cardiac action potentials. *Journal of Applied Physiology*, 25(2):191–196, 8 1968.

[NHCG98] Christopher A. Del Negro, Chie-Fang Hsiao, Scott H. Chandler, and Alan Garfinkel. Evidence for a novel bursting mechanism in rodent trigeminal neurons. *Biophysical Journal*, 75(1):174–182, 1998.

[NMC+06] Martyn P. Nash, Ayman Mourad, Richard H. Clayton, Peter M. Sutton, Chris P. Bradley, Martin Hayward, David J. Paterson, and Peter Taggart. Evidence for multiple mechanisms in human ventricular fibrillation. *Circulation*, 114(6):536–542, 2006.

[Nob62] D. Noble. A modification of the Hodgkin—Huxley equations applicable to Purkinje fibre action and pacemaker potentials. *The Journal of Physiology*, 160(2):317–352, 1962.

[NSX+15] Thao P. Nguyen, Neha Singh, Yuanfang Xie, Zhilin Qu, and James N. Weiss. Repolarization reserve evolves dynamically during the cardiac action potential: Effects of transient outward currents on early afterdepolarizations. *Circulation: Arrhythmia and Electrophysiology*, pages 694–702, 2015.

[NUF+11] Krishnakumar Nair, Karthikeyan Umapathy, Talha Farid, Stephane Masse, Erin Mueller, Radhika V. Sivanandan, Kwaku Poku, Vivek Rao, Vidhya Nair, Jagdish Butany, et al. Intramural activation during early human ventricular fibrillation. *Circulation: Arrhythmia and Electrophysiology*, 4(5):692–703, 2011.

[OGJ97] Niels F. Otani and Robert F. Gilmour Jr. Memory models for the electrical properties of local cardiac systems. *Journal of Theoretical Biology*, 187(3):409–436, 8 1997.

[Ota17] Niels F. Otani. Theory of the development of alternans in the heart during controlled diastolic interval pacing. *Chaos: An Interdisciplinary Journal of Nonlinear Science*, 27(9):093935, 2017.

[OVVR11] Thomas O'Hara, László Virág, András Varró, and Yoram Rudy. Simulation of the undiseased human cardiac ventricular action potential: Model formulation and experimental validation. *PLoS Computational Biology*, 7(5):e1002061, 2011.

[Pan98] Alexandre V. Panfilov. Spiral breakup as a model of ventricular fibrillation. *Chaos: An Interdisciplinary Journal of Nonlinear Science*, 8(1):57–64, 1998.

[PC90] Silvia G. Priori and Peter B. Corr. Mechanisms underlying early and delayed afterdepolarizations induced by catecholamines. *American Journal of Physiology - Heart and Circulatory Physiology*, 258(6):H1796–H1805, 1990.

[PCE10] A. Peñaranda, I. R. Cantalapiedra, and B. Echebarria. Slow pulse due to calcium current induces phase-2 reentry in heterogeneous tissue. In *2010 Computing in Cardiology*, pages 661–664, Sep. 2010.

[PCM+15] David S. Park, Marina Cerrone, Gregory Morley, Carolina Vasquez, Steven Fowler, Nian Liu, Scott A. Bernstein, Fang-Yu Liu, Jie Zhang, Christopher S. Rogers, et al. Genetically engineered SCN5A mutant pig hearts exhibit conduction defects and arrhythmias. *The Journal of Clinical Investigation*, 125(1):403–412, 2015.

[PG15] Sarah A. Park and Richard A. Gray. *Optical Mapping of Ventricular Fibrillation Dynamics*, pages 313–342. Springer International Publishing, Cham, 2015.

[PMR+01] Paola Pedarzani, Johannes Mosbacher, Andre Rivard, Lorenzo A. Cingolani, Dominik Oliver, Martin Stocker, John P. Adelman, and Bernd Fakler. Control of electrical activity in central neurons by modulating the gating of small conductance Ca^{2+}-activated K^+ channels. *Journal of Biological Chemistry*, 276(13):9762–9769, 2001.

[PP01] A. Panfilow and Arkady Pertsov. Ventricular fibrillation: Evolution of the multiple–wavelet hypothesis. *Philosophical Transactions of the Royal Society of London. Series A: Mathematical, Physical and Engineering Sciences*, 359(1783):1315–1325, 2001.

[PWM+10] Sandeep V. Pandit, Mark Warren, Sergey Mironov, Elena G. Tolkacheva, Jérôme Kalifa, Omer Berenfeld, and José Jalife. Mechanisms underlying the antifibrillatory action of hyperkalemia in guinea pig hearts. *Biophysical Journal*, 98(10):2091–2101, 2010.

[PYA17] Bence Patocskai, Namsik Yoon, and Charles Antzelevitch. Mechanisms underlying epicardial radiofrequency ablation to suppress arrhythmogenesis in experimental models of Brugada syndrome. *JACC: Clinical Electrophysiology*, 3(4):353–363, 2017.

[QDB+14] Xiao-Yan Qi, Jonas G. Diness, Bianca J. J. M. Brundel, Xiao-Bo Zhou, Patrice Naud, Chia-Tung Wu, Hai Huang, Masahide Harada, Mona Aflaki, Dobromir Dobrev, et al. Role of small-conductance calcium-activated potassium channels in atrial electrophysiology and fibrillation in the dog. *Circulation*, 129(4):430–440, 2014.

[QHGW14] Z. Qu, G. Hu, A. Garfinkel, and J. N. Weiss. Nonlinear and stochastic dynamics in the heart. *Physics Reports*, 543(2):61–162, 10 2014.

[QKX+00] Zhilin Qu, Jong Kil, Fagen Xie, Alan Garfinkel, and James N. Weiss. Scroll wave dynamics in a three-dimensional cardiac tissue model: Roles of restitution, thickness, and fiber rotation. *Biophysical Journal*, 78(6):2761–2775, 2000.

[QSW07] Zhilin Qu, Yohannes Shiferaw, and James N. Weiss. Nonlinear dynamics of cardiac excitation-contraction coupling: An iterated map study. *Physical Review E*, 75(1):011927, 2007.

[Qu04] Zhilin Qu. Nonlinear dynamic control of irregular cardiac rhythms. *Journal of Cardiovascular Electrophysiology*, 15(10):1186–1187, 2004.

[Qu11] Zhilin Qu. Chaos in the genesis and maintenance of cardiac arrhythmias. *Progress in Biophysics and Molecular Biology*, 105(3):247–257, 2011.

[QW15] Zhilin Qu and James N. Weiss. Mechanisms of ventricular arrhythmias: From molecular fluctuations to electrical turbulence. *Annual Review of Physiology*, 77:29–55, 2015.

[QWG97] Zhilin Qu, James N. Weiss, and Alan Garfinkel. Spatiotemporal chaos in a simulated ring of cardiac cells. *Physical Review Letters*, 78(7):1387, 1997.

[QWG99] Zhilin Qu, James N. Weiss, and Alan Garfinkel. Cardiac electrical restitution properties and stability of reentrant spiral waves: A simulation study. *American Journal of Physiology - Heart and Circulatory Physiology*, 276(1):H269–H283, 1999.

[QWG00] Zhilin Qu, James N. Weiss, and Alan Garfinkel. From local to global spatiotemporal chaos in a cardiac tissue model. *Physical Review E*, 61(1):727, 2000.

[QXGW00] Zhilin Qu, Fagen Xie, Alan Garfinkel, and James N. Weiss. Origins of spiral wave meander and breakup in a two-dimensional cardiac tissue model. *Annals of Biomedical Engineering*, 28(7):755–771, 2000.

[QXGW10] Zhilin Qu, Yuanfang Xie, Alan Garfinkel, and James N. Weiss. T-wave alternans and arrhythmogenesis in cardiac diseases. *Frontiers in Physiology*, 1:154, 2010.

[QXO+13] Zhilin Qu, Lai-Hua Xie, Riccardo Olcese, Hrayr S. Karagueuzian, Peng-Sheng Chen, Alan Garfinkel, and James N. Weiss. Early afterdepolarizations in cardiac myocytes: Beyond reduced repolarization reserve. *Cardiovascular Research*, 99(1):6–15, 2013.

[RA98] M. I. Rabinovich and H. D. I. Abarbanel. The role of chaos in neural systems. *Neuroscience*, 87(1):5–14, 1998.

[RBHH87] Richard B. Robinson, Penelope A. Boyden, Brian F. Hoffman, and Kenneth W. Hewett. Electrical restitution process in dispersed canine cardiac Purkinje and ventricular cells. *American Journal of Physiology - Heart and Circulatory Physiology*, 253(5):H1018–H1025, 1987.

[RE98] John Rinzel and G. B. Ermentrout. *Analysis of neural excitability and oscillations*, pages 251–291. MIT Press, 2 edition, 1998.

[Reu85] Harald Reuter. Membranes: A variety of calcium channels. *Nature*, 316(6027):391, 1985.

[RFK99] Wouter-Jan Rappel, Flavio Fenton, and Alain Karma. Spatiotemporal control of wave instabilities in cardiac tissue. *Physical Review Letters*, 83(2):456, 1999.

[Rod06] Dan M. Roden. Long QT syndrome: Reduced repolarization reserve and the genetic link. *Journal of Internal Medicine*, 259(1):59–69, 1 2006.

[Rod08] Dan M. Roden. Long-QT syndrome. *New England Journal of Medicine*, 358(2):169–176, 2008.

[Rul02] Nikolai F. Rulkov. Modeling of spiking-bursting neural behavior using two-dimensional map. *Physical Review E*, 65(4):041922, 2002.

[SAGB95] Jiong Sun, Farid Amellal, Leon Glass, and Jacques Billette. Alternans and period-doubling bifurcations in atrioventricular nodal conduc. *Journal of Theoretical Biology*, 173(1):79–91, 1995.

[SC73] M. F. Schneider and W. K. Chandler. Voltage dependent charge movement in skeletal muscle: A possible step in excitation–contraction coupling. *Nature*, 242(5395):244, 1973.

[SCC05] Andrey Shilnikov, Ronald L. Calabrese, and Gennady Cymbalyuk. Mechanism of bistability: Tonic spiking and bursting in a neuron model. *Physical Review E*, 71:056214, May 2005.

[SCG+07] David G. Schaeffer, John W. Cain, Daniel J. Gauthier, Soma S. Kalb, Robert A. Oliver, Elena G. Tolkacheva, Wenjun Ying, and Wanda Krassowska. An ionically based mapping model with memory for cardiac restitution. *Bulletin of Mathematical Biology*, 69(2):459–482, 2007.

[Sch06] Peter J. Schwartz. The congenital long QT syndromes from genotype to phenotype: Clinical implications. *Journal of Internal Medicine*, 259(1):39–47, 2006.

[SGS05] Zara Sands, Alessandro Grottesi, and Mark S. P. Sansom. Voltage-gated ion channels. *Current Biology*, 15(2):R44–R47, 2005.

[SJ90] Michael C. Sanguinetti and Nancy K. Jurkiewicz. Two components of cardiac delayed rectifier K^+ current. Differential sensitivity to block by class III antiarrhythmic agents. *The Journal of General Physiology*, 96(1):195–215, 1990.

[SNP09] T. K. Shajahan, Alok Ranjan Nayak, and Rahul Pandit. Spiral-wave turbulence and its control in the presence of inhomogeneities in four mathematical models of cardiac tissue. *PLoS One*, 4(3):e4738, 2009.

[SPD+14] Lasse Skibsbye, Claire Poulet, Jonas Goldin Diness, Bo Hjorth Bentzen, Lei Yuan, Utz Kappert, Klaus Matschke, Erich Wettwer, Ursula Ravens, Morten Grunnet, et al. Small-conductance calcium-activated potassium (SK) channels contribute to action potential repolarization in human atria. *Cardiovascular Research*, 103(1):156–167, 2014.

[SR03] Andrey L. Shilnikov and Nikolai F. Rulkov. Origin of chaos in a two-dimensional map modeling spiking-bursting neural activity. *International Journal of Bifurcation and Chaos*, 13(11):3325–3340, 2003.

[SR05] Jonathan Silva and Yoram Rudy. Subunit interaction determines I_{Ks} participation in cardiac repolarization and repolarization reserve. *Circulation*, 112(10):1384–1391, 2005.

[SSK05] Yohannes Shiferaw, Daisuke Sato, and Alain Karma. Coupled dynamics of voltage and calcium in paced cardiac cells. *Physical Review E*, 71(2):021903, 2005.

[SW05] Xiaoyin Sun and Hong-Sheng Wang. Role of the transient outward current (I_{to}) in shaping canine ventricular action potential–A dynamic clamp study. *The Journal of Physiology*, 564(2):411–419, 2005.

[SXN+10] Daisuke Sato, Lai-Hua Xie, Thao P. Nguyen, James N. Weiss, and Zhilin Qu. Irregularly appearing early afterdepolarizations in cardiac myocytes: Random fluctuations or dynamical chaos? *Biophysical Journal*, 99(3):765–773, 2010.

[SXS+09] Daisuke Sato, Lai-Hua Xie, Ali A. Sovari, Diana X. Tran, Norishige Morita, Fagen Xie, Hrayr Karagueuzian, Alan Garfinkel, James N. Weiss, and Zhilin Qu. Synchronization of chaotic early afterdepolarizations in the genesis of cardiac arrhythmias. *Proceedings of the National Academy of Sciences of the United States of America*, 106(9):2983–2988, 2009.

[TKL12] Qinghai Tian, Lars Kaestner, and Peter Lipp. Noise-free visualization of microscopic calcium signaling by pixel-wise fitting. *Circulation Research*, 111(1):17–27, 2012.

[TKN+08] Takeshi Tada, Kengo Fukushima Kusano, Satoshi Nagase, Kimikazu Banba, Daiji Miura, Nobuhiro Nishii, Atsuyuki Watanabe, Kazufumi Nakamura, Hiroshi Morita, and Tohru Ohe. Clinical significance of macroscopic T-wave alternans after sodium channel blocker administration in patients with Brugada syndrome. *Journal of Cardiovascular Electrophysiology*, 19(1):56–61, 2008.

[TM99] Gordon F. Tomaselli and Eduardo Marbán. Electrophysiological remodeling in hypertrophy and heart failure. *Cardiovascular Research*, 42(2):270–283, 1999.

[TRGG04] Elena G. Tolkacheva, Mónica M. Romeo, Marie Guerraty, and Daniel J. Gauthier. Condition for alternans and its control in a two-dimensional mapping model of paced cardiac dynamics. *Physical Review E*, 69:031904, 3 2004.

[TSGK03] Elena G. Tolkacheva, Daniel G. Schaeffer, Daniel J. Gauthier, and Wanda Krassowska. Condition for alternans and stability of the 1:1 response pattern in a "memory" model of paced cardiac dynamics. *Physical Review E*, 67:031904, 3 2003.

[TSY+09] Diana X. Tran, Daisuke Sato, Arik Yochelis, James N. Weiss, Alan Garfinkel, and Zhilin Qu. Bifurcation and chaos in a model of cardiac early afterdepolarizations. *Physical Review Letters*, 102(25):258103, 2009.

[tTNNP04] K. H. ten Tusscher, D. Noble, P. J. Noble, and A. V. Panfilov. A model for human ventricular tissue. *American Journal of Physiology - Heart and Circulatory Physiology*, 286(4):H1573–H1589, 2004.

[tTP06] Kirsten H. W. J. ten Tusscher and Alexander V. Panfilov. Alternans and spiral breakup in a human ventricular tissue model. *American Journal of Physiology - Heart and Circulatory Physiology*, 291(3):H1088–H1100, 2006.

[TXT+05] Dipika Tuteja, Danyan Xu, Valeriy Timofeyev, Ling Lu, Dipika Sharma, Zhao Zhang, Yanfang Xu, Liping Nie, Ana E. Vázquez, J. Nilas Young, et al. Differential expression of small-conductance Ca^{2+}-activated K^+ channels SK1, SK2, and SK3 in mouse atrial and ventricular myocytes. *American Journal of Physiology - Heart and Circulatory Physiology*, 289(6):H2714–H2723, 2005.

[TZ04] Gordon F. Tomaselli and Douglas P. Zipes. What causes sudden death in heart failure? *Circulation Research*, 95(8):754–763, 2004.

[VCMJ90] Alain Vinet, Dante R. Chialvo, Donald C. Michaels, and José Jalife. Nonlinear dynamics of rate-dependent activation in models of single cardiac cells. *Circulation Research*, 67(6):1510–1524, 1990.

[VIO+01] Laszlo Virag, Norbert Iost, Miklós Opincariu, Jenoó Szolnoky, János Szécsi, Gábor Bogáts, Pál Szenohradszky, András Varró, and Julius Gy Papp. The slow component of the delayed rectifier potassium current in undiseased human ventricular myocytes. *Cardiovascular Research*, 49(4):790–797, 2001.

[VYO+02] Miguel Valderrábano, Junzhong Yang, Chikaya Omichi, John Kil, Scott T. Lamp, Zhilin Qu, Shien-Fong Lin, Hrayr S. Karagueuzian, Alan Garfinkel, Peng-Sheng Chen, et al. Frequency analysis of ventricular fibrillation in swine ventricles. *Circulation Research*, 90(2):213–222, 2002.

[WGB+03] Mark Warren, Prabal K. Guha, Omer Berenfeld, Alexey Zaitsev, Justus M. B. Anumonwo, Amit S. Dhamoon, Suveer Bagwe, Steven M. Taffet, and José Jalife. Blockade of the inward rectifying potassium current terminates ventricular fibrillation in the guinea pig heart. *Journal of Cardiovascular Electrophysiology*, 14(6):621–631, 2003.

[Win83] Arthur T. Winfree. Sudden cardiac death. *Scientific American*, 248(5):144–161, 1983.

[WLB+04] Tsu-Juey Wu, Shien-Fong Lin, Ali Baher, Zhilin Qu, Alan Garfinkel, James N. Weiss, Chih-Tai Ting, and Peng-Sheng Chen. Mother rotors and the mechanisms of D600-induced type 2 ventricular fibrillation. *Circulation*, 110(15):2110–2118, 2004.

[WMT15] Ning Wei, Yoichiro Mori, and Elena G. Tolkacheva. The role of short term memory and conduction velocity restitution in alternans formation. *Journal of Theoretical Biology*, 367:21–28, 2015.

[WOGJ95] Mari Watanabe, Niels F. Otani, and Robert F. Gilmour Jr. Biphasic restitution of action potential duration and complex dynamics in ventricular myocardium. *Circulation Research*, 76:915–921, 1995.

[WP04] Runze Wu and Abhijit Patwardhan. Restitution of action potential duration during sequential changes in diastolic intervals shows multimodal behavior. *Circulation Research*, 94(5):634–641, 2004.

[WP06] Runze Wu and Abhijit Patwardhan. Mechanism of repolarization alternans has restitution of action potential duration dependent and independent components. *Journal of Cardiovascular Electrophysiology*, 17(1):87–93, 2006.

[WSS+95] Qing Wang, Jiaxiang Shen, Igor Splawski, Donald Atkinson, Zhizhong Li, Jennifer L. Robinson, Arthur J. Moss, Jeffrey A. Towbin, and Mark T. Keating. SCN5A mutations associated with an inherited cardiac arrhythmia, long QT syndrome. *Cell*, 80(5):805–811, 1995.

[XFJ03] Wen Xiong and James E. Ferrell Jr. A positive-feedback-based bistable 'memory module' that governs a cell fate decision. *Nature*, 426(6965):460, 2003.

[XFR+98] X.-M. Xia, B. Fakler, A. Rivard, G. Wayman, T. Johnson-Pais, J. E. Keen, T. Ishii, B. Hirschberg, C. T. Bond, Svetlana Lutsenko, et al. Mechanism of calcium gating in small-conductance calcium-activated potassium channels. *Nature*, 395(6701):503, 1998.

[XHS+07] Yuanfang Xie, Gang Hu, Daisuke Sato, James N. Weiss, Alan Garfinkel, and Zhilin Qu. Dispersion of refractoriness and induction of reentry due to chaos synchronization in a model of cardiac tissue. *Physical Review Letters*, 99(11):118101, 2007.

[XLG+15] Yuanfang Xie, Zhandi Liao, Eleonora Grandi, Yohannes Shiferaw, and Donald M. Bers. Slow $[Na]_i$ changes and positive feedback between membrane potential and $[Ca]_i$ underlie intermittent early afterdepolarizations and arrhythmias. *Circulation: Arrhythmia and Electrophysiology*, pages 1472–1480, 2015.

[XQGW01] Fagen Xie, Zhilin Qu, Alan Garfinkel, and James N. Weiss. Electrophysiological heterogeneity and stability of reentry in simulated cardiac tissue. *American Journal of Physiology - Heart and Circulatory Physiology*, 280(2):H535–H545, 2001.

[XQGW02] Fagen Xie, Zhilin Qu, Alan Garfinkel, and James N. Weiss. Electrical refractory period restitution and spiral wave reentry in simulated cardiac tissue. *American Journal of Physiology - Heart and Circulatory Physiology*, 283(1):H448–H460, 2002.

[XW09] Lai-Hua Xie and James N. Weiss. Arrhythmogenic consequences of intracellular calcium waves. *American Journal of Physiology - Heart and Circulatory Physiology*, 297(3):H997–H1002, 2009.

[YBS95] K. N. Yugay, N. V. Blinov, and I. V. Shirokov. Effect of memory and dynamical chaos in long josephson junctions. *Physical Review B*, 51(18):12737, 1995.

[ZCC+18] Xiao-Dong Zhang, Zana A. Coulibaly, Wei Chun Chen, Hannah A. Ledford, Jeong Han Lee, Padmini Sirish, Gu Dai, Zhong Jian, Frank Chuang, Ingrid Brust-Mascher, et al. Coupling of SK channels, L-type Ca^{2+} channels, and ryanodine receptors in cardiomyocytes. *Scientific Reports*, 8(1):4670, 2018.

[ZJT17] Sharon Zlochiver, Christopher Johnson, and Elena G. Tolkacheva. Constant DI pacing suppresses cardiac alternans formation in numerical cable models. *Chaos: An Interdisciplinary Journal of Nonlinear Science*, 27(9):093903, 2017.

[ZLC15] Xiao-Dong Zhang, Deborah K. Lieu, and Nipavan Chiamvimonvat. Small-conductance Ca^{2+}-activated K^+ channels and cardiac arrhythmias. *Heart Rhythm*, 12(8):1845–1851, 2015.

[ZLRR95] Jinglin Zeng, Kenneth R. Laurita, David S. Rosenbaum, and Yoram Rudy. Two components of the delayed rectifier K^+ current in ventricular myocytes of the guinea pig type: Theoretical formulation and their role in repolarization. *Circulation Research*, 77(1):140–152, 1995.

[ZW98] Douglas P. Zipes and Hein J. J. Wellens. Sudden cardiac death. *Circulation*, 98(21):2334–2351, 1998.

[ZXS+04] Stephen Zicha, Ling Xiao, Sara Stafford, Tae Joon Cha, Wei Han, Andras Varro, and Stanley Nattel. Transmural expression of transient outward potassium current subunits in normal and failing canine and human hearts. *The Journal of Physiology*, 561(3):735–748, 2004.

[ZXW+12] Zhenghang Zhao, Yuanfang Xie, Hairuo Wen, Dandan Xiao, Charelle Allen, Nadezhda Fefelova, Wen Dun, Penelope A. Boyden, Zhilin Qu, and Lai-Hua Xie. Role of the transient outward potassium current in the genesis of early afterdepolarizations in cardiac cells. *Cardiovascular Research*, 95(3):308–316, 2012.